MODELING, SCALEUP AND OPTIMIZATION OF SLURRY BUBBLE COLUMN

REACTORS FOR FISCHER-TROPSCH SYNTHESIS

by

Laurent Sehabiague

B.S. in Chemical Engineering and Chemistry, CPE Lyon, France, 2003

Submitted to the Graduate Faculty of

Swanson School of Engineering in partial fulfillment

of the requirements for the degree of

Doctor of Philosophy

University of Pittsburgh

2012

UNIVERSITY OF PITTSBURGH

SWANSON SCHOOL OF ENGINEERING

This dissertation was presented

by

Laurent Sehabiague

It was defended on

May 9, 2012

and approved by

Shiao-Hung Chiang, Ph.D., Professor, Department of Chemical & Petroleum Engineering

George E. Klinzing, Ph.D., Professor, Department of Chemical & Petroleum Engineering

Brian M. Gleeson, Ph.D., Professor, Department of Mechanical Engineering & Materials Science

Rachid Oukaci, Ph.D., Associate Professor, Department of Chemical & Petroleum Engineering

David R. Luebke, Ph.D., National Energy Technology Laboratory - U.S Department of Energy

Dissertation Director: Badie I. Morsi, Ph.D., Professor, Department of Chemical & Petroleum

Engineering

MODELING, SCALEUP AND OPTIMIZATION OF SLURRY BUBBLE COLUMN

REACTORS FOR FISCHER-TROPSCH SYNTHESIS

Laurent Sehabiague, PhD

University of Pittsburgh, 2012

The hydrodynamic and mass transfer parameters of gaseous mixtures of N_2 and He, used as surrogate components for CO and H_2 respectively, were measured in three Fischer-Tropsch (F-T) liquids in the presence and absence of solid particles (Al_2O_3, FeO_x). The data were obtained in a pilot-scale (0.29 m ID and 3 m high) slurry bubble column reactor (SBCR) within wide ranges of operating conditions covering those of F-T synthesis. The manometric method, the Transient Physical Gas Absorption technique and the Dynamic Gas Disengagement technique were employed to obtain the gas holdup, the volumetric liquid-side mass transfer coefficient and the gas bubbles Sauter mean diameter, respectively. Statistical experimental design was used to investigate the effect of these operating conditions on those parameters. The gas-liquid interfacial area appeared to control the mass transfer behavior of the SBCR operating in the churn-turbulent flow regime.

A user-friendly simulator based on a comprehensive computer model for F-T SBCRs, taking into account the hydrodynamics, kinetics, heat transfer, and mass transfer was developed. Novel hydrodynamic and mass transfer correlations, covering wide ranges of reactor geometry, gas distributor types, and operating conditions were established using our experimental data and those available in the literature; and a new relationship between the axial dispersion of large gas bubbles and their average diameter were developed and included in the reactor model. All reactor partial differential equations, equation parameters along with the pertinent boundary conditions were simultaneously solved numerically using the finite elements method. Different kinetic rate expressions available in the literature for iron and cobalt-based catalysts were included in the simulator which was used to predict the effects of the operating conditions, such

as catalyst concentration, pressure, temperature, H_2/CO ratio, and superficial gas velocity on the performance of an F-T SBCR. The predictions showed that the performance of the reactor was strongly dependent on the catalyst type and the kinetic rate expression used. The simulator was also used to optimize the reactor geometry and operating conditions in order to produce 10,000 barrels per day of synthetic hydrocarbons.

DESCRIPTORS

Absorption	Mass Transfer
Bubble size	Reactor Modeling
Dynamic Gas Disengagement	Sauter Mean Bubble Diameter
Fischer-Tropsch	Slurry Bubble Column Reactor
Gas Holdup	Statistical Experimental Design
Gas-Liquid Interfacial Area	Syngas
Hydrodynamics	Volumetric Mass transfer Coefficient

TABLE OF CONTENTS

LIST OF TABLES

xiii

LIST OF FIGURES

xviii

NOMENCLATURE

A	numerical constant,-
a	Gas-liquid interfacial area per unit liquid volume, m^{-1}
B	numerical constant,-
Be_{FT}	Dimensionless heat of the FT reaction, -
C	numerical constant,-
C*	Equilibrium gas solubility in the liquid, $mol.m^{-3}$
$C_{i,G}$	Concentration of component i in the gas phase, $mol.m^{-3}$
$C_{i,L}$	Concentration of component i in the liquid phase, $mol.m^{-3}$
$C_{P,L}$	Heat capacity of the liquid phase, J/kg/K
C_S	Catalyst concentration, $kg.m^{-3}$
C_V	Solid volumetric concentration, vol%
C_W	Solid weight concentration, wt%
d_{32}	Sauter mean bubble diameter, m
d_B	Bubble diameter, m
D_C	Column diameter, m
D_G	Gas dispersion coefficient, $m^2 s^{-1}$
D_i	Diffusivity of component i in wax, $m^2 s^{-1}$
D_L	Liquid dispersion coefficient, $m^2 s^{-1}$
d_o	Orifice diameter, m
d_P	Particles diameter, m
d_R	Reactor diameter, m
D_S	Solid particles dispersion coefficient, $m^2 s^{-1}$
d_T	Diameter of the tank, m
ΔE_i	Energy of activation, J/mol

F	Fanning factor, -
g	Acceleration due to gravity, $m\ s^{-2}$
h	Heat transfer coefficient, $W.m^{-2}.K^{-1}$
H_D	Dispersion height, m
He_i	Henry's Law constant of gas component i, $Pa.m^3.mol^{-1}$
$\Delta H_{R,i}$	Heat of reaction, J/mol
K	Pseudo kinetic constant, s^{-1}
k_{FT}	Rate constant of the FT reaction, units depend on reaction rate selected
k_L	Liquid-side mass transfer coefficient, $m.s^{-1}$
$k_L a$	Volumetric liquid-side mass transfer coefficient defined over liquid volume, s^{-1}
k_{pipes}	Heat transfer conductance of the cooling pipes, $J/m^2/s/K$
L	Reactor length, m
M_i	Molecular weight of species i, $kg.mol^{-1}$
M_w	Molecular weight of wax, $kg.mol^{-1}$
n_i	Number of moles of species i, moles
N_o	Number of Orifices in the gas distributor, -
n_{pipes}	Number of cooling pipes, -
P	Pressure, Pa
P_C	Critical pressure, Pa
P_m	Mean partial pressure of gas, Pa
P_S	Saturated vapor Pressure, Pa
P_T	Total Pressure, Pa
Q_G	Gas volumetric flow rate, $m^3.s^{-1}$
R	Universal gas constant, $J.mol^{-1}.K^{-1}$
r_i	Cooling tubes internal radius, m
r_o	Cooling tubes external radius, m
T	Temperature, K
T_{inlet}	Inlet gas/liquid temperature, K
T_C	Critical temperature, K

U_G	Superficial gas velocity, $m.s^{-1}$
U_L	Superficial liquid velocity, $m.s^{-1}$
U_P	Solid particles settling velocity, $m.s^{-1}$
U_{SL}	Superficial slurry velocity, $m.s^{-1}$
U_b	Bubble rise velocity $m.s^{-1}$
U_{TS}	Terminal settling velocity of solid particles, $m.s^{-1}$
V	Volume, m^3
v_L	Liquid molar volume, mol/m^3
V_{small}	small bubbles rise velocity, $m.s^{-1}$
x_i	Mole fraction of component i, -
z	Axial coordinates (reactor length), m
y	Steam mole fraction, -
Z	Compressibility factor, -

Greek Letters

δ	Film thickness, m
ε_G	Gas holdup, -
Ω	Heat resistance due to cooling pipes, K/W
λ_{pipes}	Heat conductivity of the cooling pipes, W/m/K
λ_R	Heat conductivity of reactor wall, W/m/K
μ	Viscosity, $kg.m^{-1}.s^{-1}$ or Pa.s
μ_{eff}	Effective viscosity, $kg.m^{-1}.s^{-1}$ or Pa.s
μ^0_w	Water viscosity at 298 K, $kg.m^{-1}.s^{-1}$ or Pa.s
ν	kinematic viscosity, m^2/s
ρ	Density, $kg.m^{-3}$
σ	Surface tension, $N.m^{-1}$
ω	Accentric factor, -
ζ	Open area of the gas distributor, $\zeta = N_o \left(\frac{d_o}{d_R}\right)^2$

Subscripts

G	Gas phase
i	Component i
In	Inlet
L	Liquid phase
Large	Large gas bubbles
Mix	Mixture
Out	Outlet
T	Total
S	Solid phase
Small	Small gas bubbles
SL	Slurry phase
W	Water

Acronyms

AARE	Average absolute relative error , -
BCR	Bubble column reactor
SBCR	Slurry bubble column reactor

Dimensionless Numbers

Froude Number
$$Fr = \frac{U_G}{\sqrt{g d_R}}$$

Peclet Number
$$Pe_\varphi = \frac{U_\varphi L}{D_\varphi}$$

Peclet Number for heat
$$Pe_H = Pe_L = \frac{U_L L}{D_L}$$

Peclet Number of the solid suspension
$$Pe_S = \frac{U_L L}{D_S}$$

Peclet Number of the solid particles
$$Pe_p = \frac{U_G d_R}{D_S}$$

Reynolds Number	$Re_G = \dfrac{\rho_L U_G d_R}{\mu_L}$
Reynolds Number (Solid particles)	$Re_G = \dfrac{\rho_L U_{TS} d_R}{\mu_L}$
Sherwood Number	$Sh = \dfrac{k_L a\, d_R^2}{D_{ij}}$
Stanton Number of Gas (large bubbles)	$St_{G,i,large} = \dfrac{L k_L a_{i,large} RT}{U_{G,inlet} He_i}$
Stanton Number of Gas (small bubbles)	$St_{G,i,small} = \dfrac{L k_L a_{i,small} RT}{U_{G,inlet} He_i}$
Stanton Number of heat transfer	$St_H = \dfrac{L U_{Heat}}{\rho_{SL} C_{P,SL} U_{SL}}$
Stanton Number of Liquid (large bubbles)	$St_{L,i,large} = \dfrac{L k_L a_{i,large}}{U_{SL}}$
Stanton Number of Liquid (small bubbles)	$St_{L,i,small} = \dfrac{L k_L a_{i,small}}{U_{SL}}$
Other Dimensionless Numbers	$\xi = \dfrac{z}{L}$
	$\tau_L = t\,\dfrac{U_L}{L}$
	$\tau_G = t\,\dfrac{U_{G,inlet}}{L}$
	$U'_{G,small} = \dfrac{U_{G,small}}{U_{G,inlet}}$
	$U'_{G,large} = \dfrac{U_{G,large}}{U_{G,inlet}}$
	$U'_P = \dfrac{U_P}{U_L}$
	$\theta = \dfrac{T}{T_{inlet}}$
	$\rho'_{SL} = \dfrac{\rho_{SL}}{\rho_{SL,0}}$

ACKNOWLEDGEMENTS

1.0   INTRODUCTION

Crude oil has been the main source of energy in the world for over a century; and progress, economy and energy policies of numerous countries are determined by its production and/or consumption. In 2007, the world oil production totaled about 81 million bbl/day and the US oil consumption was about 21 million bbl/day, almost 50% in the form of gasoline used in over 210 million motor vehicles traveling over 7 billion miles/day [1]. The US refineries produced 90% of the gasoline used. In 2006, the world's top five crude oil-producing countries are: Saudi Arabia, Russia, United States, Iran, and China. In the US, the top crude oil-producing states are: Texas, Alaska, California, Louisiana, and Oklahoma, where over one-fourth of the crude oil is produced offshore in the Gulf of Mexico. The amount of crude oil produced in the United States has been getting smaller each year; however, the use of products made from crude oil has been growing, making it necessary to bring more oil from other countries. Although the US is the world's third largest crude oil producer, less than 35% of the crude oil used by the refineries was produced in the US, and the net petroleum imports accounted for 58% of the total petroleum consumption. About 48% of the net petroleum imports were from countries in the western hemisphere, 18% from the Persian Gulf, 22% from Africa, and 12% from other regions. In the US, a refined one barrel (42 US gallon) of crude oil produces about 19.15 gallons of finished motor gasoline, 9.21 gallons of diesel, 3.82 gallons of jet fuel, 1.75 gallons of heating oil, 1.76 gallons of heavy fuel oil, 1.72 gallons of liquefied petroleum gases (LPG) and 7.27 gallons of other products. Most of these petroleum products are used to fuel cars, airplanes, and trucks, to heat homes, and to make diverse products, including polymers, plastics, medicines, ink, crayons, bubble gum, dishwashing liquids, deodorants, eyeglasses, records, tires, ammonia, heart valves, etc. [1]. Today, oil has become the backbone of the industrial revolution and modern civilization. It is largely used in transportation, buildings, medicine, roads, and warfare. It is also crucial to many

industries, including chemicals, petrochemicals and agriculture. Above all, it dominates the world energy and political scenes.

Unfortunately, oil is not an everlasting source of energy because studies in the last 50 years [2, 3] have shown that the world production would peak as a result of the rising world energy consumption and the continuous depletion of oil reserves. Predicting the peak of production year remains a difficult task and has not yet been accurately forecasted. Nevertheless, most of the studies agree that peaking would occur within few decades [4-6] as can be seen in the list of different projected peak dates presented in Table 1, which are taken from Hirsch et al. [7].

Table 1: Projections of the Peaking of World Oil Production

Projected Date	Reference
2006-2007	Bakhtiari [8]
2007-2009	Simmons [9]
After 2007	Skrebowski [10]
Before 2009	Deffeyes [11]
Before 2010	Goodstein [12]
Around 2010	Campbell [13]
After 2010	World Energy Council [14]
2010-2020	Laherrere [15]
2016	DOE EIA [16]
After 2020	Jackson et al. [17]
2025 or later	Davis [18]
No visible peak	Lynch [19]

The imminent peaking of world oil production and the need to reduce the dependency of oil-importing countries upon oil-exporting countries have been the major driving forces in the recent years to find alternative sources to oil.

In the 1920's, Franz Fischer and Hans Tropsch in Germany developed a process for producing synthetic hydrocarbons [20, 21] which is known as the Fischer-Tropsch (F-T) process. In this process, the synthesis gas, also known as syngas (Hydrogen and Carbon Monoxide), reacts in the presence of a catalyst to produce a mixture of liquid hydrocarbons. The syngas can be produced from nearly any carbon-bearing feedstock; therefore a large variety of sources ranging from natural gas or coal to biomass can be used. These resources put together represent a significantly large amount of energy (see Table 2 and Figure 1) that can be converted into useful F-T liquids.

Table 2: Worldwide Fossil Energy Reserves [22, 23]

Fossil energy	Units	Quantity
Oil	x 10^{12} tons	0.13 - 0.2
Coal	x 10^{12} tons	0.9 - 1.0
Natural Gas	x 10^{12} m^3	171 - 198

Figure 1 shows that whereas oil resources are only able to sustain current world consumption for a few decades, biomass, natural gas and especially coal can provide enough energy for many years to come. Coal alone could satisfy the current worldwide energy consumption for over 400 years while biomass provide a large source of renewable energy although some estimate that only a fraction (< 15%) could actually be used [23]. In addition, large numbers of stranded natural gas reserves, considered uneconomical until now due to problems of gas transportation, could be exploited by converting the natural gas into F-T transportable liquids [24]. Thus, synthetic fuels produced via F-T synthesis appear to be good candidates as alternative and/or complementary sources of fuel.
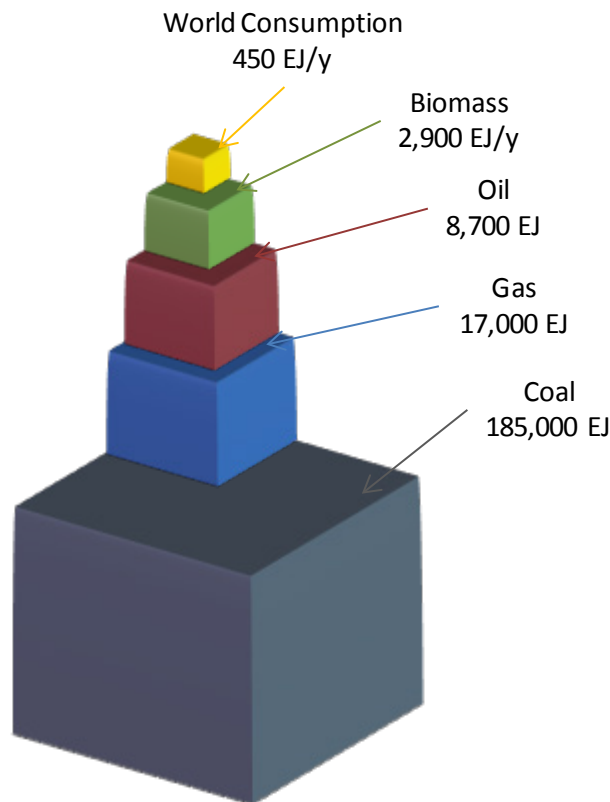
Figure 1: Order of Magnitude of Energy Resources (EJ = 10^{18} J) [25, 26]

The interest in using F-T synthesis has been arising in the last years mainly due to the concern about increasing crude oil prices [27] (see Figure 2). It was estimated that using F-T synthesis to produce fuels can become competitive if the price of the crude oil exceeded 20-24$/bbl [28-30] and more recently 50$/bbl [31] which has been clearly the case as can be seen in the trend of crude oil prices over the past 12 years presented in Figure 2.

Figure 2: Crude Oil Prices (World Average) over the Last 15 Years [1, 32]

The F-T synthesis is the central step in the Gas-To-Liquid (GTL), Coal-To-Liquid (CTL) or Biomass-To-Liquid (BTL) processes. These 3 processes can be summarized as the Everything/Anything-To-Liquid (XTL) process as shown in Figure 3. The first step involves the conversion of the initial resource into syngas. This is done via gasification in the case of biomass and coal or steam reforming and partial oxidation in the case of natural gas. Producing syngas from natural gas is less energy intensive and therefore more economical than from coal or biomass (gasification step). The syngas is cleaned and then sent into the F-T reactor where in the

presence of a catalyst it is converted into synthetic liquid hydrocarbons. Then upon further processing and upgrading, various products such as gasoline, diesel, naphtha and waxes are obtained.
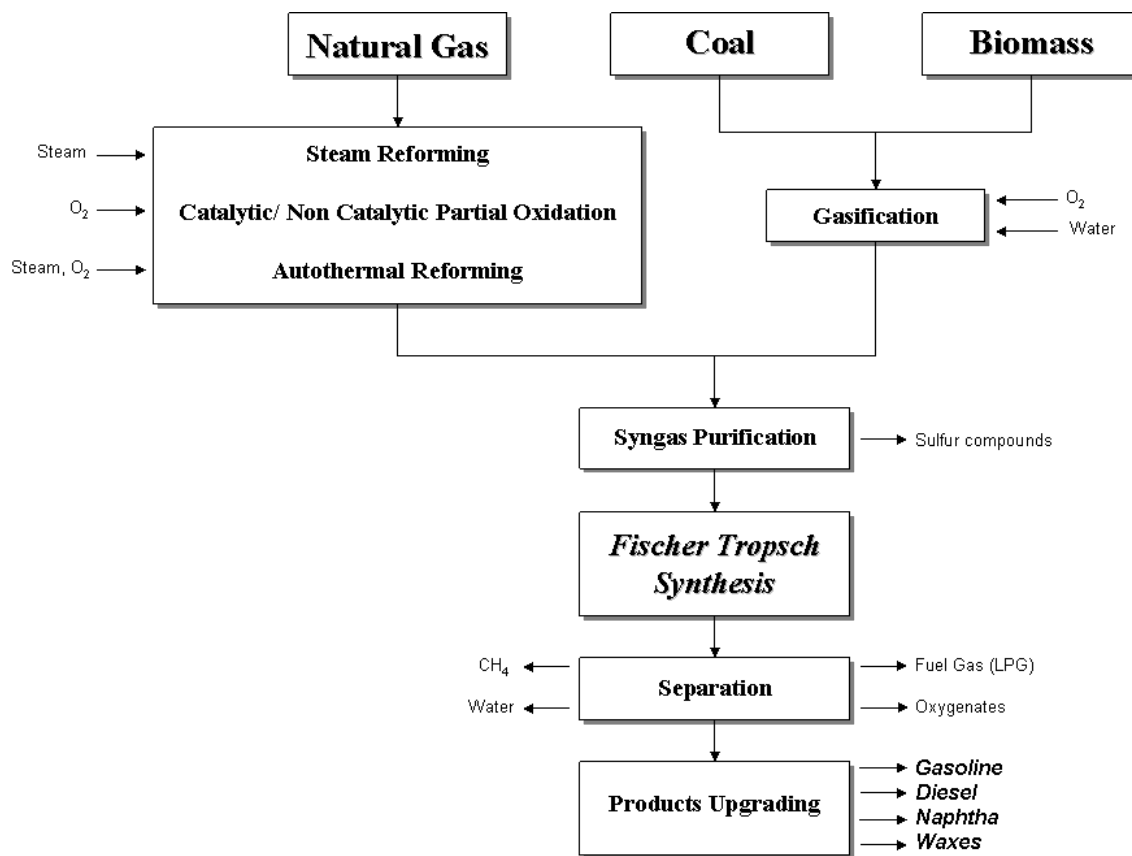
Figure 3: GTL, CTL and BTL Processes or XTL Process

Several types of multiphase reactors were proposed to carry out F-T reactions. They can be classified into three groups: fixed bed reactors, fluidized bed reactors, and slurry reactors. Fixed bed reactors (FBRs) have long been used for F-T synthesis since WWII. This type of reactors is relatively easy to scale-up, but has a high capital cost. In these reactors, the solid phase (catalyst) is stationary and the syngas flows through small diameter tubes packed with the catalyst. Therefore, a high-pressure drop is created inside the reactor due to its low voidage [33], (generally less than 40%). Since F-T synthesis is highly exothermic (ΔH = -165 kJ/mol [34]), the heat removal has been one of the major problem encountered when operating commercial F-T reactors. Coke formation on the catalyst surface due to high temperature (hot spots) is a serious

issue in fixed beds. Other types of reactors such as circulating fluidized-bed reactors (CFBRs) and fixed fluidized-bed reactors (FFBRs) were developed by Sasol (in South Africa) in order to improve the performance, but those reactors could only be used at high temperature and only produce volatile hydrocarbon products, such as gasoline.

It is known since the 1950's that slurry reactors could be used to carry out F-T synthesis. In this type of reactor, the solid-phase consists of fine catalyst particles suspended in a liquid-phase, which allows an efficient temperature control/removal. These reactors, however, have not been applied in a commercial scale until recently [27] due to the lack of existing reliable system to separate the fine catalyst from the liquid products (wax) and the limited knowledge of their hydrodynamics, mass/heat transfer characteristics, and flow patterns.

One type of slurry reactors appear to be of particular interest: Slurry Bubble Column Reactor (SBCR). In an SBCR, the Syngas is sparged through the liquid-phase from the bottom of the reactor inducing mixing and suspension of the catalyst particles. When the suspension of the catalyst is carried out not only by the gas, but also by the recirculation of the liquid-phase in the reactor, the reactor is sometimes called an Ebulating Bed Reactor (EBR). The advantage of EBRs over SBCRs is essentially the ability to use larger and heavier catalyst particles, which would not be suspended well enough by the gas flow alone.

The advantages of SBCRs over FBRs are [27, 35-37]:

- Better temperature control and heat removal
- Lower capital cost (~25% of that of a multi-tubular reactor) due to their relatively simple design
- Lower pressure drop (4 times less than in fixed bed reactor)
- Ability of using finer catalyst particles (<100 μm) allowing huge surface area and better mass transfer
- Higher yield per reactor volume
- Catalyst can be added and removed continuously, allowing longer runs since no shutdown are necessary.

Several challenges, inherent to the SBCRs, however, have to be considered [35]. They include the following:

- Important liquid back-mixing caused by the flow of the large gas bubbles

- Catalyst attrition and deactivation due to high shear created near the gas distributor
- Difficulty in separating fine solid particles from the viscous liquid (wax)
- Difficulty of scaleup due to complex flow dynamics

The design, modeling and scaleup of SBCRs for F-T synthesis require, among others, accurate knowledge of the kinetics, hydrodynamics, and heat as well as mass transfer characteristics of the gas-liquid-solid system used. More precisely, the kinetic rate expressions, liquid- and solid-side heat/mass transfer coefficients, gas, liquid and solid holdups/distributions, flow regimes and pressure drop, are the essential parameters needed for the modeling, design, and scaleup of such reactors. Furthermore, these parameters have to be obtained under actual F-T conditions, i.e., high pressure (10-45 bar), high temperature (450-610 K), and high gas throughput; large reactor diameter (up to 10 m), and high slurry concentration (up to 50 vol.%) which are required to achieve high space-time yields [38].

2.0   LITERATURE REVIEW

2.1   THE FISCHER-TROPSCH SYNTHESIS

The Fischer-Tropsch synthesis (initially called "Synthol") was developed in the 1920's in Germany at the Kaiser Wilhelm Institute by two German researchers, Franz Fischer and Hans Tropsch, with the intent of producing synthetic hydrocarbons [20, 21]. Their work was based on the 1902 discovery of Sabatier and Senderens [39] that methane can be produced from H_2 and CO in the presence of nickel catalyst. In the Fischer-Tropsch process, the synthesis gas (H_2 and CO) reacts in presence of a solid catalyst to produce a wide range of hydrocarbon products, such as olefins, paraffins and oxygenates (alcohols, aldehydes, acids, ketones, etc…). The F-T synthesis is a combination of oligomerization reactions which can be summarized as follows:

- n-Paraffins synthesis:

$$nCO + (2n + 1)H_2 \rightarrow C_nH_{2n+2} + nH_2O \qquad \text{(2-1)}$$

- 1-Olefins synthesis:

$$nCO + 2nH_2 \rightarrow C_nH_{2n} + nH_2O \qquad \text{(2-2)}$$

- Alcohols synthesis:

$$nCO + 2nH_2 \rightarrow C_nH_{2n+2}O + (n - 1)H_2O \qquad \text{(2-3)}$$

A simplified way to model the kinetics of the F-T synthesis is to represent the overall stoichiometry of the reaction by:

$$CO + \left(1 + \frac{m}{2n}\right)H_2 \xrightarrow{r_{FT}} \frac{1}{n}C_nH_m + H_2O \qquad \text{(2-4)}$$

The main products of the F-T synthesis are paraffins and the usage ratio H_2/CO is typically between the range of 2.06 to 2.16 [27, 40]. This reaction has been reported to be exothermic ($\Delta H^0 =$ -165 kJ/mol at 298 K [34]).

Side reactions may occur, including:

- Water Gas Shift (WGS) reaction, where the water (H_2O) produced by the F-T reaction reacts with carbon monoxide (CO) to form hydrogen (H_2) and carbon dioxide (CO_2):

$$CO + H_2O \overset{r_{WGS}}{\longleftrightarrow} CO_2 + H_2 \qquad (2\text{-}5)$$

The WGS reaction is also exothermic (ΔH^0 = - 41.2 kJ/mol at 298 K [41]).

- The Boudouard reaction may occur at very high temperature when hot spot are formed in the reactor due to an insufficient heat removal:

$$2CO \rightarrow C(s) + CO_2 \qquad (2\text{-}6)$$

This reaction is extremely exothermic (ΔH^0 = -170 kJ/mol at 298 K [42]). It produces coke on the catalyst surface leading to a significant decrease of the catalyst activity and must therefore be avoided.

- Hydrogenation of carbon monoxide to methane:

$$CO + 3H_2 \rightarrow CH_4 + H_2O \qquad (2\text{-}7)$$

- Oxidation/reduction of the catalyst:

$$M_xO_y + yH_2 \leftrightarrow yH_2O + xM$$
$$\qquad (2\text{-}8)$$
$$M_xO_y + yCO \leftrightarrow yCO_2 + xM$$
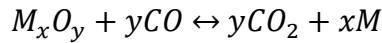
- Carbide formation:

$$xM + yC \leftrightarrow M_xC_y \qquad (2\text{-}9)$$

Two processes with different operating conditions are used industrially to carry out the F-T synthesis: the Low Temperature F-T (LTFT) process and the High Temperature F-T (HTFT) process. Table 3 summarizes the main characteristics of these 2 processes.

Table 3: LTFT and HTFT Processes Characteristics [27, 43]

	LTFT	HTFT
T (K)	450 – 530	570 - 620
P (bar)	10 – 45	~20
Products	Heavy Oil, Wax, Diesel	Gasoline

2.1.1 Catalysts

Two types of catalysts are commercially used in F-T synthesis, namely iron (Fe) and cobalt-based (Co) catalysts. Iron catalyst is cheap and has a high WGS activity and therefore it is best suited for CO rich syngas produced from coal gasification. However, it is prone to attrition and the water produced by the F-T synthesis may decrease its activity [24, 27]. Cobalt-based catalyst on the other hand has higher activity since it is not inhibited by water. It also has longer life than iron catalyst as it is more resistant to attrition. Cobalt-based catalyst, however, is more expensive (see Table 4). It also has no WGS activity and consequently it is best suited for H_2-rich syngas, such as that produced from natural gas reforming. It is important to note that both iron and cobalt-based catalysts are subject to poisoning by sulfur compounds. It is therefore recommended to keep the sulfur content in the syngas below 0.02 mg/m^3 at standard conditions of pressure and temperature [27]. Incidentally, this is the reason why F-T fuels contain very few amount of sulfur when compared with those produced from oil, and as such F-T fuels are considered more environmentally friendly.

Nickel- (Ni) and Ruthenium- (Ru) based catalyst have been used as F-T catalyst in the laboratory; however, they have not been used in industry. Nickel-based catalysts produce too much methane over most operating conditions and are poorly performing at high pressure due to the production of volatile carbonyls. Ruthenium-based catalysts, although they have high activity and produce high molecular weight compounds at low temperatures and high pressures, they are very expensive (see Table 4) and therefore could not yet be applied at industrial scale [27].

Table 4: Comparative prices of different catalysts based on Fe [27]

Catalyst type	Price index
Fe	1
Ni	250
Co	1000
Ru	50000

The cobalt-based catalyst supports commonly used in the industry include silica (SiO_2), titania (TiO_2), alumina (Al_2O_3), magnesia (MgO), activated carbon (C) and zeolites. A large range of oxides can be used as catalyst promoters, such as oxides of potassium (K), magnesium (Mg), aluminum (Al), silicium (Si), thorium (Th), zirconium (Zr), hafnium (Hf), cerium (Ce), uranium

(U), titanium (Ti), chromium (Cr), copper (Cu), selenium (Se), molybdene (Mo), manganese (Mn) and lanthanum (La). Noble metals, such as ruthenium (Ru), platinum (Pt), palladium (Pd), rhenium (Re), rhodium (Rh) and iridium (Ir), are also used as promoters [44].

2.1.2   Reaction Mechanism

Various authors have studied the reaction mechanisms of the F-T synthesis. Despite its complexity and the controversy in the research community over which reactions actually take place, most of them agree that the F-T synthesis involves a polymerization process with initiation, propagation and termination steps. The three main possible reaction mechanisms (see Figure 4) proposed are [36, 45, 46]:

- Carbide (also called carbene or alkyl) mechanism: it is the first historically proposed mechanism by Fischer and Tropsch in 1926 and it still remains the favorite mechanism among the research communities [46, 47]. In this mechanism, both CO and H_2 are dissociatively adsorbed on the catalyst surface. The adsorbed C and O are then hydrogenated into CH_2 and H_2O. The CH_2 adsorbed can then be further hydrogenated into CH_3 and/or insert itself into the carbon metal bond of an adsorbed C_nH_m species allowing the chain to grow. The termination may occur from the reduction by adsorbed hydrogen in order to give alkanes or by a β-elimination in order to yield α-olefins.

- Enol (also called oxygenates or hydroxy-carbene) mechanism: in this mechanism, H_2 reacts with CO adsorbed on the catalyst surface to form oxygenated intermediates CHOH-metal. The Chain growth occurs by surface condensation reactions of two of those intermediates, with elimination of water. The termination occurs by hydrogen assisted elimination of the –OH group.

- CO-insertion mechanism: it is similar to the carbene mechanism where an alkyl-metal species is formed. The Chain growth then occurs by direct insertion of a carbonyl intermediate (CO-metal) into the carbon metal bond. The termination is similar to that of the carbide mechanism.

It is important to note that none of the above mechanisms can successfully predict the whole products spectrum obtained using catalysts such as Fe, Co, Ni and Ru [46]. Instead, all three

mechanisms are likely to occur simultaneously with one or the other mechanism being favored depending on the catalyst used.

A recent study [47] of the F-T mechanism over a cobalt-based catalyst based on density functional theory (DFT) calculations and microkinetic simulations argued that another mechanism, where the formation of an oxymethylidyne (or formyl) CHO intermediate is the key step, is more likely to occur on cobalt-based catalyst than the carbide mechanism, however, this mechanism has yet to be confirmed experimentally.

2.1.3   Products Distribution

The products distribution of the F-T synthesis is often assumed to follow the Anderson-Schulz-Flory (ASF) distribution [36]. This simple model considers that the chain growth probability factor (α) (probability of adding a monomer to the carbon chain) is constant. Therefore, the number of moles of the products with n carbons can be related to the number of moles of products with n-1 carbons by:

$$n_{Cn} = \alpha n_{Cn-1} \tag{2-10}$$

The product distribution follows a geometric series as:

$$n_{Cn} = \alpha^{n-1} n_{C1} \tag{2-11}$$

The model assumes that every carbon atom adsorbed on the catalyst surface has $(1 - \alpha)$ probability to form a product with only one carbon (methane). Hence, the number of moles of products with only one carbon can be related to the total number of carbons in all products by:

$$n_{C1} = (1 - \alpha) n_{C,total} \tag{2-12}$$

This leads to:

$$n_{Cn} = \alpha^{n-1}(1 - \alpha) n_{C,total} \tag{2-13}$$

The total number of moles of products can be calculated as:

$$n_{Total} = \sum_n n_{Cn} = n_{C,total}(1 - \alpha) \sum_n \alpha^{n-1} \tag{2-14}$$

Assuming n becomes very large (approaching infinity), and $\alpha < 1$, the series will converge and Equation (2-14) can be simplified to:

$$n_{Total} = n_{C,total}(1 - \alpha) \frac{1}{1 - \alpha} = n_{C,total} \tag{2-15}$$
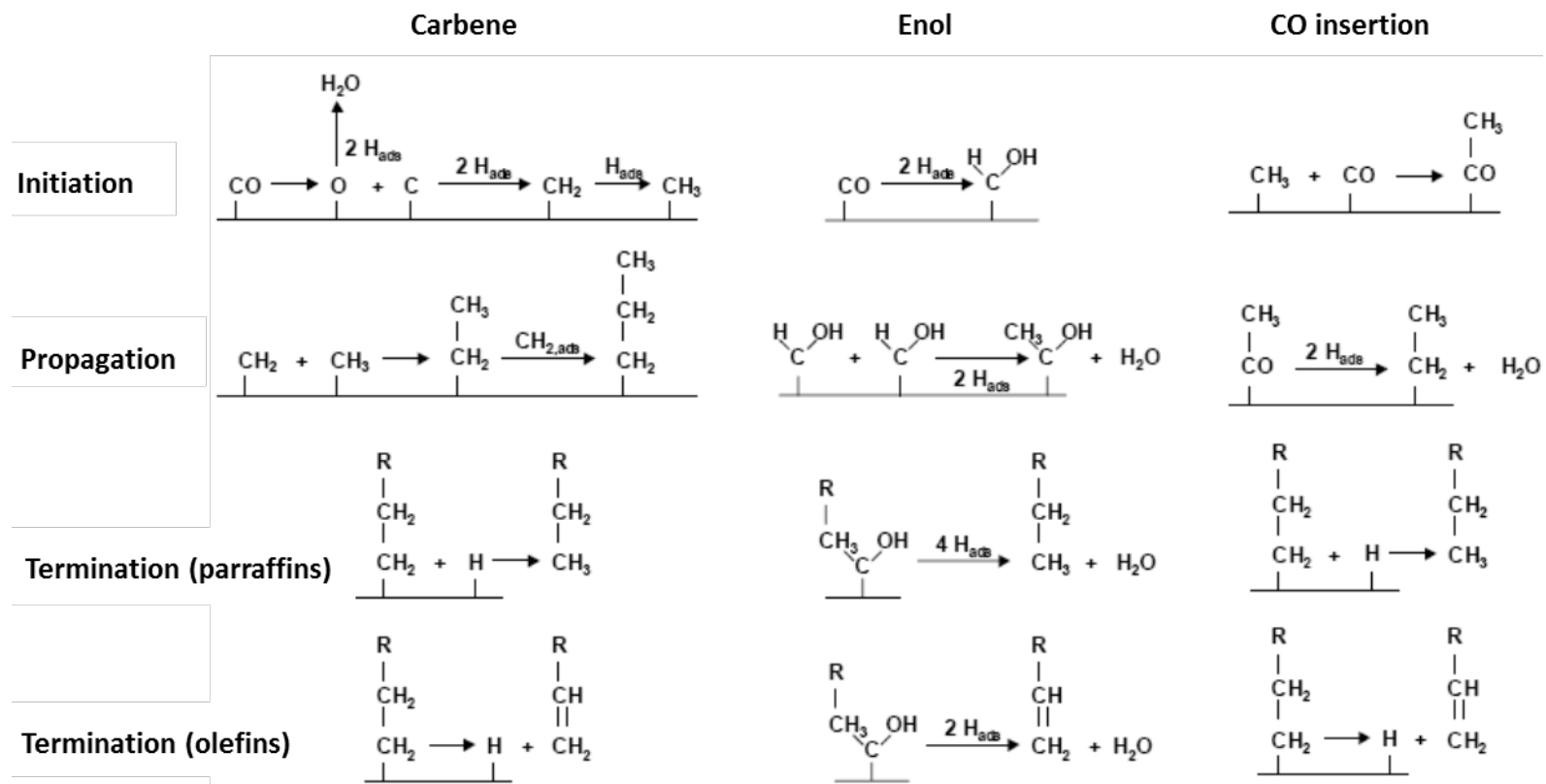
Figure 4: Main F-T Mechanisms [46]

The molar fraction of the n-carbons chain length products can then be calculated from Equations (2-13) and (2-15):

$$x_n = (1 - \alpha)\alpha^{n-1} \tag{2-16}$$

The mass fraction of the n-carbons chain length products can then be calculated:

$$w_n = \frac{x_n M_{W,Cn}}{\sum_n x_n M_{W,Cn}} = \frac{(1 - \alpha)\alpha^{n-1} M_{W,Cn}}{(1 - \alpha) \sum_n \alpha^{n-1} M_{W,Cn}} = \frac{\alpha^{n-1} M_{W,Cn}}{\sum_n \alpha^{n-1} M_{W,Cn}} \tag{2-17}$$

Since most products are linear paraffins and olefins, the molecular weight of n-carbons chain length products can be approximated as a function of their number of carbon atoms and a reference molecular weight independent of n:

$$M_{W,Cn} = n M_{W,ref} \tag{2-18}$$

Equation (2-17) then becomes:

$$w_n = \frac{\alpha^{n-1} n M_{W,ref}}{M_{W,ref} \sum_n n\alpha^{n-1}} = \frac{\alpha^{n-1} n}{\sum_n n\alpha^{n-1}} \tag{2-19}$$

The denominator in the above equation can be expressed as:

$$\sum_{n=1}^{\infty} n\alpha^{n-1} = \sum_{n=1}^{\infty} \alpha^{n-1} + \sum_{n=1}^{\infty} n\alpha^{n} \tag{2-20}$$

The two terms on the right-hand-side can be rewritten as:

$$\sum_{n=1}^{\infty} n\alpha^{n-1} = \frac{1}{1 - \alpha} + \alpha \sum_{n=1}^{\infty} n\alpha^{n-1} \tag{2-21}$$

Which leads to:

$$\sum_{n=1}^{\infty} n\alpha^{n-1} = \frac{1}{(1 - \alpha)^2} \tag{2-22}$$

Replacing this new expression for the denominator in Equation (2-19) gives:

$$w_n = \frac{\alpha^{n-1} n}{\frac{1}{(1 - \alpha)^2}} = (1 - \alpha)^2 n\alpha^{n-1} \tag{2-23}$$

The molar and mass fractions of the different products obtained in the F-T synthesis for a typical value of α (0.9) are shown in Figure 5. Jager and Espinoza [48] reported that for an existing pilot reactor, new iron and cobalt-based catalysts have shown α values between 0.8 and 0.95.

The actual product distributions of paraffins and olefins produced by Fischer-Tropsch synthesis have been found to obey this model relatively well except for C_1 and C_2 products [27].

Indeed, significant deviations have been reported in the literature [49-51] with higher yield of methane and lower yield of ethane/ethene than predicted by ASF distribution. Also, the chain growth probability factor has been observed in numerous studies to change after carbon number of about 10 [52] for both catalysts leading to the adoption of a double-α distribution model to take this phenomenon into account [53-55]. The superposition of 2-α distributions has been found experimentally to give a good approximation of the chain length distribution of products for both iron and cobalt-based catalysts [56]. In this 2-α model, 2 different growth probability factors (α_1 and α_2) are introduced for the small and long chain length products, respectively [52]. The resulting mole fraction of the n carbon chain length product can then be written as:

$$x_n = A\alpha_1^{n-1} + B\alpha_2^{n-1} \tag{2-24}$$
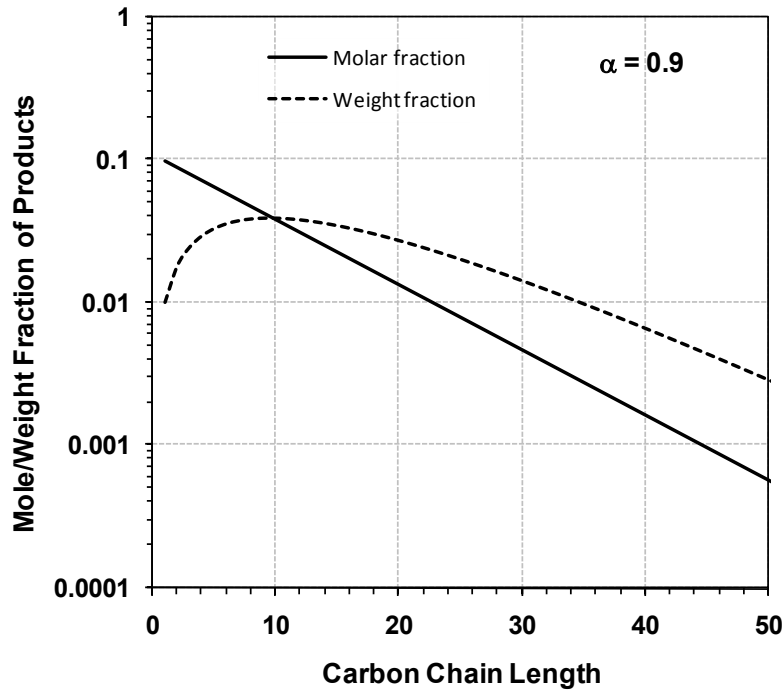
Figure 5: Typical F-T Products Distribution (ASF Model)

Coefficients A and B can be calculated by introducing the term ζ corresponding to the break point of the distribution where the contributions of both terms are equal and the fact that the sum of the mole fractions of each carbon product equals the unity:

$$A\alpha_1^{\xi-1} = B\alpha_2^{\xi-1} \tag{2-25}$$

15

$$\sum_n x_n = 1 \tag{2-26}$$

Equations (2-24) and (2-25) lead to:

$$x_n = A\left(\alpha_1^{n-1} + \left(\frac{\alpha_1}{\alpha_2}\right)^{\xi-1}\alpha_2^{n-1}\right) \tag{2-27}$$

This can be combined with Equation (2-26) to give:

$$\sum_n x_n = A\left(\sum_n \alpha_1^{n-1} + \left(\frac{\alpha_1}{\alpha_2}\right)^{\xi-1}\sum_n \alpha_2^{n-1}\right) = 1 \tag{2-28}$$

After simplifying the series, an expression for the constant A can be obtained:

$$A = \frac{1}{\dfrac{1}{1-\alpha_1} + \left(\dfrac{\alpha_1}{\alpha_2}\right)^{\xi-1}\dfrac{1}{1-\alpha_2}} \tag{2-29}$$

Inserting the above expression in Equation (2-25) allows an expression for B:

$$B = \frac{\left(\dfrac{\alpha_1}{\alpha_2}\right)^{\xi-1}}{\dfrac{1}{1-\alpha_1} + \left(\dfrac{\alpha_1}{\alpha_2}\right)^{\xi-1}\dfrac{1}{1-\alpha_2}} \tag{2-30}$$

The resulting mole fraction can therefore be expressed as [52]:

$$x_n = \frac{\alpha_1^{n-1} + \left(\dfrac{\alpha_1}{\alpha_2}\right)^{\xi-1}\alpha_2^{n-1}}{\dfrac{1}{1-\alpha_1} + \left(\dfrac{\alpha_1}{\alpha_2}\right)^{\xi-1}\dfrac{1}{1-\alpha_2}} \tag{2-31}$$

A typical 2-α product distribution is shown in Figure 6.

2.1.4   Kinetics of the Fischer-Tropsch Synthesis

The complexity of the F-T reaction mechanism and the numerous species involved in it are major obstacles to fully describe the kinetics of the F-T synthesis. In order to simplify the task, many empirical overall reaction rates have been developed in the literature. Latest studies, however, have focused on developing comprehensive kinetics based on Langmuir-Hinshelwood-Hougen-Watson (LHHW) approach since the variety of the products obtained from the F-T synthesis can only be explained and modeled by detailed kinetics models that include every

elementary reaction [57]. The reaction rates available in the literature for both iron and cobalt based catalysts are presented in the following section.

2.1.4.1 Iron Catalyst

Iron catalyst activity has been found to increase with the partial pressure of H_2 and decrease with partial pressure of H_2O [58, 59] suggesting a strong competition between CO and H_2O for the adsorption to the active sites of the catalyst. Indeed, the catalyst has a high WGS activity and therefore the rate of the WGS reaction along that of the F-T must be taken into account for simulation purposes. Numerous studies of the kinetics of the Fischer-Tropsch synthesis on iron catalyst, conducted mostly in fixed bed and slurry reactors, since the 1950's led to very different kinetic rate expressions as can be seen in Table 5. Only recently, however, comprehensive kinetic models, able to predict both the syngas consumption rate and products distribution, have been proposed [57, 60-64]. The diversity among the rate equations shown in Table 5 may arise from the diversity of the catalysts, reactors (mass transfer not always negligible) and operating conditions used in those studies. As a matter of fact, when choosing one of those expressions for modeling purposes, one has to select the correlation that has been developed within the conditions closest to the simulated ones.
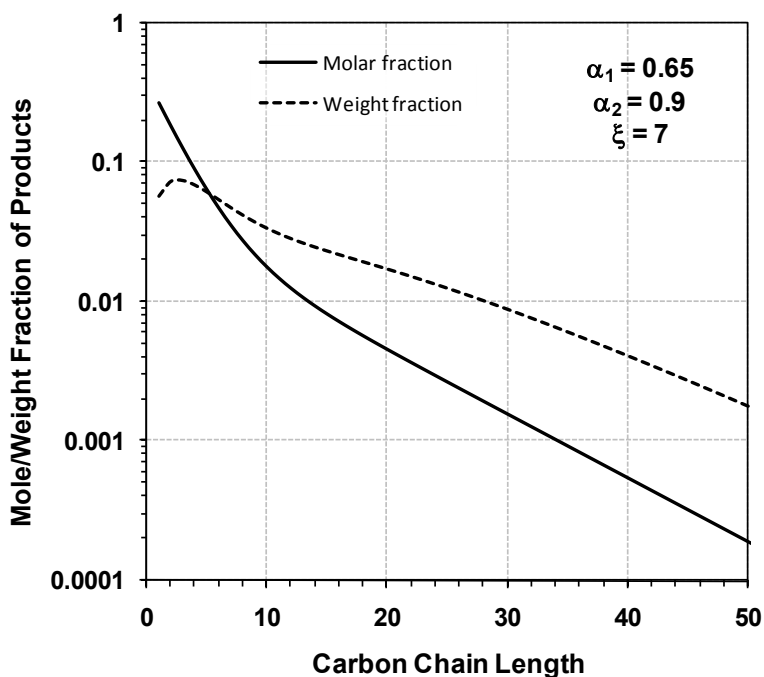
Figure 6: F-T Products Distribution (2-α Model)

17

Table 5: Kinetics Studies for the Fischer-Tropsch Synthesis on Iron Catalyst

Catalyst	Reactor	Operating Conditions			Equation	Reference
		T , C	P , MPa	H₂/CO feed		
Fe	Fixed Bed	-	-	-	$r_{FT} = k_{FT} P_{H_2}^2 P_{CO}$	Brotz [65] 1
Reduced Fused Fe/K₂O/MgO	Fixed Bed, Fluidized Bed, Slurry	250-320	2.2-4.2	2.0	$r_{FT} = k_{FT} P_{total}$	Hall et al.[66] 1
Reduced Nitrided Fe	Fixed Bed	-	-	-	$r_{FT} = k_{FT} P_{H_2}$ $r_{FT} = k_{FT} \dfrac{P_{H_2} P_{CO}}{P_{CO} + a P_{CO_2}}$	Anderson [67] 1
Reduced Nitrided Fused Fe	Fixed Bed	225-240	2.2	0.25-2.0	$r_{FT} = a P_{H_2}^{0.6} P_{CO}^{0.4} - b P_{H_2O}^{0.5} r_{FT}^{0.5}$	Anderson and Karn [68]
Fused Fe & Prec. Fe/Cu/MgO/K₂CO₃	Fixed Bed	200-280	10	3.1 2	$r_{FT} = a P_{H_2}^{1.5} P_{CO}^{0.2} + b P_{H_2O}^{0.2} P_{CO}^{0.5}$	Kolbel et al.[69] 1
Reduced Nitrided Fused Fe/Cr₂O₃/SiO₂/MgO/K₂O	Fixed Bed	225-255	2.2	0.25-2.0	$r_{FT} = k_{FT} P_{H_2}^{0.66} P_{CO}^{0.34}$	Anderson et al.[70] 1
Reduced Fused Fe/K₂O/Al₂O₃/SiO₂	Fixed Bed	225-265	1.0-1.8	1.2-7.2	$r_{FT} = k_{FT} P_{H_2}$	Dry et al.[71]
Fe	Fixed Bed, Fluidized Bed	200-340	0.5-4.0	1.0-7.3	$r_{FT} = k_{FT} \dfrac{P_{H_2} P_{CO}}{P_{CO} + a P_{H_2O}}$	Dry [72]
Reduced Nitrided Fused Fe/K₂O/Al₂O₃/SiO₂	Gradientless, Fixed Bed	250-315	2.0	2.0	$r_{FT} = k_{FT} \dfrac{P_{H_2} P_{CO}}{P_{CO} + a P_{H_2O}}$	Atwood and Bennett [73]
Plasma Sprayed Fe	Recirculating Reactor	250-300	0.77-3.1	1.5-3.9	$r_{FT} = k_{FT} \dfrac{P_{H_2} P_{CO}}{P_{CO} + a P_{H_2O}}$	Thomson et al.[74] 1
Reduced Prec. Fe/Cu/K₂O	Fixed Bed	220-270	1.0-2.0	1.0-6.0	$r_{FT} = k_{FT} \dfrac{P_{H_2}}{P_{CO}^{0.25}}$	Feimer et al.[75]
Reduced Fused Fe/K₂O/CaO/SiO₂	Slurry	232-263	0.4-1.5	0.5-1.8	$r_{FT} = k_{FT} \dfrac{P_{H_2}^2 P_{CO}}{P_{CO} P_{H_2} + a P_{H_2O}}$	Huff and Satterfield [76]

18

Table 5 (Cont'd)

Catalyst	Reactor	Operating Conditions			Equation	Reference
		T , C	P , MPa	H₂/CO feed		
Fe/Cu/K	-	265	-	-	$$r_{FT} = k_{FT} \frac{P_{H_2} P_{CO}}{P_{CO} + a P_{CO_2}}$$	Leib and Kuo [77] 3
Reduced Prec. Fe/K	Slurry	220-260	1.0	0.5-0.6	$$r_{FT} = k_{FT} \frac{P_{H_2} P_{CO}}{P_{CO} + a P_{CO_2}}$$	Ledakowicz et al. [78]
Prec. Fe & Fused Fe	Slurry	210-280	0.5-5.5	0.5-3.5	$$r_{FT} = k_{FT} \frac{P_{H_2} P_{CO}}{P_{CO} + a P_{H_2O}}$$ $$r_{FT} = k_{FT} \frac{P_{H_2} P_{CO}}{P_{CO} + a P_{CO_2}}$$	Nettelhoff et al.[79] 4
Reduced Prec. Fe/K	Slurry	220-260	-	0.5-2.0	$$r_{FT} = k_{FT} \frac{P_{H_2} P_{CO}}{P_{CO} + a P_{CO_2}}$$ $$r_{FT} = k_{FT} \frac{P_{H_2}^2 P_{CO}}{P_{CO} P_{H_2} + a P_{H_2O}}$$	Deckwer et al.[80]
Prec. Fe/Cu/K & Reduced Fe/Cu/K/SiO₂	Slurry	235-265	1.5-3.0	0.6-1.0	$$r_{FT} = k_{FT} P_{H_2}$$ $$r_{FT} = k_{FT} \frac{P_{H_2} P_{CO}}{P_{CO} + a P_{H_2O}}$$	Zimmerman and Bukur [37]

19

Table 5 (Cont'd)

Catalyst	Reactor	Operating Conditions			Equation	Reference
		T , C	P , MPa	H₂/CO feed		
Reduced Prec. Fe/CuO/K₂O/Na₂O/SiO₂	Fixed Bed	250-350	0.6-2.1	3.0-6.0	$$r_{C_nH_{2n+2}} = k_5 \frac{P_{H_2}\left(\dfrac{k_1 P_{CO}}{k_1 P_{CO} + k_5 P_{H_2}}\right)\alpha^{n-1}}{1 + \left(\dfrac{k_1 P_{CO}}{k_1 P_{CO} + k_5 P_{H_2}}\right)\dfrac{1}{1-\alpha}}$$ $$r_{C_nH_{2n}} = k_6 \frac{P_{H_2}\left(\dfrac{k_1 P_{CO}}{k_1 P_{CO} + k_5 P_{H_2}}\right)\alpha^{n-1}}{1 + \left(\dfrac{k_1 P_{CO}}{k_1 P_{CO} + k_5 P_{H_2}}\right)\dfrac{1}{1-\alpha}}$$ $$\alpha = \frac{k_1 P_{CO}}{k_1 P_{CO} + k_5 P_{H_2} + k_6}$$	Lox and Froment [60, 61]
Prec. Fe/Cu/K	Gradientless	230-264	1.0-2.6	1.1-2.4	$$r_{FT} = k_{FT}\frac{P_{H_2}P_{CO}}{P_{CO} + aP_{H_2O}}$$ $$r_{FT} = k_{FT}\frac{P_{H_2}^2 P_{CO}}{P_{CO}P_{H_2} + aP_{H_2O}}$$	Shen et al.[81] 4
Reduced Prec. Fe/Cu/K	Fixed Bed	220-300	1.0-3.2	1.1-2.8	$$r_{FT} = k_{FT}\frac{P_{H_2}P_{CO}}{P_{CO} + aP_{H_2O}}$$	Liu et al.[82]

Table 5 (Cont'd)

Catalyst	Reactor	Operating Conditions			Equation	Reference
		T , C	P , MPa	H₂/CO feed		
Reduced Prec. Fe/Cu/K/SiO$_2$	Spinning Basket	250	0.8-4.0	0.25-4.0	$$r_{FT} = k_{FT} \frac{P_{CO}P_{H_2}}{1 + aP_{CO} + bP_{H_2O}}$$ $$r_{FT} = k_{FT} \frac{P_{CO}P_{H_2}}{\left(1 + aP_{CO} + bP_{H_2O}\right)^2}$$ $$r_{FT} = k_{FT} \frac{P_{CO}P_{H_2}^{1/2}}{\left(1 + aP_{CO} + bP_{H_2O}\right)^2}$$	van der Laan and Beenackers [58, 83, 84]
Reduced Prec. Fe/Cu/K/SiO$_2$	Slurry	250	1.2-4.0	0.25-4.0	$$r_{FT} = k_{FT} \frac{P_{CO}P_{H_2}^{1/2}}{\left(1 + aP_{CO} + bP_{CO_2}\right)^2}$$	van der Laan [58]
Fe	Fixed Bed	220-260	2.4	1.87-2.0 5	$$r_{FT} = k_{FT} C_{H_2} \frac{1}{1 + 1.6 \frac{C_{H_2O}}{C_{CO}}}$$	Jess et al.[85]
Fe & Fe/Al$_2$O$_3$/Cu/K$_2$O & Fe/Mn/Cu/K$_2$O	Slurry	225-275	P$_{H2}$=0.26-3.02 P$_{CO}$=0.02-1.94-		$$r_{C,org} = \frac{k_{FT}(P_{H_2}^{3/2} \cdot P_{CO}/P_{H_2O})}{(1 + a \cdot (P_{H_2} \cdot P_{CO}/P_{H_2O}))^2}$$	van Steen and Schulz [86]
Fe & Fe/K	Slurry	200-240	1.0	1.0-3.0	$$r_{FT} = k_{FT}(P_{H_2})^x (P_{CO})^y$$	Eliason and Bartholomew [87]
Fe/Cu/K	-	-	-	-	Detailed kinetics including α-olefin readsorption using LHHW approach $$r_{CH_4} = f\left(P_{H_2}, P_{CO}, P_{H_2O}, P_{C_2H_4}, ..., P_{C_nH_{2n}}\right)$$ $$r_{C_nH_{2n+2}} = f\left(P_{H_2}, P_{CO}, P_{H_2O}, P_{C_2H_4}, ..., P_{C_nH_{2n}}\right)$$ $$r_{C_nH_{2n}} = f\left(P_{H_2}, P_{CO}, P_{H_2O}, P_{C_2H_4}, ..., P_{C_nH_{2n}}\right)$$	Wang et al.[62, 88]

Table 5 (Cont'd)

Catalyst	Reactor	Operating Conditions			Equation	Reference
		T , C	P , MPa	H$_2$/CO feed		
Reduced Fe/Cu/K	Fixed Bed	220-269	1.1-3.1	1.0-3.0	Detailed kinetics including α-olefin readsorption using LHHW approach $$r_{CH_4} = f\left(P_{H_2}, P_{CO}, P_{H_2O}, P_{C_2H_4}, ..., P_{C_nH_{2n}}\right)$$ $$r_{C_nH_{2n+2}} = f\left(P_{H_2}, P_{CO}, P_{H_2O}, P_{C_2H_4}, ..., P_{C_nH_{2n}}\right)$$ $$r_{C_nH_{2n}} = f\left(P_{H_2}, P_{CO}, P_{H_2O}, P_{C_2H_4}, ..., P_{C_nH_{2n}}\right)$$	Wang et al.[63]
Reduced Fe/Mn	Fixed Bed	267-327	1.0-3.0	1.0-3.0	Detailed kinetics including α-olefin readsorption using LHHW approach $$r_{CH_4} = f\left(P_{H_2}, P_{CO}, P_{H_2O}, P_{C_2H_4}, ..., P_{C_nH_{2n}}\right)$$ $$r_{C_nH_{2n+2}} = f\left(P_{H_2}, P_{CO}, P_{H_2O}, P_{C_2H_4}, ..., P_{C_nH_{2n}}\right)$$ $$r_{C_nH_{2n}} = f\left(P_{H_2}, P_{CO}, P_{H_2O}, P_{C_2H_4}, ..., P_{C_nH_{2n}}\right)$$	Yang et al.[64]
Fe/Mn & Fe/Cu/K	Spinning Basket	260-300	1.1-2.6	0.67-2.05	Detailed mechanisms based on elementary reactions via Langmuir-Hinshelwood-Hougen-Watson (LHHW) $$r_{CH_4OH} = f(P_{H_2}, P_{CO}, P_{H_2O}, ..., P_{C_nH_{2n}})$$ $$r_{CH_4} = f(P_{H_2}, P_{CO}, P_{H_2O}, ..., P_{C_nH_{2n}})$$ $$r_{C_nH_{2n+1}OH} = f(P_{H_2}, P_{CO}, P_{H_2O}, ..., P_{C_nH_{2n}})$$ $$r_{C_nH_{2n-1}OOH} = f(P_{H_2}, P_{CO}, P_{H_2O}, ..., P_{C_nH_{2n}})$$ $$r_{C_nH_{2n+2}} = f(P_{H_2}, P_{CO}, P_{H_2O}, ..., P_{C_nH_{2n}})$$ $$r_{C_nH_{2n}} = f(P_{H_2}, P_{CO}, P_{H_2O}, ..., P_{C_nH_{2n}})$$	Teng et al.[89]

Table 5 (Cont'd)

Catalyst	Reactor	Operating Conditions			Equation	Reference
		T , C	P , MPa	H$_2$/CO feed		
Fe/Cu/K/SiO$_2$	Slurry	250-290	1.0-2.5	0.67-1.5	Detailed kinetics based on insertion of methylene (CH$_2$) via alkylidene propagation mechanism including α-olefin readsorption using LHHW approach $$r_{CH_4} = f\left(P_{H_2}, P_{CO}, P_{H_2O}, P_{C_2H_4}, ..., P_{C_nH_{2n}}\right)$$ $$r_{C_nH_{2n+2}} = f\left(P_{H_2}, P_{CO}, P_{H_2O}, P_{C_2H_4}, ..., P_{C_nH_{2n}}\right)$$ $$r_{C_nH_{2n}} = f\left(P_{H_2}, P_{CO}, P_{H_2O}, P_{C_2H_4}, ..., P_{C_nH_{2n}}\right)$$	Chang et al.[57]

1 as reported in [76]
2 CO/H$_2$O feed
3 as reported in [37]
4 as reported in [58]
5. N$_2$ rich (50%) H$_2$/CO feed

Table 6: Kinetics Studies for the WGS Reaction on Iron Catalyst

Catalyst	Reactor	Operating Conditions			Equation	Reference
		T , C	P , MPa	H$_2$/CO feed		
Fe	Fixed Bed, Fluidized Bed	200-340	0.5-4.0	1.0-7.3	$r_{WGS} = k_{WGS} P_{CO}$	Dry [72]
Reduced Prec. Fe/Cu/K$_2$O	Fixed Bed	220-270	1.0-2.0	1.0-6.0	$r_{WGS} = k_{WGS} P_{CO}$	Feimer et al.[75]
Fe/Cu/K	-	265	-	-	$r_{WGS} = k_{WGS} \dfrac{\left(P_{H_2O} P_{CO} - \dfrac{P_{CO_2} P_{H_2}}{K_{eq}} \right)}{P_{CO} + a P_{H_2O}}$	Leib and Kuo [77] 1
Prec. Fe/Cu/K & Reduced Fe/Cu/K/SiO$_2$	Slurry	235-265	1.5-3.0	0.6-1.0	$r_{WGS} = k_{WGS} \dfrac{\left(P_{H_2O} P_{CO} - \dfrac{P_{CO_2} P_{H_2}}{K_{eq}} \right)}{P_{CO} + a P_{H_2O}}$ $r_{WGS} = k_{WGS} \dfrac{\left(P_{H_2O} P_{CO} - \dfrac{P_{CO_2} P_{H_2}}{K_{eq}} \right)}{P_{CO} P_{H_2} + a P_{H_2O}}$	Zimmerman and Bukur [37]
Reduced Prec. Fe/CuO/K$_2$O/Na$_2$O/SiO$_2$	Fixed Bed	250-350	0.6-2.1	3.0-6.0	$r_{WGS} = k_{WGS} \dfrac{\left(P_{H_2O} P_{CO} - \dfrac{P_{CO_2} P_{H_2}^{1/2}}{K_{eq}} \right)}{\left(1 + a \dfrac{P_{H_2O}}{P_{H_2}^{1/2}} \right)^2}$	Lox and Froment [60, 61]

24

Table 6 (Cont'd)

Catalyst	Reactor	Operating Conditions			Equation	Reference
		T , C	P , MPa	H₂/CO feed		
Prec. Fe/Cu/K	Gradientless	230-264	1.0-2.6	1.1-2.4	$$r_{WGS} = k_{WGS} \frac{\left(P_{H_2O} P_{CO} - \frac{P_{CO_2} P_{H_2}}{K_{eq}} \right)}{P_{CO} P_{H_2} + a P_{H_2O}}$$ $$r_{WGS} = k_{WGS} \frac{\left(P_{H_2O} P_{CO} - \frac{P_{CO_2} P_{H_2}}{K_{eq}} \right)}{P_{CO} + a P_{H_2O} + b P_{CO_2}}$$	Shen et al.[81]2
Reduced Prec. Fe/Cu/K/SiO₂	Spinning Basket	250	0.8-4.0	0.25-4.0	$$r_{WGS} = k_{WGS} \frac{\left(P_{H_2O} P_{CO} - \frac{P_{CO_2} P_{H_2}}{K_{eq}} \right)}{\left(1 + a P_{CO} + b P_{H_2O}\right)^2}$$ $$r_{WGS} = k_{WGS} \frac{\left(\frac{P_{H_2O} P_{CO}}{P_{H_2}^{1/2}} - \frac{P_{CO_2} P_{H_2}^{1/2}}{K_{eq}} \right)}{\left(1 + a P_{CO} + b P_{H_2O}\right)^2}$$	van der Laan and Beenackers [58, 83, 84]
Reduced Prec. Fe/Cu/K/SiO₂	Slurry	250	1.2-4.0	0.25-4.0	$$r_{WGS} = k_{WGS} \frac{\left(P_{H_2O} P_{CO} - \frac{P_{CO_2} P_{H_2}}{K_{eq}} \right)}{\left(P_{CO} + a P_{H_2O} \right)^2}$$	van der Laan [58]
Reduced Prec. Co/MnO	Micro-Fixed Bed	210-250	0.6-2.6	1.6-4.1	$$r_{WGS} = k_{WGS} P_f \left(P_{CO} - \frac{P_{CO_2} P_{H_2}}{K_{eq} P_{H_2O}} \right) \text{ with}$$ $$P_f = P^{\left(0.5 - P/250\right)}$$	Keyser et al.[90]

Table 6 (Cont'd)

Catalyst	Reactor	Operating Conditions			Equation	Reference
		T , C	P , MPa	H_2/CO feed		
Fe/Cu/K	-	-	-	-	$r_{WGS} = a \dfrac{\left(\dfrac{P_{H_2O} P_{CO}}{P_{H_2}^{1/2}} - \dfrac{P_{CO_2} P_{H_2}^{1/2}}{K_{eq}} \right)}{\left(1 + b \dfrac{P_{H_2O} P_{CO}}{P_{H_2}^{1/2}} \right)^2}$	Wang et al.[62, 88]
Reduced Fe/Cu/K	Fixed Bed	220-269	1.1-3.1	1.0-3.0	$r_{WGS} = a \dfrac{\left(\dfrac{P_{H_2O} P_{CO}}{P_{H_2}^{1/2}} - \dfrac{P_{CO_2} P_{H_2}^{1/2}}{K_{eq}} \right)}{\left(1 + b \dfrac{P_{H_2O} P_{CO}}{P_{H_2}^{1/2}} \right)^2}$	Wang et al.[63]
Reduced Fe/Mn	Fixed Bed	267-327	1.0-3.0	1.0-3.0	$r_{WGS} = a \dfrac{\left(\dfrac{P_{H_2O} P_{CO}}{P_{H_2}^{1/2}} - \dfrac{P_{CO_2} P_{H_2}^{1/2}}{K_{eq}} \right)}{\left(1 + b \dfrac{P_{H_2O} P_{CO}}{P_{H_2}^{1/2}} \right)^2}$	Yang et al.[64]
Fe/Mn & Fe/Cu/K	Spinning Basket	260-300	1.1-2.6	0.67-2.05	$r_{WGS} = a \dfrac{P_{CO} P_{H_2O} - \dfrac{P_{H_2} P_{CO2}}{K_{eq}}}{c P_{H_2}^{0.5} + P_{H_2} + d \dfrac{P_{CO} P_{H_2O}}{P_{H_2}}}$	Teng et al.[89]

Table 6 (Cont'd)

Catalyst	Reactor	Operating Conditions			Equation	Reference
		T , C	P , MPa	H$_2$/CO feed		
Fe/Cu/K/SiO$_2$	Slurry	250-290	1.0-2.5	0.67-1.5	$r_{WGS} = a \dfrac{\left(\dfrac{P_{H_2O} P_{CO}}{P_{H_2}^{1/2}} - \dfrac{P_{CO_2} P_{H_2}^{1/2}}{K_{eq}} \right)}{\left(1 + b \dfrac{P_{H_2O} P_{CO}}{P_{H_2}^{1/2}} \right)^2}$	Chang et al.[57]

[1] as reported in [37]
[2] as reported in [58]

2.1.4.2 Cobalt-Based Catalyst

The main difference between the kinetics of a cobalt-based catalyst and an iron catalyst is its inactivity towards the WGS reaction since H_2O is not adsorbed on the catalyst active sites. As a result, the WGS reaction can be neglected when modeling the kinetics of F-T synthesis using cobalt-based catalysts. Table 7 shows the kinetic rate expressions available in the literature for F-T cobalt-based catalysts.

2.1.5   Effect of Water

Water is produced by the F-T reaction and can be present in the reactor in large quantities, especially in the case of cobalt-based catalysts which possess a low WGS activity. The presence of water will affect the activity and the selectivity of the F-T synthesis. It has been found to increase C_{5+} selectivity and decrease CH_4 selectivity when using cobalt [91]. Also it has been reported that in the case of Al_2O_3 supported cobalt catalyst, the addition of water results in increased rate of deactivation [92]. The presence of water affects the solubilities of the syngas. Water at saturation level was found to increase the solubilities of both H_2 and CO in an F-T liquid with a more pronounced effect on H_2 (+110%) than CO (+50%) [93, 94]. The same water-saturated F-T liquid exhibited increased k_La values for CO and reduced k_La values for H_2 when compared with the water-free F-T liquid under the same total pressure in an agitated slurry reactor. This effect of water on the gas solubility and mass transfer in F-T liquids needs further investigation to understand such behavior.

Table 7: Kinetics Studies for the Fischer-Tropsch Synthesis on Cobalt-Based Catalyst

Catalyst	Reactor	Operating Conditions			Equation	Reference
		T , C	P , MPa	H₂/CO feed		
Co	-	-	-	-	$r_{FT} = k_{FT} \dfrac{P_{H_2}^2}{P_{CO}}$	Brotz [65] 1
Co/ThO₂/kieselguhr	-	-	-	-	$r_{FT} = k_{FT} \dfrac{P_{H_2}^2 P_{CO}}{1 + a P_{H_2}^2 P_{CO}}$	Anderson [67] 2
Co	-	-	-	-	$r_{FT} = k_{FT} P_{H_2} P_{CO}^{1/2}$	Yang et al.[95] 1
Co	-	-	-	-	$r_{FT} = k_{FT} \dfrac{P_{H_2}^{0.55}}{P_{CO}^{0.33}}$	Pannell et al.[96] 1
Reduced Prec. Co/Al₂O₃	Fixed Bed	250	0.015-0.1	0.25-5	$r_{FT} = k_{FT} \dfrac{P_{H_2} P_{CO}^{1/2}}{\left(1 + a P_{CO}^{1/2} + b P_{H_2}^{3/2}\right)}$	Rautavuoma and van der Baan [97]
Co/Kieselguhr	Berty	190	0.2-1.5	0.5-8.3	$r_{FT} = k_{FT} \dfrac{P_{H_2}^{1/2} P_{CO}^{1/2}}{\left(1 + a P_{CO}^{1/2} + b P_{H_2}^{1/2}\right)^2}$ $r_{FT} = k_{FT} \dfrac{P_{H_2}^{1/2} P_{CO}}{\left(1 + a P_{CO} + b P_{H_2}^{1/2}\right)^2}$	Sarup and Wojciechowski [98]
Co/Zr/SiO₂	Slurry	220-280	2.1	0.5-2.0	$r_{FT} = k_{FT} \dfrac{P_{H_2}^2 P_{CO}}{P_{CO} P_{H_2} + a P_{H_2O}}$	Withers et al.[99]
Co/MgO/SiO₂	Slurry	220-240	1.5-3.5	1.5-3.5	$r_{FT} = k_{FT} \dfrac{P_{H_2} P_{CO}}{\left(1 + a P_{CO}\right)^2}$	Yates and Satterfield [100]

Table 7 (Cont'd)

Catalyst	Reactor	Operating Conditions			Equation	Reference
		T , C	P , MPa	H₂/CO feed		
Co/MgO/ThO₂/SiO₂ & Co/SiO₂	Slurry	190-210	$P_{H_2} = 0.01\text{-}1.93$ $P_{CO} = 0.05\text{-}2.54$		$r_{C,org} = \dfrac{k_{FT}(P_{H_2}^{3/2} \cdot P_{CO} / P_{H_2O})}{(1 + a \cdot (P_{H_2} \cdot P_{CO} / P_{H_2O}))^2}$	van Steen and Schulz [86]
Reduced Prec. Co/MnO [3]	Micro-Fixed Bed	210-250	0.6-2.6	1.6-4.1	$r_{FT} = k_{FT} \dfrac{P_{H_2} P_{CO}}{P_{CO} + a P_{H_2O}}$	Keyser et al.[90]
Co/ZrO₂/SiO₂	Fixed Bed	200-230	1.5-4.0	1.0-3.0	Detailed kinetics based on alkyl mechanism considering olefin readsorption using LHHW approach $r_{CH_4} = f\left(P_{H_2}, P_{CO}, P_{H_2O}, P_{C_2H_4}, ..., P_{C_nH_{2n}}\right)$ $r_{C_nH_{2n+2}} = f\left(P_{H_2}, P_{CO}, P_{H_2O}, P_{C_2H_4}, ..., P_{C_nH_{2n}}\right)$ $r_{C_nH_{2n}} = f\left(P_{H_2}, P_{CO}, P_{H_2O}, P_{C_2H_4}, ..., P_{C_nH_{2n}}\right)$	Chang et al.[101]
Co/Al₂O₃	Fixed Bed (micro)	210-235	0.8-2.5	1.8-2.7	Detailed kinetics based on elementary reactions in terms of θ (fraction of the catalyst sites occupied by species)	Visconti et al.[102]
Co/Al₂O₃	Slurry	220	2.0	1.6-3.35	Detailed kinetics based on hydrocarbon productions considering olefin readsorption based on van Steen and Schulz $r_{C,org} = k_{FT} \dfrac{P_{H_2}^{3/2} P_{CO}}{\left(P_{H_2O} + a P_{H_2} P_{CO}\right)^2}$	Anfray et al.[103]

[1] as reported in [48]
[2] as reported in [90]
[3] this catalyst was WGS active

2.2   F-T REACTORS

2.2.1   Fixed-Bed Reactors

The high exothermicity of the F-T synthesis and consequently the heat removal are major issues encountered when operating commercial F-T reactors. The first commercial reactors designed for the F-T synthesis came on stream in 1955 at Sasol (South Africa). They consisted of 5 multitubular ARGE reactors (Figure 7) containing more than 2000 tubes of 0.05 m diameter, 12 m long packed with iron catalyst and surrounded by water. This type of reactors is relatively easy to scale up but has a high capital cost. In these reactors, the syngas flows through small diameter tubes packed with the catalyst. Therefore, a high-pressure drop is created inside the reactor due to its low voidage [33] (generally < 40%), and high energy is needed to push the syngas through the reactor increasing the operating cost. This type of reactor has been successfully used to carry out the LTFT process, however, it is risky to use it in the HTFT process since the high temperatures used in the latter process could lead to carbon deposits on the catalyst surface and serious plugging of the reactor tubes [104].

2.2.2   Fluidized-Bed Reactors

In an attempt to carry out the HTFT process and improve conversion and catalyst life, fluidized bed reactors have been developed (see Figure 7). These include Circulating-Fluidized-Bed Reactors and Fixed-Fluidized-Bed Reactors.

2.2.2.1 Circulating-Fluidized-Bed Reactors

In a circulating-fluidized bed reactor (CFBR), the gas flow entrains some of the fine catalysts particles along with it where the reaction takes place. The gaseous products and unreacted gas then leave at the top of the reactor through a cyclone while the catalyst particles are recycled back through a side arm or standpipe. No liquid products appear in the reactor.
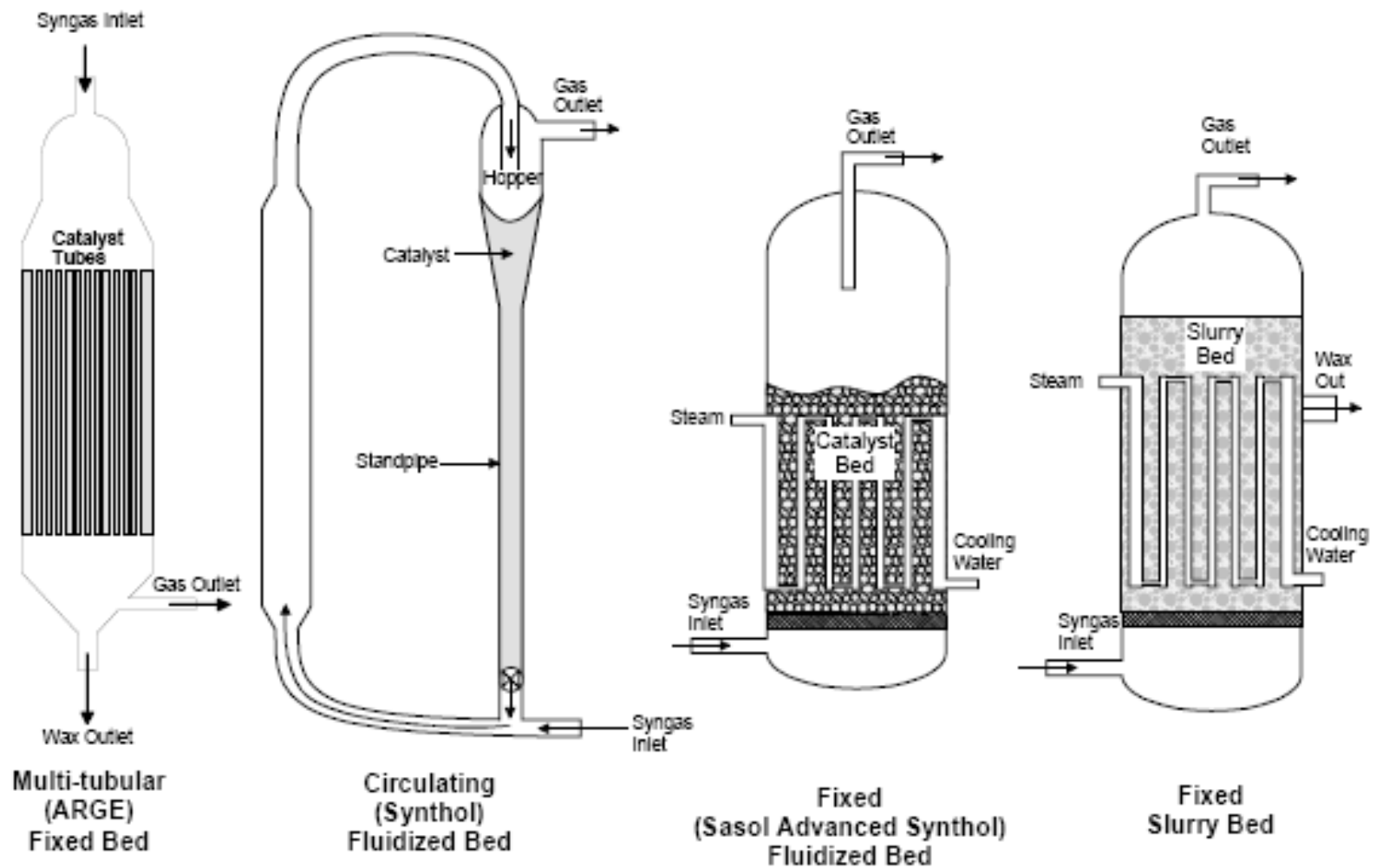
Figure 7: Commercial F-T Reactors [105]

2.2.2.2 Fixed-Fluidized-Bed Reactors

In a fixed-fluidized bed reactor (FFBR), the catalyst is also in the form of fine catalyst particles which are suspended inside the reactor by the upward flow of gas reactants. The bed of catalyst is "fixed", i.e., the solid particles height is stationary. The FFBR has several advantages over the CFBR [104]: its capital cost is 50% lower; the pressure drop and therefore its operating cost is also lower; and higher catalysts holdup can be achieved in the FFBR. The FFBR and CFBR require the products to be volatile in order to avoid wetting of the catalysts particles which could cause particles agglomeration and lead to defluidization of the catalyst bed [104]. They are therefore best suited to carry out the HTFT process that yields low carbon number products, such as gasoline.

2.2.3   Slurry Reactors

The alternatives to FBRs for the production of heavy wax (LTFT process) are the slurry reactors which can be classified into 2 types: Slurry Bubble Column Reactors (SBCRs) and Ebulating Bed Reactors (EBRs).

2.2.3.1 Slurry Bubble Column Reactors

In an SBCR, the solid phase consists of fine catalyst particles suspended in a stationary or slow moving liquid-phase. The mixing and suspension of the solid phase is achieved by the flowing gas reactants through the slurry-phase in an upward manner. The presence of a liquid-phase allows efficient heat transfer and therefore better temperature control permitting the reactor to be run at higher temperatures and subsequently higher conversions. The SBCRs have a relatively simple design and thus have smaller capital costs when compared with the multitubular reactors. However, their commercial development has been delayed because of a lack of existing reliable system to separate the fine catalyst particles from the liquid products. The first efficient filtration device was developed in 1990 and 3 years after the first F-T commercial slurry reactor was commissioned at Sasol in South Africa [27]. Advantages of slurry reactors over fixed bed reactors include [27, 35-37]: better temperature control/removal; lower capital cost (~25% of that of a multi-tubular reactor) due to their relatively simple design; low pressure drop (4 times less than in

33

fixed bed reactor); ability of using fine catalyst particles (<100 μm) allowing huge surface area and better mass transfer; higher yield per reactor volume; and catalyst can be added and removed continuously, allowing longer runs since no shutdown are necessary. However, the important liquid back-mixing caused by the flow of the large gas bubbles; the high shear created near the gas distributor may cause catalyst attrition and deactivation; the important side products obtained due to the high liquid to solid ratio; the difficulty in separating the fine solid particles from the viscous liquid (wax); and the complex flow dynamics make the scaleup of SBCRs a difficult task.

2.2.3.2 Ebulating Bed Reactors

An EBR is basically an SBCR in which the solid particles are held in suspension mostly by the upward movement of the liquid-phase rather than only the gas-phase as in SBCR. A typical EBR therefore operates at higher superficial liquid velocities than those in SBCRs, allowing the use of larger and denser catalyst particles. The advantages of slurry reactors over FBRs and the fact that FFBRs and CFBRs can only be used under HTFT process conditions make them a technology of choice to carry out the LTFT process. This is outlined in Table 8 which represents a list of the planned and existing F-T plants around the world. As can be seen in this table, the majority of F-T plants rely on the slurry technology. Companies such as Sasol and Rentech are already focusing on slurry reactors, while Shell seems to favor the old fixed-bed technology.

2.2.4   Other Types of Reactors

As a mean to intensify the F-T process, other types of reactors are being investigated at laboratory and pilot scales. Such efforts include [106]: honeycomb monolithic reactors which could be used to carry out the LTFT process, microstructured reactors, and membrane reactors. The monolithic reactors are characterized by low pressure drop, good catalyst utilization, and highly efficient mass transfer; also the liquid products can be recycled and used to remove the heat of reaction using an external heat exchanger. The costs associated with external heat removal and the monolithic geometry; however, remain too high for a commercial-scale. Microreactors allow higher conversions and better temperature control than monolithic reactors, but are plagued with challenges such as plugging of the micro channels, replacement of

deactivated catalyst and the cost of scaling up the "micro-geometry". Membrane reactors add some interesting features, such as distributed feed of reactants, in situ removal of water, forced-through membrane contactor, in addition to the use of zeolite encapsulated catalysts, which allow hydrocracking and isomerization of the products. Concerns about sealing, heat removal, membrane material and high cost of membrane module, however, remain important obstacles to their commercial development.

2.3 SBCR HYDRODYNAMICS AND MASS TRANSFER CHARACTERISTICS

2.3.1 Flow Regimes

In SBCRs, the gas-phase is conventionally sparged in the slurry from the bottom of the reactor through a specially-designed distributor, leading to different flow regimes and complex hydrodynamic as well as mass/heat transfer behaviors. There are no flow regime maps available in the literature for SBCRs or EBRs, however, several flow regime maps were proposed to delineate the hydrodynamic flow regimes in Bubble Column Reactors (BCRs), including the one by Oshinowo and Charles [107], which identifies six different flow regimes in an upward flow; and that by Deckwer et al. [108] based on the reactor diameter and gas velocity for air/water system. From these observations it can be concluded that for 3-phase reactors such as SBCRs and EBRs, 3 main types of flow regimes may occur [109-111] depending upon the operating conditions and reactor/distributor geometry.

2.3.1.1 Homogeneous Flow

In BCRs operating with superficial gas velocities ≤ 0.05 m/s, the homogeneous (also called bubbly or dispersed) flow regime prevails, which is characterized by a homogeneous gas bubbles distribution, weak interactions among gas bubbles and between gas and liquid phases, almost constant gas bubbles residence time, sharp unimodal size distribution of the gas bubbles and almost no liquid back-mixing. In this regime, the gas injection point was reported to have a

strong impact on the gas bubbles formation, whereas the reactor diameter was not as important [112, 113].

2.3.1.2 Slug Flow

In small BCRs with internal diameters ≤ 0.15 m, increasing the superficial gas velocity could lead to the formation of large gas bubbles in the reactor, which is designated as a slug flow regime. In this regime, the wall effect [114, 115] is important and has a strong impact on the hydrodynamic and mass transfer parameters. Liquid properties, such as high viscosity has also been found to facilitate the formation of slugs even at low superficial gas velocities [116]. The slug flow regime exhibits very poor mixing and mass transfer. It is, however, mostly observed in small laboratory reactors and would not occur in large-scale industrial reactors.

2.3.1.3 Heterogeneous or Churn-Turbulent Flow

In large-scale BCRs, increasing the superficial gas velocity above a certain point (> 0.05-0.1 m/s) increases the interactions among the gas bubbles, and enhances the coalescence and break-up of these bubbles creating a wider bubbles size distribution [109]. This leads the reactor to operate in the heterogeneous (also called churn-turbulent or coalesced bubble [110]) flow regime. In this regime, large and fast-rising gas bubbles induce strong circulations and create back-mixing or re-circulation zones wherein the small gas bubbles are entrained [117-119]. This regime is therefore characterized by strong gas-liquid mixing and optimal mass/heat transfer. Visual observations and photographic methods revealed the coexistence of distinctly two classes of gas bubbles (small and large) in BCRs [119-123] operating in the churn-turbulent flow regime.

2.3.1.4 Transitional Flow

The transition from homogeneous flow to heterogeneous flow is characterized by the formation of local liquid recirculation patterns in the reactor created by the increasing population of large gas bubbles [109]. The knowledge of this transitional flow is important for the design and scaleup of industrial reactors as the hydrodynamics and mass transfer properties dramatically change during this regime.

Table 8: Planned and Existing F-T Plants in the World

Plant Name	Country/Location	Capacity (bbl/day)	Start Date	Status	Type	FT Process	Reactor	Catalyst	Resource
Sasol	South Africa/Sasolburg	8,000	1955	Existing	Commercial	Sasol	Fixed-bed	Fe	CTL
Sasol	South Africa/Secunda	160,000	1980	Existing	Commercial	Sasol	CFB	Fe	CTL
Sasol	South Africa/Sasolburg	100	1983	Existing	Commercial	Sasol	Advanced Synthol	Fe	GTL
Sasol	South Africa	100	1990	Existing	Pilot	Sasol	Slurry	Fe	GTL
Syntroleum	USA/Tulsa, OK	2	1990	Closed	Pilot	Syntroleum	Slurry		GTL
Rentech Colorado	USA/Pueblo, CO	235	1992	Closed	Pilot	Rentech	Slurry	Fe/Co	GTL
Petro SA/StatoilHydro/Lurgi	South Africa/Mossel Bay	36,000	1992	Existing	Commercial	Sasol	Synthol CFB	Fe	GTL
DOE	USA/LaPorte, TX	35	1992	Existing	Pilot		Slurry		GTL
Exxon Mobil	USA, Baton Rouge, LA	200	1993	Closed	Pilot	Exxon AGC 21	Slurry	Co	GTL
Sasol	South Africa/Sasolburg	2,500	1993	Existing	Commercial	Sasol	Slurry	Fe	GTL
Shell/Petronas/Mitsubishi Corporation	Malaysia/Bintulu	14,700	1993	Existing	Commercial	SMDS	Fixed-bed	Co	GTL
BP Amoco/ARCO (Cherry Point)	USA/Cherry Point, WA	70	1999	Closed	Pilot	Syntroleum	Slurry	Co	GTL
Synergy/Stone Canyon Resources	Canada/Calgary	4	2000	Existing	Pilot	SynGen			GTL
Synfuels	USA/TX	12	2000	Existing	Pilot				GTL
IFP/ENI	Italy	20	2001	Existing	Pilot	IFP/ENI			GTL
Donyi Polo Petrochemicals Ltd.	India/Arunachal Pradesh	360	2001	Existing	Commercial	Rentech	Slurry	Fe/Co	GTL
BP Amoco (Nikiski)	USA/Nikiski, AK	300	2002	Existing	Pilot	BP/Kvaerner			GTL
Conoco	USA/Ponca City, OK	400	2002	Closed	Pilot	Conoco			GTL
JNOC Tomakomai	Japan/Hokkaido	7	2002	Existing	Pilot	JNOC-TRC			GTL
Petro SA/StatoilHydro	South Africa/Mossel Bay	1,000	2004	Existing	Pilot	Statoil	Slurry	Co	GTL
Syntroleum/Marathon	USA/Tulsa, OK	70	2004	Existing	Pilot	Syntroleum	Slurry		GTL
Sasol Chevron/QP (Oryx)	Qatar/Ras Laffan	34,000 TBE 100,000	2007	Existing	Commercial	Sasol	Slurry		GTL
Compact GTL	UK, Wilton	0.15	2008	Existing	Pilot	Compact GTL	Fixed-bed		GTL
World GTL Inc./Petrotrin	Trinidad/Pointe-a-Pierre	2,250	2008	Existing	Commercial	Worlf GTL	Fixed-bed	Co	GTL
Shenhua (Erdos CTL)	China/Inner Mongolia	22,200	2009	Existing	Commercial				CTL
CHOREN	Germany/Freiberg	300	2010	Existing	Commercial	SMDS	Fixed-bed	Co	BTL
Peabody Energy/Rentech	USA/East Dubuqe, IL	6,000	2010	Planned	Commercial	Rentech	Slurry	Fe	CTL
Baard Energy/Ohio Clean Fuels	USA/Wellsville, OH	53,000	2012	Planned	Commercial	Rentech	Slurry		GTL
Rentech	USA/Rialto, CA	640	2012	Planned	Commercial	Rentech	Slurry		BTL
Chevron Nigeria Ltd./Sasol Synfuel International (Escravos GTL)	Nigeria/Escravos	34,000	2012	Planned	Commercial	Sasol	Slurry	Fe	GTL
Sasol Chevron	Australia	30,000	2012	Planned	Commercial	Sasol	Slurry		GTL
Shell (Pearl GTL)	Qatar	140,000	2012	Planned	Commercial	SMDS	Fixed-bed	Co	GTL

Table 8 (Cont'd)

Plant Name	Country/Location	Capacity (bbl/day)	Start Date	Status	Type	FT Process	Reactor	Catalyst	Resource
Velocys/Toyo Engr/MODEC	Offshore Location		2012	Planned	Commercial	Velocys	Microchannels		GTL
Shell/Shenhua	China/Ningxia	70,000	2012	Potential	Commercial	SMDS	Fixed-bed	Co	CTL
Sasol/Shenhua	China/Shaanxi	80,000	2012	Potential	Commercial	Sasol			CTL
Petrobras	Brazil/Aracaju	20	2012	Potential	Commercial	Compact GTL	Fixed-bed		GTL
Sasol	South Africa	80,000	2016	Planned	Commercial	Sasol			CTL
Sasol/Shenhua	China/Ningxia	80,000	2016	Planned	Commercial	Sasol			CTL
Anglo American/Shell	Australia	60,000	2016	Planned	Commercial	SMDS	Fixed-bed	Co	CTL
Narkangan GTL	Iran/Shiraz	12,500		Planned	Commercial				GTL
Rentech	USA/Natchez, MS	30,000		Planned	Commercial	Rentech	Slurry	Fe	CTL
Sicor	Ethiopia	20,000		Planned	Commercial				GTL
WMPI	USA/Gilberton, PA	5,000		Planned	Commercial	Sasol			CTL
KUFPEC/Syntroleum	Papua New Guinea/Gulf of Papua	50,000		Planned	Commercial	Syntroleum	Slurry	Co	GTL
YPFB/Franklin Mining	Bolivia/Santa Cruz	10,000		Planned	Commercial	Rentech	Slurry		GTL
Orobos steel facility	Sweden			Potential	Commercial	Rentech	Slurry		GTL
Peabody Energy/Rentech	USA/MT	1,250		Potential	Commercial	Rentech	Slurry	Fe	CTL
Sasol Chevron/QP	Qatar/Ras Laffan	130,000		Potential	Commercial	Sasol	Slurry		GTL
Ivanhoe Energy/Egyptian Natural Gas Holding Co.	Egypt			Potential	Commercial	Syntroleum	Slurry	Co	GTL
AK Nat. Gas to Liquids (North Slope)	USA/AK	70,000		Potential	Commercial	Sasol or Rentech	Slurry		GTL
Syntroleum	Papua New Guinea/Moresby	50,000		Potential	Commercial	Syntroleum	Slurry	Co	GTL
Syntroleum/PT Elnusa	Indonesia			Potential	Commercial	Syntroleum	Slurry	Co	GTL
Sasol	India	80,000		Potential	Commercial				CTL
Syntroleum/Sustec Industries AG	Germany/Spreetal	3,000 TBE 20,000		Potential	Commercial	Syntroleum	Slurry	Co	CTL
Yakutgazprom	Russia/Yakutsk	13,000		Potential	Commercial	Syntroleum	Slurry	Co	GTL
Bechtel	Bolivia	50,000		Potential	Commercial				GTL
ConocoPhillips/QP	Qatar	80,000		Cancelled	Commercial	ConocoPhillips			GTL
Exxon Mobil/QP	Qatar	154,000		Cancelled	Commercial	Exxon AGC 21	Slurry	Co	GTL
PDVSA	Venezuela	15,000		Cancelled	Commercial	Intevep	Slurry	Co	GTL
FT Solutions/GTI	USA/Des Plaines, IL	10		Cancelled	Pilot	Rentech	Slurry		GTL
Pertamina	Indonesia	15,000		Cancelled	Commercial	Rentech	Slurry		GTL
Shell	Argentina	75,000		Cancelled	Commercial	SMDS	Fixed-bed	Co	GTL
Shell/EGPC	Egypt/West Demiatta	75,000		Cancelled	Commercial	SMDS	Fixed-bed	Co	GTL
ENAP	Chile	10,000		Cancelled	Commercial	Syntroleum	Slurry	Co	GTL

38

Table 8 (Cont'd)

Plant Name	Country/Location	Capacity (bbl/day)	Start Date	Status	Type	FT Process	Reactor	Catalyst	Resource
Ivanhoe	Qatar	185,000		Cancelled	Commercial	Syntroleum	Slurry	Co	GTL
Marathon/QP	Qatar	120,000		Cancelled	Commercial	Syntroleum	Slurry	Co	GTL
Repsol/Syntroleum	Bolivia	103,500		Cancelled	Commercial	Syntroleum	Slurry	Co	GTL
Syntroleum	Australia/Burrup peninsula	11,500		Cancelled	Commercial	Syntroleum	Slurry	Co	GTL
Syntroleum/BPZ	Peru/Talara Basin	5,000		Cancelled	Commercial	Syntroleum	Slurry	Co	GTL
Forest Oil	South Africa	12,500		Cancelled	Commercial				GTL
PDVSA	Venezuela	100		Cancelled	Pilot		Slurry	Co	GTL
Rentech	Papua New Guinea/Wewak	15,000		Cancelled	Commercial				GTL
	Algeria/Tinrhert	36,000		Cancelled	Commercial				GTL

2.3.2 Gas Holdup

The gas holdup (ε_G) defined as the fraction of the volume occupied by the gas phase is an important hydrodynamic parameter [124]. In SBCRs and EBRs, it can be derived as:

$$\varepsilon_G = \frac{V_G}{V_G + V_L + V_S} \qquad (2\text{-}32)$$

Gas holdup has a direct impact on the performances of the reactor since the heat and mass transfer are dependent upon it through the gas liquid interfacial area. It strongly depends upon the operating conditions, the physical properties of the gas-liquid-solid system used, and reactor geometry (see Figure 9). Thus, the precise knowledge of the effects of all these parameters on the gas holdup is therefore of prime importance in order to design and scale-up SBCRs.

2.3.3 Gas Bubbles Sizes

The knowledge of the bubble size distribution in SBCRs is important. The size of the gas bubbles present combined with the gas holdup will determine how much interfacial area is available for the transfer of the gaseous species to and from the liquid-phase. The distribution of the sizes and shapes of the gas bubbles will mostly be influenced by the flow regime in which the SBCR is operating as described previously and will be affected by the operating conditions, the physical properties of the gas-liquid-solid system used as well as the reactor geometry.

2.3.4 Mass Transfer

2.3.4.1 Resistances to Mass Transfer

In an F-T SBCR, all the following steps have to be considered in order to describe the transfer process of the reactants and products through the different phases:

- Transfer of the reactants from the gas-phase to the gas-liquid interface
- Transfer of the reactants form the gas-liquid interface to the liquid bulk
- Mixing and diffusion of the reactants in the bulk liquid phase

- Transfer of the reactants to the external surface of the catalyst particles
- Diffusion of the reactants inside the catalyst pores to the catalyst active sites
- Conversion of the reactants into products on the catalyst active sites
- Diffusion of the products from the catalyst active sites to the external surface of the catalyst
- Transfer of the products from the catalyst to liquid bulk
- Mixing and diffusion of products in the liquid bulk
- Transfer of the products from the liquid bulk to the gas-liquid interface
- Transfer of the products from the gas-liquid interface to the gas-phase

A schematic of the concentration profile for a species undergoing all the above mentioned steps can be seen in Figure 8. Since the diameter of catalyst particles used are usually very small in the range of 30 to 90 μm [125], the interfacial area between the liquid and the catalyst particles is very large and accordingly the resistance to the mass transfer due to the steps 4, 5, 7 and 8 can be neglected. Steps 3 and 9 can also be neglected if the reactor is operated in the churn-turbulent flow regime due to the efficient mixing obtained in this flow regime. The products formed in an F-T reactor are liquids, and the gas-phase will consist mainly of the reactants (CO & H_2) and subsequently the resistance associated with steps 1 and 11 will be negligible. The largest resistances in all the steps are then the resistance due to kinetics (step 6), the diffusion of species from the gas-liquid interface into the liquid bulk (step 2), and the reverse step (step 10). It therefore appears that besides the kinetics, the precise knowledge of the rate of mass transfer between the gas-liquid interface and the liquid bulk (i.e., within the liquid film) is of utmost importance for designing F-T SBCRs.

2.3.4.2 Interfacial Area

The interfacial area between the gas bubbles and the liquid-phase is an important parameter as it defines the surface where the transfer of species, from the gas to the liquid-phases and vice versa, is taking place. It is usually defined as the ratio of the surface of the gas bubbles per unit liquid-phase volume. By assuming the gas bubbles to be spherical and using the average bubble diameter, it can be written as:

$$a = \frac{6\varepsilon_G}{d_{average}(1 - \varepsilon_G)} \qquad (2\text{-}33)$$

From Equation (2-33), one can determine the behavior of the gas-liquid interfacial area by prior knowledge of the average bubble size coupled with the gas holdup.
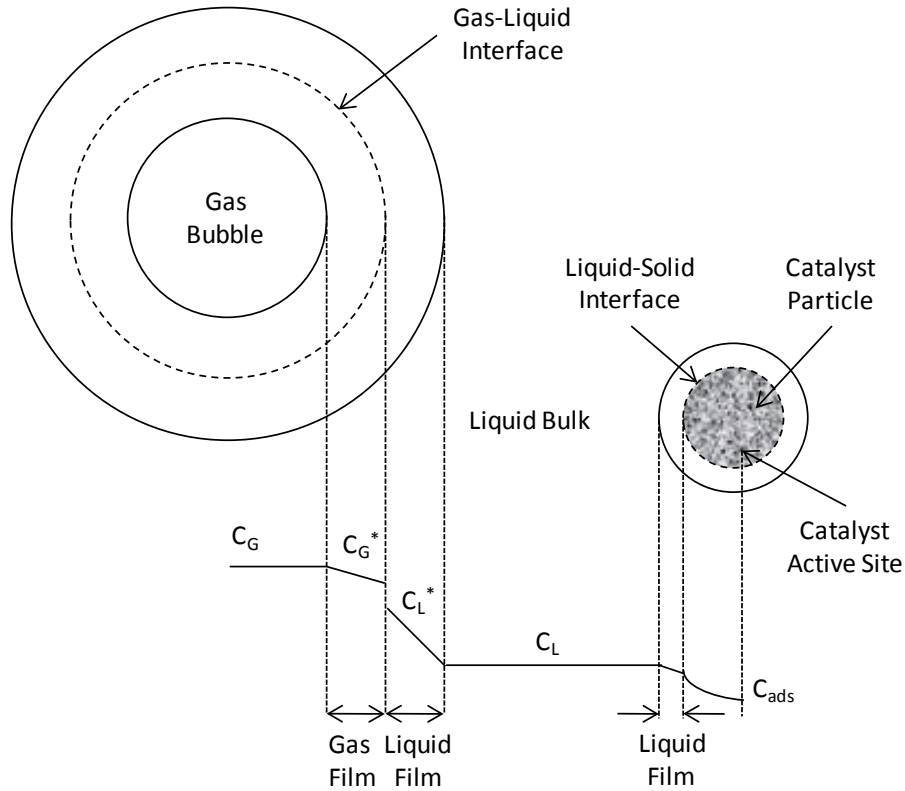
Figure 8: Schematic of the Concentration Profile for a Triphasic System

2.3.4.3 Mass Transfer Coefficient

The mass transfer flux across the gas-liquid interface can be written according to the two film model [126] as:

$$J = k_L a(C^* - C_L) \tag{2-34}$$

Where C^* is the equilibrium concentration of the gas species at the gas-liquid interface, C_L is the liquid bulk concentration, and $k_L a$ is the volumetric liquid-side mass transfer coefficient which is the product of the interfacial area (a) and the mass transfer coefficient (k_L). According to this model, k_L can be derived as a function of the diffusion coefficient and the film thickness:

$$k_L = \frac{D_{ij}}{\delta} \tag{2-35}$$

Other theoretical models have been proposed, such as the penetration theory and the surface renewal theory where the mass transfer coefficient is proportional to the square root of the diffusivity $\left(k_L \sim \sqrt{D_{ij}}\right)$.

2.3.5   Factors Affecting Hydrodynamics and Mass transfer

The hydrodynamics and mass transfer characteristics in SBCRs are affected by numerous parameters ranging from the physico-chemical properties of the gas-liquid-solid system to the operating variables and reactor geometry as can be seen in Figure 9. Tables 9 and 10 list most of the literature available on experimental work on BCRs and SBCRs, respectively. Due to the numerous factors affecting hydrodynamics and mass transfer parameters it is impossible to cover every possible condition. Nevertheless, most of the experimental studies found in the literature used air-water and most of the mass transfer measurements involved the measurement of k_La for O_2. Also none of them covered all the conditions encountered in an industrial F-T reactor (T > 450 K, P > 20 bar, U_G > 0.15 m/s, C_S > 10 vol%, mixture of hydrocarbons as liquid-phase, H_2 and CO as gas-phase, micron sized Fe or Co-based particles as solid-phase) and fewer studies are available for SBCRs than for BCRs. While the literature already available can give important qualitative information on the effects of the different factors on the behavior of SBCRs, there is still a great need for accurate hydrodynamics and mass transfer quantitative data under actual F-T conditions.

2.3.6   Effect of Gas-Liquid-Solid System

In the following section, the impact of the physico-chemical properties of the gas-liquid-solid system on the hydrodynamics and mass transfer parameters of SBCRs operating in the churn-turbulent flow regime are briefly discussed.
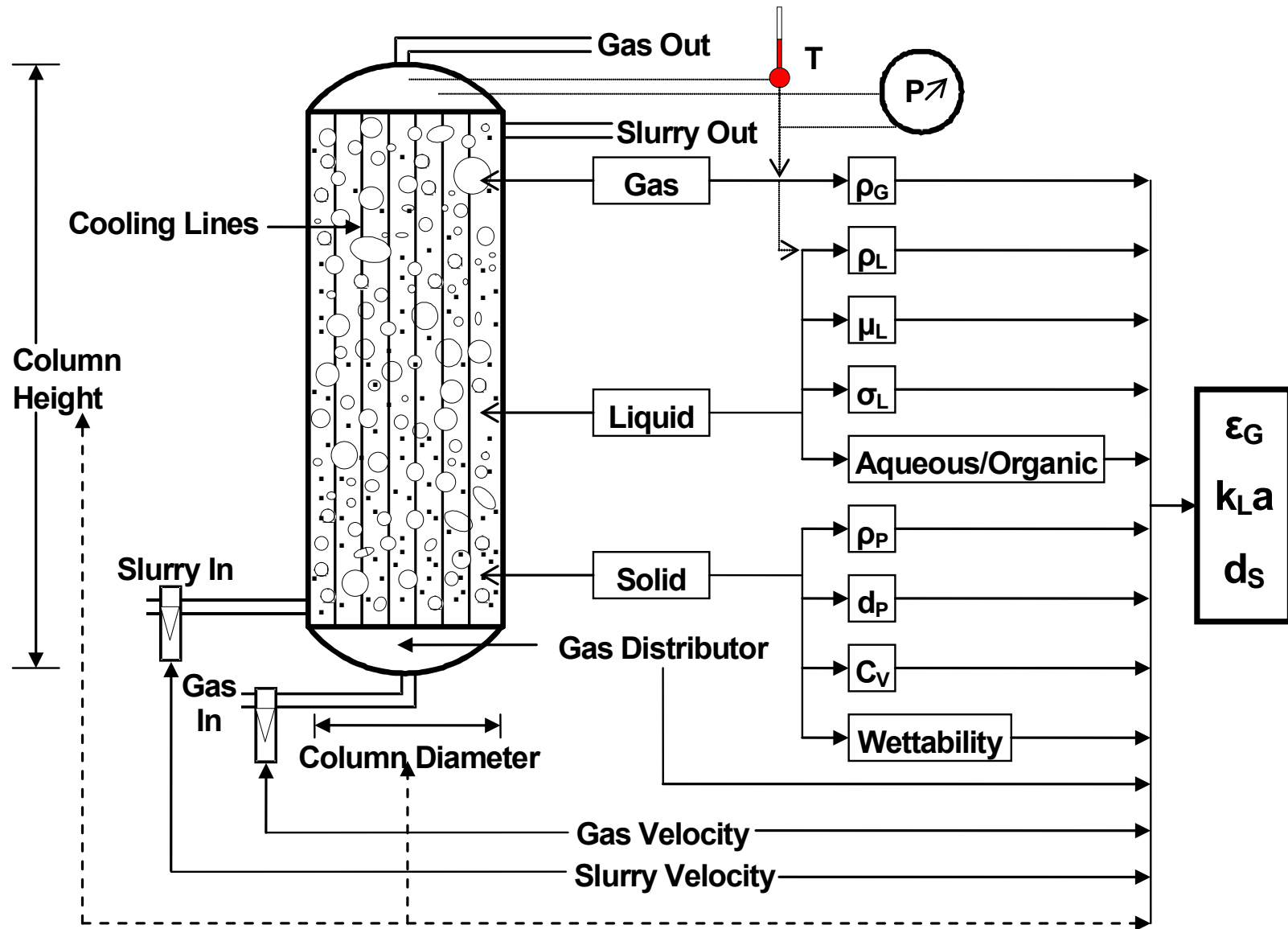
Figure 9: Factors Affecting Hydrodynamic and Mass Transfer Parameters in SBCRs [127]

2.3.6.1 Molecular Weight and Density of the Gas Phase

The density of the gas-phase has been mostly reported to have a positive effect on the gas holdup [124, 128-132], and denser gases led to higher gas holdups. It was also reported that an increase of gas density resulted in the shrinkage of the gas bubbles [120, 123, 132-135].

The impact of the molecular weight of the gas phase is similar to that of the gas density. Indeed, an increase of the molecular weight will translate into an increase of gas density and as such will lead to higher gas holdup and smaller gas bubbles [132]. It is, however, important to note that the increase of gas holdup with density/molecular weight is not true under all conditions. Clark [136] for example reported that at low gas velocities below 0.05 m/s (corresponding to the homogeneous or bubbly flow regime), the gas holdup of N_2 was smaller than that of H_2.

2.3.6.2 Density, Viscosity and Surface Tension of the Liquid Phase

The effect of the liquid density on the gas holdup has been studied by many investigators, but still remains unclear. Some investigators reported an increase [129, 130, 137, 138] of gas holdup with increasing the liquid density while others reported a decrease [124, 131, 139]. The volumetric mass transfer coefficient was found to decrease with decreasing liquid density [121, 140-143].

Increasing the liquid viscosity has been found to decrease the gas holdup [124, 128-130, 137, 138, 144, 145] and increase the gas bubbles size [146]. The volumetric mass transfer coefficient has been reported to decrease with increasing the liquid-phase viscosity [121, 140-143].

The liquid surface tension was reported to have a similar effect to that of the liquid viscosity on gas holdup, i.e., an increase of liquid surface tension leads to a decrease of gas holdup [124, 128-131, 138, 139, 147-149]. Also, an increase of liquid surface tension leads to the formation of larger gas bubbles [146] and smaller volumetric mass transfer coefficients [140, 150].

2.3.6.3 Size, Density and Wettability of Solid Particles

Slurry suspensions of denser solid particles led to lower the gas holdup [151] than similar suspensions of particles with lower density.

Increasing the size of solid particles was found to increase [151] the gas holdup for non-wettable solid particles, however, it was found to decrease [151, 152] the gas holdup for wettable

solid particles. The solid particles diameter was reported, in some cases, to have no significant effect [153] on gas holdup.

The wettability of the solid particles has no clear effect on the gas holdup. In some cases, it was found to increase the gas holdup [151] and in others to decrease it [153].

2.3.7 Effect of Operating Conditions

2.3.7.1 Temperature

Increasing temperature has been found to increase the gas holdup [138, 148, 154, 155] through the decrease of both liquid surface tension and viscosity. Increasing temperature was also reported to increase the volumetric mass transfer coefficient [129, 130] due in part to the increase of the gas diffusivity.

2.3.7.2 Pressure

The gas holdup was found to increase with pressure [122, 156-165] which was attributed to the increase of the gas density. The volumetric mass transfer coefficient was also found to increase with pressure [121, 158, 166-168].

2.3.7.3 Gas Velocity

Numerous experimental studies have shown that increasing the superficial gas velocity led to the increase of the gas holdup [108, 124, 128-131, 137-140, 149, 155] and the volumetric mass transfer coefficient [158, 166].

2.3.7.4 Liquid/Slurry Velocity

The effect of liquid superficial velocity on the gas holdup has been investigated by several authors. Increasing liquid velocity was found to decrease the gas holdup in the absence [169-171] and presence [152, 153] of solid particles.

2.3.7.5 Solid Loading

The presence of fine micron-size catalyst particles in the liquid-phase greatly affects the properties of the slurry-phase such as density and viscosity. While a few studies [147, 169] have found an increase of gas holdup with increasing solid concentration, adding more particles has mostly been found to decrease the gas holdup [120, 143, 152, 172-175] by increasing the slurry viscosity. A decrease of the volumetric mass transfer coefficient and the formation of larger gas bubbles due to the increase of the rate of bubbles coalescence was also reported when increasing the solid loading [143, 176]. It was also observed, particularly at low solid concentrations [177, 178] that the volumetric mass transfer coefficient appeared to increase with increasing the solid concentration. It should be noted that those results have to be considered along with the effects of the physical properties of the solids used, such as shape, size and wettability.

2.3.8   Effect of Reactor Geometry

The Reactor geometry has a strong influence on the gas holdup. In SBCRs, 3 zones can be identified where the gas holdups are significantly different. The first zone corresponds to the bottom of the reactor in the vicinity of the gas sparger, which is strongly affected by the sparger design. The second zone is the bulk region. The third zone is the top region, where the gas holdup will behave very differently from the bulk region, if foaming occurs. It is important to note that if the reactor is long enough the effect of the first and third regions on the total gas holdup will become negligible [149].

2.3.8.1 Column Diameter

The effect of column diameter on the gas holdup has been found to be strong in the case of small diameter reactors with diameter ≤ 0.15 m [141, 179], however, several investigators have found that this effect would level off or disappear for diameters ≥ 0.15 m [118, 140, 141, 149, 179-181].

2.3.8.2 Column Length

The length to diameter (L/D) ratio is frequently used instead of the reactor length when studying the effects of reactor geometry on the hydrodynamics. Several studies found that the gas holdup remained unaffected when the length to diameter ratio was ≥ 6 [149, 180, 182, 183].

2.3.8.3 Gas Distributor

The design of the gas distributor, the number of openings, their sizes and their orientations play an important role in affecting the hydrodynamics of the SBCRs not only in the bottom region at the vicinity of the gas distributor but also in the bulk region. The initial bubble size and distribution at the orifice could be controlled by the sparger characteristics, but due to the balance between coalescence and breakup of gas bubbles, the initial bubble size created at the gas sparger would not describe the behavior of gas bubble size distribution in the entire column [146]. Under the same operating conditions, different designs of the gas sparger were found to give different volumetric mass transfer coefficient values [129]. For 2 different designs of the gas distributor, increasing the size of the openings was found to decrease gas holdup due to the formation of larger gas bubbles [184]. However, several investigators have reported that the gas sparger had a minimal effect on the bubble sizes and gas holdup if the orifice diameters were > 0.001–0.002 m [146, 149]. This suggests that for a certain size of the openings, the gas bubble size and gas holdup reach a maximum and a minimum value, respectively.

2.3.8.4 Internals

Since F-T synthesis is an exothermic reaction, cooling tubes are needed in the reactor in order to remove the heat released by the reaction. The presence of those internals will affect the performance of the reactor in terms of hydrodynamics and mass transfer. Saxena et al. [185] have studied 3 different configurations of internals representing 1.9%, 2.7% and 14.3% of the column cross section area and could not find any clear effect of the number of internals on the gas holdup. O'Dowd et al. [186] found slightly higher gas holdup value in a column equipped with cylindrical baffles occupying 15% of the cross section area than in an unbaffled column of the same size. However, the difference lies within the range of errors of their experimental measuring technique. Also, another study [187] reported slightly higher gas holdup value when internals representing 5% of the cross section area were present. Yamashita [188] studied the effect of the separation distance between the internals and found out that gas holdup decreased when the separation distance was small (0.006 m) and increased when the separation distance was larger than 0.008 m. He attributed the decrease and increase in gas holdup values to the reduction of the radial mobility of gas bubbles and to the increase in interstitial gas velocity, respectively. Indeed, it is important to note that the slight increase in gas holdup reported in the

above mentioned studies might be the result of the increase of interstitial velocity inside the reactor when adding internals.

2.3.9 Experimental Studies under F-T Industrial Conditions

Although there are numerous experimental studies in the literature dealing with the hydrodynamic and mass transfer parameters in SBCRs (see Tables 9 and 10), only few of them covered conditions similar to those encountered in an industrial F-T SBCR (T > 450 K, P > 25 bar, U_G > 0.15 m/s, C_S > 10 vol%, mixture of hydrocarbons as the liquid-phase, H_2 and CO mixture as a gas-phase, micron sized FeO_x or Co-based or typical catalyst support as solid-phase). Deckwer et al.[108] measured the gas holdup and volumetric mass transfer coefficient for N_2 in a paraffin wax in the presence of up to 16 wt.% of alumina particles at 416 and 543 K. However, their experiments were carried out in small columns of 0.04 and 0.1 m ID at low superficial gas velocities < 0.04 m/s and pressures < 11 bar. The gas holdup for N_2 in paraffin wax was also investigated by Bukur et al.[169] who used iron oxide and silica as solid phases. Their data, however, were measured in small column of 0.05 m ID and at low range of gas velocities and low pressure (1 atm.). Krishna et al. [189] reported gas holdup data obtained in a relatively large column of 0.38 m inside diameter with a three-phase system consisting of air, paraffin oil and silica particles and covered ranges of solid concentrations and gas velocities typical to those of industrial F-T reactor, but they conducted their experiments at ambient temperature and atmospheric pressure. Vandu et al. [190] measured the volumetric mass transfer coefficients of air in a paraffin oil in the presence of alumina particles, but they used a small SBCR of 0.1 m inside diameter operating at ambient temperature and atmospheric pressure. Gas holdup data were recently obtained by Woo et al. [191] while carrying out F-T synthesis over alumina supported cobalt catalyst in a small SBCR of 0.05 m inside diameter. They reported that optimal conditions were reached when using gas velocities in the range of 0.068-0.1 m/s and catalyst concentration of 15 wt.%, however, in larger SBCRs, higher gas flow rates and solid loading would be expected in order to increase the productivity of the reactor. Behkish et al. [120, 166] measured the hydrodynamic and mass transfer parameters of H_2, CO, N_2, CH_4 and He in Isopar-M (an isoparaffinic liquid mixture of $C_{10} - C_{16}$) in the presence of alumina particles under

49

high pressures (up to 30 bar) and temperatures (up to 473 K) as well as high gas velocities (up to 0.39 m/s) and solid concentrations (up to 36 vol.%). While the typical F-T operating conditions were covered, they did not use gas mixtures which could mimic the syngas. Although Isopar-M could be used as a startup liquid for an F-T reactor, its composition varies greatly from the molten reactor wax which would be present in the SBCR once a steady state operation is reached. It should be mentioned that the hydrodynamics in SBCRs have been consistently shown to depend on the reactor size and operating conditions and accordingly, using such available data in the literature obtained in small reactor diameters or under ambient conditions or with a single gas for the design of commercial SBCRs with inside diameter reaching several meters and operating in the churn-turbulent flow regime, could be very risky.

Table 9: Literature Experimental Hydrodynamics and Mass Transfer Studies in BCRs

Reference	Gas-Liquid-Solid System	Reactor Geometry [m]	Sparger	Operating Conditions (U_G [m/s]; U_L [m/s]; P [bar]; T [K])	Parameter Measured $k_L/a/k_La/\varepsilon_G/d_B$	Correlation	Remarks
Fair et al.[141]	Air, H_2O	D_C=0.4572, 1.0668 H_C=3.048	PfP	U_G up to 0.18	ε_G		
Argo and Cova [192]	N_2, H_2, H_2O	D_C =0.45 H_C=8.1	S-ON	U_G up to 0.16	d_B		No effect of P
Hughmark [139]	Air, H_2O, Kerosene, Oil	D_C=0.0254, 0.0508, 0.1524, 0.3048, 0.4064, 1.0668	N/A	P_{atm} U_G: 0.004-0.45	k_La, ε_G	ε_G	
Akita and Yoshida [140]	He, Air, O_2, Glycol, CCl_3, Methanol, CO_2, Water, Solution	D_C=0.15, 0.3, 0.6 H_C=2	S-ON	P_{atm} U_G: 0.003-0.4 U_L: 0-0.044	ε_G, d_B, k_La	ε_G, d_B, k_La	Effect of ρ_G; Effect of D_C on k_La and d_{32}
Akita and Yoshida [146]	Air, O_2, H_2O, Glycol, Methanol, Glycerol, Na_2SO_3, CCl_4	D_C=0.077, 0.15, 0.30 H_C=2.5	PfP, PoP, S-ON	U_G up to 0.07	k_L, d_B		Effect of D_C on k_La and d_{32}
Bach and Pilhofer [193]	Air, Alcohol, Hydrocarbons	D_C=0.100 H_C=2.000	PfP	U_G: 0-0.2	ε_G	ε_G	
Gestrich et al.[194]	N/A	N/A	N/A	N/A	k_La	k_La	Obtained data and measurements from different studies
Mersmann [195]	N/A	N/A	N/A	N/A	ε_G	ε_G	Obtained data and measurements from different studies
Hikita et al.[150]	Air, H_2, CO_2, CH_4, C_3H_8, H_2O, 30, 50wt% Sucrose, Methanol, n-Butanol, Aniline	D_C=0.10, 0.19 H_C=1.5, 2.4	S-ON	P_{atm} U_G: 0.042-0.38	ε_G, k_La		Effect of U_G on k_La
Godbole et al.[142]	Air, Sotrol, Turpentine 5, CMC, N_2, Sodium Sulfate	D_C=0.305 H_C=3.4	PfP	P_{atm} U_G up to 0.24	ε_G, k_La	k_La	Small and large bubbles
Tarmy et al.[196]	N_2, C_7H_{16}	D_C=0.61 H_C=8.5	BC	U_G up to 0.20	d_B		Effect of P
Molerus and Kurtin [197]	Air, Water, Butanol	D_C=0.19 H_C=2.5	PfP, PoP	Re<2000	d_B, ε_G		In the bubbly regime, bubble sizes deduced from gas throughput and ε_G
Grover et al.[198]	Air, H_2O, NaCl, $CuCl_2$	D_C=0.1 H_C=1.5	SP	P_{atm} U_G: 0.001-0.045 T: 303-353	ε_G		ε_G decreased with T for air/H_2O. but increased for air/electrolyte at low U_G)
Guy et al.[182]	Air, Water, Glycerol, Cellulose, Polyacrylamide	D_C=0.254 H_C=0.9	PfP	U_G up to 0.10	ε_G		Effect of μ_L and sparger plate on ε_G
Idogawa et al.[199]	H_2, He, Air, H_2O, CH_3OH, C_2H_5OH, Acetone, Aqueous Alcohol Solutions	D_C =0.05	PfP	P: 1-50 U_G: 0.005-0.05	ε_G	ε_G	

Table 9 (Cont'd)

Reference	Gas-Liquid-Solid System	Reactor Geometry [m]	Sparger	Operating Conditions (U_G [m/s]; U_L [m/s]; P [bar]; T [K])	Parameter Measured $k_L/a/k_La/\varepsilon_G/d_B$	Correlation	Remarks
Kawase et al.[200]	Air, Carbopol, Water, CMC	D_C=0.23, 0.76 H_C=1.22, 3.71	S-ON, R	U_G up to 0.07	k_La	k_La	Effect of k_La in Newtonian and non-Newtonian systems
Moo Young and Kawase [201]	CO_2, Water, Poly-acrylamide	D_C=0.23 H_C=1.22	PfP	U_G up to 0.07	ε_G, k_La		Elasticity increases ε_G but not k_La
öztürk et al.[202]	Air, N_2,CO_2, He, H_2, 17 Pure Organic Liquid, 5 Inherently Mixed Liquids, 17 Adj. Mixtures, Xylene, Tetralin, H_2O, C_7H_8, Ethylacetate, Decalin, Ligroin A,B	D_C=0.095 H_C=0.85	S-ON	P_{atm} U_G: 0.008-0.1	ε_G, k_La	k_La	ε_G and k_La increases with ρ_G
Popovic and Robinson [203]	Air, Water, Na_2SO_3	D_C=0.152 H_C=1.88	S-ON	U_G up to 0.1	k_La		k_La in Newtonian Fluids
Popovic and Robinson [204]	Air, Water, CMC, Na_2SO_3	D_C=0.152 H_C=1.88	S-ON	U_G up to 0.09	a		Effect of viscosity in re-circulating BCR
Cho and Wakao [205]	N_2, Aq. Solution, C_6H_6, CCl_4, $CHCl_3$, $(CH_2Cl)_2$	D_C=0.11 H_C=0.4	S-ON, PG	U_G up to 0.054	k_La		k_La measured by desorption
de Bruijn et al.[206]	H_2, Zerice Oil	D_C=0.0508 H_C=2.4	S-ON	P: 50-140 U_G up to 0.02 T: 573	ε_G		ε_G increased with pressure
Zou et al.[138]	Air, H_2O, Alcohol, 5% NaCl	D_C=0.1 H_C=1.05	S-ON	P_{atm} U_G: 0.01-0.16 U_L: 0.007 T: 298-369.56	ε_G		ε_G increased with U_G and T.
Akita [207]	Air, Water, Electrolytes Solution	D_C=0.155 H_C=3	PfP	U_G: 0.2	k_La		k_La is system dependant
Allen and Robinson [208]	Air	D_C=0.152	PfP	Filter-Sterilized Air Flow Rate=65L/min	k_La		k_La in fermentation sol.
Halard et al.[209]	Air, Water, CMC	D_C=0.76, 0.35 H_C=3.2	R	U_G up to 0.053	k_La		k_La in viscous solutions
Medic et al.[210]	Air, Na_2SO_3, $CoCl_2$ Solution	1x2x6	PfP	U_G up to 0.045	k_La		k_La decreases with H
Popovic and Robinson [211]	Air, Water, CMC	D_C=0.152 H_C=1.88	PfP	U_G up to 0.26	a		Down-comer is a dead zone for mass transfer
Uchida et al.[212]	Air, Water, Glycerol Butanol Solution	D_C=0.046 H_C=1.36	PG, S-ON	U_L up to 0.11 T: 293, 308, 323	k_La		k_La not f (gas sparger)
Vatai and Tekic [213]	CO_2, Water, CMC	D_C=0.05, 0.1, 0.15, 0.2 H_C=2.5	S-ON	U_G up to 0.15	k_La		k_La decreases with D_C in pseudo-plastic systems

Table 9 (Cont'd)

Reference	Gas-Liquid-Solid System	Reactor Geometry [m]	Sparger	Operating Conditions (U_G [m/s]; U_L [m/s]; P [bar]; T [K])	Parameter Measured $k_L/a/k_La/\varepsilon_G/d_B$	Correlation	Remarks
Seno et al.[214]	Air, Water, Glycerol Butanol	D_C=0.046 H_C=1.36	S-ON	U_G up to 0.45	k_La		k_La f(U_G, U_L, system)
Huynh et al.[215]	Air, Water	D_C=0.095 H_C=0.79	Venturi	U_G up to 0.25	k_La, ε_G		k_La proportional to ε_G
Kawase and Moo-Young [216]	Air, Water, Carboxypoly-methylene	D_C=0.23 H_C=1.22	PfP	U_G up to 0.075	k_La		-
Oyevaar et al.[163]	CO_2, DEA	D_C=0.081 H_C=0.081, 0.81	PfP, SP	U_G: 0.01, 0.03, 0.05	a		
Rodemerck and Seidel [217]	Air, n-Pentadecane	D_C=0.04 H_C=2	SP	U_G: 0.0111, 0.0221, 0.0553, 0.1105	k_La		-
Suh et al.[218]	Air, Water, Sucrose, Xantan P.A.A.	D_C=0.15 H_C=2.9	PoP, SP	U_G up to 0.32	k_La		Effect of elastic fluids on k_La.
Terasaka and Tsuge [219]	Air, Water, Glycerol	D_C=0.1, 0.2 H_C=1.21, 2.48	M-ON	U_G up to 0.15	k_La		Effect of viscosity and sparger design on k_La.
Daly et al.[220]	N_2, FT-300 Paraffin, SASOL wax	D_C=0.05, 0.20 H_C=3	PfP	P_{atm} U_G up to 0.12 T: 538	d_B		Effect of axial position, column diameter and temperature; Sauter-mean bubble diameters were higher in the smaller column for FT-300 wax
Goto and Gaspillo [221]	Air, Water	D_C=0.1 H_C=3.7	S-ON	U_G up to 0.06	k_La		Mixer increases k_La
Grund et al.[121]	Air, H_2O, Oils, CH_3OH	D_C=0.15 H_C=4.3	PfP	U_G up to 0.2	ε_G, d_B		Effect of liquid properties
Merchuk and Ben-Zvi [222]	Air, Water	D_C=0.19 H_C=2.4	R	U_G up to 0.1	k_La		Analysis is based on the power per unit volume
Muller and Davidson [223]	Air, Water	D_C=0.14 H_C=2.5	PfP	U_G up to 0.08	k_La		k_La of small bubbles is 20-50% of total
Wilkinson et al.[149]	N_2, n-Heptane, Water, Mono-ethylene Glycol	D_C=0.16, 0.23 H_C=1.5, 1.2	PfP, S-ON	P: 1-20 U_G up to 0.2	ε_G	ε_G	Effect of D_C, H, sparger design, ρ_G and liquid properties on ε_G and flow regime
Chabot and de Lasa [154]	N_2, Paraffinic Oil (LP-100)	D_C=0.2 H_C=2.4	PfP	P_{atm} U_G: 0.022-0.147 T: 373-448	ε_G, d_B		Effect of T, z and U_G on ε_G and d_B. Bubble chord length increased with decreasing T.
Kawasaki et al.[224]	Air, Water	D_C=0.157 H_C=2.03	S-ON	U_G up to 0.1	k_La		k_La proportional to ε_G

Table 9 (Cont'd)

Reference	Gas-Liquid-Solid System	Reactor Geometry [m]	Sparger	Operating Conditions (U_G [m/s]; U_L [m/s]; P [bar]; T [K])	Parameter Measured k_L/a/k_La/ε_G/d_B	Correlation	Remarks
Kawasaki et al.[225]	Air, Water	D_C=0.15 H_C=2	PfP	U_G up to 0.05	k_La		Number of tubes increases k_La
Reilly et al.[131]	Air, N_2, He, Ar, CO2, Isopar-G, Isopar-M, TCE, Varsol, H_2O	D_C=0.15 H_C=2.7	M-ON	P up to 11 bar U_G: 0.006-0.23	ε_G	ε_G	Effect of M_G on ε_G under bubbly and churn-turbulent flow regimes
Sotelo et al.[226]	Air, CO_2, H_2O, C_2H_5OH, Saccharose, Glycerin	D_C=0.08, 0.04 H_C=2.00, 1.50	PG	P_{atm} U_G: 0-0.2	ε_G	ε_G	
Wilkinson et al.[165]	Air, Water, Hydrocarbons	D_C=0.158, 0.25	PfP	U_G up to 0.2	k_La, d_B		Effect of pressure
Zhao et al.[227]	CO_2, Water, Hydrocarbons	D_C=0.14, 0.09 H_C=2.5	PfP	U_G up to 0.06	k_La		Internals increases k_La
Eickenbusch et al.[180]	O_2, Xanthan, Hydroxypropyl guar Solution	D_C=0.19, 0.29, 0.60 H_C=2.8, 4.5, 5.75	PfP, R	U_G up to 0.10	k_La		Effect of pseudoplastic liquid on k_La
Salvacion et al.[176]	Air, N_2, H_2O, Alcohol Solutions, Calcium Alginate Gel, Polystyrene	D_C=0.14, 0.218, 0.30	PfP	P_{atm} U_G up to 0.15 C_S: 20 vol.%	k_La	k_La	
DeSwart [228]	Air, Oil, H_2O, Alcohol	D_C=0.05, 0.174, 0.19, 0.38 H_C=4	SP	U_G up to 0.55	ε_G, d_B		
Krishna and Ellenberger [229]	Air, H_2O, H_2O, Separan, Paraffin Oil, Tetradecane	D_C=0.1, 0.174, 0.19, 0.38, 0.63 H_C=4	SP	P_{atm} U_G: 0.001-0.866	ε_G	ε_G	
Stegeman et al.[164]	CO_2, N_2, H_2O, DEA, ETG	D_C=0.156	PfP	U_G up to 0.06	ε_G, a		Effect of P, U_G, μ_L on ε_G and a
Kojima et al.[158]	N_2, O_2, H_2O, Enzyme Solutions	D_C=0.045 H_C=0.9-1.2	S-ON	P: 1-11 U_G: 0.005-0.15	ε_G, k_La	ε_G, k_La	
Laari et al.[230]	Air, Water, Phenol	D_C=0.19, 0.97 H_C=0.67-4.64	M-ON	U_G up to 0.03	ε_G, d_B, k_La		Effect of D_C, U_G, additives on ε_G, d_B; Effect of H, U_G, C on k_La
Letzel et al.[161]	Air, Water, Salt	D_C=0.10, 0.19 H_C=4.0	PoP	U_G up to 0.30	ε_G		Transition from homogeneous to heterogeneous flow regime
Letzel et al.[159]	N_2, Water	D_C=0.15 H_C=1.2	PfP	U_G up to 0.30	ε_G		Effect of P on flow regimes and U_{trans}
Miyahara et al.[231]	Air, H_2O, Glycerol, Ethanol Solutions, CMC, Polystyrene.	D_C=0.10 H_C=0.80	PfP, S-ON	U_G up to 0.01	d_B	d_B	
Soong et al.[232]	N_2, Drakeol-10 Oil	D_C=0.1 H_C=2.44	PfP	P: 1, 13.6 U_G up to 0.09 T: 293, 538	d_B		d_B decreased with T

54

Table 9 (Cont'd)

Reference	Gas-Liquid-Solid System	Reactor Geometry [m]	Sparger	Operating Conditions (U_G [m/s]; U_L [m/s]; P [bar]; T [K])	Parameter Measured $k_L/a/k_La/\varepsilon_G/d_B$	Correlation	Remarks
Letzel et al.[134]	N_2, Water	D_C=0.15 H_C=1.2	PfP	U_G up to 0.30	ε_G		Effect of ρ_G on ε_G of large bubble
Terasaka et al.[233]	Air, Water, Xanthan, Gellan	D_C=0.06 H_C=0.114	PfP	U_G up to 0.15	k_La		Effect of U_G on k_La
Kang et al.[156]	Air, CMC	D_C=0.152 H_C=2.0	PfP	P: 1-6 U_G: 0.02-0.2	ε_G, k_La	k_La	Effect of pressure on ε_G
Lin et al.[234]	N_2, Paratherm NF	D_C=0.0508, 0.1016 H_C=0.8, 1.58	M-ON, R	P up to 152 U_G: 0.02-0.08 T up to 351	ε_G		Regime transition delayed with P and T; Maximum stable bubble size decreased with P and T
Pohorecki et al.[148]	N_2, H_2O	D_C=0.304 H_C=3.99	M-ON	P: 1-11 U_G up to 0.02 T: 303-433	ε_G, d_B		ε_G and d_B are independent of P and T; No effect of P, T, z and sparger on d_{32}, ε_G only dependent on U_G
Sarrafi et al.[113]	Air, Water	D_C=0.08, 0.155	PfP	P_{atm} U_G: 0-0.08	ε_G	ε_G	Effect of column geometry, sparger on transition velocity and ε_G
Álvarez et al.[235]	CO_2, Aqueous Solution of Sucrose and Surfactants	D_C=0.113	PfP	P_{atm} U_G up to 0.0016	k_La	k_La	
Krishna et al.[122]	Air, Water, Alcohol	D_C=0.15 H_C=4	SP	U_G up to 0.5	ε_G, d_B		Effect of P on the flow regime, ε_G, d_B.
Vázquez et al.[236, 237]	CO_2, O_2, (Na) or (K) Carbonate, Bicarbonate, (Na) or (K) Arsenite	D_C=0.113 H_C=1.086	PG	U_G up to 0.002	a, k_La	k_La	k_La decrease with addition of surfactant
Bouaifi et al.[238]	Air, Water	D_C=0.15, 0.20 H_C=2	PfP, SP	U_G up to 0.04	ε_G, d_B	d_B	Effect of power input on ε_G
Ishibashi et al.[239]	H_2, Oil	D_C=1 H_C=11	N/A	P: 168-187 U_G: 0.07-0.08 T: 322-731	ε_G		Coal properties had little effect on ε_G
Jordan et al.[129, 130, 240]	He, N_2, Air, C_2H_5OH, C_4H_9OH, Decalin, C_7H_8	D_C=0.1, 0.115 H_C=1.3, 1.0	PfP	U_G up to 0.21	ε_G, k_La		Effect of D_{AB}, distributors, U_G, ρ_G and T on k_La; Effect of D_C, distributors, gas velocity, ρ_G and T on ε_G
Jordan and Schumpe [129]	N_2, He, Ethanol, 1-butaol, Toluene, Decalin	D_C=0.1 H_C=2.4	PfP	P: 1-40 U_G: 0.01-0.21	ε_G, k_La	ε_G, k_La	
Kemoun et al.[157]	Air, Water	D_C=0.162 H_C=2.5	PfP	U_G up to 0.18	ε_G		P delayed the churn–turbulent regime
Magaud et al.[112]	Air, Water, Polarograhic Solution	0.1x0.3x4	PfP	U_G up to 0.07 U_L up to 0.125	d_B		Study of the wall and core region in the homogeneous regime

55

Table 9 (Cont'd)

Reference	Gas-Liquid-Solid System	Reactor Geometry [m]	Sparger	Operating Conditions (U_G [m/s]; U_L [m/s]; P [bar]; T [K])	Parameter Measured $k_L/a/k_La/\varepsilon_G/d_B$	Correlation	Remarks
Moustiri et al.[181]	Air, Water	D_C=0.15, 0.20 H_C=4.25, 4.5	PfP	U_G up to 0.055 U_L up to 0.022	ε_G		Effects of D_C on ε_G and liquid mixing
Pohorecki et al.[155]	N_2, Cyclohexane	D_C=0.3 H_C=4	M-ON	P: 2-11 U_G up to 0.06 T: 303-433	d_B, ε_G		Effects of P and T on d_{32} and ε_G; ε_G increased with temperature.
Pohorecki et al.[241]	Air, C_6H_{12}, C_7H_8, CH_3OH, n-C_7H_{16}, CH_3COH, CH_2O, iso-C_3H_7OH	D_C=0.09, 0.3 H_C=2, 4	S-ON	U_G up to 0.027	d_B		Effects of U_G on d_{32}
Yang et al.[242]	H_2, CO, Paraffin Oil, Silica Gel	D_C=0.37 H_C=0.480	N/A	U_G up to 0.025	a	k_L	
Urseanu et al.[243]	N_2, Tellus Oil, Glucose Solutions	D_C=0.15, 0.23 H_C=1.22	PfP, R	P: 1-10 U_G up to 0.3	ε_G	ε_G	
Lau et al.[244]	N_2, Air, Paratherm NF	D_C=0.0508, 0.1016	PfP	P up to 42.4 U_G up to 0.4 U_L: 0.0008-0.0089 T up to 365	ε_G		ε_G increased with P and T; Influence of column diameter. Influence of U_G and U_L on ε_G. Mass transfer was not measured at high T.

Table 10: Literature Experimental Hydrodynamics and Mass Transfer Studies in SBCRs

Reference	Gas-Liquid-Solid System	Reactor Geometry [m]	Sparger	Operating Conditions (U_G [m/s]; U_L [m/s]; P [bar]; T [K])	Parameter Measured $k_I/a/k_La/\varepsilon_G/ d_B$	Correlation	Remarks
Deckwer et al.[108]	N_2, Paraffin Wax, Al_2O_3	D_C=0.04, 0.1	SP	P up to 11 U_G up to 0.04 T: 416 & 543 C_S up to 16 wt.%	ε_G, k_La		ε_G decreased with T in small column, but independent in large column. No effect of P on ε_G
Kara et al.[152]	Air, H_2O, Coal, Dried Mineral Ash	N/A	PfP	P_{atm} U_G: 0.03-0.3 U_L: 0-0.1 C_S: 0-40wt.%	ε_G	ε_G	
Koide et al.[143]	N_2, H_2O, Glycerol, Glycol, Barium Chloride, Sodium Sulphate, Glass, Bronze	D_C=0.100, 0.140, 0.218, 0.300 H_C=2.0	S-ON, PfP, PG	P_{atm} U_G: 0.03-0.15 C_S: 0-200 kg/m³	ε_G, k_La	ε_G, k_La	
Reilly et al.[245]	Air, H_2O, Solvent, TCE, Glass Beads	D_C=0.30 H_C=0.50	PfP, S-ON, M-ON	P_{atm} U_G: 0.02-0.2 C_S up to 10 vol.%	ε_G	ε_G	
Fukuma et al.[246]	Air, H_2O, Glycerol, Glass Beads	D_C=0.15 H_C=1.2, 1.7, 3.2	M-ON	U_G up to 0.10	d_B	d_B	
Sauer and Hempel [137]	Air, H_2O, Various Plastics, Sand	D_C=0.14 H_C=2.6	PfP, SP	P_{atm} U_G: 0.01-0.08 C_S: 0-20 vol.%	ε_G	ε_G, k_La	
Schumpe et al.[178]	N_2, O_2, H_2O, 0.8M Na_2SO_4, Carbon, Kiselguhr, Aluminum Oxide	D_C=0.095 H_C=0.85	S-ON	P_{atm} U_G: up to 0.07 C_S: up to 300 kg/m³	ε_G, k_La, a	ε_G, k_La	
Bukur et al.[169]	N_2, FT-300 Paraffin Wax, Iron Oxide, Silica	D_C=0.05 H_C=3	S-ON	P_{atm} U_G: 0.02-0.12 C_S: 10-30 wt.% T: 538	ε_G		Effect of slurry circulation and solid concentrations.
Clark [136]	N_2, H_2, H_2O, CH_3OH, Coal Oil, Glass	D_C=0.075 H_C=3	SP	P: P_{atm}-100 U_G up to 0.06 T: 293-453	ε_G		Liquid vapor at high T increased ε_G. $\varepsilon_{G(H2)}$>$\varepsilon_{G(N2)}$
Saxena et al.[185]	Air, H_2O, Glass	D_C=0.305 H_C=3.25	BC	P_{atm} U_G up to 0.3 C_S: 0-30 wt.% T: 298-363	ε_G		Effect of internal tubes on the gas holdup.
Dewes and Schumpe [168]	He, N_2, Air, Sulfur Hexafluoride (0.8 M) Sodium Sulfate, Xantham Gum, Kiselghur, Alumina	D_C=0.115 H_C=1.37	PfP	P: 1-10 U_G: 0.01-0.08 C_S up to 18 vol.%	k_La	k_La	

Table 10 (Cont'd)

Reference	Gas-Liquid-Solid System	Reactor Geometry [m]	Sparger	Operating Conditions (U_G [m/s]; U_L [m/s]; P [bar]; T [K])	Parameter Measured $k_L/a/k_La/\varepsilon_G/d_B$	Correlation	Remarks
Neme et al.[145]	N_2, Fe(CN), NaOH, CMC, $HNaCO_3$, Na_2CO_3, Glass, Diatomite, Silicon Carbide, Alumina	D_C=0.05 H_C=0.750	S-ON	U_G: 0.007-0.09	k_L	k_L	
Luo et al.[162]	N_2, Paratherm NF, Alumina	D_C=0.102 H_C=1.37	PfP	P: 1-56.2 U_G up to 0.4 T: 301, 351 C_S: 8.1, 19.1 vol.%	ε_G, d_B	ε_G	Maximum stable bubble size is independent of slurry concentration at high pressure
Krishna and Sie [247]	Air, Paraffin Oil, Tellus Oil, Silica	D_C=0.1, 0.19, 0.38, 0.63	N/A	P_{atm} U_G up to 0.5 C_S: 0-36 vol.%	ε_G	ε_G	
Yang et al.[248]	N_2, Paratherm NF, Glass Beads	D_C=0.1016 H_C=1.37	PfP	P up to 42 U_G up to 0.2 C_S up to 35 vol.% T up to 354	k_La, ε_G		Heat transfer coefficient decreases with pressure.
Chen and Leu [249]	Air, H_2O, Nickel	D_C=0.05 H_C=0.5	PfP	P_{atm} U_G up to 0.04	ε_G, k_La	ε_G, k_La	
Behkish et al.[166]	H_2, CO, N_2, CH_4, Isopar-M, Hexanes, Glass Beads, Iron Oxide	D_C=0.316 H_C=2.8	S	P: 1.7-7.9 U_G: 0.05-0.25 C_S: 0-36 vol.%	k_La	k_La	

3.0   OBJECTIVES

The overall goal of this research is to investigate the hydrodynamics and mass transfer parameters in a pilot-scale SBCR operating under typical F-T industrial conditions and develop a mathematical model based on the experimental results to simulate the Fischer-Tropsch synthesis in an SBCR in order to optimize and scaleup these reactors. In order to achieve this goal, the main objectives of this research are as follows:

- Obtain the volumetric mass transfer coefficients (k_La), gas holdup (ε_G), Sauter mean bubble diameter (d_{32}), bubble size distribution, and axial catalyst distributions for surrogate components (N_2 and He) of syngas H_2 and CO in three F-T liquids: a Sasol molten wax, a reactor wax and a liquid mixture of linear paraffins, in the presence and absence of different solid particles (deactivated FeO_x catalyst, alumina powder, and Puralox alumina). The data will be determined under high pressures and temperatures as well as different superficial gas, and catalyst concentrations typical to those used in F-T synthesis. The experiments will be performed in a large-scale SBCR of 0.3-m diameter and 3-m height;

- Correlate the experimental data along with those available in the literature for F-T synthesis;

- Build a comprehensive mathematical model and a user-friendly simulator for the SBCR operating in the churn-turbulent flow regime;

- Use the simulator to design, scaleup and optimize the performance of a conceptual commercial-scale F-T SBCR.

4.0 EXPERIMENTAL

4.1 EXPERIMENTAL SETUP

The characteristics of the pilot-scale SBCR used in this study are given in Table 11, the mechanical specifications are given in Figure 10 and Figure 11. A schematic diagram and photographs of the experimental setup are shown in Figures 17 and 18, respectively. The SBCR setup consists mainly of: a reactor (tubular column), a gas sparger, a damper, a filter, a demister, a gas compressor, a liquid pump, a vacuum pump, a Coriolis mass flow-meter, a turbine flow-meter, a gas supply vessel, and various gas cylinders. The reactor is provided with two Jerguson sight-windows in order to observe and record the gas bubbles size/behavior.

Table 11: Characteristics of the SBCR

Nominal Diameter	12 in
Schedule	80
Material	Stainless Steel
Outside diameter, m	0.324
Inside diameter, m	0.289
Wall thickness, m	0.017
Inside C.S. area, m^2	0.066
Outside surface area, m^2/m	1.017
Inside surface area, m^2/m	0.908
Weight, kg/m	131.895
Height, m	3.00
Height/Diameter ratio	10.38
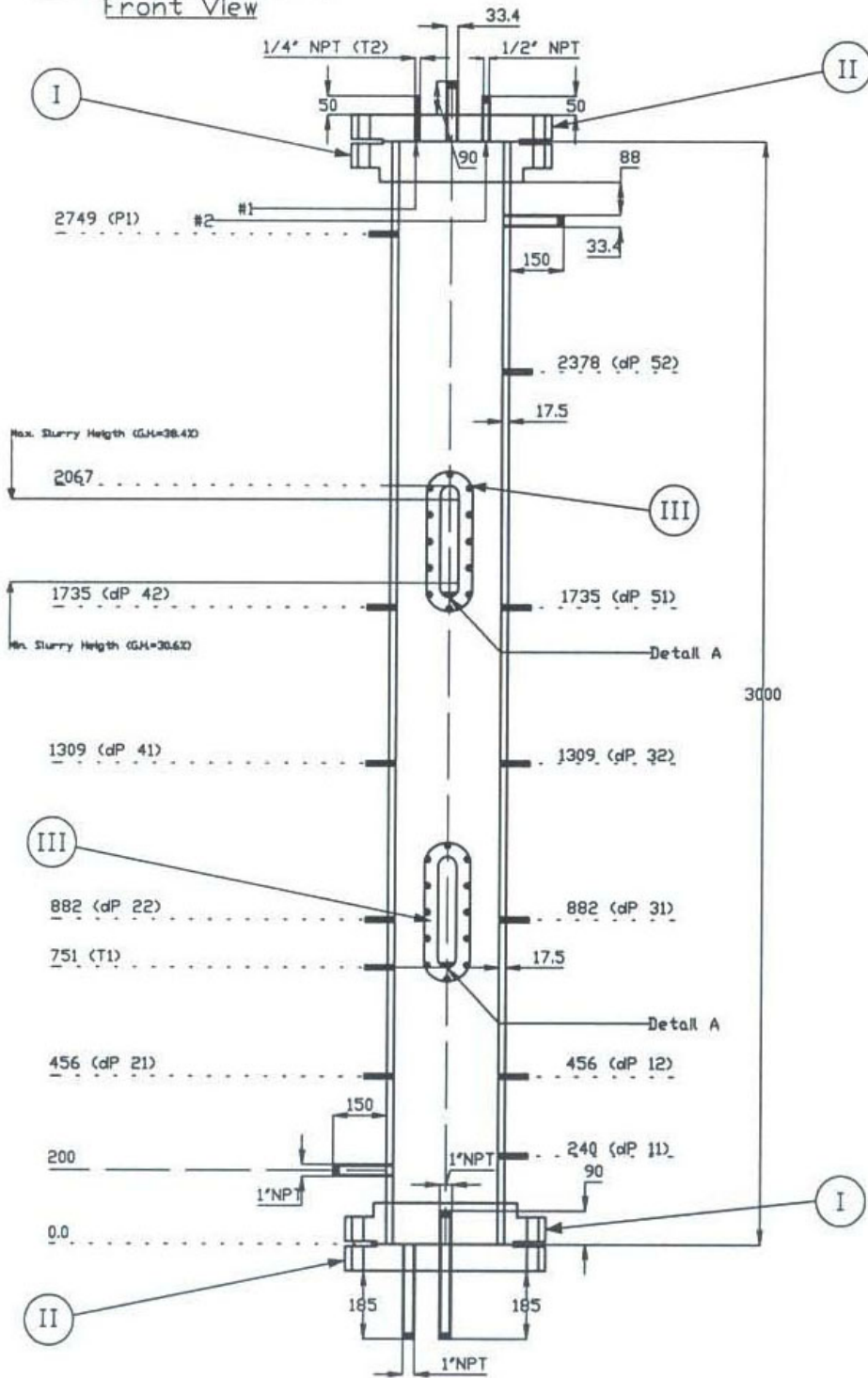
Figure 10: Mechanical Specifications of the SBCR part a

Top Flange: Side View

1'NPT

1/2' NPT   1/2' NPT

50   50

#4

#3

1/2' NPT   1/2' NPT

Top Flange: Top View

Ø289

71   71

#3
#2
#1   71
#4

71

Ø400

Ø559

Bottom view:

61   Detail A

Ø289

100

Item	Qty	Description	Mat'l
I	2	12in. 600lb slip-on flange	SS-304
II	2	12in. 600lb blind flange	SS-304
III	2	2×12in JACOBY-TARBOX sigth window (5300 model)	SS-304

Notes:

1.-) All dimmensions are in mms unless otherwise specified

2.-) Design pressure = 825 psig @ 250C

3.-) Operating pressure = 500 psig @ 250C

4.-) Hydrostatic test pressure = 1606 psia @ RT

5.-) Total weigth = 2089 lb

6.-) Blind flange pipes STD SS-304 (1 in). Other pipes Sch80 (1 in & 1/4 in).

7.-) All ports 6.4 o.d. (1/4 NPT) × 81.0 length

8.-) Band heaters are bolted to the outer diameter of the reactor. Thermal transfer material is inserted between heaters and reactor. Insulation blanket is located around the reactor.

9.-) Detail A in SBCR MECHANICAL DESIGN (II)

Top view:

ports + sigth glasses orientations

T1,P1

dP11,12

dP21,22   dP31,32

dP41,42   dP51,52

61

SBCR_MECHANICAL_DESIGN(I)

BUILT: 04/25/2000

R.A.P.E.L
ARSAM_BEHKISH

Figure 11: Mechanical Specifications of the SBCR part b

62

The reactor hydro-pressure is 85.5 bar at 295 K and its maximum allowable working pressure is 57 bar at a maximum temperature of 590 K. The reactor is equipped with 8 outside heating elements and an internal cooling coil of 0.306 m^2 total contact area. The heating elements, covered with a heavy-duty insulation jacket, operate with 460 V and are controlled by two Solid State Contactors rated up to 50 A.

The gas is introduced through the bottom of the column using a six-arm spider-type gas distributor. The gas sparger is designed so that the reactor could operate in the fully developed hydrodynamic regime. This condition is attained if Weber number in Equation (4-1) is maintained at a value ≥ 2 within the range of sparger geometry in combinations with the operating conditions [127].

$$We = \frac{\rho_G U_{G,o}^2 d_o}{\sigma} = \frac{\rho_G U_G^2 d_R^4}{N_o^2 d_o^3 \sigma} > 2 \qquad (4\text{-}1)$$

The gas sparger has six identical arms. Each arm has 6 orifices of 0.005 m inside diameter (ID) on each side and on the bottom, totaling 18 holes in each arm and a total of 108 on the sparger. There are no orifices oriented towards the top of the arms so that solid particles could not block the orifices and the gas should be able to lift any solid particles which might settle at the bottom flange. The gas sparger is screwed to a 0.0254 m ID pipe and its height from the bottom of the column is about 0.152 m (6 in).

Figure 12: Photographs of the Gas Sparger

The gas is recycled through the reactor using a single-stage compressor built by Fluitron Inc., Ivy land, USA. The compressor has a nominal displacement of 4.8x10^{-3} m^3/rev. using 30 Horsepower, 1160 RPM electric motor. The gas flow rate is measured using a Coriolis mass and

density meter model CMF100M330NU that gives a current output signal through a transmitter model RFT9739E4SUJ, manufactured by MicroMotion, USA. The gas velocity can be adjusted with a needle valve through a bypass line around the compressor inlet and outlet. The damper vessel is placed at the compressor's outlet and prior to the flow-meter in order to dampen the vibrations and fluctuations created by the movements of the piston.

The demister is placed at the outlet of the column in order to prevent the liquid and solid particles from entering the compressor. In addition, a filter manufactured by Parker Hannifin Corp., USA is inserted between the demister and the compressor as a second stage device to prevent any solid particles or liquid mist from entering the compressor.

The SBCR is also equipped with a liquid recirculation loop in order to allow the reactor to operate as an EBR and recycle liquid from the inside of the reactor through the bottom of the reactor. The loop consists of a filtration device, a liquid pump, a flow-meter, a bypass line, a gas trap and four Jerguson windows. In order to remove the catalyst particles from the liquid phase being recirculated by the pump, 2 different filtration systems, namely hydrocyclone and membrane filter were considered. The steps as well as the equations needed to design a hydrocyclone to remove the solid particles from the recirculating liquid are described in Appendix B. A Stainless steel membrane filter of 50 cm in length and 1" in diameter manufactured by GKN Sinter Metals (Addison, IL) was instead selected to remove the particles from the liquid phase. In order to avoid the formation of a cake on the surface of the filter, pressurized gas such as nitrogen can be flown through the filter between each experiment. This filter has a retention capacity of 98% for 35 μm dust particles in water. Table 12 lists the filter properties and a schematic of the filter can be seen in Figure 13.

Table 12: Filter Properties

Filter grade	SIKA-R 30 IS
Inside diameter (mm)	22.1
Filter thickness (mm)	1.65
Filter length (mm)	500
Filter surface (cm^2)	347.1
Permeability coefficient (m^2)	17x 10^{-12}
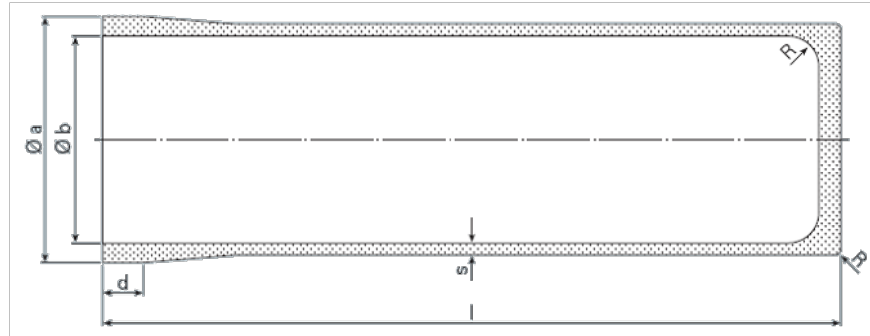
Figure 13: Schematic of the Filter Element [250]

A triple-screw pump with magnetic coupling model CGZF 85.48W90 from KRAL AG (Austria) is used to recirculate the liquid. This type of pump is typically used for oils and other self-lubricating liquid. The pump is equipped with a motor/pump coupling housing and a flexible magnetic coupling to eliminate any mechanical shaft seal that could leak. A schematic of the operating principle of the pump taken from KRAL website [251] is shown in Figure 14. The pump is able to operate at temperatures ranging from -10°C to 260°C, with a maximum working pressure of 64 bar and a pressure drop between the suction and discharge sections of 5 bar. It is driven by an electrical motor of 3.6 kW and 1420 rpm and can deliver a maximum flow rate of 78 L/min. A photograph of the pump is shown in Figure 15.
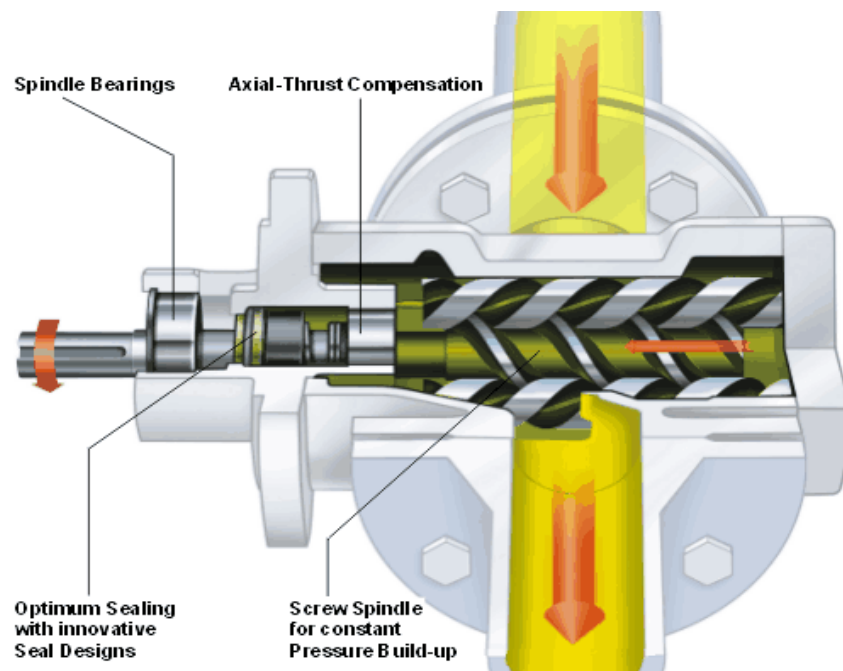
Figure 14: Schematic of a Triple Screw Pump [251]

65

Figure 15: Triple-screw Pump

A high-temperature (up to 426 °C) Stainless Steel precision turbine-meter with remote display from LH Boleky Co. (Coraopolis, PA) is used to measure the flow rate of liquid in the recirculation loop. This flow-meter is a cost-effective alternative to Coriolis and vortex flow-meters and is capable of measuring flow-rate up to 23 gpm with an accuracy and repeatability of 0.5 % and 0.1 %, respectively. It consists in 3 main units: a turbine, a high-temperature magnetic pickup coil with its enclosure and a remote display with 4-20 mA output, which is connected to the data acquisition system. The characteristics of the pre-calibrated ¾" stainless steel turbine meter are listed in Table 13.

Table 13: Characteristics of the Turbine Flowmeter

Model		GNT-075EHT
Design		Turbine
Housing		Stainless Steel
Fitting Size		3/4 inch
Fitting Type		MNPT
Flow Range		2.3 - 23 GPM (8.7 - 87 LPM)
Accuracy		± 0.5% of reading
Repeatability		± 0.1%
Operating Temperature Range		-268 to 426 °C
Typical K factor		2608
Wetted Components	Housing	316 SS
	Sleeve Bearings	Tungsten Carbide
	Shaft	Tungsten Carbide
	Rotor	CD4MCu
	Rotor Supports	Tungsten Carbide
Frequency Range		100 - 1000 Hz at 2.3 - 23 GPM
Maximum Internal Fluid Pressure		5000 Psig

A gas trap consisting of 1 stainless steel cylinder of 0.146 m inside diameter and 0.902 m length is installed before the pump in the liquid recirculation loop in order to prevent gas bubbles from entering and damaging the pump by cavitation. Two Jerguson sight-windows are placed underneath in order to allow visual monitoring of the liquid level in the gas trap, as can be seen in the schematic shown in Figure 16. This setup allows gas bubbles as small as 0.7 mm to disengage from the liquid being recirculated.
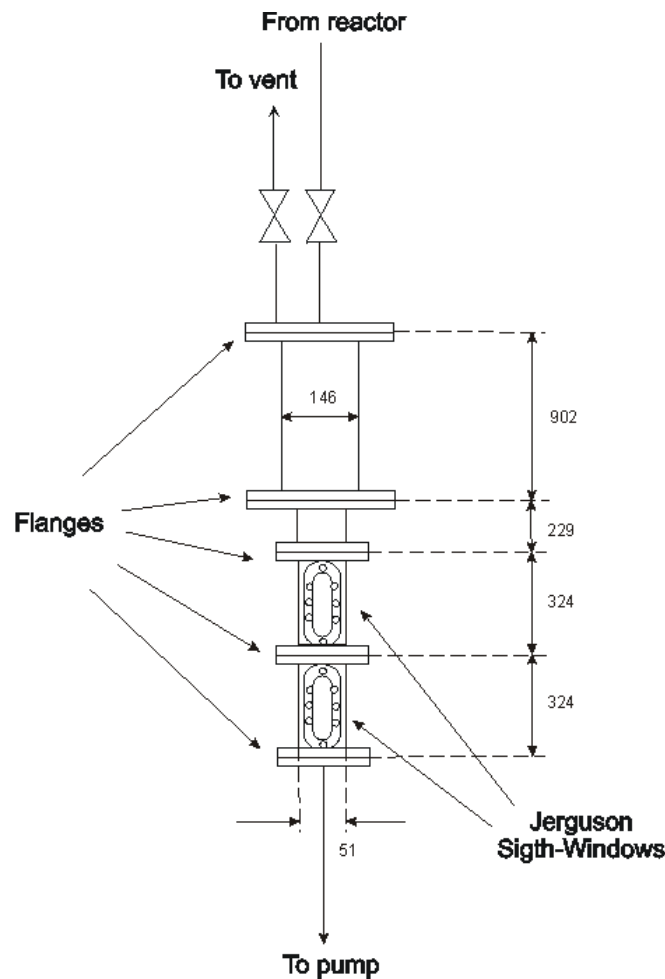
Figure 16: Schematic of the Gas Trap (dimensions are in mm)

There are two differential pressure cells (dP), model IDP10-V20A11F manufactured by Foxboro, USA rated at 7.5 kPa connected at different positions on the reactor, which allow the measurement of the hydrostatic pressure head between any two levels in the reactor. The pressure and the temperature in the system are recorded with 7 pressure transducers

67

manufactured by Wika, Germany, including 2 pressure transmitters type S-10 equipped with a protective diaphragm seal, and 7 thermocouples type J manufactured by Omega Engineering Inc., USA. The design of the entire unit allows the gas to flow through or bypass the liquid using the two pneumatically actuated valves (AV-1 and AV-2); and permits up to 60% of the gas in the reactor to be sent back to the supply vessel and recycled later without venting to the gas exhaust.

An online data acquisition from the thermocouples, pressure transducers, dP cells and the Coriolis mass flow meter is performed using the National Instrument FieldPoint modules FP-TC-120 and FP-AI-110, which are connected to a serial bus module (FP-1000) with RS-232 interface to a host PC. The output signals from the host PC are received by the FieldPoint module FP-AO-V10 for controlling the pneumatically activated valves and the heating elements of the reactor. The LabView software is used to monitor the entire process system and perform the appropriate programs for I/O applications.

4.2   GAS-LIQUID-SOLID SYSTEM

4.2.1   Gas-Phase

The gases used in this study were Nitrogen and Helium (N_2, He) as surrogates of Carbon Monoxide (CO) and Hydrogen (H_2) respectively. It should be mentioned that CO and H_2 could not be directly used in this study for safety purposes within the Swanson School of Engineering laboratory setting. All gases were purchased from Valley National Gases (USA). Some thermodynamic parameters [252] of these gases are given in Table 14.

Table 14: Thermodynamic Properties of the Gases used

Gas	M_W (kg/kmol)	Tb (K)	T_C (K)	P_C (bar)	V_C (m³/kmol)	Z_C	ω
N_2	28.013	77.35	126.10	33.94	0.0901	0.292	0.040
He	4.003	4.22	5.20	2.28	0.0573	0.302	-0.390
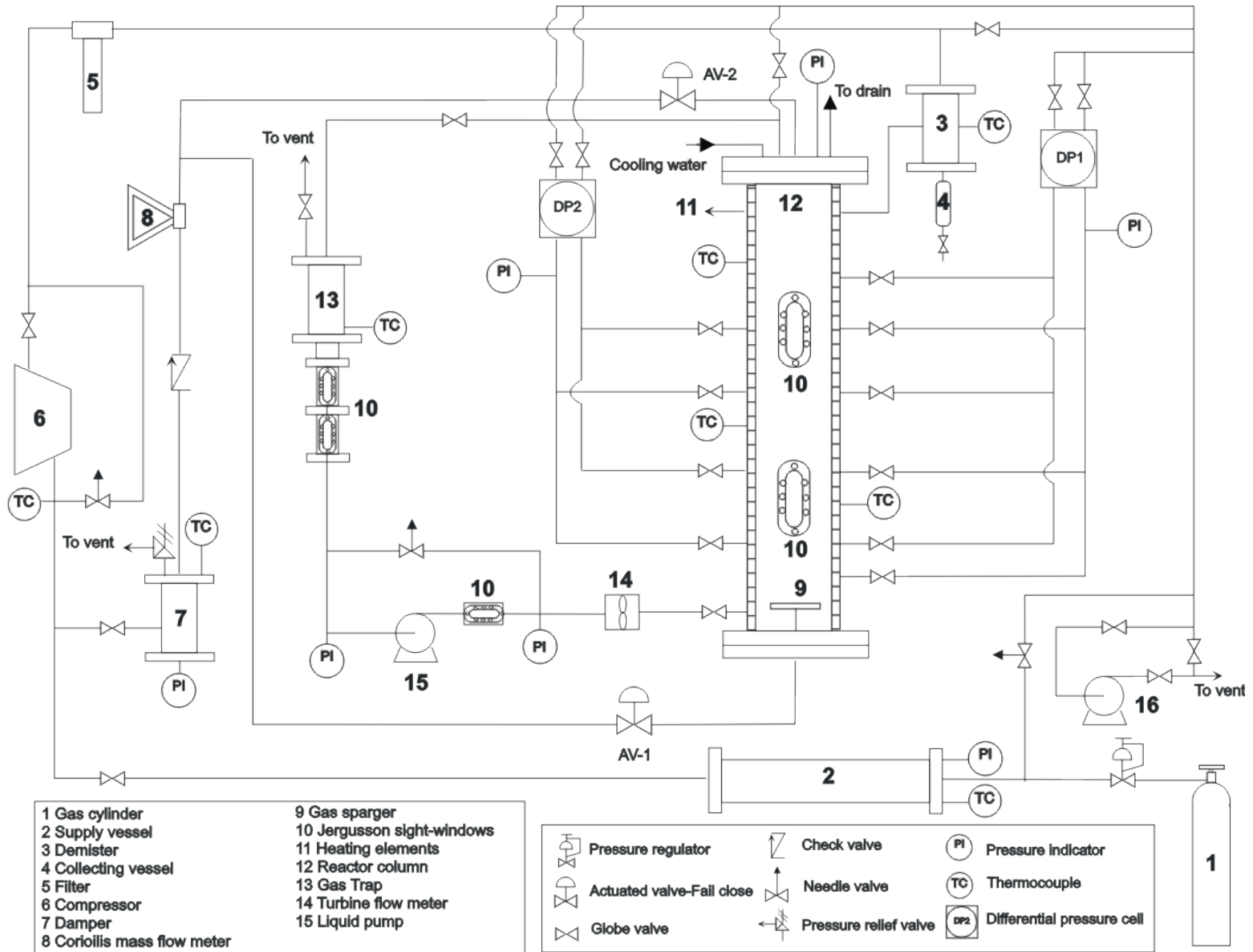
Figure 17: Schematic of the Experimental Setup

Figure 18: Photographs of the Experimental Setup With and Without Insulation at Different Angles

4.2.2 Liquid-Phase

The first liquid used in the experiments is a molten Sasol wax (C_{80}), manufactured by Moore & Munger, Inc. (The name of this company was changed to Sasol Wax Americas, Inc., effective July 1st, 2006). Sasol wax (Paraflint™) is produced by Sasol, South Africa using Fischer Tropsch process. This wax consists in saturated and straight chains hydrocarbons with almost no branches. Sasol wax is solid at room temperature with a melting point around 83ºC. The molar composition of the Sasol wax is given in Figure 19; and as can be seen the carbon number (C_N) is ranging from C_{17} up to C_{79} with a C_N between C_{29} and C_{53} accounting for almost 93 mol% of the total molar composition.
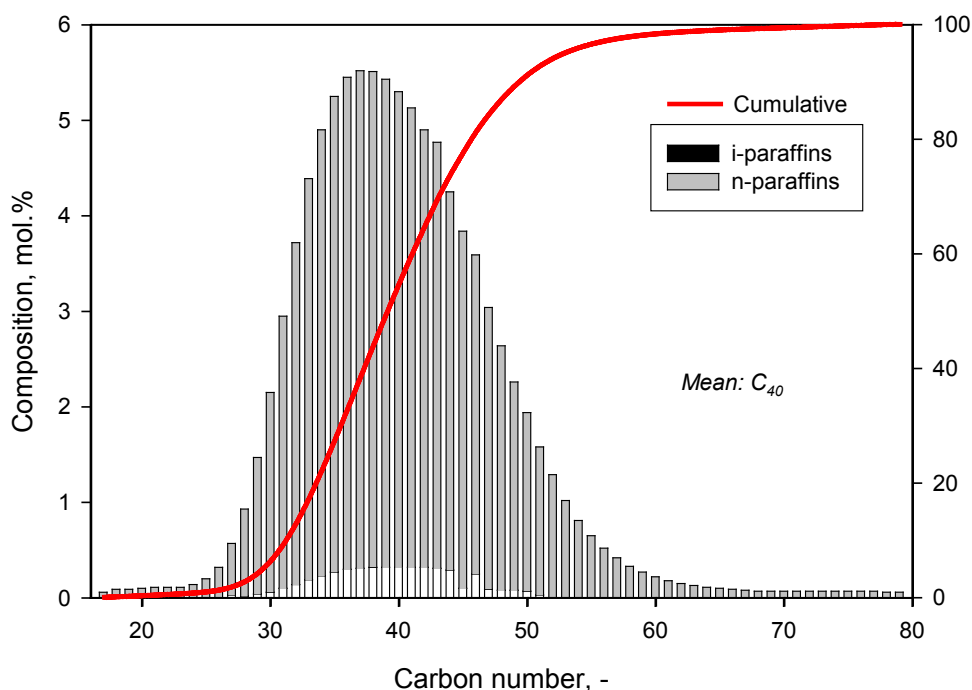
Figure 19: Molar Composition of Sasol Wax

The other liquids used are a C_{12}-C_{13} liquid paraffins mixture and a molten reactor wax produced by Sasol, South Africa using the low temperature F-T process. The paraffins mixture composition, shown in Table 15, was provided by Sasol.

Table 15: Paraffins Mixture Composition

C_{11} and lighter	~ 3 wt.%
C_{12}	50 wt.%
C_{13}	47 wt.%
C_{14+}	< 1 wt.%

The reactor wax is solid at room temperature with a melting point around 70ºC (343 K). The actual molar composition of the reactor wax was not provided. It was therefore estimated assuming the F-T product composition follows the superposition of 2 Anderson-Schulz-Flory (ASF) distribution [36]. The values for the different parameters were taken from Donnelly et al. [52] and the resulting composition is shown in Figure 6. Since the volatile components with low carbon number do not remain in the final reactor wax, only products with carbon number above 20 were considered for the estimation of the physical properties of the reactor wax.

4.2.2.1 Molecular Weight and Critical Properties

The molecular weight of the Sasol wax, reactor wax and the paraffins mixture are 568 kg/kmol, 408.08 kg/kmol and 176.36 kg/kmol, respectively, as calculated from their compositions according to the following equation:

$$Mw_{wax} = \sum_{i=1}^{n} x_i \, Mw_i \qquad (4\text{-}2)$$

x_i represents the mole fraction of species i. Other important thermodynamic properties of the liquids, given in Table 16, were also estimated [253] from the composition or taken from the work of Soriano [254].

Table 16: Thermodynamic Properties of Sasol Wax [254]

Liquid	M_W (kg/kmol)	T_C (K)	P_C (bar)	Z_C	ω
Sasol Wax	568.4	883.23	4.223	0.2165	1.5384
Reactor Wax	408.1	823.74	7.455	0.2266	1.1785
Paraffins Mixture	176.4	666.13	17.764	0.2485	0.5876

4.2.2.2 Liquid Densities

The densities of the molten Sasol wax, the molten reactor wax and the liquid paraffins mixture were measured in our laboratory over a wide range of temperatures (290 to 500 K). They were

also predicted using the Asymptotic Behavior Correlations (ABC) developed by Marano and Holder [255, 256]. From the resulting data, the densities of the 3 liquids were correlated as a function of temperature by the expressions shown in Table 17.

Table 17: Liquid Densities Correlations

Liquid	Correlation	Equation #
Sasol Wax	$\rho_L = 959.08 - 0.513\,T$	(4-3)
Reactor Wax	$\rho_L = 937.86 - 0.511\,T$	(4-4)
Paraffins Mixture	$\rho_L = 958.79 - 0.712\,T$	(4-5)

The measured densities of the 3 liquids are shown as functions of temperature in Figure 20 along with the predicted values using Marano and Holder [255, 256] correlations when considering only an average carbon number of 28 (for the reactor wax) as well as when considering the composition (for both reactor wax and paraffins mixture).

4.2.2.3 Liquid Viscosity

The viscosities of the molten Sasol wax, the molten reactor wax and the paraffins mixture were measured in our laboratory over a wide range of temperature (290 to 500 K) using the Cannon-Fenske routine viscometers. They were also predicted according to the ABC developed by Marano and Holder [255, 256]. From the resulting experimental data, the viscosities of the 3 liquids were correlated as functions of temperature (see Table 18).

Table 18: Liquid Viscosities Correlations

Liquid	Correlation	Equation #
Sasol Wax	$ln(\mu_L) = -4.3284 + \dfrac{2319.4}{T}$	(4-6)
Reactor Wax	$ln(\mu_L) = -3.5733 + \dfrac{1302.7}{T} + \dfrac{1.875 \times 10^5}{T^2}$	(4-7)
Paraffins Mixture	$ln(\mu_L) = -3.9708 + \dfrac{1043.0}{T} + \dfrac{8.321 \times 10^4}{T^2}$	(4-8)
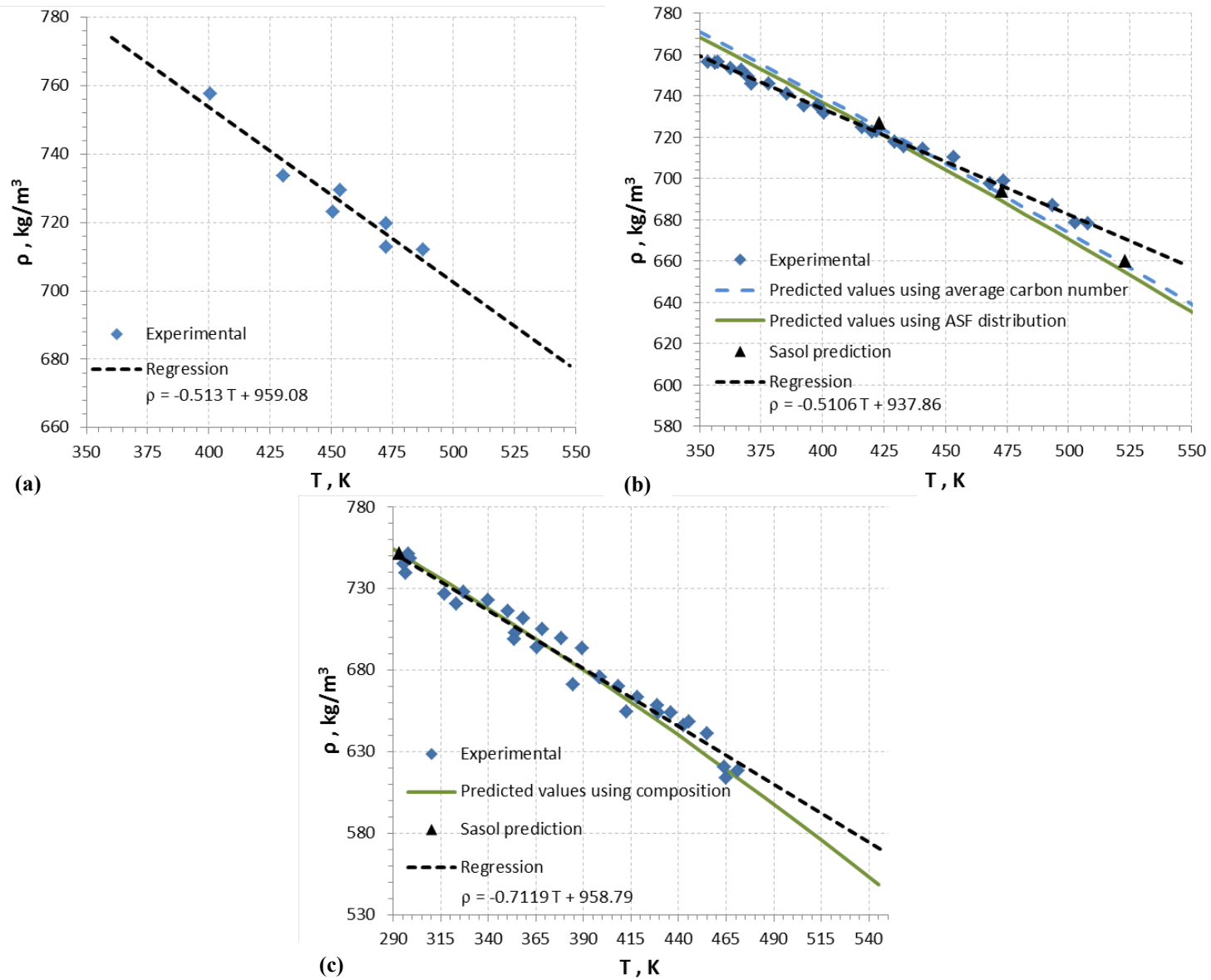
Figure 20: Effect of Temperature on the Densities of the Molten Sasol Wax (a), the Molten Reactor Wax (b) and the Paraffins Mixture (c)
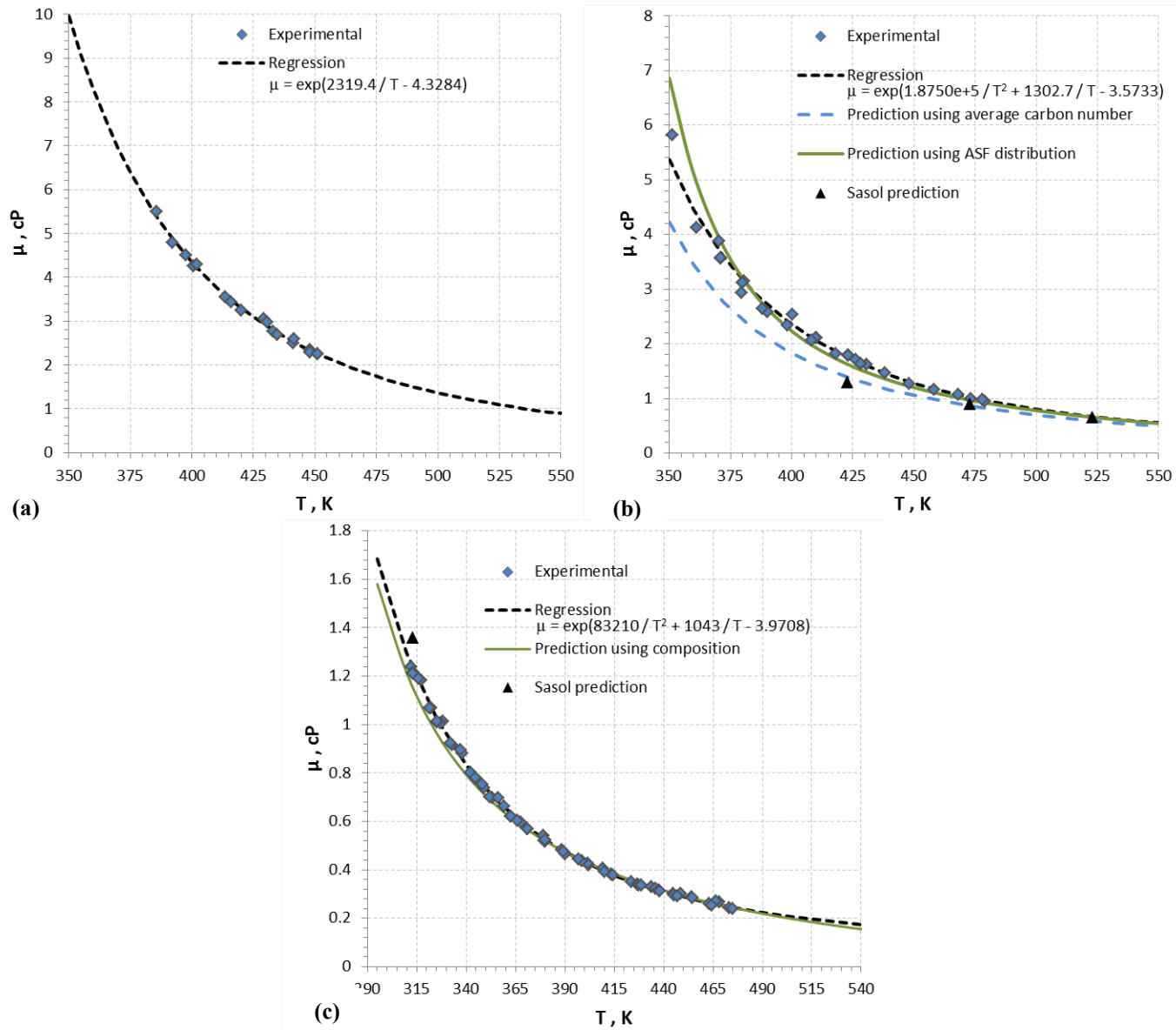
Figure 21: Effect of Temperature on the Viscosities of the Molten Sasol Wax (a), the Molten Reactor Wax (b) and the Paraffins Mixture (c)

The measured viscosities of the 3 liquids are shown as functions of temperature in Figure 21 along with the predicted values using the correlations by Marano and Holder [255, 256] when considering only an average carbon number of 28 (for the reactor wax) as well as when considering the composition (for both reactor wax and paraffins mixture).

4.2.2.4 Liquid Surface Tension

The surface tensions of the three liquids were predicted using the ABC developed by Marano and Holder [255, 256] when considering only an average carbon number of 28 (for the reactor wax) as well as when considering the composition (for all liquids). The surface tensions of the 3 liquids are shown as functions of temperature in Figure 22. The estimated values were used to develop correlations for the surface tension of the 3 liquids as simple function of temperature and are listed in Table 19.

Table 19: Liquid Surface Tension Correlations

Liquid	Correlation	Equation #
Sasol Wax	$\sigma = 0.001 \times (70.57 - 0.1725\,T + 1.404 \times 10^{-4}\,T^2)$	(4-9)
Reactor Wax	$\sigma = 0.001 \times (69.03 - 0.1703\,T + 1.338 \times 10^{-4}\,T^2)$	(4-10)
Paraffins Mixture	$\sigma = 0.001 \times (64.05 - 0.1633\,T + 1.123 \times 10^{-4}\,T^2)$	(4-11)

4.2.2.5 Vapor Pressure

The vapor pressures of the three liquids were estimated assuming they follow Raoult's law from their molar composition and the vapor pressure data for each hydrocarbons component taken from Kudchadker et al.[257] and Yaws [252]. The vapor pressure of the molten reactor wax was predicted when considering only an average carbon number of 28 as well as when considering the composition. For practical purposes, the vapor pressures of the 3 liquids were correlated as a function of temperature as shown in Table 20 and Figure 23.
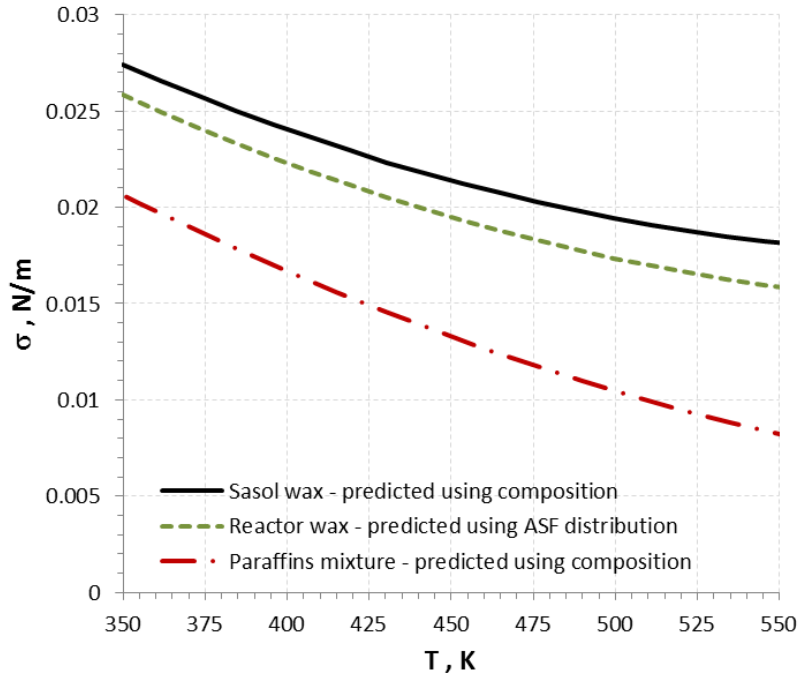
Figure 22: Effect of Temperature on the Surface Tension of Molten Sasol Wax, Molten Reactor Wax and Paraffins Mixture
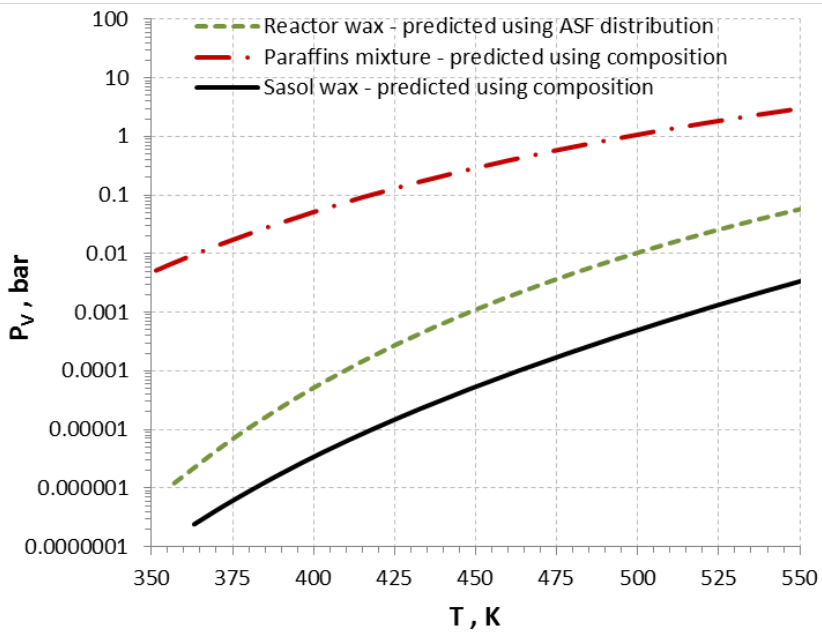
Figure 23: Effect of Temperature on the Vapor Pressure of Molten Sasol Wax, Molten Reactor Wax and Paraffins Mixture

Table 20: Liquid Saturated Vapor Pressure Correlations

Liquid	Correlation	Equation #
Sasol Wax	$log_{10}(P_V) = 6.39159 - \dfrac{5165.43}{T} + \dfrac{164347.29}{T^2}$	(4-12)
Reactor Wax	$log_{10}(P_V) = -\dfrac{9.0041 \times 10^5}{T^2} - \dfrac{583.04}{T} + 2.7911$	(4-13)
Paraffins Mixture	$log_{10}(P_V) = -\dfrac{2.6755 \times 10^5}{T^2} - \dfrac{1439.5}{T} + 3.9819$	(4-14)

4.2.3 Gas-Liquid Diffusivities

The diffusivities of H_2 and CO and their surrogates He and N_2 in the paraffins liquid mixture and molten reactor wax were calculated using the widely used Wilke and Chang [258] equation as well as a correlation specifically developed for hydrocarbons by Erkey et al. [259] who measured the diffusion coefficients of H_2, CO, CO_2 and several n-alkanes up to C_{16} into n-alkanes ranging from C_7 to C_{28} using the Taylor dispersion technique. The two correlations are given by Equations (4-15) and (4-16), respectively.

$$D_{ij} = 1.1728 \; 10^{-16} \frac{T\sqrt{M_j}}{\mu_j \upsilon_i^{0.6}}$$
(4-15)

$$D_{ij} = \frac{94.5.10^{-9}\sqrt{T}}{M_i^{0.239}M_j^{0.781}(\sigma_i\sigma_j)^{1.134}}\left[V_j - \left(1.206 + 0.0632\frac{\sigma_i}{\sigma_j}\right)\frac{N_A\sigma_j^3}{\sqrt{2}}\right]$$
(4-16)

In the above correlations, the subscript i represents the solute and j stands for the solvent; V_j is the molar volume of the solvent and υ_i is the solute molar volume at its boiling point. The molecular weight (M_j) and effective hard sphere diameter (σ_j) of the different liquids, consisting mainly of n-alkanes, were estimated from their mole fractions as:

$$M = \sum_n x_n M_n$$
(4-17)

$$\sigma = \sum_n x_n \sigma_n$$
(4-18)

It should be noted that Equation (4-16) was developed within a temperature range of 298 to 570 K, which is similar to that covered in this present work. The estimated molecular weight (M_j) and diameter (σ_j) of the 3 liquids and the 4 gases are listed in Table 21.
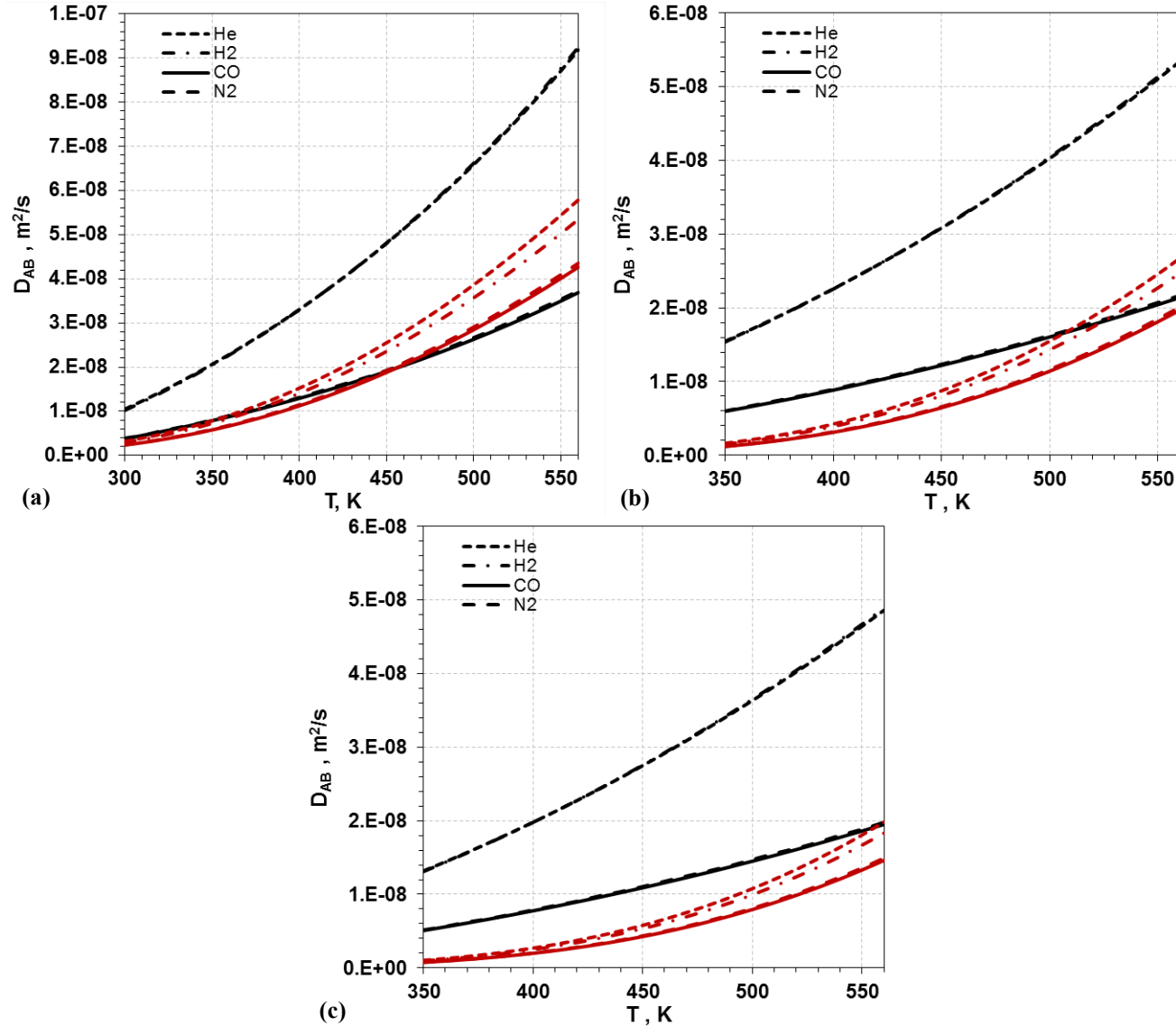
Figure 24: Diffusivities of Gases in the Paraffins Liquid Mixture (a), Molten Reactor Wax (b) and Molten Sasol Wax (c)

(Black curves using Erkey et al. [259] correlation; Red curves using Wilke and Chang [258] correlation)

Table 21: Molecular Weights and Diameters of the Gases and Liquids Used [259-261]

Liquid or Gas	σ (Å)	M_W (kg/kmol)
Paraffins Mixture	7.52	176.4
Reactor Wax	9.78	408.1
Sasol Wax	10.96	568.4
H_2	2.915	2.016
CO	3.72	28.01
N_2	3.681	28.01
He	2.551	4.00

Figure 24 show the diffusivities of the four gases in the 3 liquids as a function of temperature. From this figure, the following observations can be made: (1) both correlations predict similar diffusivities for He and H_2 and identical diffusivities for CO and N_2 in each liquid, which emphasizes the argument that N_2 and He could be used as surrogates for CO and H_2, respectively; (2) in general, the correlation by Erkey et al. [259] predicts greater diffusivities for He and H_2 in both liquids than those predicted with the correlation by Wilke and Chang [258]; however, both correlations predict similar diffusivities for N_2 and CO only in the C_{12}-C_{13} paraffins mixture; and (3) the correlation by Erkey et al. [259] predicts H_2 diffusivities identical to those of He whereas the correlation by Wilke and Chang [258] predicted diffusivities for He slightly greater than those of H_2 at high temperature.

4.2.4 Solid-Phase

4.2.4.1 Alumina

The first solid-phase used in this study is alumina powder particles (Al_2O_3) which are commonly used in the industry as support for F-T catalysts. Those particles were analyzed by Behkish [127] using Scanning Electron Microscopy (SEM) and the particle size distribution was obtained from the SEM images. The mean particle size and the Sauter-mean particle diameter were found to be 32.33 and 42.37 μm, respectively. The density of the particles was measured using the displacement method with water and a graduated pycnometer and was found to be 3,218.3 kg/m^3.

4.2.4.2 Iron Oxide Catalyst

The second solid-phase used in this study consisted of a mixture of Iron oxides (FeO$_x$). SEM analysis of these particles was performed by Inga [133]. Those particles were found to exhibit a bimodal distribution with a "large particles" mode situated at 40 μm and a "small particles" mode corresponding to broken particles around 1.5 μm. The bulk and skeletal densities of the particles were 2,230 kg/m^3 and 4,000 kg/m^3 respectively, as reported by Inga [133].

4.2.4.3 Puralox Alumina

The third solid-phase used is Puralox Alumina particles (provided by Sasol) that can be used as support for the F-T Co catalyst. The skeletal density of this material is about 3,900 kg/m^3 with a porosity of 70%. The size distribution of these particles, listed in Table 22, was provided by Sasol.

Table 22: Size Distribution of Puralox Alumina Solid Particles

Diameter (μm)	Volume % finer than
22	1%
44	10%
150	65%
250	98%

4.3   OPERATING CONDITIONS

The study of the mass transfer and hydrodynamic parameters for a multi-variable system requires a huge number of experiments. To avoid this, a statistically designed specific number of experiments were carried out using the Central Composite Statistical Design (CCSD) approach in order to minimize the number of experiments and obtain statistical correlations with high degree of confidence.

In this study, the CCSD and analysis technique are similar to that employed previously by Behkish [127] and Lemoine [262]. This approach determines the effect of the four independents variables (k = 4): pressure (P), superficial gas velocity (U$_G$), solid concentration (C$_S$) and

temperature (T); at five levels on the hydrodynamics and mass transfer characteristics of the SBCR. The operating conditions used in the SBCR are given in Table 23. The numbers of replicates at the central point is given by the following equation:

$$N_{central} = \gamma \left(\sqrt{N_F} + 2 \right)^2 - N_F - 2k \tag{4-19}$$

Where N_F is the number of factorial points, and γ is defined by the following equation:

$$\gamma = \frac{(k+3) + \sqrt{9k^2 + 14k - 7}}{4(k+2)} \tag{4-20}$$

The factorial and axial points are equidistant from the central point to offer rotatability properties of the design. In fact, this property becomes important in the examination of the response surface since the orientation of the design does not influence anymore the precision of estimated surfaces [263]. The response surface can be described by the following equation:

$$\alpha = \sqrt[4]{2^k} \tag{4-21}$$

The total number of test runs is:

$$n = 2^k + 2k + N_{central} \tag{4-22}$$

For this study, the latter equation leads to a total number of experiments of 25 (four variables at five different levels). There are 8 central points (0, 0, 0, 0), 16 factorial points (±1, ±1, ±1, ±1) and 8 axial points (±2, 0, 0, 0), (0, ±2, 0,0), (0, 0, ±2, 0) and (0, 0, 0, ±2). Therefore a total of 32 experiments should be carried out using each gas (N_2 and He). However, more than 32 experiments were performed in order to directly obtain and compare experimental profiles of the different hydrodynamic and mass transfer parameters measured over wide ranges of operating conditions.

Table 23: Operating Conditions and Values of the Coded Variables for the CCSD with Sasol Wax

Variable	Coded variable	Values of the coded variables				
		-2	-1	0	1	2
T, (K)	X_1	370	410	450	490	530
P, (Psig)	X_2	100	175	250	325	400
U_G, (cm/s)	X_3	14	17	20	23	26
C_S, (vol.%)	X_4	0	5	10	15	20
Gas Phase		He; N_2				
Liquid Phase		Sasol wax				
Solid Phase		Al_2O_3; FeO_x				

The approach described above was applied to the experiments performed with the Sasol wax. For the molten reactor wax and paraffins mixture experiments, the CCSD approach was not used as the effect of most of the operating conditions were already covered by the Sasol wax experiments. Instead the experiments with the 2 latter liquids were focused on the impact of gas nature and composition on the hydrodynamics and mass transfer parameters. The ranges of operating conditions used in the SBCR with the molten reactor wax and the paraffins mixture are shown in Table 24.

Table 24: Operating Conditions for the Molten Reactor Wax and Paraffins Mixture Experiments

Variable	Values
Pressure (bar)	4 - 31
Temperature (K)	320 - 500
Superficial Gas Velocity (m/s)	0.14 - 0.26
Solid Concentration (vol.%)	0 - 7
Gas Phase	He/N_2 Gas Mixture
He/N_2 Gas Mixture Composition (% He)	0 - 100
Liquid-Phase	Paraffins Mixture Molten Reactor Wax
Solid-Phase	Puralox

4.4   EXPERIMENTAL PROCEDURE

The experimental procedures to obtain the volumetric liquid-side mass transfer coefficients (k_La), gas holdup (ε_G), and the Sauter-mean bubble diameter (d_{32}) are detailed in the following sections.

4.4.1   Volumetric Liquid-Side Mass Transfer Coefficient

The Transient Physical Gas Absorption (TPGA) technique was employed to obtain k_La for the gases into the liquid phase or slurry phase under the operating conditions used. The experimental procedure is similar to that used by Behkish et al. [166] and is described below:

1. A predetermined amount of liquid or slurry is charged into the reactor (95 liters).
2. Reactor content is heated to the desired temperature.

3. The vent valve at the top of the liquid recirculation line is opened fully to ensure that any liquid trapped above is allowed to drain. The valve is then shut.

4. The entire system is vacuumed to remove any gases which might be dissolved in the liquid-phase. Once the pressure in the reactor reaches the vapor pressure of the liquid-phase, the vacuum is stopped.

5. A small amount of gas is charged to the reactor to ensure enough pressure (2 bar) to fill the liquid recirculation line with liquid.

6. Any gas present in the recirculation line is vented by opening the valve at the top of the liquid recirculation line until liquid reaches the top.

7. The gas is charged to the reactor to a high enough pressure (3 bar) in order to overcome the pressure drop in the liquid recirculation line and properly operate the pump.

8. The pump is turned on and the flow rate is regulated by the bypass valve and the liquid inlet valve until the desired liquid flow rate is reached.

9. The gas is then charged to the reactor from gas cylinder until the desired pressure for the experiment is reached.

10. The cooling water and drain valves for the compressor are opened.

11. Once the gas is charged, the compressor is turned on and the gas is initially recirculated only through the top of the reactor with valve AV-2 open and valve AV-1 closed. The gas velocity is adjusted to the desired flow rate, regulated by the gas bypass valve.

12. The top valve AV-2 is closed while simultaneously opening the bottom gas valve AV-1 allowing the gas to flow through the liquid or slurry. The reactor pressure is recorded as a function of time during the gas absorption in the liquid or slurry phase until thermodynamic equilibrium is reached.

The volumetric mass transfer coefficient, $k_L a$, is then calculated from the transient part of the pressure-time data. If performing the experiment without any liquid recirculation, steps 3, 5, 6, 7 and 8 can be skipped.

4.4.2   Gas Holdup

The manometric method was used to obtain the gas holdup. Once the system reaches thermodynamic equilibrium (i.e., steady state), the following procedure for obtaining the gas holdup is applied:

1. The differential pressure (dP) cells legs are purged of liquid or slurry and pressurized with the gas being used.
2. The hydrostatic pressure is measured at different positions along the height of the reactor by opening and closing the corresponding valves.
3. The computer collects the dP cells readings and calculates the gas holdup at any given position along the reactor.

4.4.3   Gas Bubbles Size Distribution and Sauter Mean Diameter

The Dynamic Gas Disengagement (DGD) technique was employed to obtain the gas bubbles size distribution and the Sauter mean diameter. In this procedure, once $k_L a$ and ε_G measurements have been successfully completed at given temperature:

1. The dP cell legs at given positions are opened.
2. Using the pneumatically actuated valves, the inlet valve at the bottom of the reactor is closed while the valve at the top of the reactor is opened, directing the gas from the bottom to the top of the reactor, the compressor is turned off and as a result the gas retained in the liquid disengages.
3. The dP cell readings are recorded until all the gas bubbles are completely disengaged and the pressure leveled off.
4. The computer collects the dP cell readings and calculates the gas holdup.

The bubble sizes are then calculated using the gas holdup versus time data.

4.4.4   Solid Particles Distribution

Slurry samples were withdrawn from the sampling ports located on the legs of the dP cells at different heights in the reactor in order to measure the mass fraction of solids in the reactor using the liquid paraffins mixture at different heights from 0.240 m to 1.309 m. Four sampling ports were used and a total of eight samples were withdrawn for each experiment. To collect solid particles at a given concentration, the same procedure described in section 4.4.2 to obtain the gas holdup was followed; however the dP cells legs were not pressurized in order to allow the slurry to flow from the reactor through the dP cell legs and the sampling ports. After flushing the sampling line, the slurry was collected from each sampling ports. The samples were placed into pre-weighed glass jars and sealed immediately. The solids were then separated from the liquid paraffins mixture using the following procedure:

- The initial sample weight was recorded.
- The samples were then gravity filtered.
- After filtering, the filter paper containing the "wet" solid particles as well as the sample jars containing some remnants of solids and liquid were placed for 3 days into a furnace with the temperature set just above the boiling point of the paraffins mixture.

Once the samples were dried, the final total weight including the dried glass jar and catalyst was recorded to determine the catalyst percentage by weight.

5.0   CALCULATIONS

5.1   PENG-ROBINSON EQUATION OF STATE

The Peng-Robinson Equation of State (PR-EOS) was used to calculate the number of moles of gas in the reactor before and after gas absorption. A general form of the PR-EOS can be written as:

$$P = \frac{RT}{v - b} - \frac{a}{v(v + b) + b(v - b)} \tag{5-1}$$

This equation can be expressed in terms of the compressibility factor, Z as:

$$Z^3 - (1 - B)Z^3 + (A - 3B^2 - 2B)Z - (AB - B^2 - B^3) = 0 \tag{5-2}$$

Where:

$$A = \frac{aP}{R^2T^2} \tag{5-3}$$

$$B = \frac{bP}{RT} \tag{5-4}$$

$$Z = \frac{Pv}{RT} \tag{5-5}$$

For a single-component, one-phase system, the solution of Equation (5-2) results in three real roots or one real and two imaginary roots. The real root is referred to a single gas phase. At the critical point:

$$a(T_C) = 0.45724 \frac{R^2T_C^2}{P_C} \tag{5-6}$$

At any temperature:

$$a(T) = a(T_C)\alpha(T_R, \omega) \tag{5-7}$$

$$b = 0.07780 \frac{RT_C}{P_C} \tag{5-8}$$

Where

$$\sqrt{\alpha} = 1 + \kappa\left(1 - \sqrt{T_R}\right) \tag{5-9}$$

$$\kappa = 0.37464 + 1.5422\omega - 0.26992\omega^2 \tag{5-10}$$

5.2   GAS HOLDUP

The gas holdup was determined using the manometric method (also known as the hydrostatic head method) with the following assumptions: (1) the reactor is operating under steady-state condition; (2) the liquid or slurry and gas phases are well mixed in the volume between the 2 dP cell legs; and (3) the impact of the frictional effects on the pressure drop is negligible [264, 265].

The passage of gas bubbles throughout the slurry phase alters the pressure drop along the reactor which can be expressed by the following expression:

$$\frac{dP}{dh} = -\rho_D g \tag{5-11}$$

Where ρ_D is the density of the dispersed phase containing gas, liquid and solid and can be derived as:

$$\rho_D = \varepsilon_G \rho_G + \varepsilon_L \rho_L + \varepsilon_S \rho_S \tag{5-12}$$

Introducing c_V as the volumetric concentration of catalyst in the slurry phase, the equation above becomes:

$$\rho_D = \varepsilon_G \rho_G + (1 - \varepsilon_G)[c_V \rho_S + (1 - c_V)\rho_L] \tag{5-13}$$

Replacing this expression of ρ_D in Equation (5-11), the latter can be integrated as follows:

$$\int_{P_B}^{P_T} dP = -\int_{h_B}^{h_T} (\varepsilon_G \rho_G + (1 - \varepsilon_G)[c_V \rho_S + (1 - c_V)\rho_L])g dh \tag{5-14}$$

The lower and higher limits are defined by the position of the dP cell legs on the column. If assumption #2 is used, the gas holdup and the catalyst concentration can be considered constant between the two dP cell legs leading to:

$$P_T - P_B = -\left[\varepsilon_G \rho_G + (1 - \varepsilon_G)[c_V \rho_S + (1 - c_V)\rho_L]\right]g(H_T - H_B) \tag{5-15}$$

The pressure difference between the lower and the upper legs is directly measured by the dP cell and since the distance between the legs is known, the following expression for gas holdup can be written:

$$\varepsilon_G = \frac{c_V \rho_S + (1 - c_V)\rho_L}{c_V \rho_S + (1 - c_V)\rho_L - \rho_G}\left(1 - \frac{\Delta P_{\text{cell}}}{(c_V \rho_S + (1 - c_V)\rho_L)g\Delta H_{\text{cell}}}\right) \tag{5-16}$$

5.3   GAS BUBBLES SIZE

The DGD technique was used to obtain the gas bubbles size distribution and the Sauter mean diameter. The corresponding gas holdups of the small and large gas bubbles in the SBCR were calculated using the technique introduced by Inga and Morsi [266] and successfully used by Behkish et al. [120, 166] and Lemoine et al. [123]. This technique relies on the assumption that large gas bubbles have greater rise velocity and therefore disengage first, whereas small gas bubbles, retained within the slurry or entrained in the wakes created by the flow of the large gas bubbles, have smaller rise velocity and therefore they disengage in a later stage.

The following assumptions were made in order to derive the equations needed for calculating the gas bubble sizes: (1) the rate of gas disengagement of each bubble is constant under given experimental conditions; (2) once the gas flow is stopped, there is no coalescence or breakup of gas bubbles, meaning that the bubbles sizes remain constant as they disengage; and (3) the liquid internal circulation does not affect the bubble rise velocity [267].

The assessment of the ε_G with time after the gas flow inside the SBCR has been stopped using Equation (5-16) can lead to the estimation of the rate of disengagement of each bubble size. An example of the behavior of ε_G with time is shown in Figure 25. From $t = 0$ to t_1, the dP cell shows no decline in ε_G, however, no more gas is entering the bottom of the reactor. This means that the amount of gas that leaves the dP cell section (from L_B to L_T) is the same as the one which leaves the lower section (from L_0 to L_B). From t_1 to t_2, the large gas bubbles having a bubble rise velocity (U_b) ranging from L_T/t_1 to $\Delta H_{\text{cell}}/t_2 = (L_T - L_B)/t_2$ disengage from the cell region and during this period, the small gas bubbles present in the lower section (L_0 to L_B) do not affect the dP cell reading. From t_2 to t_3, the small gas bubbles are disengaging from the cell region (L_B to L_T) and the dP cell reflects the small gas bubbles with U_b ranging from $\Delta H_{\text{cell}}/t_2$ to $\Delta H_{\text{cell}}/t_3$.

The volume of the gas bubbles that leaves the dP cell region ($\Delta H_{\text{cell}} = L_T - L_B$) can therefore be represented by the decrease of the total gas holdup as follows:

$$\Delta\varepsilon_{G,i} = \int_{t_{i-1}}^{t_i} \frac{d\varepsilon_G}{dt} dt \qquad (5\text{-}17)$$

Consequently the total gas holdup is:

$$\varepsilon_G = \sum_{i=1}^{n} \Delta\varepsilon_{G,i} \qquad (5\text{-}18)$$

The rise velocity of each size class of gas bubbles can then be calculated at any time t from:

$$U_{b,i} = \frac{L_T - \frac{L_B}{2}}{t} \qquad (5\text{-}19)$$

This method is valid when dealing with gas-liquid system, however, the presence of solids should be accounted for, due to the settling velocity of the solid particles. In this study, the correlation proposed by Fukuma et al. [268], who used up to 50 vol.% glass beads, was used to calculate the gas bubble size $d_{b,i}$:

$$d_{b,i} = \frac{U_{b,i}^2}{1.69g} \qquad (5\text{-}20)$$

The Sauter-mean bubble diameter was thus calculated using the following equation:

$$d_{32} = \frac{\sum_i n_i d_{b,i}^3}{\sum_i n_i d_{b,i}^2} \qquad (5\text{-}21)$$

5.4 VOLUMETRIC LIQUID-SIDE MASS TRANSFER COEFFICIENT

The volumetric mass transfer coefficient, k_La, was calculated using the Transient Physical Gas Absorption technique. During the absorption of the gas into the liquid, the decline of reactor pressure was recorded as a function of time until the equilibrium was reached. The rate of mass transfer of the solute gas into the liquid phase can be calculated using the two-film model:

$$\frac{dn_L}{dt} = k_La(C^* - C_L)V_L \qquad (5\text{-}22)$$

This can be rewritten when the liquid is not recirculated as:

$$\frac{dn_L}{dt} = k_La(n^* - n_L) \qquad (5\text{-}23)$$

For experiments with liquid recirculation, Equation (5-23) becomes:

$$\frac{dn_L}{dt} = k_L a(n^* - n_L) - F\frac{n_L}{V_L} \tag{5-24}$$

In Equation (5-24), *F* is the flow rate of liquid being recirculated by the pump. Both equations are numerically solved using the parameter estimation module from Athena Visual Studio Software version 11.0 with FORTRAN compiler g95 until a $k_L a$ value which best fits the experimental data is obtained.

5.5 SOLID PARTICLES DISTRIBUTION

The "dispersion-sedimentation model" is widely employed to describe the behavior of the solid in slurry reactors. The solid concentration profile in a slurry bubble column is a result of buoyancy and gravitational forces as well as kinetic energy. Quantitative description of the axial solid distribution has been frequently expressed by this sedimentation-dispersion model. In this model, a steady state material balance for the solid phase over a differential element leads to the following differential equation [5]:

$$D_S \frac{d^2 C_S}{dz^2} + U_P \frac{dC_S}{dz} = 0 \tag{5-25}$$

Where U_p is the particle settling velocity, D_S is solid phase axial dispersion coefficient, and z is the height.

The general solution of Equation (5-25) can be obtained as:

$$C_S = C_1 + C_2 exp\left(\frac{-U_P z}{D_S}\right) \tag{5-26}$$

When z approaches infinity, $C_S = 0$ and we can therefore drop the term C_1 and obtain:

$$C_S = C_2 exp\left(\frac{-U_P z}{D_S}\right) \tag{5-27}$$

The experimental values of solid concentration obtained from the slurry samples can therefore be fitted with an exponential function from which the ratio (U_p/D_S) can then be estimated.
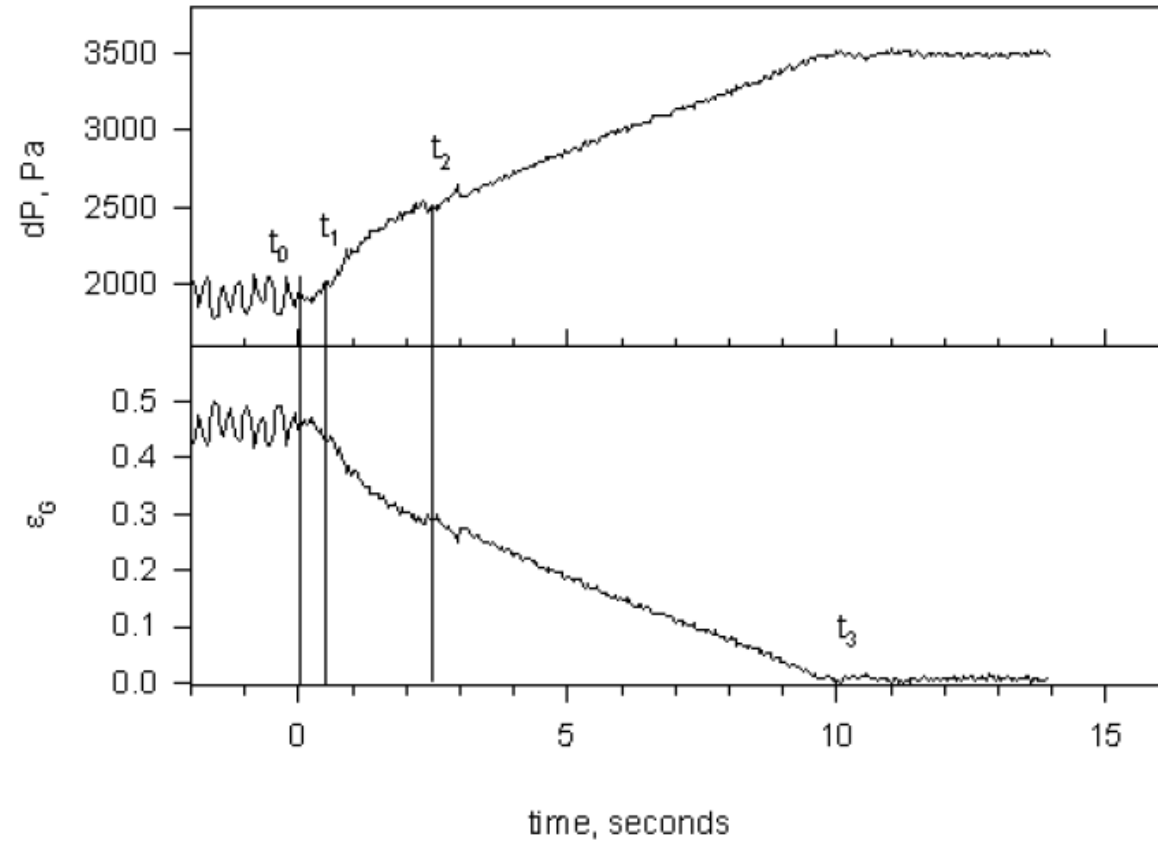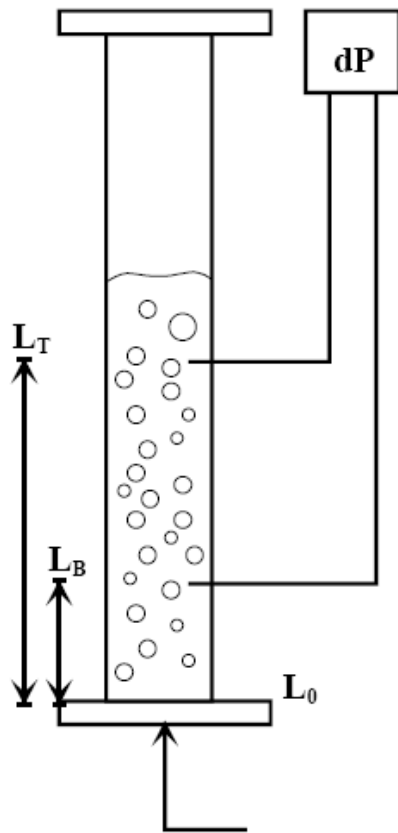
Figure 25: Dynamic Gas Disengagement in SBCR [166]

6.0   RESULTS AND DISCUSSION

6.1   HYDRODYNAMIC AND MASS TRANSFER PARAMETERS IN THE PILOT SBCR UNDER F-T CONDITIONS

In this section, the effects of pressure, temperature, gas and liquid velocities, gas nature and composition, solid concentration, liquid and solid phases natures on the hydrodynamics (ε_G and d_{32}) and mass transfer (k_La) parameters for N_2 and He as single components as well as for different mixtures of these two gases obtained in the 3 F-T liquids in the presence and absence of 3 different solids using the pilot-scale SBCR are discussed.

6.1.1   Effect of Pressure

The effect of pressure on the gas holdup for He and N_2 as well as their mixtures in the three liquids under the operating conditions studied showed that the gas holdup increases with the operating pressure as can be seen in Figures 29 (a), 26 and 27. This behavior is in agreement with the previous findings of numerous authors [120, 122, 123, 130, 131, 134, 155-165, 266, 269]. This is because the increase of operating pressure increases the gas density and consequently its momentum. High gas density is known to increase the gas holdup [124, 128-132]. High gas momentum was reported to lead to the creation of small and rigid gas bubbles by promoting the rate of gas bubbles break-up [120] resulting in high gas holdup values [120, 123, 166].

High gas densities are responsible for gas bubbles shrinkage leading to small rigid gas bubbles [120, 123, 132-135]. This behavior can be seen in Figures 29 (b), 28 and 31 where the Sauter mean bubble diameter generally decreases with increasing pressure under the different sets of operating conditions used. It can be noted that an opposite behavior was obtained for the system N_2-molten reactor wax at 450 K where one set of the bubbles sizes appeared to slightly increase

with pressure. By inspecting the gas bubbles size distribution shown in Figure 32, one can note that increasing the pressure from 4 to 22 bar increases the population of the small gas bubbles with d_b < 1 mm and decreases the population of gas bubbles having d_b < 0.1 mm in diameter which are responsible for increasing the Sauter-mean bubble diameter as shown in Figure 29 (b). The addition of He or solid particles to the system decreased the Sauter mean bubble diameter with increasing pressure. Figure 33 illustrates that increasing pressure increases the population of gas bubbles with d_b < 1 mm in diameter and slightly decreases the population of the larger gas bubbles.
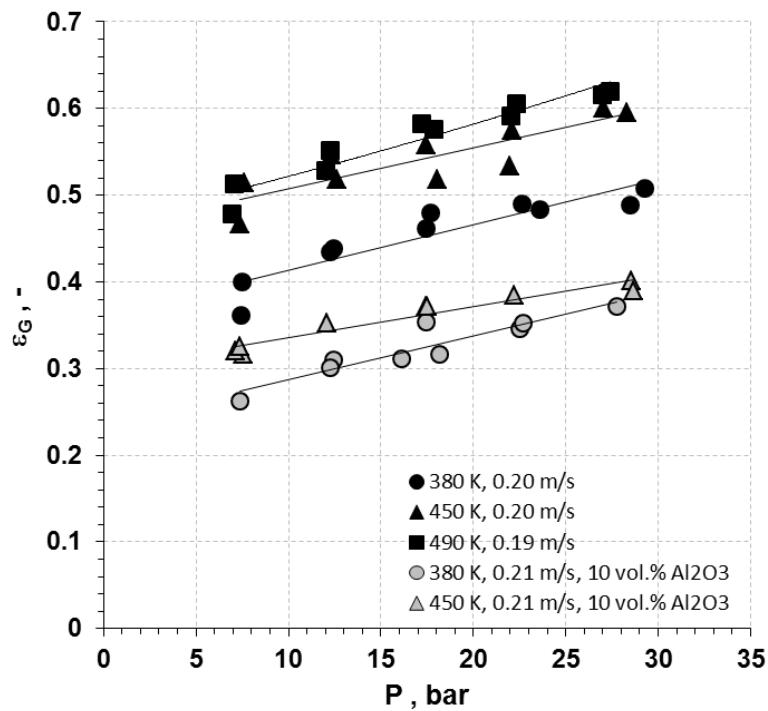
Figure 26: Effect of Pressure and Temperature on ε_G for N_2-Sasol wax

Figures 29 (c), 34 and 35 show the effect of pressure on the volumetric liquid-side mass transfer coefficient ($k_L a$) for both gases in the paraffins mixture as well as in the molten reactor wax and Sasol wax in the absence and presence of the solid particles under different operating conditions. As can be observed, the overall $k_L a$ values increase with increasing pressure, which is similar to the gas holdup behavior and in agreement with previous studies [121, 158, 166-168]. This behavior can be explained by the effect of pressure on the gas holdup and the gas bubbles Sauter mean diameter. As mentioned above the gas holdup appeared to increase with pressure, while the gas

bubbles size decreased and the combination of these two trends would increase the gas-liquid interfacial area, a, according to Equation (2-33). On the other hand, the effect of pressure on the mass transfer coefficient k_L is less obvious as its value could increase or decrease [123]. In the present work, the decrease of the bubble size with pressure would indicate a decrease of k_L since smaller bubbles are usually associated with low turbulences. The increase of k_La values with pressure observed in Figures 29 (c), 34 and 35, however, suggests that k_La in the SBCR operating in the churn-turbulent flow regime is controlled by the behavior of the gas-liquid interfacial area, a [123, 166, 266], not by k_L.
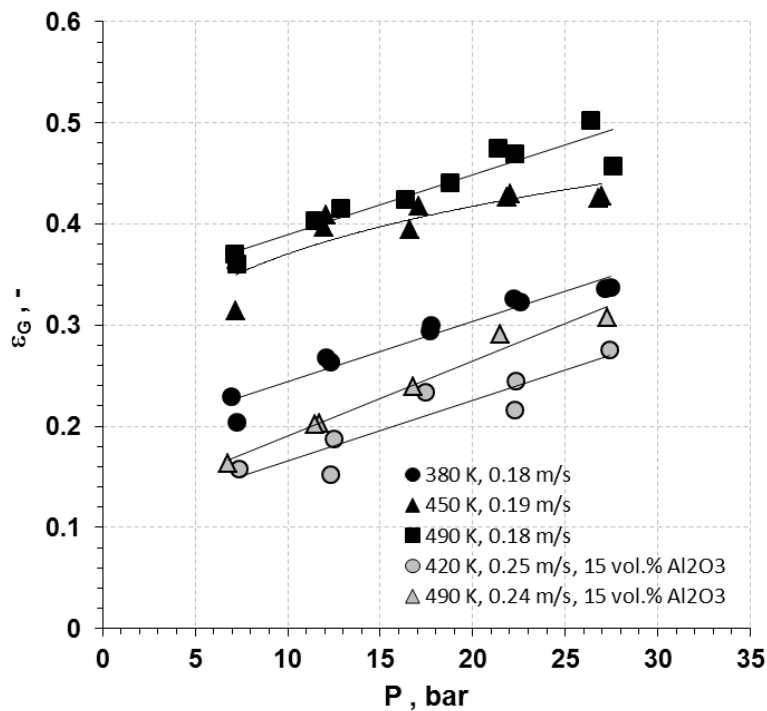
Figure 27: Effect of Pressure and Temperature on ε_G for He-Sasol wax

6.1.2   Effect of Gas Density

The effect of gas density on the hydrodynamics and mass transfer parameters is related to the effect of pressure and actually they are identical when the gas density is increased solely by increasing the system pressure. In this case, the same conclusions drawn for the effect of pressure on the k_La, ε_G and d_{32} given in the preceding section would be similar to that of the gas

density. However, when using the He/N_2 gas mixture, the gas density can be varied by changing the composition of the gas-phase while maintaining a constant total pressure. The effect of such variation on the gas holdup is illustrated in Figure 30 (a) and as can be observed for both He/N_2-paraffins mixture and He/N_2-reactor wax systems, increasing the gas density at constant pressure and temperature by changing the composition of the gas-phase leads to a systematic increase of the gas holdup. Figure 30 (a) also shows the increase of gas holdup with increasing pressure for the systems N_2-paraffins mixture as well as N_2-Sasol wax and He-Sasol wax. Thus, increasing the gas density whether by increasing pressure or changing the gas composition is found to similarly increase the gas holdup. This increase of gas density leads to the shrinkage of the gas bubbles [120, 123, 132-135] as shown in Figure 30 (b), which combined to the increase of gas holdup results in the increase of the overall volumetric liquid-side mass transfer coefficients shown in Figure 30 (c). These findings confirm that the gas density is an important variable which directly affects the hydrodynamics and mass transfer coefficients in SBCRs.
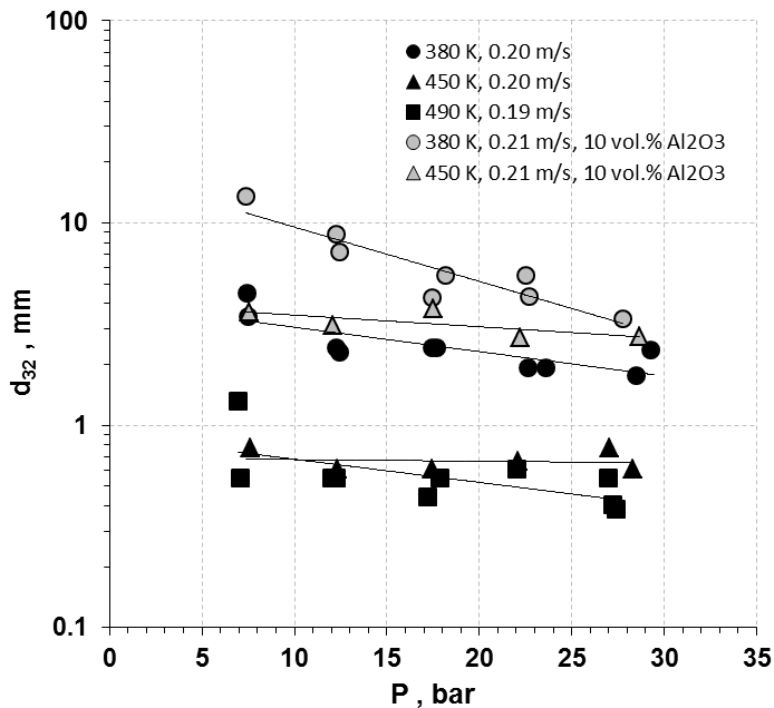
Figure 28: Effect of Pressure and Temperature on d$_{32}$ for N$_2$-Sasol Wax

96
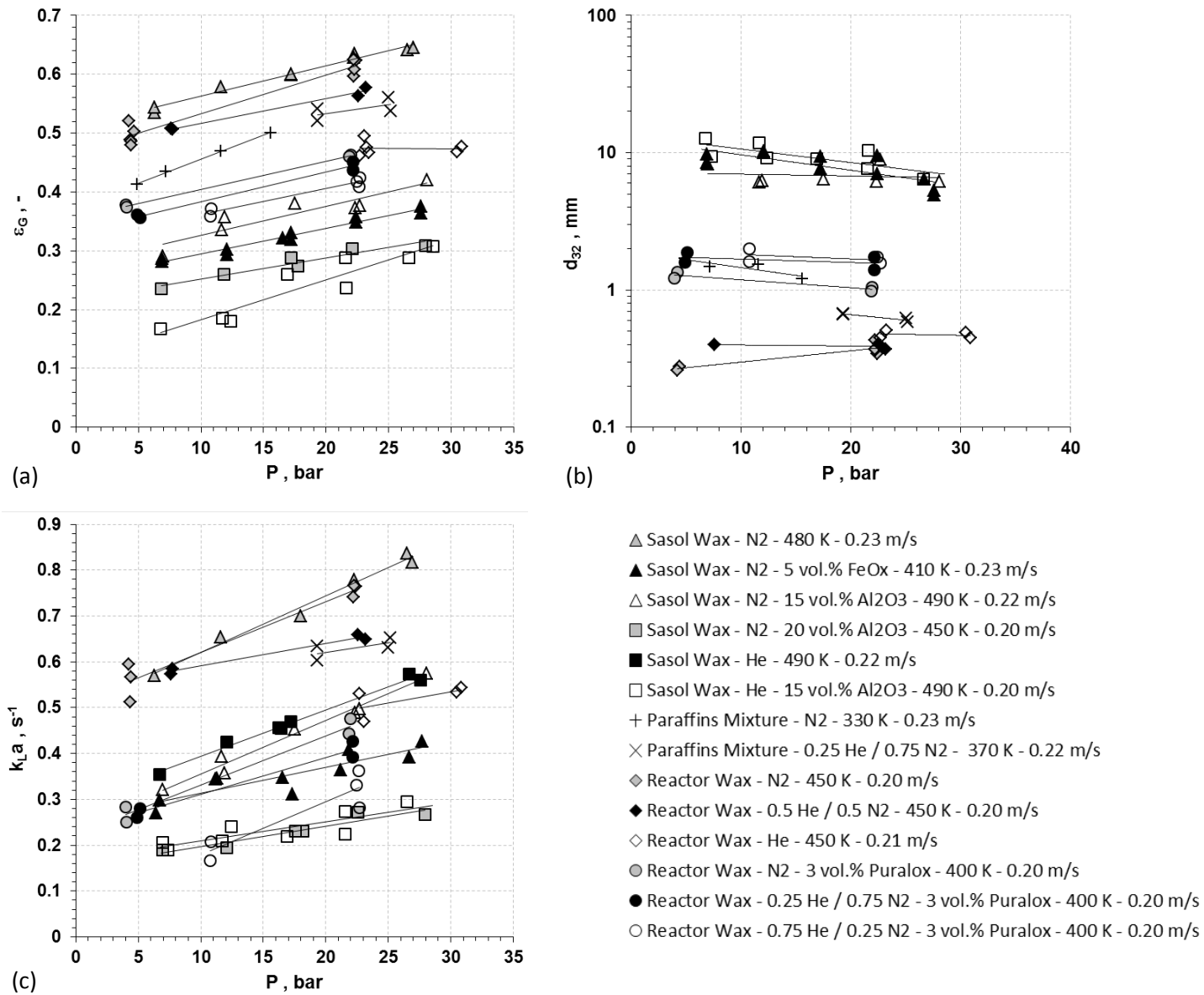
Figure 29: Effect of Pressure on ε_G (a), d_{32} (b) and $k_L a$ (c)

Legend:

△ Sasol Wax - N2 - 480 K - 0.23 m/s
▲ Sasol Wax - N2 - 5 vol.% FeOx - 410 K - 0.23 m/s
△ Sasol Wax - N2 - 15 vol.% Al2O3 - 490 K - 0.22 m/s
▨ Sasol Wax - N2 - 20 vol.% Al2O3 - 450 K - 0.20 m/s
■ Sasol Wax - He - 490 K - 0.22 m/s
□ Sasol Wax - He - 15 vol.% Al2O3 - 490 K - 0.20 m/s
+ Paraffins Mixture - N2 - 330 K - 0.23 m/s
✕ Paraffins Mixture - 0.25 He / 0.75 N2 - 370 K - 0.22 m/s
◇ Reactor Wax - N2 - 450 K - 0.20 m/s
◆ Reactor Wax - 0.5 He / 0.5 N2 - 450 K - 0.20 m/s
◇ Reactor Wax - He - 450 K - 0.21 m/s
● Reactor Wax - N2 - 3 vol.% Puralox - 400 K - 0.20 m/s
● Reactor Wax - 0.25 He / 0.75 N2 - 3 vol.% Puralox - 400 K - 0.20 m/s
○ Reactor Wax - 0.75 He / 0.25 N2 - 3 vol.% Puralox - 400 K - 0.20 m/s

Figure 30: Effect of Gas Density on ε_G (a), d_{32} (b) and k_La (c)

Legend:

⊠ Sasol Wax - N2 - 15 vol.% Al2O3 - 490 K - 0.19 m/s
⊞ Sasol Wax - He - 15 vol.% Al2O3 - 490 K - 0.20 m/s
○ Paraffins Mixture - N2 - 330 K - 0.23 m/s
● Paraffins Mixture - N2 - 410 K - 22 bar - 0.21 m/s
◆ Paraffins Mixture - 0.25 He / 0.75 N2 - 410 K - 23 bar - 0.20 m/s
■ Paraffins Mixture - 0.5 He / 0.5 N2 - 410 K - 23 bar - 0.20 m/s
▲ Paraffins Mixture - 0.75 He / 0.25 N2 - 410 K - 23 bar - 0.19 m/s
✕ Paraffins Mixture - He - 410 K - 23 bar - 0.19 m/s
⬤ Reactor Wax - N2 - 450 K - 0.21 m/s
◇ Reactor Wax - 0.25 He / 0.75 N2 - 450 K - 0.20 m/s
▢ Reactor Wax - 0.5 He / 0.5 N2 - 450 K - 0.20 m/s
△ Reactor Wax - 0.75 He / 0.25 N2 - 450 K - 0.19 m/s
✚ Reactor Wax - He - 450 K - 0.19 m/s

Figure 31: Effect of Pressure and Temperature on d$_{32}$ for He-Sasol Wax
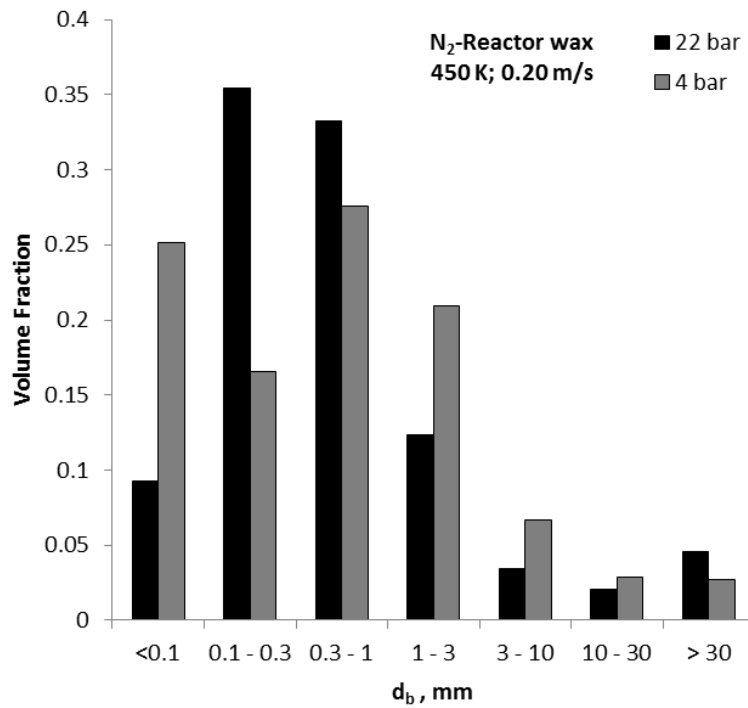
Figure 32: Effect of Pressure on the Gas Bubbles Size Distribution for N$_2$-Molten Reactor Wax
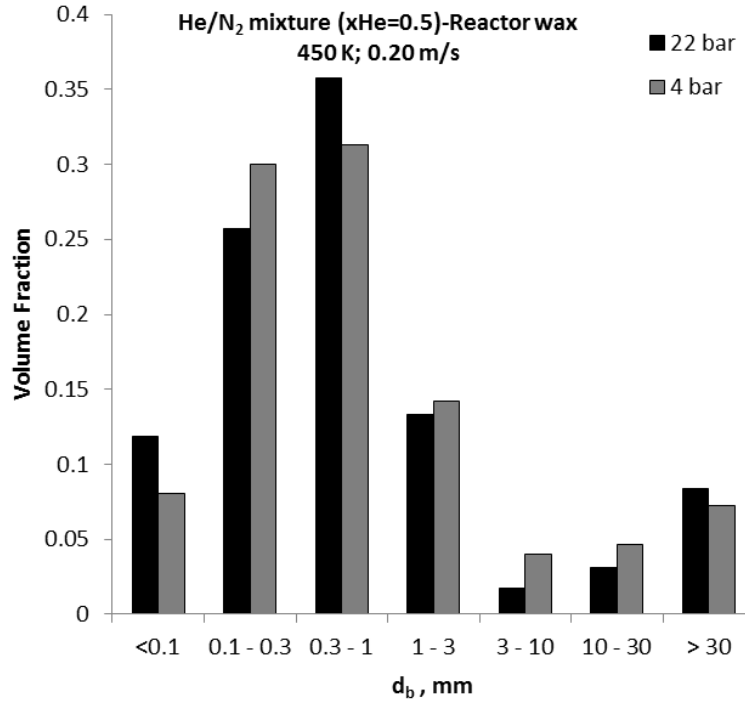
Figure 33: Effect of Pressure on the Gas Bubbles Size Distribution for He/N$_2$ Mixture-Molten Reactor Wax

6.1.3 Effect of Temperature

Figures 37 (a), 26 and 27 represent the effect of temperature on the gas holdup for N$_2$ and He in the paraffins mixture as well as in the molten reactor and Sasol waxes in the absence and presence of solid particles. As can be seen in these figures, for both N$_2$ and He increasing temperature increases the gas holdup. This behavior agrees with many other reported findings [138, 148, 154, 155]. The increase of gas holdup with temperature can be related to the alteration of the physical properties of the liquid-phase. For instance, increasing temperature decreases the liquid viscosity and surface tension which lead to higher gas holdup values [124, 128, 131, 137-139, 144, 145, 147-149].

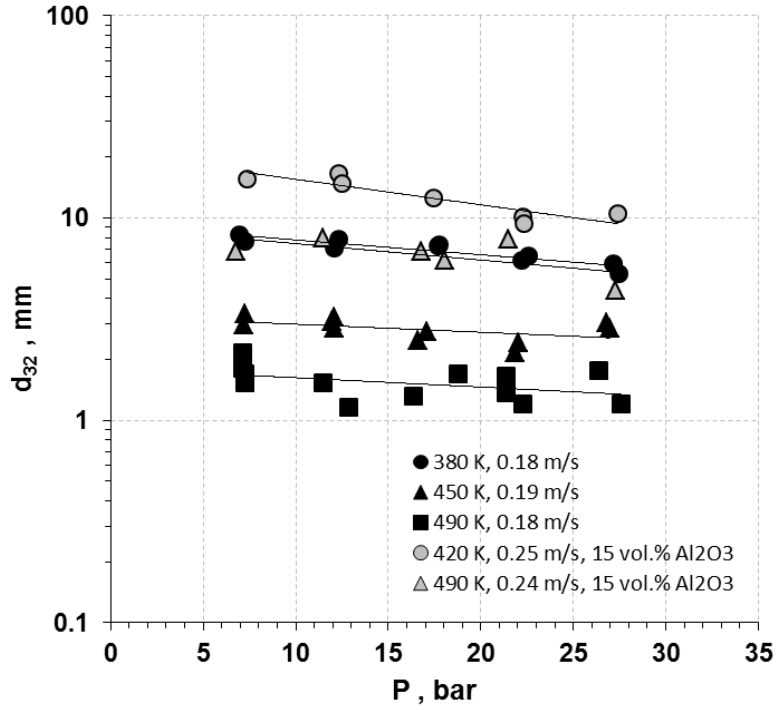For the N$_2$-molten reactor wax system in the absence of solid particles, however, the gas holdup appeared to remain constant with increasing temperature from 400 to 500 K. Jordan and Schumpe [129] found that increasing temperature had little influence on the gas holdup in ethanol and decalin. Also, Deckwer et al. [108] did not find any change of the gas holdup when increasing temperature from 143 to 285 $^{\circ}$C when measuring the gas holdup for N$_2$ in molten paraffin in the

100

presence of 10 wt.% Al_2O_3 particles in a 10 cm slurry bubble column. Nonetheless, it should be noted that Deckwer et al. [108]only used superficial gas velocities up to 0.04 m/s and accordingly they were limited to the homogeneous flow regime.
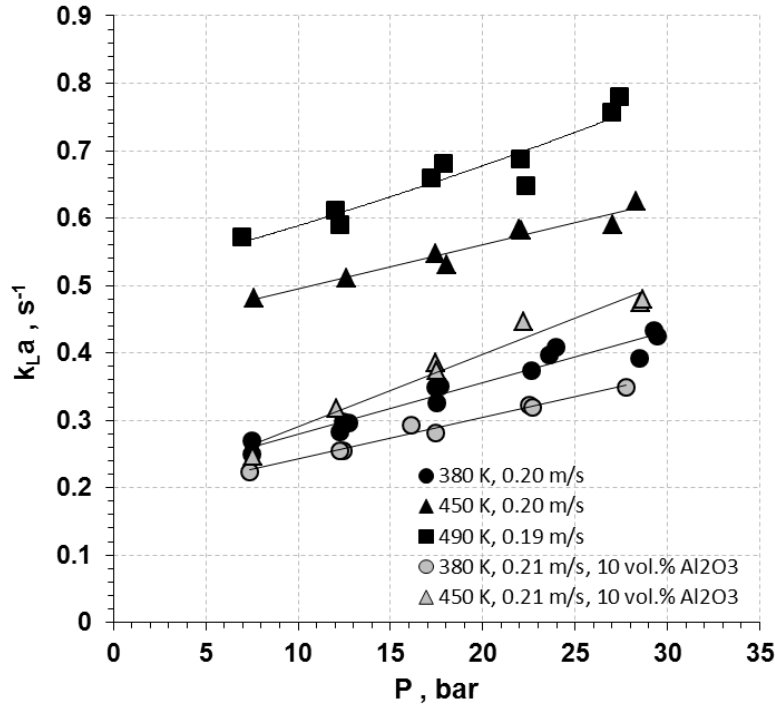
Figure 34: Effect of Pressure and Temperature on k_La for N_2-Sasol Wax

Figures 37 (b), 28 and 31 depict the effect of temperature on the Sauter mean bubble diameter and as can be observed d_{32} generally decreases with increasing temperature within the range studied, such in the case for the 0.25/0.75 (He/N_2) gaseous mixture which is similar to literature findings [146]. This is because increasing temperature decreases the liquid viscosity and surface tension, which are responsible for the formation of small gas bubbles [146]. In the case of 0.75/0.25 (He/N_2) gaseous mixture in the paraffins liquid mixture containing solid particles concentration of 2 vol.%, however, d_{32} values increased with increasing temperature, which shows the effect of solid particles on d_{32}. This behavior is similar to that by Behkish et al. [120] who reported an increase of d_{32} values with temperature when increasing the solid concentration from 5 to 10 vol.%. They attributed this behavior to the decrease of the froth (foam) stability of the liquid phase at high temperature and high solid concentration. As matter of fact, unstable foam was observed in this study up to 3 vol.% solid concentration in the paraffins mixture.

Furthermore, it seems that increasing the He content in the gas mixture also reduced the froth stability which resulted in increasing the Sauter mean bubble diameter with increasing temperature.
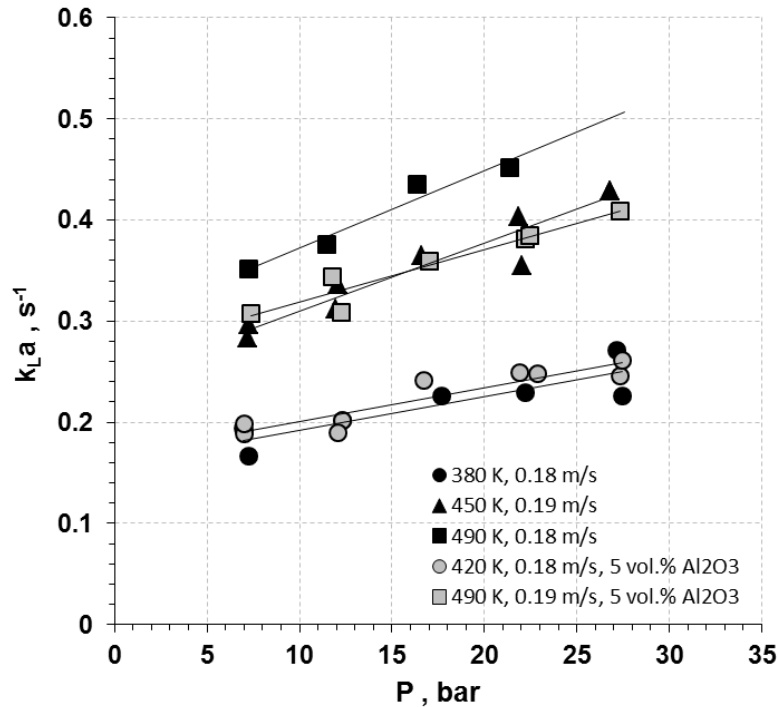
Figure 35: Effect of Pressure and Temperature on k_La for He-Sasol Wax

In the case of N_2-molten reactor wax without any solid present, when increasing temperature from 400 K to 500 K, d_{32} values appeared to slightly decrease with increasing temperature. This behavior could be attributed the fact that a minimum gas bubble size has been already reached at 400 K. As can be seen in Figure 38, in the absence of solid particles, the bubble size distribution remains almost identical from 400 to 500 K, which could explain why the gas holdup for this system remains constant even with increasing temperature. A similar behavior can be observed in the case of N_2 in Sasol wax also in the absence of solid, when increasing temperature from 450 K to 490 K at superficial gas velocities around 0.20 m/s (Figure 28).

Figure 38 also shows that in the presence of Puralox particles, increasing temperature increases the population of small gas bubbles and consequently decreases the population of large gas bubbles. It is also important to note that at high temperatures, the solid particles have a weak effect on the gas bubble size in the N_2-molten reactor wax system. In fact, as can be seen in

Figure 37 (b), at temperature above 475 K, increasing the solid particles concentration was found to have negligible effect on d_{32}.

Figures 37 (c), 34 and 35 show the effect of operating temperature on the overall liquid-side volumetric mass transfer coefficients (k_La) for the gases in the paraffins mixture as well as in the Sasol and reactor waxes in the absence and presence of solid particles. As can be seen, k_La values strongly increase with increasing temperature which is in accordance with previous findings [129, 130]. This behavior is due to the decrease of the liquid viscosity and surface tension with increasing temperature, which was reported to increase k_La [121, 140-143, 150]. More precisely, it can be explained by the effect of temperature on the mass transfer coefficient (k_L) and the gas liquid interfacial area (a). The increase of temperature results in an increase of gas diffusivity which increases k_L values ($k_L \propto D_i^{0.5-1}$). Also, increasing temperature decreases the viscosity and surface tension of the liquid which increases the gas-liquid interfacial area (a) due to its effect on the gas holdup and gas bubble size. Thus, the effects of temperature on both a and k_L led to the increase of k_La values.
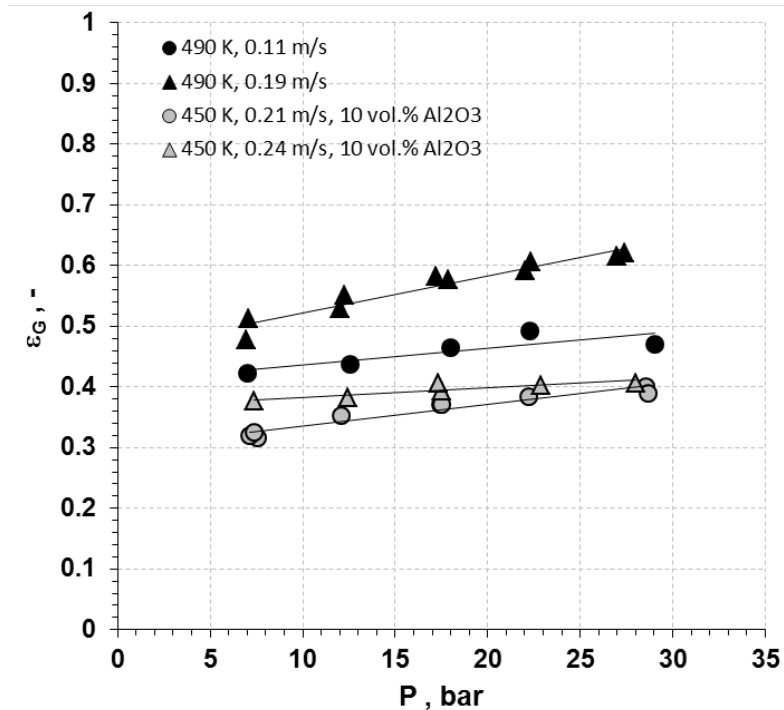
Figure 36: Effect of U_g on ε_G for N_2-Sasol wax
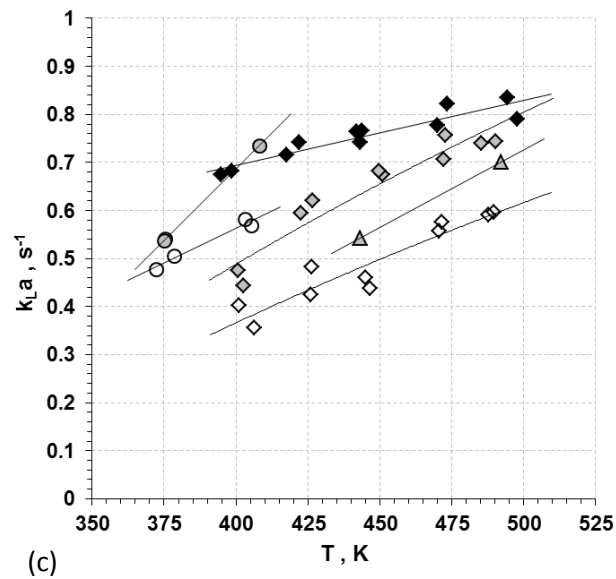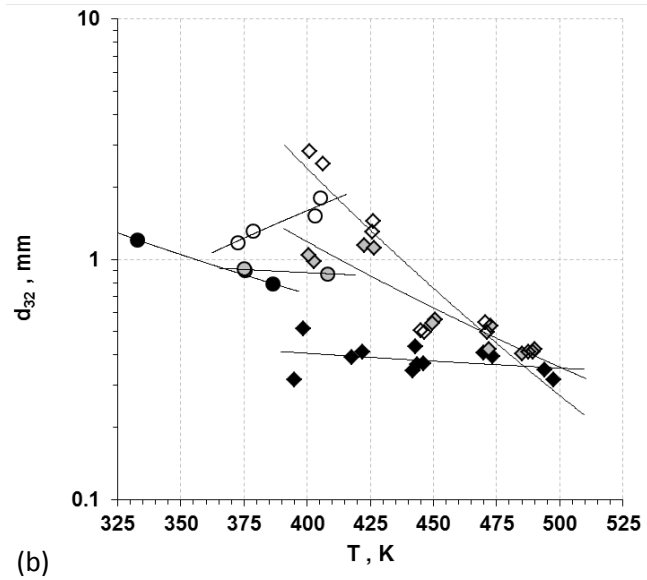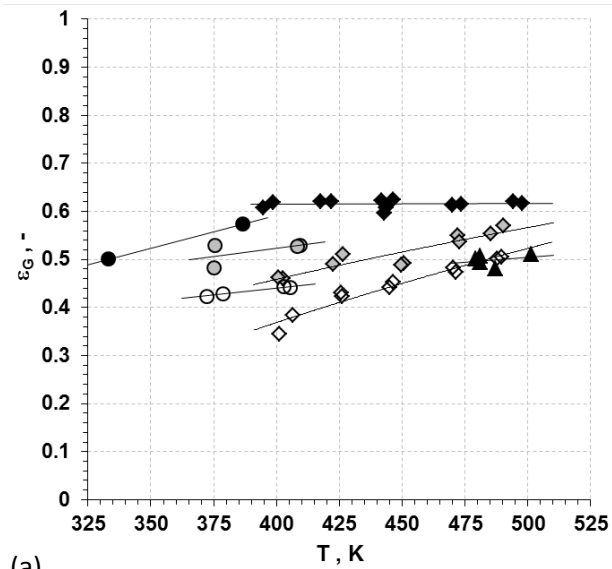
Figure 37: Effect of Temperature on ε_G (a), d_{32} (b) and k_La (c)
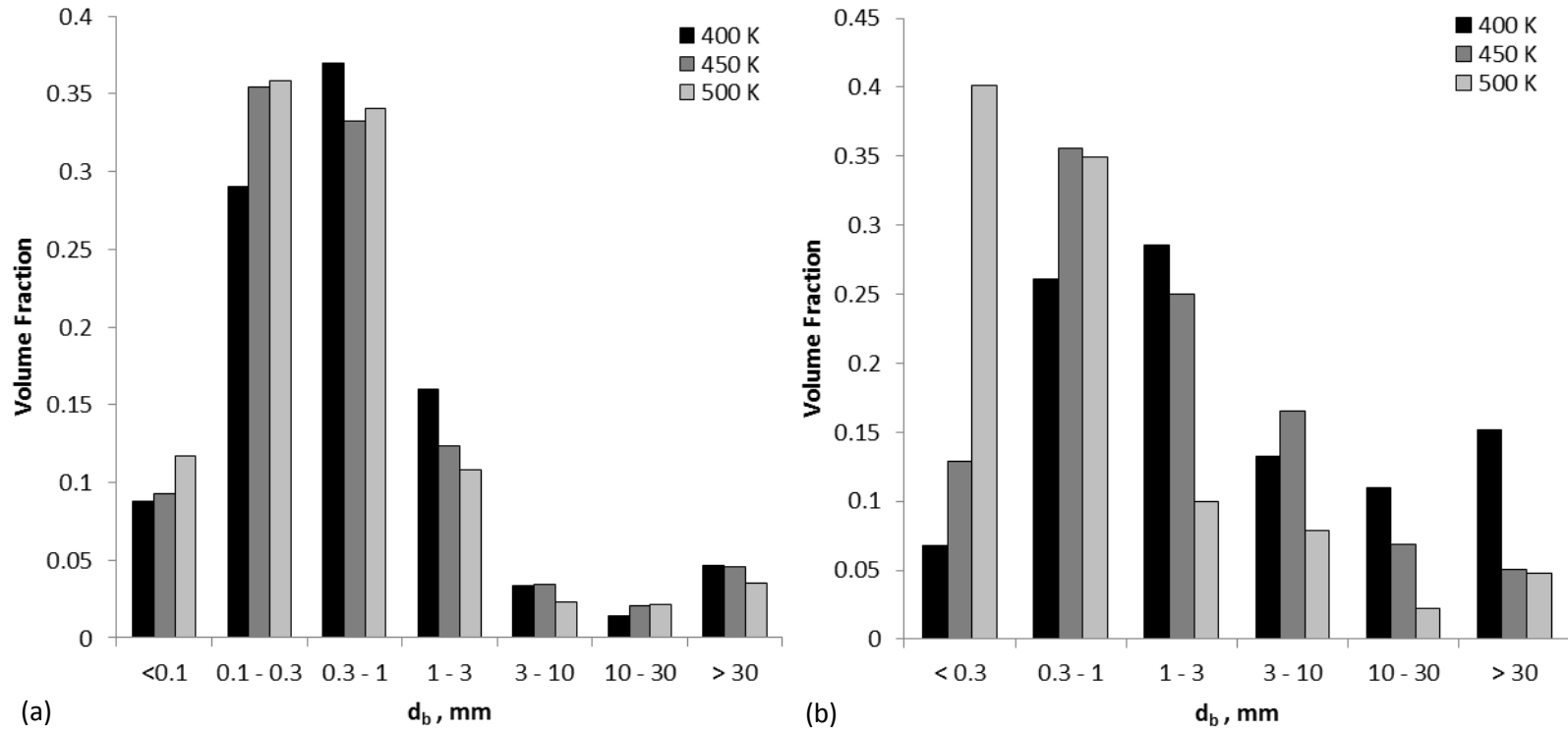
Figure 38: Effect of Temperature and Solid Concentration on the Gas Bubbles Size Distribution of N_2 in Molten Reactor Wax with Puralox particles

($C_S = 0$ vol.% (a), $C_S = 3$ vol.% (b))

6.1.4 Effect of Superficial Gas Velocity

The increase of the superficial gas velocity (U_g) appears to increase the gas holdup, as shown in Figures 43 (a), 36 and 39, for both gases in the paraffins mixture as well as in the Sasol and reactor waxes in the absence and presence of solid particles. Numerous authors [108, 124, 128-131, 137-140, 149, 155] also reported an increase of gas holdup while increasing the gas flow rate.
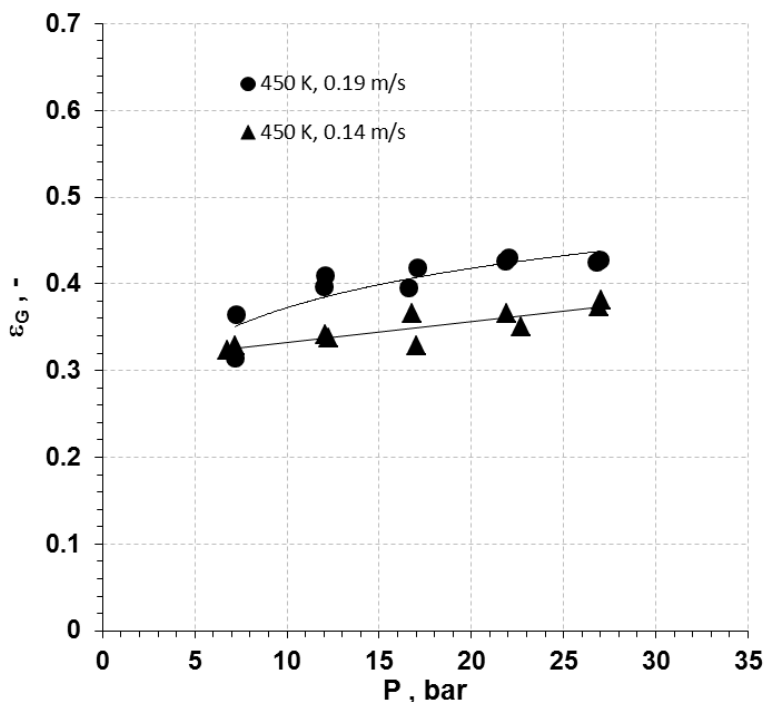
Figure 39: Effect of U$_g$ on ε$_G$ for He-Sasol wax

The effect of superficial gas velocity on the Sauter-mean bubble diameter, however, is not clear, as it can lead to a decrease (see Figures 43 (b) and 40), an increase (see Figures 43 (b) and 40) or have no effect (see Figures 43 (b) and 41) on the Sauter mean bubble diameter depending on the conditions used. In fact, the increase of the gas flow rate increases the momentum and leads to both higher probabilities of bubbles coalescence and breakage. The increase of the gas momentum is responsible for increasing the gas holdup [120, 123, 166]. Under the operating conditions used in this study, the increase of the superficial gas velocity led, in some cases, to the increase of the frequency of bubble coalescence which resulted in a slight increase of the gas

106

bubbles Sauter-mean diameter [123, 133-135] and in others cases it resulted in the increase of the rate of bubbles breakage which showed an opposite effect, i.e., smaller gas bubbles.
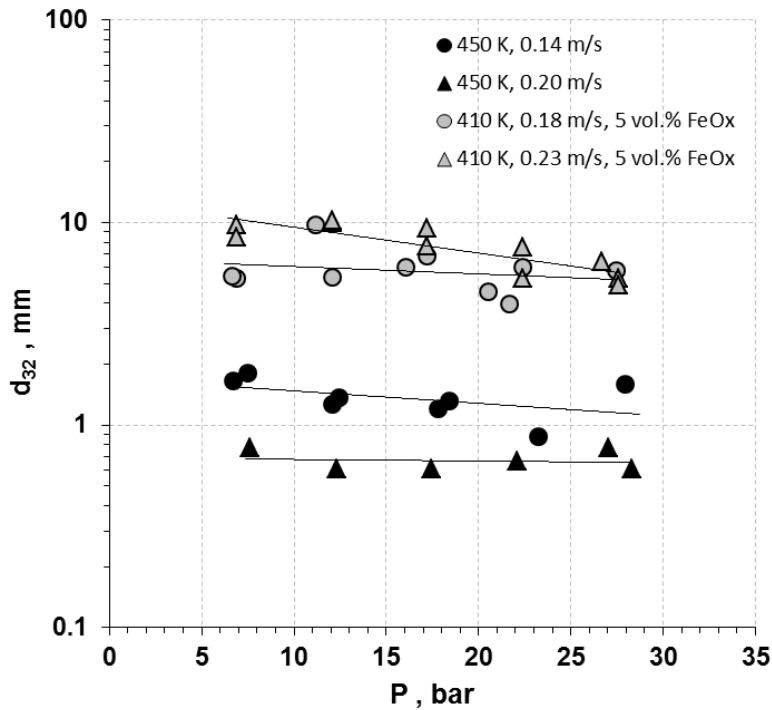
Figure 40: Effect of U_g on d_{32} for N_2-Sasol wax

The volumetric liquid-side mass transfer coefficient appears to slightly increase with increasing the superficial gas velocity as can be observed in Figures 43 (c) and 42. This behavior, which is in accordance with previous studies [158, 166], can be related to the effect of the superficial gas velocity on the gas holdup and the gas bubbles Sauter-mean diameter. As can be seen in Figures 43 (a), 36 and 39, increasing the superficial gas velocity increases the gas holdup, which increases the gas-liquid interfacial area according to Equation (2-33). Also, increasing the superficial gas velocity, in some cases, decreases the Sauter mean-bubble diameter (see Figures 43 (b) and 40) which further increases the gas-liquid interfacial area according to the same equation. When increasing U_g the d_{32} increases (see Figures 43 (b) and 40), these two opposing effects might offset the effect of the superficial gas velocity on the gas-liquid interfacial area, a. On the other hand, the larger gas bubbles induce more turbulences leading to high k_L values. It seems that the resultant effect of gas velocity on the gas-liquid interfacial area and the mass

transfer coefficient has always resulted in the increase of $k_L a$ under all conditions studied as shown in Figures 43 (c) and 42.
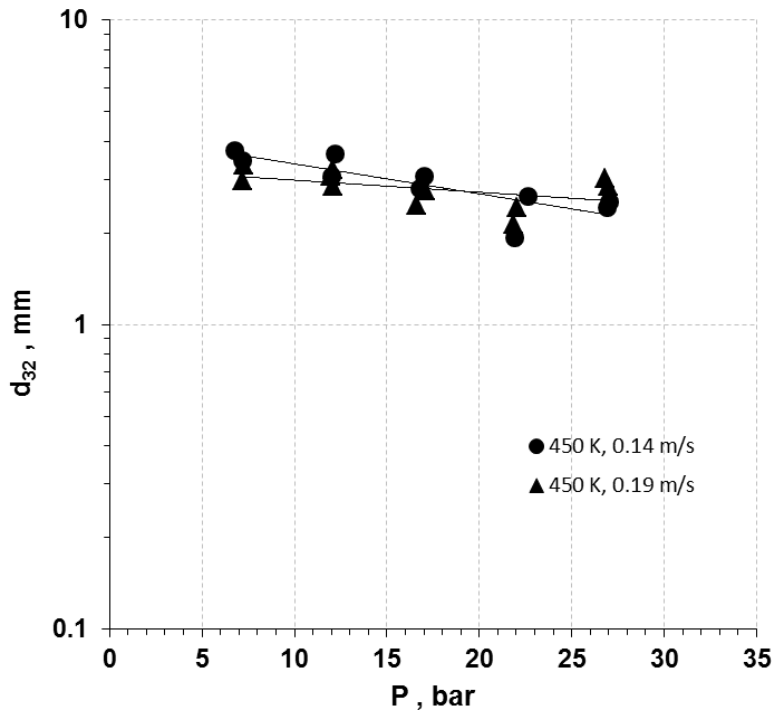
Figure 41 Effect of U_g on d_{32} for He-Sasol wax at 453 K
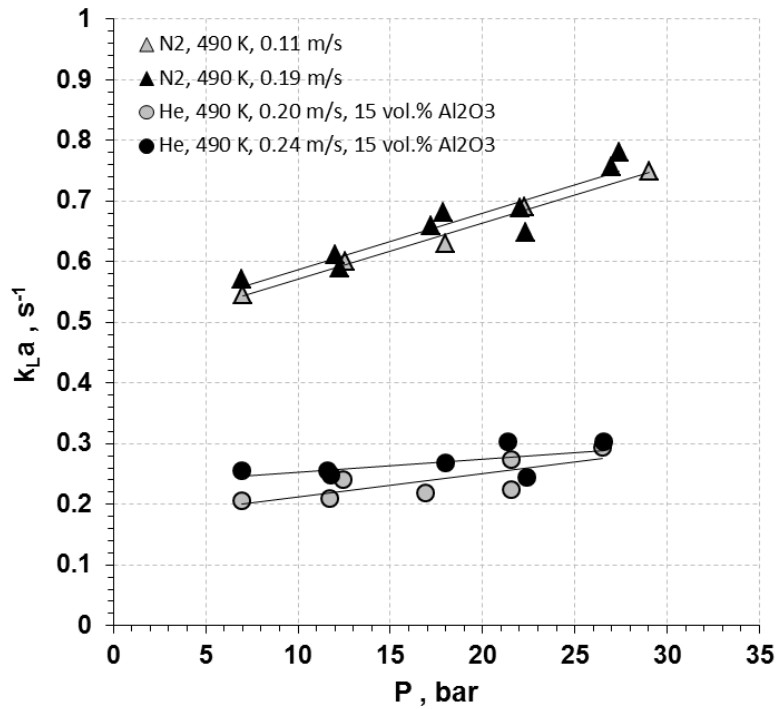
Figure 42: Effect of U_g on $k_L a$ for He or N_2-Sasol wax
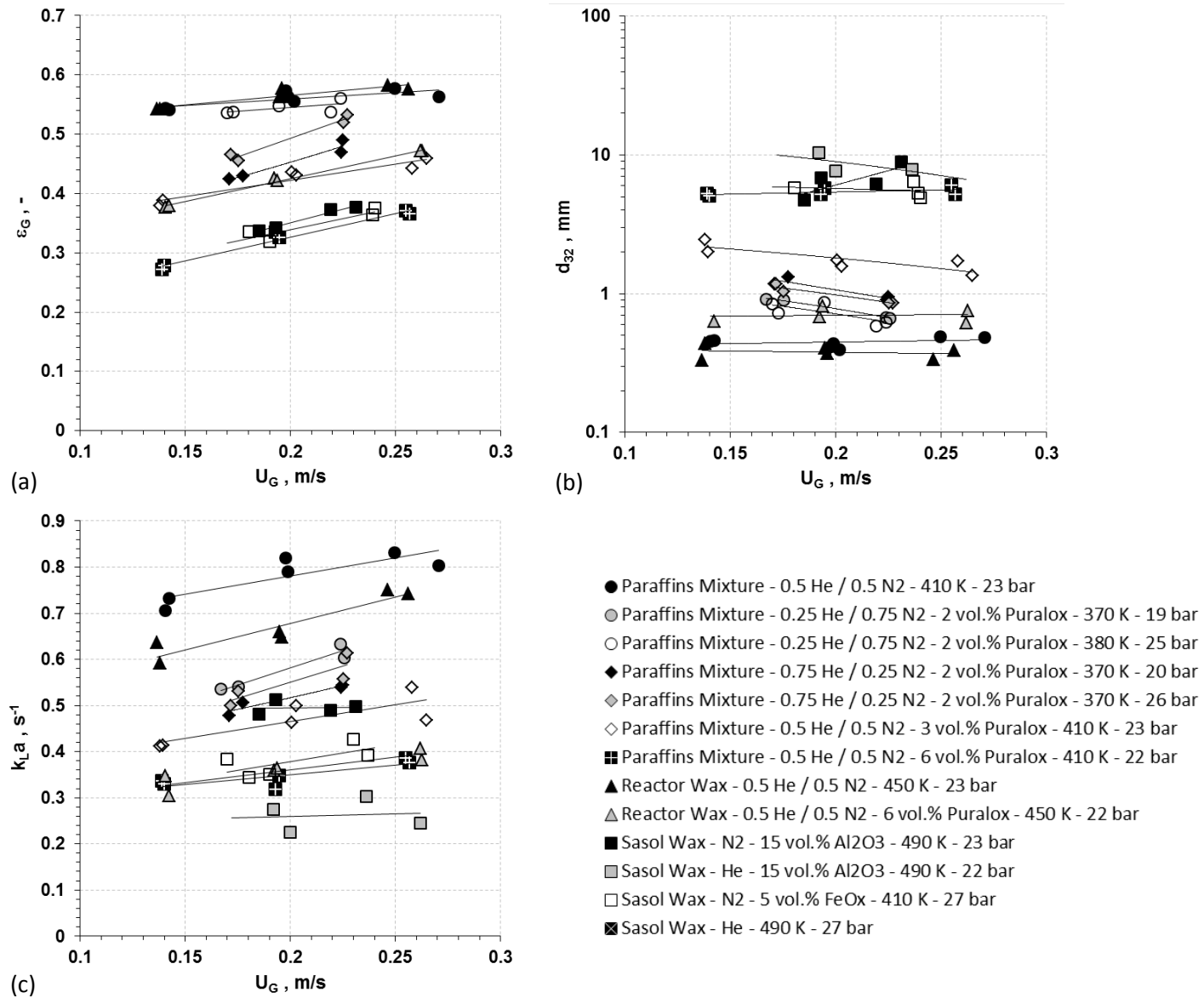
Figure 43: Effect of Superficial Gas Velocity on ε_G (a), d_{32} (b) and $k_L a$ (c)

6.1.5   Effect of Solid Concentration

The effect of solid concentration on the gas holdups of N_2 and He in the paraffins mixture, the molten reactor wax and the Sasol wax in the presence of suspended solid particles under various operating conditions is shown in Figures 44 (a), 45 and 46. As can be seen in these figures, the presence of solid particles decreases the gas holdup (ε_G) values for all systems studied, which is in agreement with several literature findings [120, 143, 152, 172-175]. This behavior can be attributed to the increase of slurry viscosity by adding small solid particles leading to large bubbles and consequently small gas holdup [124, 128, 131, 137-139, 144, 145, 147-149]. Literature studies on the gas holdup in similar F-T systems, however, reported different behaviors. Bukur et al. [169] used iron oxides and silica particles ($d_P < 44$ µm) at solid loading up to 30 wt.% and reported that for an upward slurry flow (0.005 m/s), the gas holdup slightly decreased when adding solids. Under batch mode conditions they reported that the gas holdup increased with solid loading up to 20 wt.%, but then decreased with further increase of the solid concentration to 30 wt.%. They attributed this behavior to the poor wettability of the particles used which caused the particles to adhere to the small gas bubbles and stabilize them thus preventing their coalescence. This effect was negated in the presence of liquid circulation due to the increase in the relative velocity between the solid and liquid phases leading to smaller contact angles and higher wettability of the particles. It should be noted that these authors conducted their experiments in a small diameter (5 cm) SBCR and hence the behavior observed could be strongly affected by the wall effect. Deckwer et al. [108] found a slight decrease of the gas holdup with increasing solid concentration, using alumina particles < 5 µm. In addition, Vandu et al. [190] using Puralox alumina particles ($10 < d_P < 39$ µm) in a C_9-C_{11} paraffins mixture, Krishna et al. [189] using silica particles ($27 < d_P < 47$ µm) in paraffin oil and Behkish et al. [120] using alumina particles ($d_P = 32$ µm) in an Isoparaffins mixture (Isopar-M), all reported a significant decrease of the gas holdup with increasing solid concentration similar to that obtained in the present work.
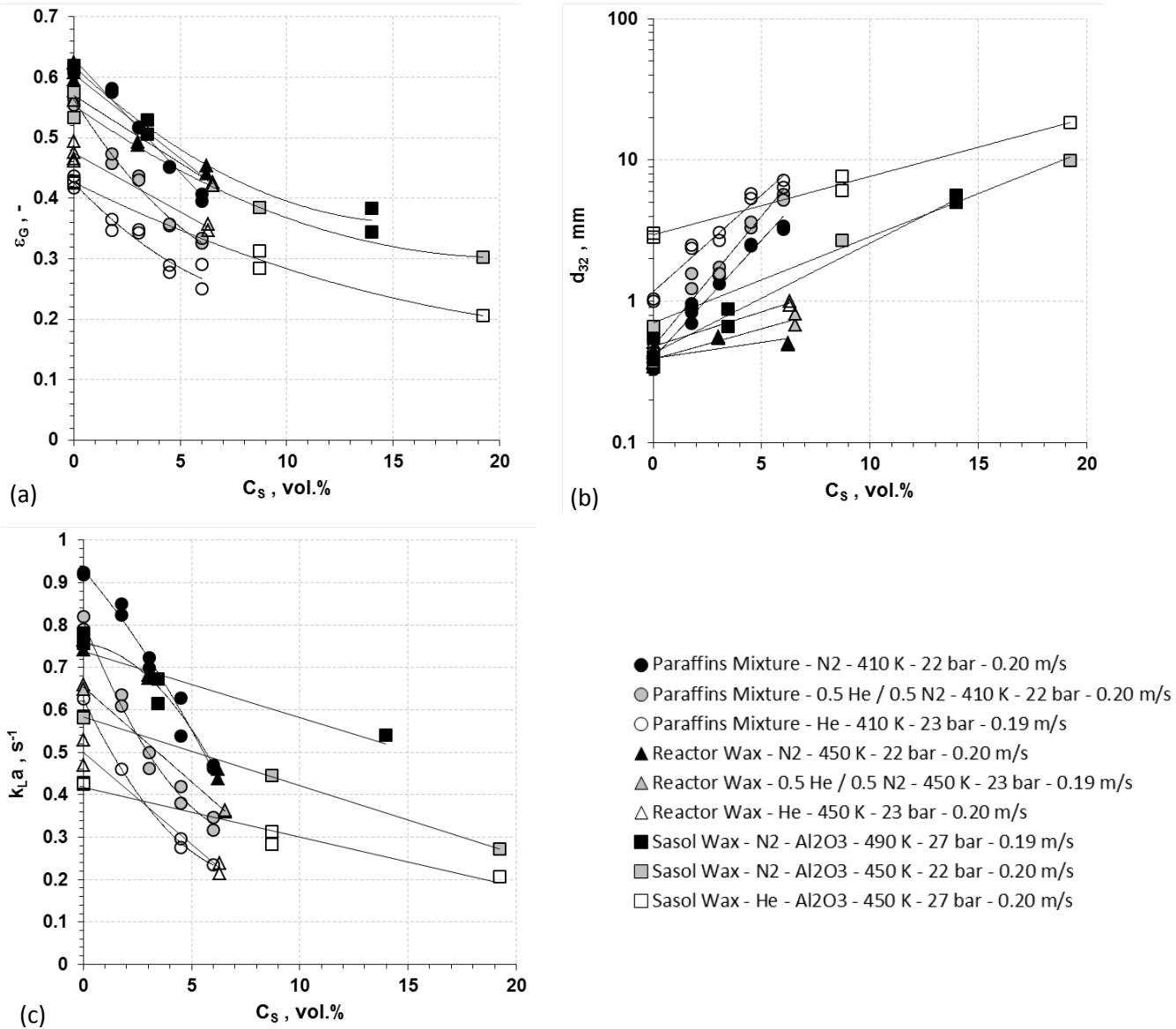
Figure 44: Effect of Solid Concentration on ε_G (a), d_{32} (b) and k_La (c)
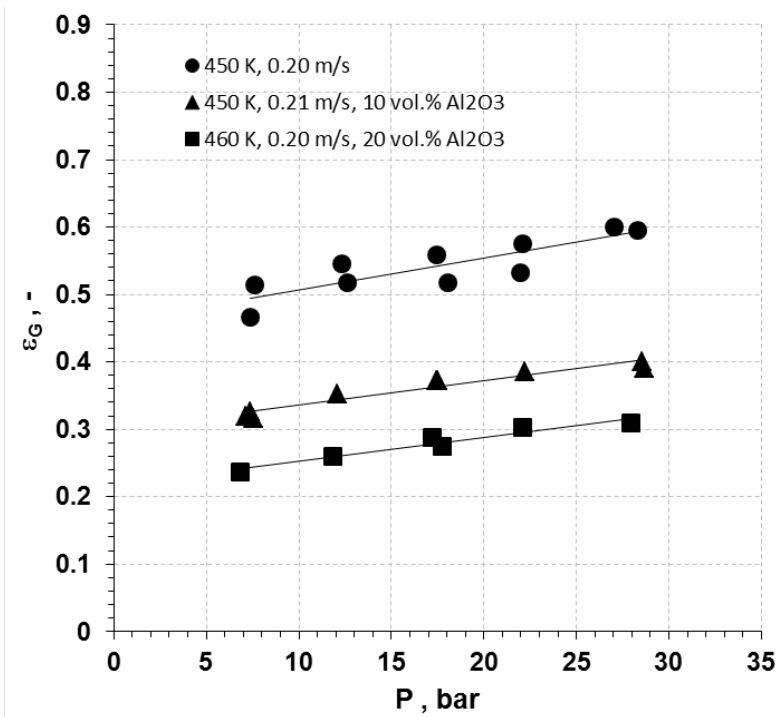
Figure 45: Effect of Solid Concentration on ε_G of N_2-Sasol Wax
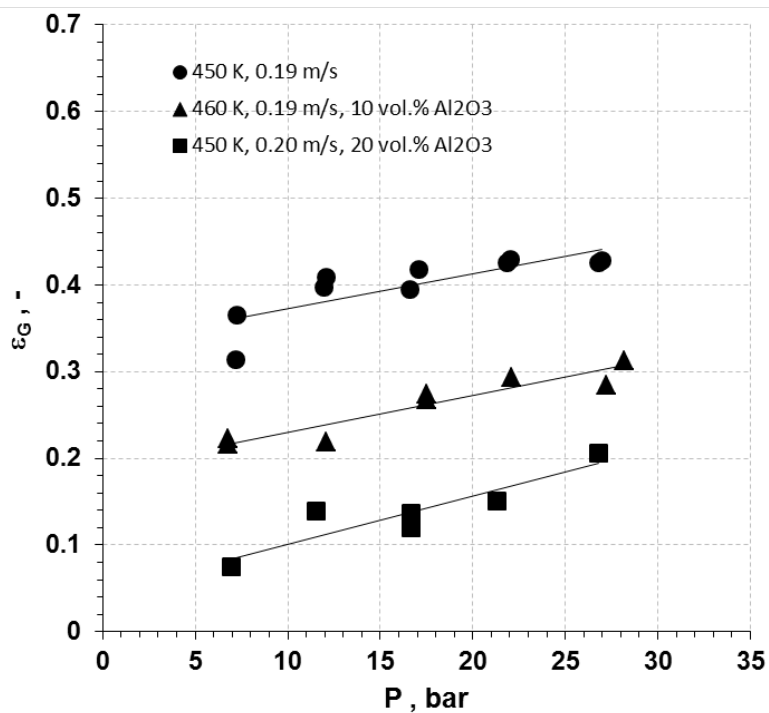
Figure 46: Effect of Solid Concentration on ε_G of He-Sasol Wax

Figures 44 (b), 47 and 48 show the effect of solid concentration on the gas bubbles Sauter mean diameter under different operating conditions; and as can be seen, under all conditions used, the gas bubble size increases with increasing the concentration of the solid particles. Figure 38 shows that adding solid particles greatly increases the rate of coalescence of the gas bubbles and adding only 3 vol.% of Puralox particles to the molten reactor wax led to a dramatic reduction of the small gas bubbles population (d_b < 0.3 mm) accompanied by an increase of the population of medium and large gas bubbles. This behavior is in agreement with previous findings that reported the formation of large gas bubbles due to the increase of the rate of bubbles coalescence when increasing solid loading [143, 176]. This increase in bubble size can be related to the increase of slurry viscosity due to the addition of small solid particles, which was reported to increase the size of the gas bubbles [146]. As previously described in Figures 38 and 37 (b), higher temperatures appeared to hinder this effect. It is also important to note that the impact of the solid concentration seems dependent upon the liquid-phase used, as the increase of bubble size with solid concentration appears to be greater in the paraffins mixture than in the Sasol wax and reactor wax.
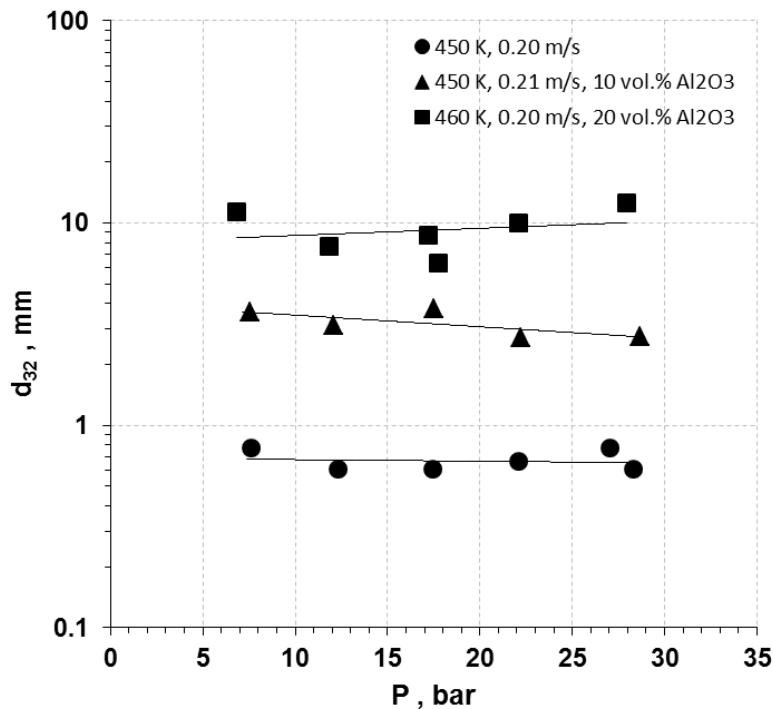
Figure 47: Effect of Solid Concentration on d_{32} of N_2-Sasol wax-Al_2O_3
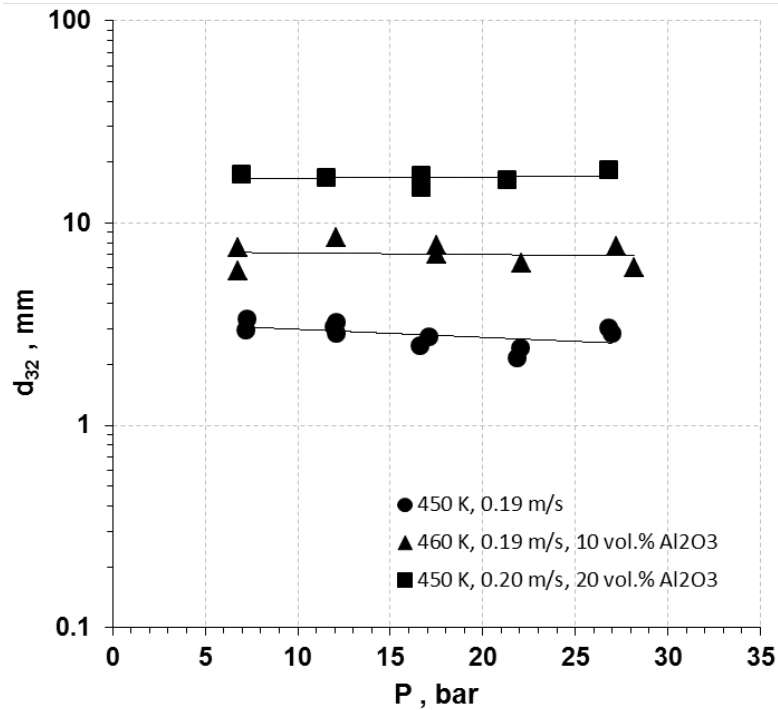
Figure 48: Effect of Solid Concentration on d_{32} of He-Sasol wax-Al_2O_3

The volumetric liquid-side mass transfer coefficients were found to decrease with increasing the solid concentration in the paraffins mixture and both molten waxes as can be seen in Figures 44 (c), 49 and 50. This finding agrees well with reported literature data [143, 176] and can be explained by the increase of the slurry-phase viscosity, which was reported to decrease k_La [121, 140-143]. However, Vandu et al. [190] reported that k_La values were independent of solid concentration when using a slurry of C_9-C_{11} paraffin oil with Puralox alumina particles. They concluded that the nature of the liquid and solid phases play an important role in the behavior of k_La with solid concentration. In the present work, however, under similar conditions, the gas holdup decreases and the gas bubble size increases with solid concentration suggesting that the interfacial area should decrease with the addition of solid particles. Although k_L should increase due to the presence of large gas bubbles which create more turbulences, the results obtained under the conditions used showed that k_La behavior follows that of the gas-liquid interfacial area (a) as previously reported [123, 166, 266].

114
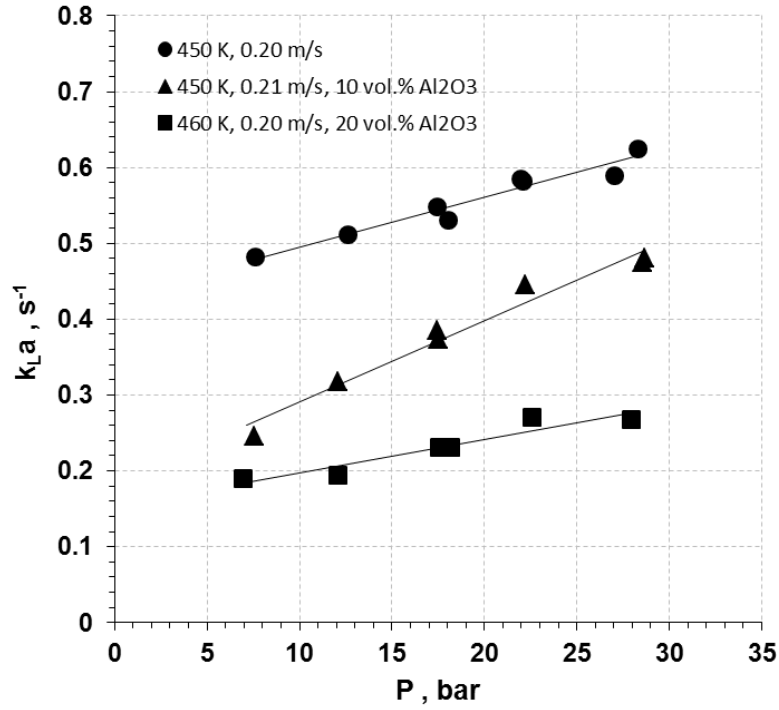
Figure 49: Effect of Solid Concentration on k_La of N_2-Sasol wax-Al_2O_3
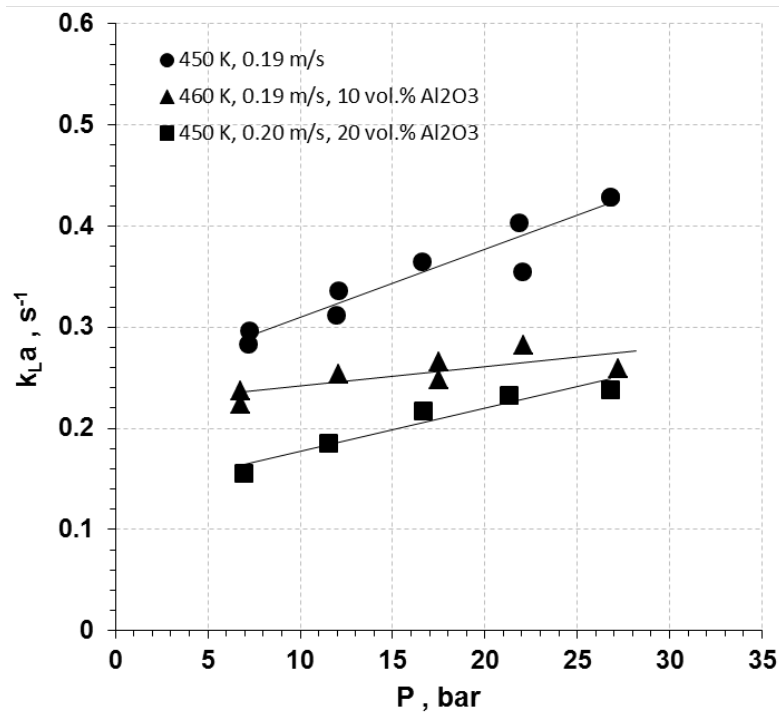
Figure 50: Effect of Solid Concentration on k_La of He-Sasol wax-Al_2O_3

6.1.6 Effect of Gas Nature and Composition

Figures 55 (a) and 51 show the effect of gas nature and composition on the gas holdup in the molten reactor and Sasol waxes in the absence and presence of solid particles. As can be observed in these figures, the gas holdup values decrease with increasing the mole fraction of He; and the gas holdup of N_2 is always greater than that of He under similar operating conditions. This is similar to that reported by Behkish et al. [120] with He and N_2 in an isoparaffinic mixture (Isopar-M). The presence of the heavier gas (N_2) which has a molecular weight of about 28 kg/kmol increases the density and momentum of the gaseous mixture when compared with that of a gaseous mixture which is rich in the lighter gas (He) with a molecular weight of about 4 kg/kmol.
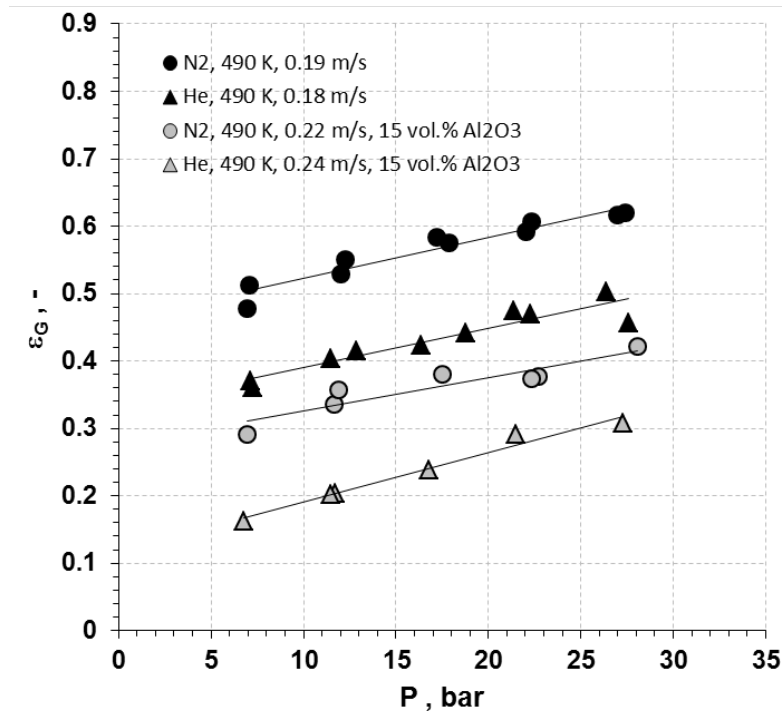
Figure 51: Effect of Gas Nature on ε_G in Sasol Wax

It should be noted that some of the gas holdup values presented in Figure 55 (a) are obtained at constant pressure, and therefore changing the composition of the gaseous mixture directly affects its density. Figure 30 indicates a similar behavior to that observed in Figures 55 (a) and 51 in the 3 liquids used. In order to separate the effect of gas composition from the effect of gas density,

experiments were carried out in the molten reactor wax under constant gas density by changing the gas composition and accordingly the total pressure. The behavior of the gas holdup under such conditions is shown in Figure 55 (a) and as can be seen, varying the gas composition while keeping the gas density constant has almost no effect on the gas holdup. This confirms the fact that the gas holdup is directly related to gas density and consequently the gas momentum as reported by Reilly et al. [131]. Thus, higher gas momentum increases the turbulence and mixing characteristics of the system, and consequently leads to high gas holdup values.
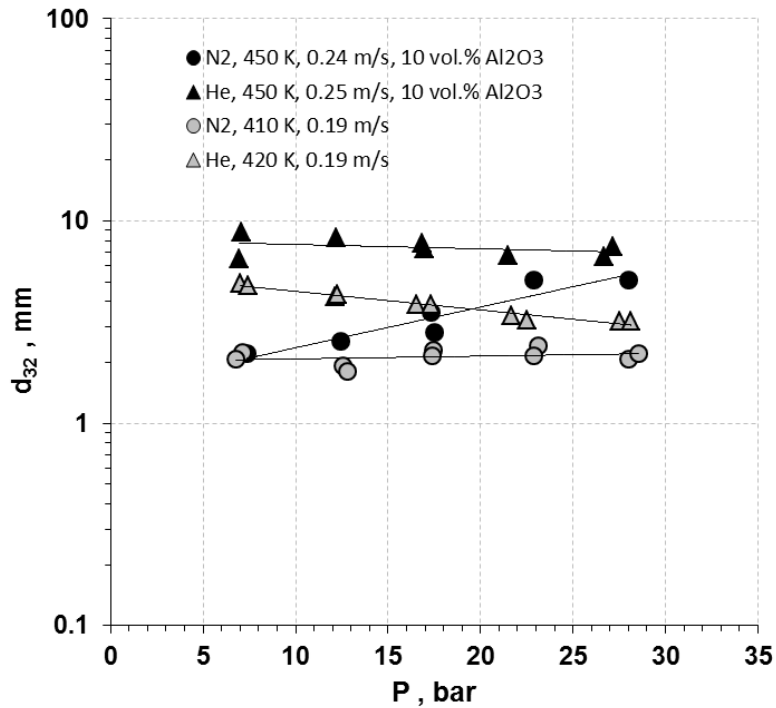
Figure 52: Effect of Gas Nature on d$_{32}$ in Sasol Wax

Figures 55 (b) and 52 present the effect of gas nature and composition on the Sauter mean bubble diameter in the molten reactor and Sasol waxes in the absence and presence of solid particles. As can be seen in these figures, d_{32} values increase with increasing the mole fraction of He; d_{32} of He as a single-gas is much greater than that for N$_2$. This behavior underlines the fact that higher gas molecular weight and consequently gas density leads to small gas bubbles [132]. Again, the effect of gas density at constant pressure (varied by the gas composition) on the bubble size, as shown in Figure 30, underscores the importance of the gas density. However, under constant gas density, obtained by varying the total pressure and gas composition the size of the gas bubbles

was found to be affected similarly to that when varying the gas composition at constant pressure. This can be seen in Figure 55 (b), where d_{32} values increase with increasing the mole fraction of He in the gaseous mixture even though the pressure increases at the same time. This means that the gas nature has direct effect on the bubble size independently of its density. This is further illustrated in Figure 56 where increasing the He mole fraction in the gas mixture shifts the gas bubbles population towards larger gas bubbles.
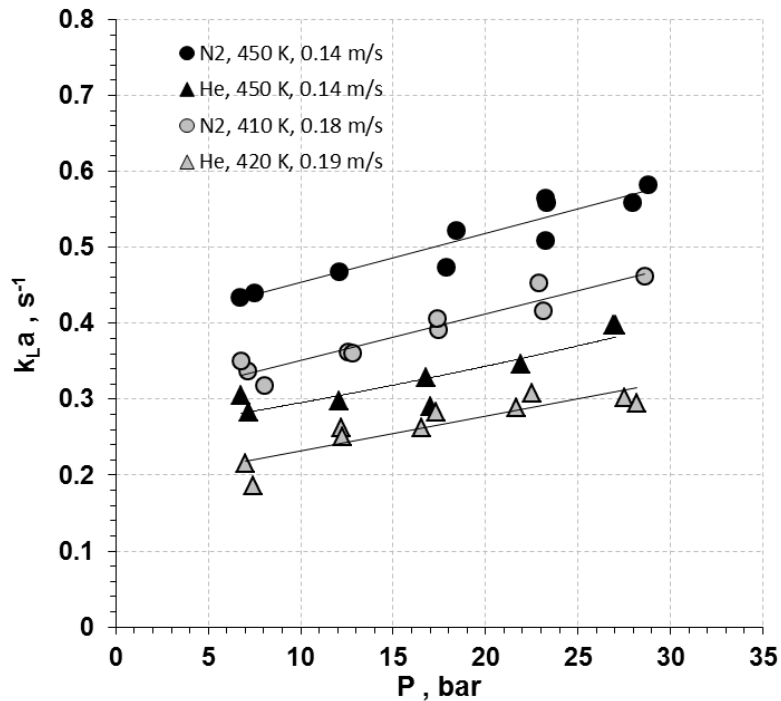
Figure 53: Effect of Gas Nature on k$_L$a in Sasol Wax

Figures 55 (c) and 53 show the effect of gas nature and composition on the overall k_La values for He/N$_2$ gas mixtures in the molten reactor and Sasol waxes. As can be seen in these figures, the overall k_La values appear to increase with increasing the mole fraction of N$_2$ in the gas mixture and k_La values for N$_2$ as a single gas are much greater than those of He under similar conditions. The N$_2$-rich mixtures have a greater gas-liquid interfacial area due to their smaller gas bubbles and greater gas holdup as a consequence of their higher gas densities (see Figure 30) when compared with those of the He-rich mixtures. The N$_2$-rich mixtures exhibit therefore greater k_La values since the gas-liquid interfacial area (a) is controlling the behavior of the mass transfer in the SBCR [123, 166, 266]. The effect of gas composition on k_La, illustrated in Figure 55 (c), is

118

decreased when keeping the gas density constant. In fact, the overall k_La appeared to remain almost constant as the gas holdup. The higher concentration of N_2 in the gaseous mixture leads to smaller gas bubbles size (see Figure 55 (b)) without changing the gas holdup (see Figure 55 (a)), which results in higher gas-liquid interfacial area and lower mass transfer coefficient k_L, however, the resultant effect of the gas nature on both parameters led to the slight increase of k_La values.

6.1.7 Effect of Liquid and Solid Nature

The effect of liquid and solid nature on the hydrodynamic and mass transfer parameters of N_2 is shown in Figures 54 through 60. Under similar operating conditions, the nature of the liquid and solid phases appeared to have a significant impact on the gas holdup, the gas bubbles size and the overall volumetric mass transfer coefficient.
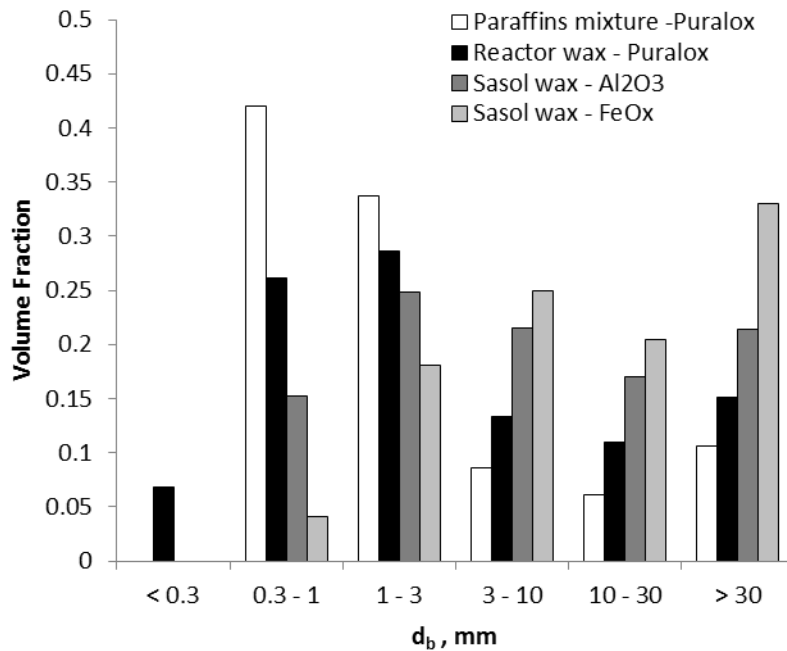
Figure 54: Effect of Liquid and Solid Nature on the Gas Bubbles Size Distribution (C_S = 2.4 - 3.5 vol.%)
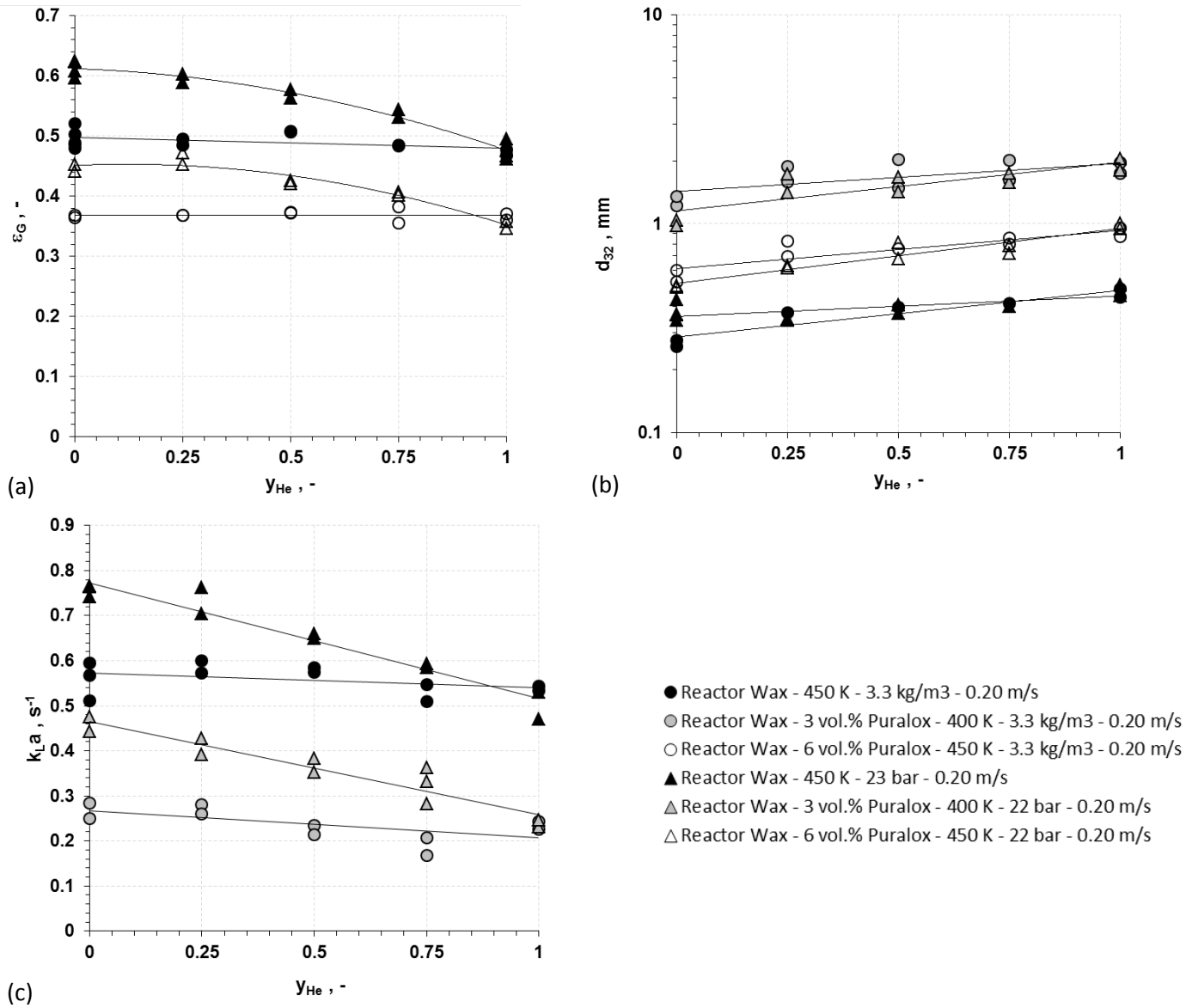
Figure 55: Effect of Gas Composition on ε_G (a), d_{32} (b) and $k_L a$ (c) under Constant Pressure (triangles) or Gas Density (circles)
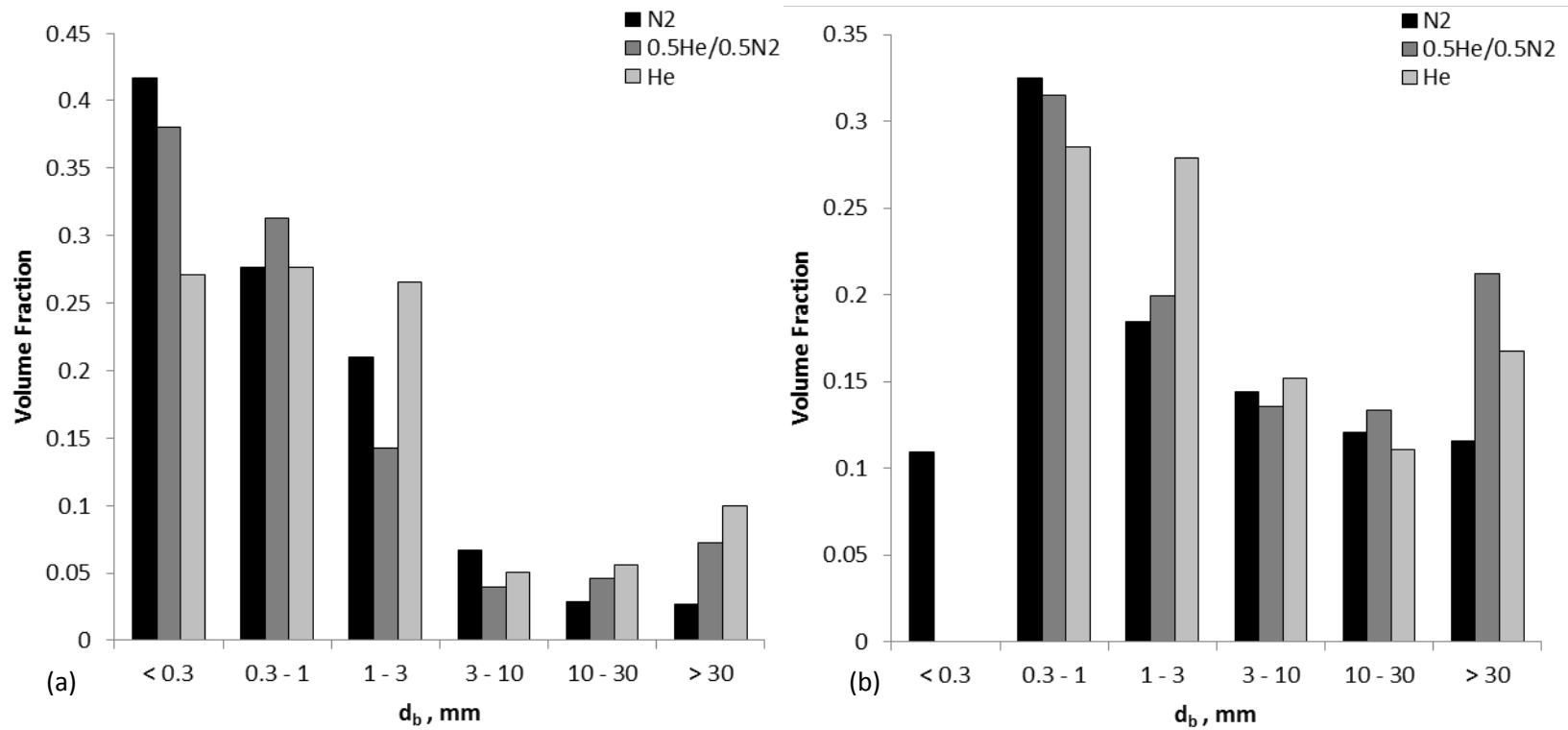
Figure 56: Effect of Gas Nature and Composition on the Gas Bubbles Size Distribution in Molten Reactor Wax

(a) C_S = 0 vol.%, T = 450 K ; (b) C_S = 3 vol.%, T = 400 K

The gas holdup and the Sauter mean bubble diameter of N_2 obtained in the paraffins mixture and in the reactor wax were similar. Figure 54 shows that the least fraction of large gas bubbles was obtained when using the Puralox particles in the paraffins liquid mixture. In the molten reactor wax, however, the population of both large and small gas bubbles increased, which led to similar Sauter mean bubble diameters as shown in Figure 60. Also, the population of small bubbles with diameters d_b < 3 mm is slightly greater in the paraffins mixture than in the molten reactor wax and as a result the gas holdup in the paraffins mixture is greater than in the reactor wax. The k_La values of N_2 in the paraffins liquid mixture are found to be greater than in the reactor wax. When increasing the solid concentration, however, k_La values in both liquids became similar. This is expected as the diffusivity of N_2 and therefore its mass-transfer coefficient k_L is greater in the paraffins mixture than in the reactor wax under the same temperature according to the correlation by Erkey et al. [259]. Moreover, at low solid concentrations the gas-liquid interfacial area is similar in both liquids due to similar gas holdup and gas bubbles size. At high solid concentrations, on the other hand, the gas bubbles size in the paraffins liquid mixture increases with increasing the solid concentration at a greater rate than in the reactor wax, and therefore the gas-liquid interfacial area becomes smaller in the paraffins liquid mixture than in the reactor wax and as a result k_La values in both liquids become closer as can be observed in Figure 60. Operating the SBCR with the molten Sasol wax led to lower gas holdup values and larger gas bubbles which result in low interfacial area and consequently k_La values. Figure 54 shows that using molten Sasol wax with alumina particles increased the population of large gas bubbles (d_b > 3 mm) and greatly reduced the population of the small gas bubbles (d_b < 3 mm). Even though when using the iron oxides particles more gas bubbles coalescence is expected than with alumina, in this case, only a small fraction of gas bubbles (d_b < 1 mm) does not coalesce. This led to high values of the Sauter mean bubble diameter and low gas holdup in the Sasol wax as shown in Figure 60. These findings confirm that operating the SBCR with a heavy F-T liquid, composed of long hydrocarbon chains having high density and viscosity; will lead to larger gas bubbles and lower values of gas holdup and k_La than those to be expected in a lighter F-T Liquid with shorter hydrocarbon chains.

In the case of the Sasol wax, the use of alumina particles led to greater ε_G (see Figure 57) and k_La (see Figure 58) values, and lower d_{32} values (see Figure 59) than when using Iron oxides (FeOx) particles under similar operating conditions. The Iron oxides particles were smaller and

denser than the alumina ones (see sections 4.2.4.1 and 4.2.4.2). The decrease of gas holdup with the heavier particles (FeOx) is in agreement with some literature finding [151]. The smaller gas holdup and larger gas bubbles obtained in the case of FeOx can be due to the higher viscosity of the slurry phase observed when using FeOx as compared with that of Al_2O_3, which is probably due to the smaller size of the FeOx particles. As explained previously, higher viscosities lead to large gas bubbles [146] and small gas holdup [124, 128, 131, 137-139, 144, 145, 147-149] and k_La values [121, 140-143]. Under similar conditions the decrease of gas holdup and the increase of the gas bubble size resulted in the decrease of the gas-liquid interfacial area and consequently k_La when using FeOx.
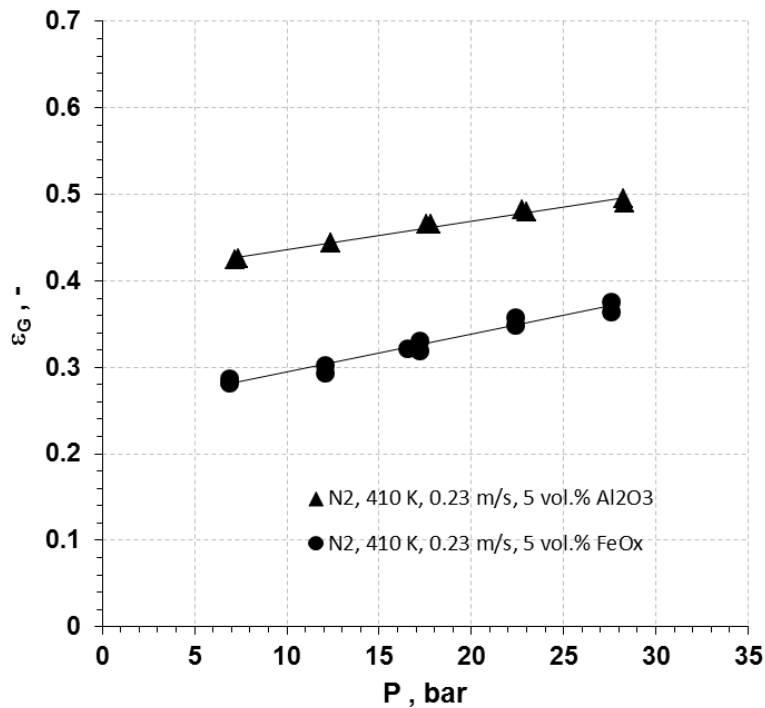
Figure 57: Effect of Solid Nature on ε_G of N_2-Sasol wax-FeOx/Al$_2$O$_3$

The liquid-solid systems studied showed that increasing the solid particles concentration decreased the gas holdup and increased the Sauter mean bubble diameter and consequently led to low k_La values as presented in Figures 44 and 60. These figures also show that the impact of solid concentration on the hydrodynamics and mass transfer of the SBCR is dependent on the nature of the liquid and solid phases used. The Alumina particles in the molten Sasol wax appeared to have less impact on the SBCR behavior than that of FeOx particles. Also, the

123

alumina particles in the molten Sasol wax have less effect on the SBCR behavior than that of the alumina Puralox particles in the molten reactor wax and in the paraffins mixture.
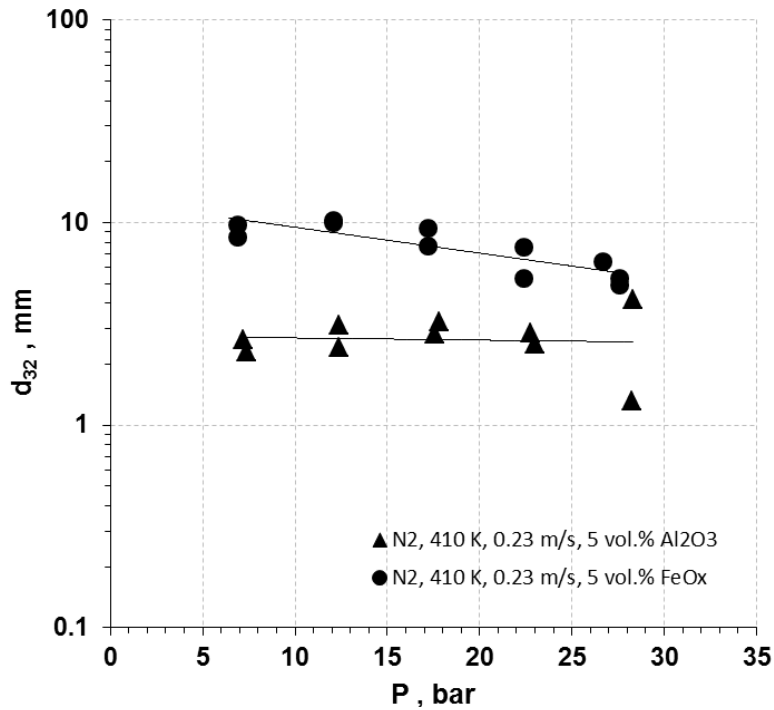
Figure 58: Effect of Solid Nature on d_{32} of N_2-Sasol wax-FeOx/Al$_2$O$_3$
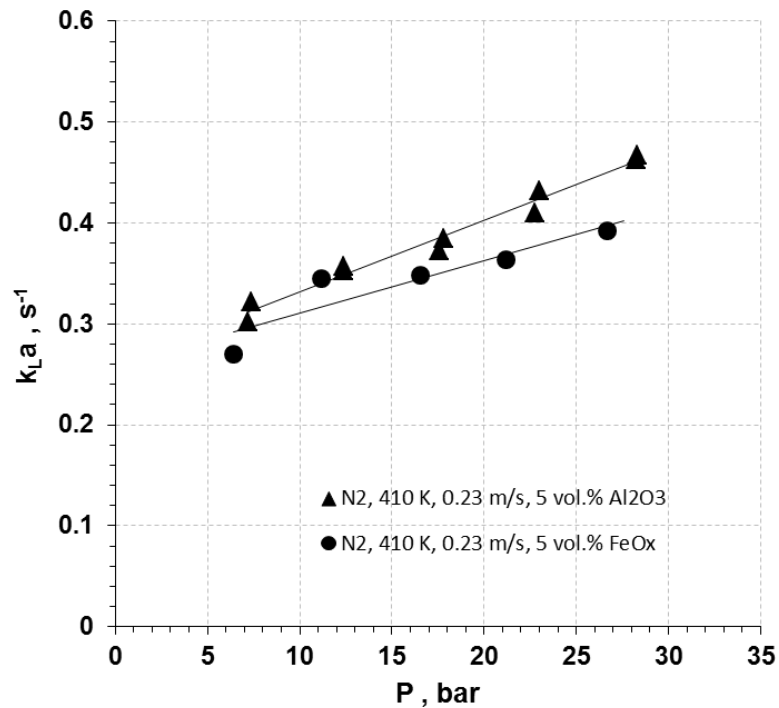
Figure 59: Effect of Solid Nature on $k_L a$ of N_2-Sasol wax-FeOx/Al$_2$O$_3$
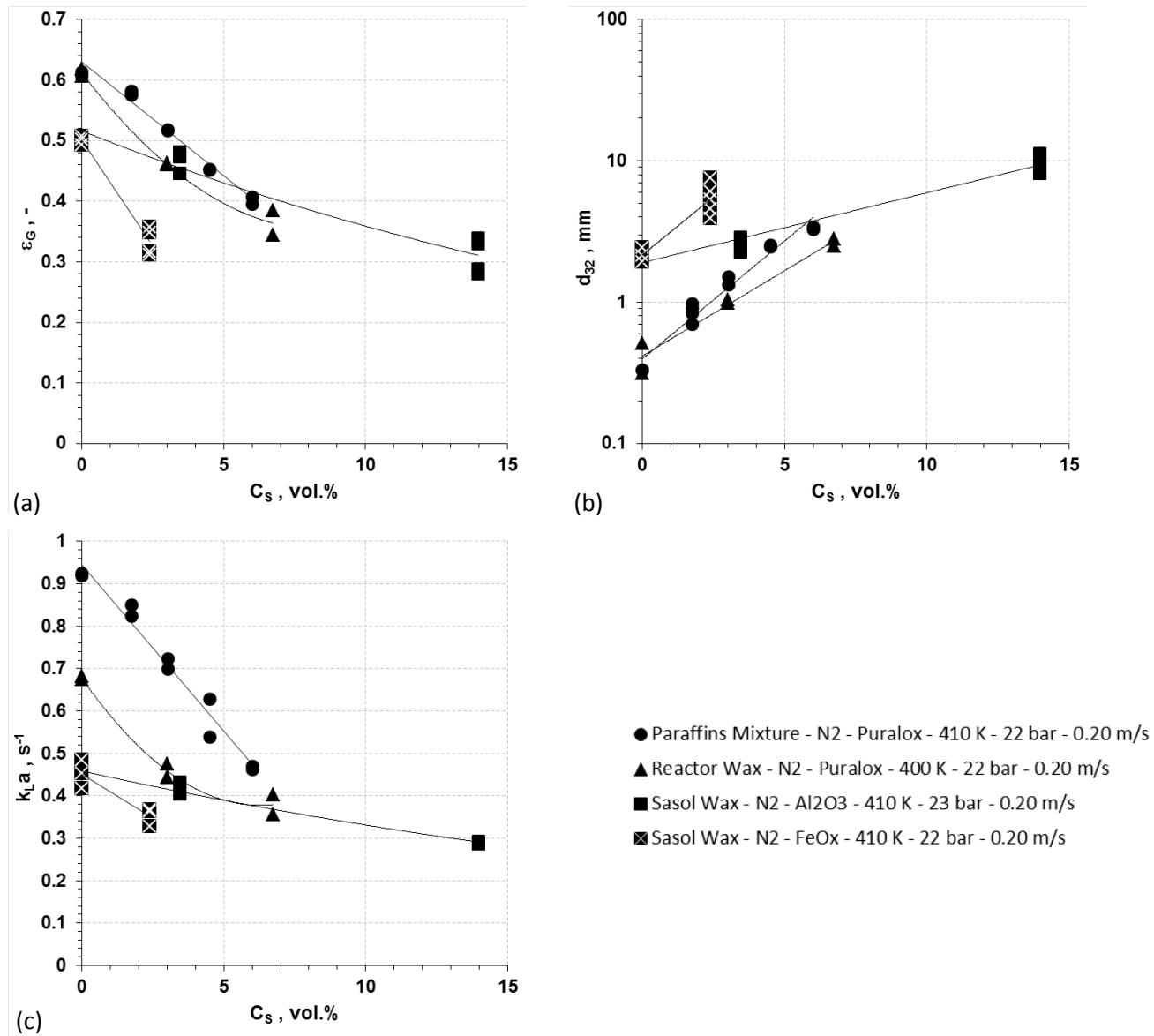
Figure 60: Effect of Liquid and Solid Nature on ε_G (a), d_{32} (b) and $k_L a$ (c)

Legend:

● Paraffins Mixture - N2 - Puralox - 410 K - 22 bar - 0.20 m/s

▲ Reactor Wax - N2 - Puralox - 400 K - 22 bar - 0.20 m/s

■ Sasol Wax - N2 - Al2O3 - 410 K - 23 bar - 0.20 m/s

⊠ Sasol Wax - N2 - FeOx - 410 K - 22 bar - 0.20 m/s

6.1.8   Solid Particles Distribution Profile

Figure 61 shows the catalyst concentration profiles measured in the SBCR for various gaseous mixtures in the paraffins liquid mixture under similar operating conditions. As can be seen, Equation (5-26) fits the experimental data fairly well, validating the model described in section 5.5. The calculated values of the ratio (U_P/D_S) are listed in Table 25 as well as other values predicted using different literature correlations. As can be seen, the three correlations tested failed to account for the effect of the gas composition and that the presence of He gas decreases the (U_P/D_S) values. Also, the correlation by Kato et al. [270] appears to give the best prediction for the present system.

Table 25: Ratios of the Particle Settling Velocity to the Solid Phase Axial Dispersion Coefficient

Gas	U_P/D_S (m^{-1})	U_P/D_S (m^{-1}) from Literature Correlations		
		Kato et al. [270]	O'Dowd et al. [186]	Smith and Reuther [271]
N$_2$	0.330			
He/N$_2$ (50/50)	0.259	0.286	0.397	0.199
He	0.245			
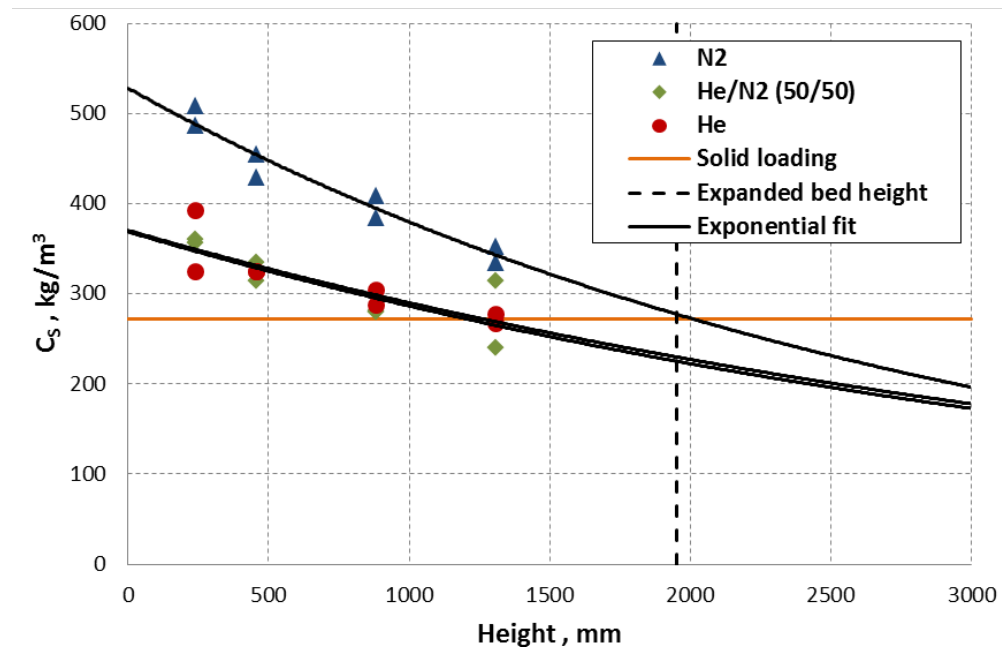
Figure 61: Catalyst Concentration Profile in the SBCR

The effect of the gas nature and composition can also be seen in Figure 61 as the solid concentrations profiles are found to be identical when using He as a single gas or as a 50/50 (He/N_2) gaseous mixture. When using N_2 as a single gas, however, the solid concentration values obtained were always greater at all heights sampled. The integration of the 3 profiles obtained would lead to 2 different average concentrations, while all experiments were carried out at the same original solid loading minus the negligible weight of solids withdrawn with the slurry for sampling purposes. Also, considering that the expanded bed height does not reach the top of the reactor but was always below 2 m, the average solid concentrations calculated were 387 and 293 kg/m^3, which all appear to be above the actual solid loading in the reactor (272 kg/m^3). This means that either the solid samples were not sufficiently dried or were contaminated and therefore the sampled weights were inaccurate, or the solid particles were not distributed uniformly in the reactor cross-sectional area, i.e., the solid concentration at the wall is greater than that at the reactor's center. It should be pointed out that the sampling ports are located at the walls of the reactor and it is possible that the samples withdrawn reflect only the solid distribution near the wall. Analysis of the samples using a Philips XL-30 field emission Scanning Electron Microscope (SEM) did not reveal the presence of any paraffins mixture (in fact the presence of liquid would have prevented proper operation of the SEM) or contaminants in the sample, which means that Figure 61 represents the profiles of the solid concentrations at the wall of the reactor. The greater solid concentration at the wall can be explained by the particular flow pattern of the churn/turbulent flow regime. At the center of the reactor large and fast-rising gas bubbles induce strong circulations and create back-mixing or recirculation zones along the wall wherein the small gas bubbles and some solid particles are entrained. This phenomenon leads to conclude that the average measured solid concentration is that at the wall. This seems to be amplified when using N_2 as the gas-phase when compared with He or with 50/50 He/N_2 gas mixture. As discussed in section 6.1.6, the presence of He in the gas phase was found to increase the average gas bubbles size as shown in Figure 62. Using He and the 50/50 He/N_2 gas mixture led to similar bubble size distributions, while using N_2 as a single gas led to a significant increase in the population of gas bubbles less than 3 mm in diameter. Thus, the high concentration of solid particles at the walls could be related to the large population of small gas bubbles with fine solid particles attached to their surfaces.
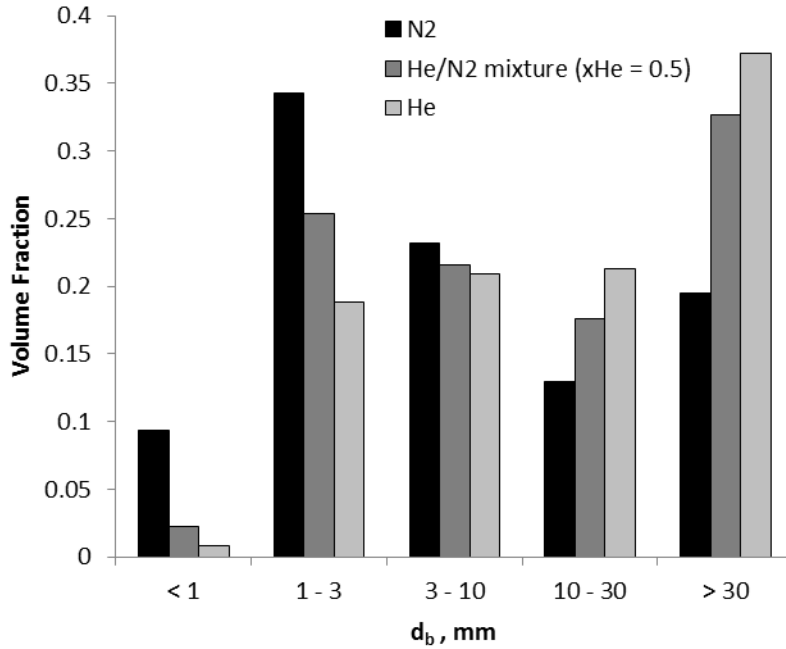
Figure 62: Gas Bubbles Size Distribution during Solid Particles Distribution Experiments

6.2 CORRELATIONS OF THE HYDRODYNAMICS AND MASS TRANSFER PARAMETERS

The knowledge of the hydrodynamics and mass transfer characteristics of small and large bubble classes is essential [272-274] for modeling SBCRs. The available literature correlations summarized by Behkish et al. [184] and Lemoine et al. [275] along with those proposed by Krishna et al. [189], Koide et al. [143] and Fukuma et al [268] could be used to predict the hydrodynamics and mass transfer parameters for gases in F-T liquids. These correlations considered the effect of several variables, such as liquid/solid properties, operating conditions, and reactor diameter, on these parameters. Recently, correlations and a calculation algorithm [184, 262, 275, 276] have been developed to predict the hydrodynamics and mass transfer parameters in bubble column reactors (BCRs) and slurry bubble column reactors (SBCRs) based on a large experimental database covering, among others, typical F-T conditions. The empirical correlations by Behkish et al [184]. and Lemoine et al. [277] shown in Table 26, take into account not only the liquid/solid properties,

operating conditions, and reactor diameter similar to available literature correlations, but also the gas distributor type, number/size of nozzles, catalyst loading, and foamability of the F-T products, which have been shown to dramatically impact the hydrodynamics and mass transfer characteristics in SBCRs.

Table 26: Gas Holdup, Sauter Mean Diameter and Volumetric Mass Transfer Coefficient Correlations [184, 275]

Gas holdup [184]

$$\varepsilon_G = 0.00494 \frac{\rho_L^{0.415}\rho_G^{0.177}U_g^{0.553}\Gamma^{0.053}}{\mu_L^{0.174}\sigma_L^{0.27}e^{2.231C_S+0.157\rho_p d_p+0.242X_W}}\left(\frac{P}{P-P_v}\right)^{0.203}\left(\frac{d_R}{d_R+1}\right)^{-0.117} \tag{6-1}$$

Gas holdup of large gas bubbles [184]

$$\varepsilon_{G,large} = \varepsilon_G^{0.84}\left(1-3.04.10^{-6}\frac{\rho_L^{0.97}}{\mu_L^{0.16}}e^{4.5X_W-4.49C_S}\right) = \varepsilon_G^{0.84}(F) \tag{6-2}$$

Gas holdup of small gas bubbles [184]

If ε_G is > $(F)^{25/4}$ $\varepsilon_{G,small} = \varepsilon_G - \varepsilon_{G,large}$

If ε_G is $\leq$ $(F)^{25/4}$,   small gas bubbles do not exist $\tag{6-3}$

Gas bubbles Sauter mean diameter [275]

$$d_{32} = 37.19\frac{\mu_L^{0.08}\sigma_L^{1.22}\rho_G^{0.02}U_g^{0.14}T^{1.66}(1-\varepsilon_G)^{1.56}}{\rho_L^{1.52}M_{W,gas}^{0.12}\Gamma^{0.02}}\left(\frac{d_R}{d_R+1}\right)^{0.30}e^{2.81C_S+2.77\rho_p d_p-2.29X_W} \tag{6-4}$$

Sauter mean diameter of large gas bubbles [275]

$$d_{32,large} = d_{32}^{0.96}\left(1-10^{-5}\rho_L^{0.22}\mu_L^{0.03}\sigma_L^{8.60}U_g^{0.04}\varepsilon_G^{2.37}\varepsilon_{G,large}^{2.74}\right) \tag{6-5}$$

Sauter mean diameter of small gas bubbles [275]

$$\frac{\varepsilon_{G,small}}{d_{32,small}} = \frac{\varepsilon_G}{d_{32}} - \frac{\varepsilon_{G,large}}{d_{32,large}} \tag{6-6}$$

Volumetric mass transfer coefficient [275]

$$k_L a = 6.14.10^4\frac{\rho_L^{0.26}\mu_L^{0.12}\varepsilon_G^{1.21}D_{ij}^{0.5}\Gamma^{0.11}}{\sigma_L^{0.52}\rho_G^{0.06}U_g^{0.12}d_{32}^{0.05}T^{0.68}}\left(\frac{d_R}{d_R+1}\right)^{0.40} \tag{6-7}$$

In Table 26, X_W designates the concentration of the primary liquid in a liquid mixture, and its value varies between 0.5 and 1. For a single-component or an organic liquid mixture, consisting of different chain length hydrocarbons, such as F-T products, X_W equals 1. Also, Γ which represents the gas sparger type is defined as:

$$\Gamma = K_d N_o d_o^\alpha \tag{6-8}$$

The values of the coefficient K_d and the exponent α for several distributors are given in Table 27. For perforated plates, the exponent α depends on ζ, which is expressed as shown in equation (6-9).

$$\zeta = N_o \left(\frac{d_o}{d_R}\right)^2 \qquad\qquad (6\text{-}9)$$

Table 28 presents the ranges of the conditions of applicability of the different correlations. It should be noted that the correlations listed in Table 26 are valid when the volume of internals, commonly used in SBCRs for cooling or heating purposes, is ≤ 20% of the reactor volume. This is because several literature findings [115, 185-188, 278-281] showed limited or no effect of internals on the hydrodynamic and mass transfer parameters as long as their volume fraction remains under 20%. Also, these correlations should be valid for reactor height/inside diameter ratio (L/d_R) varying from 4 to 20, because the considerable data available in the literature used to develop these correlations cover such an L/d_R range. It should be mentioned also that Lemoine et al. [275] have argued that the use of Equation (6-7) to calculate $k_L a$ for small and large gas bubbles using their corresponding gas holdup and Sauter mean bubble diameter is a more accurate approach than the ones used by de Swart and Krishna [272] and Grund et al. [121]; because it underscores the fact that the mass transfer behavior of SBCRs is controlled by the gas-liquid interfacial area [123, 166, 282].

Table 27: Values of α Used in Equation (6-8) [275]

Distributor	ζ (%)	α	K_d (m$^{-\alpha}$)
	< 0.055	0.017	1.364
PfP	≥ 0.055 and ≤ 0.3	0.303	1.364
	> 0.3	0.293	1.364
M-ON		0.303	1.364
S-ON		0.134	1.205
R, S		0.015	1.000
BC		0.500	1.553
PoP, SP		0.650	1.533

The correlations presented in Table 26 are valid for almost any gas-liquid-solid system. Using the experimental data obtained in the pilot-scale SBCR and discussed in the present study, two novel correlations to estimate the hydrodynamic and mass transfer parameters of SBCR specifically for F-T were developed. The novel empirical correlations for gas holdup (ε_G) and for the mass transfer coefficient ($k_L a$) were based on the ones previously developed by Behkish et al [184] and Lemoine et al.,[277] respectively and are shown in Table 26. The terms accounting for the solid concentration as well as the gas-liquid-solid system properties have been optimized for F-T liquids. The foaming tendency of the liquid-phase was accounted for by introducing the term

"*X*" which equals either 0 for single-component and non-foaming liquid mixtures or 1 for foaming liquid mixtures. The gas holdup (ε_G) and the overall volumetric liquid-side mass transfer coefficients ($k_L a$) were thus correlated as:

$$\varepsilon_G = 11241.6 \frac{\rho_G^{0.174} U_g^{0.553}}{\rho_L^{1.59} \mu_L^{0.025} \sigma_L^{0.105}} \left(\frac{P}{P - P_v}\right)^{0.203} \left(\frac{d_R}{d_R + 1}\right)^{-0.117} \Gamma^{0.053}$$
$$\times \exp\left(-0.0012 \rho_p C_S - 0.4 \left(\frac{\rho_p C_S}{1000}\right)^2 - 4339 d_p + 0.434 X\right)$$

(6-10)

$$k_L a_L = 7.99 \ 10^{-9} \frac{\rho_L^{1.82} \rho_G^{0.270} U_g^{0.387}}{\mu_L^{0.250} \sigma_L^{0.976} M_{WG}^{0.020}} \left(\frac{P}{P - P_v}\right)^{0.242} \left(\frac{d_R}{d_R + 0.3}\right)^{0.1} \Gamma^{0.173}$$
$$\times exp\left(-0.0013 \rho_p C_S + 0.8 \left(\frac{\rho_p C_S}{1000}\right)^2 - \left(\frac{\rho_p C_S}{1000}\right)^3 - 1675.7 d_p + 0.176 X\right)$$

(6-11)

Table 28: Upper and Lower Limits of the Variables Used in Equations (6-1) through (6-7) [275]

Variables	Units	Minimum value	Maximum value
P_T	MPa	0.1	19.8
P_V	MPa	0.0	0.7
U_G	m/s	$3.5 \ 10^{-3}$	0.574
Cv	vol%	0	0.36
X_w	wt.%	0.5	1
T	K	275	538
$M_{W\text{-}Gas}$	kg/kmol	2	44
D_{AB}	$10^9.m^2/s$	$2.78 \ 10^{-8}$	$1.25 \ 10^{-11}$
d_P	10^{-6} m	5	300
ρ_P	kg/m^3	700	4000
ρ_G	kg/m^3	0.06	223.77
ρ_L	kg/m^3	633	1583
μ_L	10^{-3} Pa s	0.16	398.80
σ_L	10^{-3} N/m	8.4	75
d_R	m	0.0382	7.6200
Γ	-	0.06	143800
ζ	%	0.0097	75

Table 29: Statistical Comparison of Correlations Performances

Parameter	Equation	This Study's Data		All Available Data	
		AARE	σ(AARE)	AARE	σ(AARE)
ε_G	(6-1)	18.2 %	16.1 %	21.6 %	26.0 %
	(6-10)	12.3 %	13.0 %	24.6 %	23.2 %
$k_L a$	(6-7)	52.4 %	38.7 %	38.9 %	61.7 %
	(6-11)	15.2 %	12.2 %	35.7 %	61.4 %

(a)

(b)
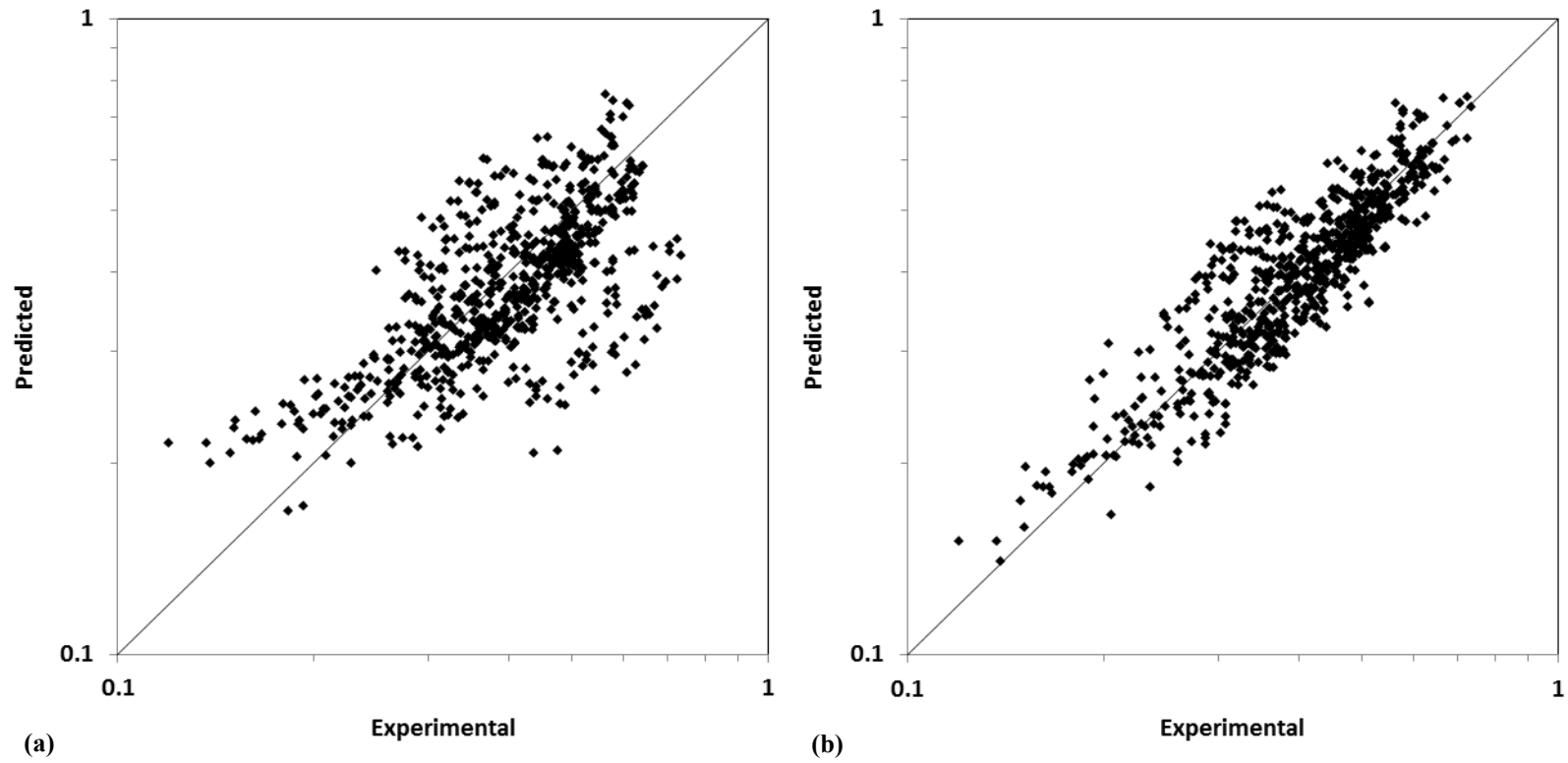
Figure 63: Comparison between Experimental Data of Gas Holdup and Predicted Values using Equations (6-1) (a) and (6-10) (b)
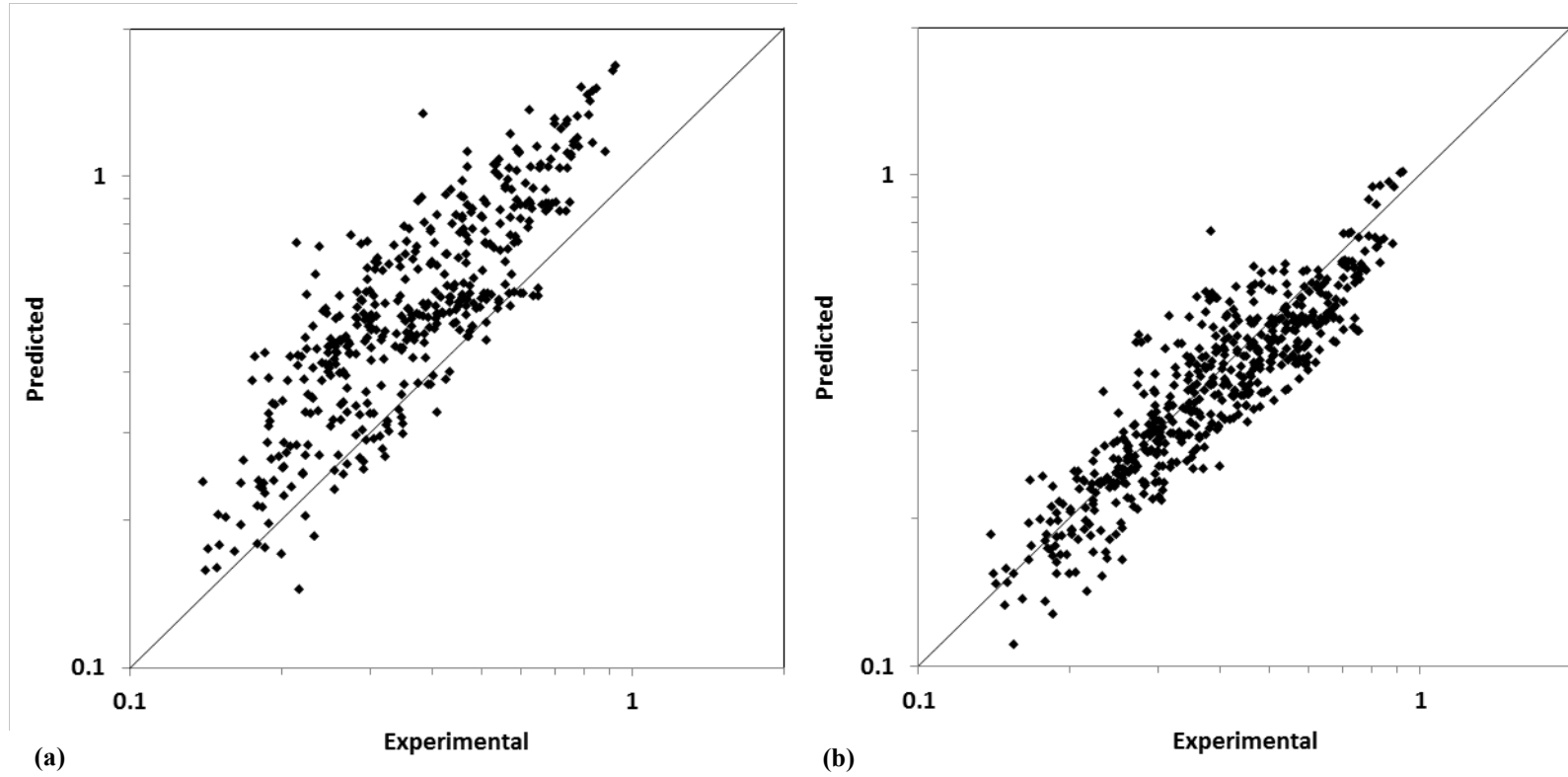
Figure 64: Comparison between Experimental Data of $k_L a$ and Predicted Values using Equations (6-7) (a) and (6-11) (b)

All the experimental data obtained in this study were plotted against the predicted values from both new correlations as well as the predicted values obtained from the correlations in Table 26 and were compared as can be seen in Figures 63 and 64. Table 29 also presents a statistical comparison between the different correlations that shows that the accuracy is improved when using the newly developed correlations which is in accordance with what can be observed in Figures 63 and 64. It should be noted that equation (6-11) presents the advantage of not requiring the prior knowledge of the gas holdup or gas bubble size contrary to the correlation of Lemoine et al. [277]. The different correlations were also tested against all literature data available including this present study (3731 gas holdups [119, 121, 127, 129, 133, 138, 147, 149, 154, 155, 160, 162, 165, 167, 172, 180, 185, 186, 198, 199, 202, 206, 209, 220, 230, 244, 262, 269, 283-300] and 1917 $k_L a$ values [119, 121, 127, 129, 130, 133, 160, 165, 167, 180, 202, 230, 262, 287, 289, 294, 297, 301]) and statistically compared. As can be seen in Table 29 the new correlations are able to predict all the data available with better precision than the correlations presented in Table 26. For F-T process modeling and scaleup purposes, Equations (6-10) and (6-11) present therefore a significant increase in precision, while for any other process equations (6-1) and (6-7) could also be used.

6.3 MODEL FOR F-T SBCR

The purpose of this section is to build a comprehensive mathematical model for the SBCRs using the correlations and algorithm previously developed [184, 262, 275] and to use this model for the design and optimization of a commercial-size F-T SBCR.

6.3.1 Brief Review of F-T SBCR Models

Table 30 shows a summary of the F-T SBCR models available in the literature and the following comments can be made. Generally, in all models, three distinct phases (gas-phase, liquid-phase and solid-phase) are used, and in almost all models, the solid-phase dispersed in the liquid phase is referred to as the "slurry-phase". The solid (catalyst) concentration in the reactor is often assumed constant, and in several models, the Sedimentation-Dispersion Model (SDM) is used to

134

estimate the catalyst concentration. The syngas consumption is not always considered or is estimated using a linear relationship between the gas consumption and the syngas conversion, and in several models, an overall mass balance on the gas-phase is formulated in order to simulate the effect of syngas consumption. [302-309].

Early models treated the gas phase as plug flow while the slurry-phase is often assumed to be perfectly-mixed. This latter assumption is inappropriate for simulating small-scale reactors, however, it could be viable for large-scale reactors since the liquid phase back-mixing and the dispersion coefficients were found to increase with reactor diameter [310]. Recent models introduced the dispersion coefficients in the mass balance equations when using the Axial Dispersion Model (ADM) for the gas and slurry phases. Rados et al. [305] showed that utilizing the ADM to model the F-T SBCR back-mixing is more versatile than the combination of ideal reactor models, such as plug flow and perfectly-mixed. For large-scale F-T reactors, nevertheless, the combination the gas-phase as plug flow and the slurry-phase as perfectly mixed appeared to give the closest results to those obtained from the ADM [305].

Visual observations and photographic methods revealed the coexistence of distinctly two classes of gas bubbles (small and large) in Bubble Column Reactors (BCRs) operating in the churn-turbulent (heterogonous) flow regime. [119-121, 123, 247] This finding led to the separations of the gas phase into two distinct phases, large gas bubbles phase and small gas bubbles phase in the latest literature models. The large gas bubbles phase is often modeled as plug flow while the small gas bubbles phase is assumed to be perfectly mixed, similar to the slurry-phase. This is an adequate assumption since in large-scale F-T SBCRs operating in the churn-turbulent flow regime, the fast-rising large gas bubbles induce strong circulations and create back-mixing or re-circulation zones wherein the small gas bubbles are entrained.[117, 119] Few models employed the ADM for the large gas and small gas bubble phases as well as the slurry-phase. de Swart and Krishna [272] used the ADM and a 1st order reaction kinetics with respect to H_2 to simulate F-T reactor. These authors also estimated the gas consumption using a simple linear relationship for the conversion. Rados et al. [311] also used the ADM for all phases, however, they introduced a gas bubbles interaction term to account for the interactions among gas bubbles of different classes. The authors assumed that the magnitude of the interaction is proportional to a dimensionless cross-flow coefficient and the slip velocity between the two classes of gas bubbles interacting; nonetheless, they only provided a guessed value for this coefficient corresponding to

moderate interactions between the small and large gas bubbles. The authors included the change of gas holdup and gas velocity due to the syngas consumption and considered all of the variables as space-dependent in the derivation of the mass balances. Thus, it is obvious that the reactor model by Rados et al. [311] is quite different from earlier models which assumed constant parameters along the reactor height or used a linear relationship between the syngas conversion and the gas velocity to represent the gas consumption. However, like de Swart and Krishna [272], they used 1st order kinetics with respect to H$_2$ in order to simulate the F-T reaction and assumed the catalyst to be uniformly distributed. Iliuta et al. [312] introduced a pseudo 2-dimensional model based on the two classes of gas bubbles model (2-class model) and the ADM by separating the reactor radially into a core region and an annulus region; and included the gas bubbles interactions term developed by Rados et al. [311]. They took the Water-Gas-Shift (WGS) reaction into account and used detailed kinetics for the F-T reaction; and also estimated the gas consumption from the overall mass balance, and the gas phase and liquid phase concentrations from the vapor-liquid-equilibria (VLE). Although the reactor model by Iliuta et al. [312] appears to be the most complete to date, without considering the field of computational fluid dynamics (CFD), it requires the knowledge of many parameters which are not readily available, especially for high-pressure, high-temperature systems with organic liquids, such as the F-T synthesis. Obviously, this could be a disadvantage, since the estimation of so many unknown parameters may compound the errors, leading to significant uncertainties in the reactor model predictions.

6.3.2   Reactor Model

The SBCR for F-T synthesis was simulated using an axial dispersion model (ADM) in conjunction with the two-class gas bubbles model [117, 123, 228, 272, 311] since visual observations and photographic methods revealed the coexistence of distinctly two-class gas bubbles (small and large) in BCRs [119-123] operating in the churn-turbulent flow regime. The catalyst particles suspension is modeled using the Sedimentation-Dispersion model (SDM). Interactions between small and large bubbles are included in the model using the cross-flow mass exchange term from Rados et al. [311].

The model was built with the following features: (1) The SBCR is operated in the churn-turbulent flow regime; (2) The gas is sparged at the bottom of the reactor trough a multiple

orifices gas distributor; (3) The catalyst used is a cobalt-supported catalyst; (4) The slurry is moving upward; (5) The total heat of reaction is removed using saturated water flowing in a bundle of cooling tubes.

The model was also based on the following key assumptions: (1) The mass transfer resistance in the bulk gas-phase and liquid-solid interface are negligible when compared with that in the liquid film; (2) The slurry superficial velocity is constant, (3) The slurry temperature is constant; (4) The catalyst suspension behavior follows the sedimentation-dispersion model [127, 173, 186, 270, 271]; (5) The reactor is operating in steady-state.

6.3.2.1 Mass & Energy Balances

According to the above assumptions and model features, the mass balances of each component in the liquid and gas phases over a differential element of the reactor can be derived as:

$$\frac{\partial(\varepsilon_L C_{i,L})}{\partial t} = \frac{\partial}{\partial z}\left(\varepsilon_L D_L \frac{\partial C_{i,L}}{\partial z}\right) - \frac{\partial(U_L C_{i,L})}{\partial z} + k_L a_{i,large}\left(C^*_{i,large} - C_{i,L}\right)$$
$$+ k_L a_{i,small}\left(C^*_{i,small} - C_{i,L}\right) + \varepsilon_L r_i \qquad (6\text{-}12)$$

The following Danckwerts' type boundary conditions can be used:

$$z = 0 \qquad U_L C_{i,L} - \varepsilon_L D_L \frac{\partial C_{i,L}}{\partial z} = 0 \qquad (6\text{-}13)$$

$$z = L \qquad \frac{\partial C_{i,L}}{\partial z} = 0 \qquad (6\text{-}14)$$

As mentioned before, the gas phase is divided into 2 classes of bubbles (small and large):

$$\frac{\partial(\varepsilon_{G,small} C_{i,G,small})}{\partial t} = \frac{\partial}{\partial z}\left(\varepsilon_{G,small} D_{G,small} \frac{\partial C_{i,G,small}}{\partial z}\right) - \frac{\partial(U_{G,small} C_{i,G,small})}{\partial z}$$
$$+ \frac{K}{L}\left(U_{G,large} - U_{G,small}\right)\left(C_{i,G,small} - C_{i,G,large}\right) \qquad (6\text{-}15)$$
$$- k_L a_{i,small}\left(C^*_{i,small} - C_{i,L}\right)$$

$$\frac{\partial(\varepsilon_{G,large} C_{i,G,large})}{\partial t} = \frac{\partial}{\partial z}\left(\varepsilon_{G,large} D_{G,large} \frac{\partial C_{i,G,large}}{\partial z}\right) - \frac{\partial(U_{G,large} C_{i,G,large})}{\partial z}$$
$$+ \frac{K}{L}\left(U_{G,large} - U_{G,small}\right)\left(C_{i,G,large} - C_{i,G,small}\right) \qquad (6\text{-}16)$$
$$- k_L a_{i,large}\left(C^*_{i,large} - C_{i,L}\right)$$

The boundary conditions for a multiple bubble class model can be written as in equation (6-17).

$$\sum \left(U_{G,\varphi} C_{i,G,\varphi} - \varepsilon_{G,\varphi} D_{G,\varphi} \frac{\partial C_{i,G,\varphi}}{\partial z} \right) = \left(U_G C_{i,G} \right)_{inlet} \tag{6-17}$$

In order to obtain a boundary condition for each bubble class we can define $U_{G,inlet}$:

$$U_{G,inlet} = \sum \left(U_{G,\varphi} \right)_{inlet} \tag{6-18}$$

Therefore, the boundary condition for each bubble class becomes:

$$U_{G,\varphi} C_{i,G,\varphi} - \varepsilon_{G,\varphi} D_{G,\varphi} \frac{\partial C_{i,G,\varphi}}{\partial z} = \left(U_{G,\varphi} C_{i,G} \right)_{inlet} \tag{6-19}$$

In the case of the 2 bubble-class model, the boundary conditions become:

$$z = 0 \qquad \begin{cases} U_{G,small} C_{i,G,small} - \varepsilon_{G,small} D_{G,small} \dfrac{\partial C_{i,G,small}}{\partial z} = U_{G,small} C_{i,G,inlet} \\[2mm] U_{G,large} C_{i,G,large} - \varepsilon_{G,large} D_{G,large} \dfrac{\partial C_{i,G,large}}{\partial z} = U_{G,large} C_{i,G,inlet} \end{cases} \tag{6-20}$$

$$z = L \qquad \begin{cases} \dfrac{\partial C_{i,G,small}}{\partial z} = 0 \\[2mm] \dfrac{\partial C_{i,G,large}}{\partial z} = 0 \end{cases} \tag{6-21}$$

The axial dispersion model (ADM) can also be used to derivate the mass balance for the catalyst suspension:

$$\frac{\partial \left((1 - \varepsilon_G) C_S \right)}{\partial t} = \frac{\partial}{\partial z} \left((1 - \varepsilon_G) D_S \frac{\partial C_S}{\partial z} \right) + \frac{\partial \left(((1 - \varepsilon_G) U_P - U_L) C_S \right)}{\partial z} \tag{6-22}$$

The average catalyst concentration in the reactor ($C_{average}$) is used to derivate the boundary conditions:

$$\int_0^L C_S dz = \overline{C_S} \tag{6-23}$$

$$z = L \qquad U_L C_S = U_L C_S|_{inlet} \tag{6-24}$$

Assuming that the gas and liquid phases have identical temperature, the following energy balance can be used:

$$\frac{\partial \left((1 - \varepsilon_G) \rho_{SL} Cp_{SL} T \right)}{\partial t} = \frac{\partial}{\partial z} \left(\rho_{SL} Cp_{SL} (1 - \varepsilon_G) D_H \frac{\partial T}{\partial z} \right) + \frac{\partial (\rho_{SL} Cp_{SL} U_L T)}{\partial z} \tag{6-25}$$
$$- U_{Heat} (T - T_{cool}) + (1 - \varepsilon_G) r_{Heat}$$

The boundary conditions are:

$$z = 0 \qquad U_L \rho_{SL} T - \rho_{SL} (1 - \varepsilon_G) D_H \frac{\partial T}{\partial z} = (U_L \rho_{SL} T)_0 \tag{6-26}$$

$$z = L \qquad \frac{\partial T}{\partial z} = 0 \tag{6-27}$$

The pressure profile was obtained from the hydrostatic head pressure:

$$\frac{\partial P}{\partial z} + [(1 - \varepsilon_G)\rho_{SL} + \varepsilon_G \rho_G]g = 0 \tag{6-28}$$

Also, the change of gas velocity due to gas consumption was estimated using the total gas-phase mass balance:

$$\frac{\partial U_G}{\partial z} + \sum_i \left[\frac{k_L a_{i,small}}{C_{i,G,small}} \left(C_{i,small}^* - C_{i,L} \right) + \frac{k_L a_{i,large}}{C_{i,G,large}} \left(C_{i,large}^* - C_{i,L} \right) \right] = 0 \tag{6-29}$$

With the following boundary conditions:

$$z = 0 \qquad U_G = U_{G,inlet} \tag{6-30}$$

$$z = L \qquad \frac{\partial U_G}{\partial z} = 0 \tag{6-31}$$

The gas velocity of the small bubbles was taken from de Swart [228]:

$$U_{G,small} = 2.25 \frac{\sigma_L}{\mu_L} \left(\frac{\sigma_L^3 \rho_L}{g\mu_L^4} \right)^{-0.273} \left(\frac{\rho_L}{\rho_G} \right)^{0.03} \varepsilon_{G,small} \tag{6-32}$$

Then the gas velocity of the large bubbles can be calculated from:

$$U_{G,large} = U_G - U_{G,small} \tag{6-33}$$

6.3.3   Model Parameters Estimation

In order to solve the set of equations derived above, several key parameters need to be estimated, such as the settling velocities of solid particles (U_P); the axial dispersion coefficients of the liquid (D_L), small gas bubbles ($D_{G,small}$), large gas bubbles ($D_{G,large}$) and solid (D_S) phases; the volumetric liquid-side mass transfer coefficients of the species in the small gas bubbles ($k_L a_{i,small}$) and large gas bubbles ($k_L a_{i,large}$); the phase holdups for the liquid (ε_L), small gas bubbles ($\varepsilon_{G,small}$) and large gas bubbles ($\varepsilon_{G,large}$); and the kinetic rate (r_i). The estimation of the parameters needed is detailed in the following sections.

Table 30: Literature F-T SBCR Models

Authors/Ref.	Kinetics	Species involved in MB	Gas Phase LB	Gas Phase SB	Liquid/Slurry Phase	Solid Phase	Energy	Gas Consumption	Steady-State or Transient?
Calderbank et al. [313]	FTS, 1st order	H_2	PF		PF	Uniform	-	-	-
Satterfield and Huff [314]	FTS, 1st order	H_2	PF		PM	Uniform	Isothermal	No	Steady-State
Deckwer et al. [315]	FTS, 1st order	H_2	PF		PM	Uniform	Isothermal	Linear f(X)	Steady-State
Deckwer et al. [316]	FTS, 1st order	H_2	ADM		ADM	SDM	ADM	Linear f(X)	Steady-State
Bukur [317]	FTS, 1st order	H_2	PF		PM; PF	Uniform	Isothermal	Linear f(X)	Steady-State
Kuo [318]	FTS, 1st order FTS, L-H WGS, L-H	H_2 H_2, CO, H_2O, CO_2	PF		PF; PM; ADM	Uniform	Isothermal	Linear f(X)	Steady-State
Stern et al. [319]	FTS, 1st order	H_2	PF		PM	Uniform	Isothermal	No	Steady-State
Leib and Kuo [77]	FTS, L-H WGS, L-H	H_2, CO, H_2O, CO_2	PF		Unmixed	SDM	-	Linear f(X)	Steady-State
Stern et al. [308]	FTS, 1st order WGS, 2nd order	$H_2, CO, H_2O, CO_2, C_nH_m$	ADM		ADM	SDM	Isothermal	Overall gas MB	Steady-State
Bukur and Zimmerman [302]	FTS, L-H WGS, L-H	$H_2, CO, H_2O, CO_2, C_nH_m$	PF		Unmixed	SDM	Isothermal	Overall gas MB	Steady-State
Turner and Mills [320]	FTS, 1st order	H_2	MCM; PF ADM		MCM ADM	Uniform SDM	Isothermal ADM	Linear f(X)	Steady-State
Prakash [304]	FTS, L-H WGS, L-H	H_2, CO, H_2O, CO_2	ADM		ADM	SDM	Isothermal	Overall gas MB	Steady-State
Leib et al. [321]	FTS, 1st order	H_2	MCM		MCM	Uniform	Isothermal	Linear f(X)	Steady-State
Inga and Morsi [322]	FTS, L-H WGS, L-H	H_2, CO, H_2O, CO_2	PF		MCM	Uniform	Isothermal	No	Steady-State
Mills et al. [323]	FTS, 1st order	H_2	ADM		ADM	SDM	ADM	Linear f(X)	Steady-State
Maretto and Krishna [324]	FTS, L-H	H_2, CO	PF	PM	PM	Uniform	Isothermal	No	Steady-State
van der Laan et al. [34]	FTS, L-H WGS, L-H	$H_2, CO, H_2O, CO_2,$ n products	PF	PM	PM	Uniform	Isothermal	Linear f(X)	Steady-State
de Swart and Krishna [272]	FTS, 1st order	H_2	ADM	ADM	ADM	SDM	ADM	Linear f(X)	Transient
Rados et al. [305, 311]	FTS, 1st order	$H_2, CO, H_2O,$ pseudo product	ADM	ADM	ADM	Uniform	ADM	Overall gas MB	Transient
Song et al.[307]	FTS, L-H	$H_2, CO, H_2O,$ pseudo product	PF		PM	Uniform	Isothermal	Overall gas MB	Steady-State
Song et al. [325]	FTS, L-H	H_2, CO, H_2O, CO_2	PM		PM	Uniform	Isothermal	No	Steady-State

Authors/Ref.	Kinetics	Species involved in MB	Gas Phase		Liquid/Slurry Phase	Solid Phase	Energy	Gas Consumption	Steady-State or Transient?
			LB	SB					
Fernandes [326]	FTS, L-H WGS, L-H	H_2, CO, H_2O, CO_2, n products	PF	PM	PM	Uniform	Isothermal	Linear f(X)	Steady-State
Iliuta et al. [303, 312]	FTS, L-H WGS, L-H	H_2, CO, H_2O, CO_2, n pseudo products	Core ADM	Core & Annulus ADM	Core & Annulus ADM	Core & Annulus ADM	ADM	Overall gas MB	Steady-State
Sehabiague et al. [306]	FTS, L-H	H_2, CO, H_2O, CO_2, N_2, n products	ADM	ADM	ADM	SDM	ADM	Overall gas MB	Steady-State
Wang et al. [309]	FTS, L-H WGS, L-H	H_2, CO, H_2O, CO_2, N_2, n products	PF	PM	PM	Uniform	Isothermal	Overall gas MB	Steady-State
Guettel and Turek [327]	FTS, 1st order	H_2	PF		PM	Uniform	PF	Linear f(X)	Steady-State
Troshko and Zdravistch [328]	FTS, L-H	H_2, CO, H_2O, pseudo product	CFD		CFD	Uniform	Isothermal	CFD	Transient

L-H: Overall reaction rate based on Langmuir-Hinshelwood kinetics.
ADM: Axial-Dispersion Model
MCM: Mixing-Cell Model
SDM: Sedimentation-Dispersion Model
PF: Plug-Flow
PM: Perfectly Mixed
MB: Mass Balance

6.3.3.1 Dispersion Coefficients

The dispersion coefficients for the gas, liquid and solid phases were estimated from the available literature, although possible experimental methods for measuring the dispersion coefficients in the pilot-scale SBCR were considered as presented in Appendix A.

Liquid-Phase Dispersion

The axial liquid phase dispersion coefficient (D_L) was predicted using Equation (6-34) introduced by Baird and Rice [310] who used a large number of experimental data reported by various authors to obtain such an equation.

$$D_L = 0.35 d_R^{1.33} (g U_G)^{0.33} \qquad (6\text{-}34)$$

It should be noted that Equation (6-35) proposed by Deckwer et al. [108, 316] can also be used instead of Equation (6-34) and predicts similar values for the dispersion coefficient.

$$D_L = 0.768 d_R^{1.34} U_G^{0.32} \qquad (6\text{-}35)$$

The dependency of the liquid phase dispersion coefficient (D_L) on the reactor diameter was accounted for by the scale-up index (n), introduced by Yang et al. [329] and defined as:

$$D_L \sim d_R^n \qquad (6\text{-}36)$$

These authors found that the operating pressure has an effect on the scale-up index since the axial dispersion coefficient was found to decrease with increasing pressure. They proposed the following equation to take into account the effect of pressure:

$$\frac{n}{n_0} = 1 - 0.11 \ln\left(\frac{\rho_G}{\rho_{G,0}}\right) \qquad (6\text{-}37)$$

In the above equation, n_0 and $\rho_{G,0}$ represent the scale-up index and the gas density at atmospheric pressure, respectively.

It should be noted that the decrease of the liquid phase axial dispersion coefficient with increasing gas density could be related to the increase of the gas holdup or more precisely to the increase and decrease of the populations of small gas bubbles and large gas bubbles, respectively [120]. The decrease of the large gas bubbles population results in less back-mixing in the SBCR i.e., lower values of the liquid-phase axial dispersion coefficient (D_L).

Gas-Phase Dispersion

The axial gas phase dispersion coefficient (D_G) can be predicted using several correlations available in the literature, such as those by Mangartz and Pilhofer [330], Towell and Ackerman [331] or Field and Davidson [332]. These correlations, however, cannot be applied to the 2-class ADM because they were developed considering the gas bubbles as only a single-phase. They also overpredict the axial dispersion coefficient values for large reactor diameters. While the small-bubbles axial dispersion coefficient can adequately be assumed to be identical to that of the liquid phase since the small bubbles are entrained by the liquid recirculation, the axial dispersion of the large gas bubbles, which rise fast in the reactor in a plug flow, is more difficult to estimate. It should be mentioned that to our knowledge, no one has measured the axial dispersion of the small or large gas bubbles. de Swart and Krishna [272] assumed a constant value of 100 for the Peclet Number of the large gas bubbles (P_e)$_{Large}$ in order to account for this phenomena. Their assumption, however, neglected the impact of the other operating variables on the size and population of the large gas bubbles and thus on their axial dispersion. In this study, the axial dispersion coefficient of the gas-phase was assumed to be a function of the diameters of the gas bubbles. For small gas bubbles, the axial dispersion coefficient should be equal or similar to that of the liquid-phase, whereas for large gas bubbles the axial dispersion coefficient should be small to obtain plug flow like conditions. The following relationship is therefore proposed to estimate the dispersion of each class of gas bubbles:

$$\frac{D_G}{D_L} = 1 - \frac{d_B{}^a}{d_{B,0}{}^a + d_B{}^a} \tag{6-38}$$

This relationship shows that for small gas bubbles diameter ($d_B \approx 0$) the gas phase dispersion is equal to the liquid-phase dispersion. For large gas bubbles (d_B is large) the gas phase dispersion approaches 0. The constant $d_{B,0}$ in Equation (6-38) represents the diameter of the gas bubbles at the point of designation as large gas bubbles in the 2-class model and was set at 0.01 m. The value of the exponent in Equation (6-38) was chosen so that Equation (6-38) predicts the large gas bubbles Peclet number assumption of de Swart and Krishna [272] under the conditions theses authors used.

Solid-Phase Dispersion Coefficient and Particles Settling Velocity

The direct measurements of the solid concentration performed along the pilot SBCR have shown that the dispersion-sedimentation model was able to fit well the data obtained (see Section 6.1.8).

Behkish [127] performed similar measurements of the solid concentration using the same reactor; and also found that the dispersion-sedimentation model fitted well the data obtained with average absolute relative error and standard deviation of 1.5 and 2.5 %, respectively. Unfortunately the number of experimental data points obtained by Behkish [127] and in this present study was not sufficient to allow a precise estimation of the particles settling velocity and solid dispersion coefficient. These two parameters were therefore estimated using the data of several other authors [173, 186, 270, 271]. Using the data/correlations developed by the authors listed in Table 31, the following two correlations were developed:

$$Pe_S = 8.5 Fr_G^{0.76} Re_G^{-0.052} + 0.025 Re_P^{1.07} Fr_G^{-0.067} \tag{6-39}$$

$$U_P = 1.37 U_G^{0.17} U_{TS}^{0.78} (1 - c_V)^{2.43} \tag{6-40}$$

Table 31: Models used for Predicting the Axial Solid Dispersion Coefficient and Particle Settling Velocity

Authors	Solid System	Correlation
Kato et al. [270]	Glass beads ρ_P = 2520 kg/m³ 75.5<d_P<163 µm C_S: 48-202 kg/m³	$\dfrac{U_G d_R}{D_S} = 13 Fr_G \dfrac{1 + 0.009 Re_P Fr_G^{-0.8}}{1 + 8 Fr_G^{0.85}}$ $U_P = 1.33 U_{t,\infty} \left(\dfrac{U_G}{U_{t,\infty}}\right)^{0.25} (1 - c_V)^{2.5}$
Kojima et al. [173]	Glass beads 105 <d_P<125 µm C_S: 3.1-62 kg/m³	$\dfrac{U_G d_R}{D_S} = 10 Fr_G^{0.76}$
O'Dowd et al. [186]	Glass beads ρ_P = 2420 kg/m³ 88<d_P<105 µm C_S: up to 420 kg/m³	$\dfrac{U_G d_R}{D_S} = 7.7 \left(\dfrac{Fr_G^6}{Re_G}\right)^{0.098} + 0.019 Re_P^{1.1}$ $U_P = 1.69 U_G^{0.23} U_{T,\infty}^{0.8} (1 - c_V)^{1.28}$
Smith and Reuther [271]	Glass beads ρ_P = 2420, 3990 kg/m³ 48.5<d_P<164 µm C_S: up to 420 kg/m³	$\dfrac{U_G d_R}{D_S} = 9.6 \left(\dfrac{Fr_G^6}{Re_G}\right)^{0.1114} + 0.019 Re_P^{1.1}$ $U_P = 1.1 U_G^{0.026} U_{T,\infty}^{0.8} (1 - c_V)^{3.5}$

The particles terminal settling velocity was estimated as follows [333]:

$$U_{TS} = \frac{(\rho_S - \rho_L) g d_P^2}{18 \mu_L} \tag{6-41}$$

6.3.3.2 Hydrodynamics and Mass Transfer

The gas holdup, gas bubble sizes, and volumetric liquid-side mass transfer coefficient were estimated using the correlations presented in Section 6.1.8. The gas holdup for the large gas

bubbles was estimated using Behkish et al. [184] correlation listed in Table 26 and the gas holdup for the small bubbles was obtained from:

$$\varepsilon_{G,small} = \varepsilon_G - \varepsilon_{G,large} \qquad (6\text{-}42)$$

The bubbles sizes for the large and small gas bubbles were estimated from the correlation by Lemoine et al. [277]

The overall volumetric liquid-side mass transfer coefficient ($k_L a_L$) obtained from Equation (6-11) includes all gas components and gas bubbles. Its value can be obtained from the rate of multicomponent gas absorption in the liquid phase:

$$-\frac{dn_G}{dt} = k_L a_L (C^* - C_L) V_L \qquad (6\text{-}43)$$

Where n_G is the total number of moles of gas and C* is the total equilibrium concentration of dissolved gas components in the liquid phase.

In the case of F-T SBCR reactor, the gas phase is composed of a mixture (syngas + gaseous products + inert) and is in the form of gas bubbles of different sizes. Therefore, in a bubble "n", we can define a "$(k_L a_L)_{i,n}$" for the "i" component of the gas mixture as:

$$-\frac{dn_{G,i,n}}{dt} = (k_L a_L)_{i,n} (C^*_{i,n} - C_{L,i}) V_L \qquad (6\text{-}44)$$

Where $n_{G,I,n}$ is the number of moles of gas component "i" in the bubble "n". The overall rate of mass transfer is the sum of all the individual rates:

$$-\frac{dn_G}{dt} = \sum_n \sum_i -\frac{dn_{G,i,n}}{dt} = \sum_n \sum_i (k_L a_L)_{i,n} (C^*_{n,i} - C_{L,i}) V_L \qquad (6\text{-}45)$$

Substituting Equation (6-45) into Equation (6-43), we obtain the relationship between the individual "$(k_L a_L)_{i,n}$" and the overall $k_L a_L$ coefficient:

$$k_L a_L = \frac{\sum_n \sum_i (k_L a_L)_{i,n} (C^*_{n,i} - C_{L,i})}{(C^* - C_L)} \qquad (6\text{-}46)$$

If we assume that at time t = 0, there is no dissolved gas in the liquid phase, the relationship can be simplified to:

$$k_L a_L = \frac{\sum_n \sum_i (k_L a_L)_{i,n} C^*_{n,i}}{C^*} \qquad (6\text{-}47)$$

The volumetric liquid-side mass transfer coefficients as well as the solubilities of N_2/He gas mixtures were measured in the paraffins mixture by Rakymkul [334] using a 4 liters stirred tank reactor connected to a mass spectrometer. For each experiment with any N_2/He gas mixture, 3

volumetric mass transfer coefficients were obtained using a TPGA technique similar to that used in the pilot SBCR: one for the overall gas (k_La), one for He (k_La_{He}), and one for N$_2$ (k_La_{N2}). Applying Equation (6-47), an expression for the overall k_La as a function of the individual k_La and solubilities is obtained:

$$k_L a = \frac{k_L a_{He} C^*_{He} + k_L a_{N2} C^*_{N2}}{C^*_{He} + C^*_{N2}} \tag{6-48}$$

Using the solubility data from Rakymkul [334], equation (6-48) can be used to calculate the overall k_La values and compare them to the experimental ones. Figure 65 shows the overall k_La values obtained from equation (6-48) presented against the measured overall k_La values obtained by Rakymkul,[334] and as can be seen a very good agreement between the measured and predicted values is obtained.
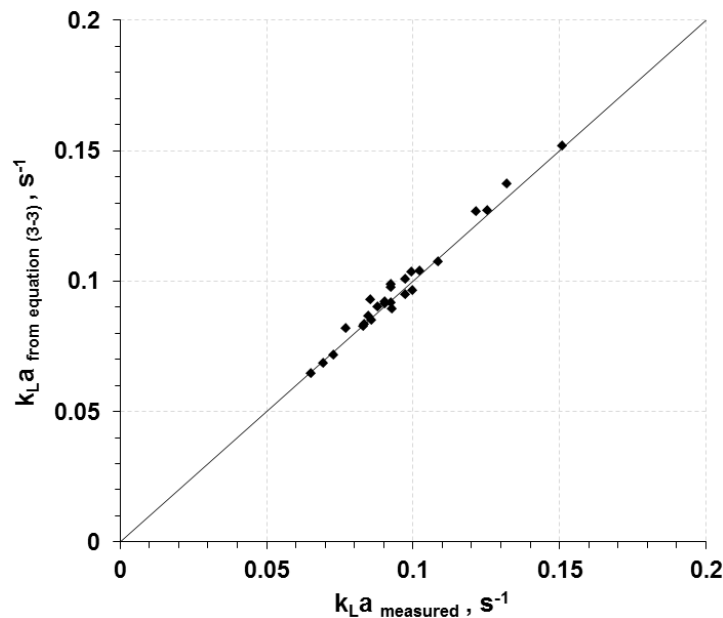
Figure 65: Overall k_La Obtained from Equation (6-48) Versus Overall k_La Measured
(He/N$_2$ Gas Mixture; C$_S$ = 10 vol.%; N = 1100 RPM)

According to the surface renewal and penetration theories,[335] the mass transfer coefficient of the gas component "i" in a bubble "n" is proportional to the square root of its diffusivity into the liquid phase. A relationship between the mass transfer coefficients of components "i" and "j" for a gas bubble "n" can therefore be suggested as in Equation (6-49).

$$\frac{k_{L,i,n}}{k_{L,j,n}} = \left(\frac{D_i}{D_j}\right)^{0.5} \tag{6-49}$$

Substituting Equation (6-49) into Equation (6-47) leads to:

$$k_L a_L = \frac{\sum_n (k_L a_L)_{j,n} \sum_i \sqrt{D_i}\, C_{n,i}^*}{\sqrt{D_j}\, C^*} \tag{6-50}$$

At this point, if we regroup all the gas bubble into 1 class, we have an expression for the individual $(k_L a_L)_j$ of each component "j" in the gas mixture:

$$(k_L a_L)_j = \frac{k_L a_L \sqrt{D_j}\, C^*}{\sum_i \sqrt{D_i}\, C_i^*} = \frac{k_L a_L \sqrt{D_j}\, x^*}{\sum_i \sqrt{D_i}\, x_i^*} \tag{6-51}$$

Thus, with the knowledge of the overall mass transfer coefficient ($k_L a$), through direct measurements using the gas mixture under actual conditions or through the use of adequate mass transfer coefficient correlation, and the knowledge of the gas diffusivity (D_i) and equilibrium solubility (C_i^*), one can predict the mass transfer coefficient of each component ($k_L a$)$_i$ in the mixture in the reactor with high precision using Equation (6-51).

For the modeling purposes in this study, the gas bubbles distribution is divided into 2 classes (small and large) according to their size, and subsequently equation (6-50) becomes:

$$k_L a_L = \frac{(k_L a_L)_{j,small} \sum_i \sqrt{D_i}\, C_{small,i}^* + (k_L a_L)_{j,large} \sum_i \sqrt{D_i}\, C_{large,i}^*}{\sqrt{D_j}\, C^*} \tag{6-52}$$

The correlations by Calderbank and Moo-Young [336] of the mass transfer coefficients for small and large gas bubbles leads to:

$$\frac{k_{L,j,large}}{k_{L,j,small}} = 1.3548 \left(\frac{\mu_{SL}}{\rho_{SL} D_j}\right)^{1/6} \tag{6-53}$$

From the assumption that all the gas bubbles have spherical shapes, an expression for the interfacial area of a bubble "n" (or class "n") is derived as:

$$a_{L,n} = \frac{6\varepsilon_{G,n}}{d_{b,n}(1 - \varepsilon_G)} \tag{6-54}$$

Where ε_G is the overall gas holdup, $\varepsilon_{G,n}$ is the gas holdup of the gas bubbles from the class "n" and $d_{b,n}$ is their corresponding average diameter.

From Equations (6-53) and (6-54), the relationship shown in Equation (6-55) between the individual "$(k_L a_L)_{i,n}$" of two classes of gas bubbles is obtained.

$$\frac{(k_L a_L)_{j,large}}{(k_L a_L)_{j,small}} = 1.3548 \left(\frac{\mu_{SL}}{\rho_{SL} D_j}\right)^{1/6} \frac{\varepsilon_{G,large} d_{b,small}}{\varepsilon_{G,small} d_{b,large}} \qquad (6\text{-}55)$$

Substituting in Equation (6-52), the final expression for the individual "$(k_L a_L)_{i,small}$" of the small bubbles class becomes as follows:

$$(k_L a_L)_{j,small} = \frac{k_L a_L \sqrt{D_j} C^*}{\sum_i \sqrt{D_i} C^*_{small,i} + 1.3548 \left(\frac{\mu_{SL}}{\rho_{SL} D_j}\right)^{1/6} \frac{\varepsilon_{G,large} d_{b,small}}{\varepsilon_{G,small} d_{b,large}} \sum_i \sqrt{D_i} C^*_{large,i}} \qquad (6\text{-}56)$$

The individual "$(k_L a_L)_{i,large}$" of the large bubbles class can then be obtained from equation (6-55). The diffusivity coefficients of the different gaseous compounds were estimated using the correlation developed by Erkey et al. [259] and presented in Section 4.2.3.

6.3.3.3 Catalysts and Kinetics

The kinetic rate expressions for the F-T reactions available in the literature for the iron and cobalt-based catalysts are listed in Tables 32 and 34, respectively. Each expression was independently used in the simulator; and in the case of iron catalyst, one of the WGS reactions given in Table 33 was employed. For instance, the kinetic expressions by Deckwer et al. [80], Huff and Satterfield [76], and Ledakowicz et al. [78] were coupled with the rate expression for the WGS reaction from Chang et al. [57]. In the case of the kinetic expressions by Zimmerman and Bukur,[37] their rate expressions for the WGS reaction were used. It should be noted that these F-T kinetic rate expressions were obtained in slurry reactors, at different temperatures and were easily incorporated in the reactor model. The kinetic rate expressions by Atwood and Bennett [73] and Yang et al. [64], however, were obtained in a fixed-bed reactor, and due to the relatively small size (300 and 305 μm) of the catalytic particles used, they were used in this study. Also, due to the similarity of their catalysts, the rate of F-T from Atwood and Bennett [73] was paired with the WGS rate from Yang et al. [64]. Most of the coefficients for the F-T and WGS reactions listed in Tables 32 through 34 are expressed as function of the operating temperature in an Arrhenius form as:

$$k_{FT \ (or \ WGS)} = k_0 e^{-\frac{Ea}{RT}} \qquad (6\text{-}57)$$

$$b = b_0 e^{-\frac{Ea}{RT}} \qquad (6\text{-}58)$$

Table 32: F-T Kinetics and Characteristics of the Iron Catalysts

Reference	Catalyst	Operating Conditions			Equation	k_{FT}		b		ρ (g/L)	d (mm)
		T (C)	P (MPa)	H_2/CO		k_0	Ea	b_0	Ea		
Atwood and Bennett [73]	Reduced Nitrided Fused Fe/K_2O/Al_2O_3/SiO_2	250-315	2	2	$r_{FT} = k_{FT} \dfrac{P_{H_2} P_{CO}}{P_{CO} + bP_{H_2O}}$	0.1013	80.4	0.1640	-8.83	5324	300
Chang et al. [57]	Fe/Cu/K/SiO_2	250-290	0.95-2.55	0.65-1.51	See Chang et al. [57]	-	-	-	-	5000 [1]	< 44 (34)[1]
Deckwer et al. [80]	Reduced Prec. Fe/K	220-260	-	0.5-2.0	$r_{FT} = k_{FT} \dfrac{P_{H_2}^2 P_{CO}}{P_{CO}P_{H_2} + bP_{H_2O}}$	4.239	85.3	0.01847	-80	5389	< 50 (40)[1]
Huff and Satterfield [76]	Reduced Fused Fe/K_2O/CaO/SiO_2	232-263	0.4-1.5	0.5-1.8	$r_{FT} = k_{FT} \dfrac{P_{H_2}^2 P_{CO}}{P_{CO}P_{H_2} + bP_{H_2O}}$	1.198	82.2	1.786E-4	-98.1	5414	< 44 (34)[1]
Ledakowicz et al. [78]	Reduced Prec. Fe/K	220-260	1.0	0.5-0.6	$r_{FT} = k_{FT} \dfrac{P_{H_2} P_{CO}}{P_{CO} + bP_{CO_2}}$	513.9	108	0.0241	-9.2	5389	< 50 (40)[1]
Zimmerman and Bukur [37]	Prec. Fe/Cu/K	235-265	1.5-3.0	0.6-1.0	$r_{FT} = k_{FT} \dfrac{P_{H_2} P_{CO}}{P_{CO} + bP_{H_2O}}$	6.763	86	5.3	0	5474	< 44 (34)[1]
	Reduced Fe/Cu/K/SiO_2	235-265	1.5-3.0	0.6-1.0	$r_{FT} = k_{FT}P_{H_2}$	2.502	86		-	4469	< 44 (34)[1]

[1] values assumed

Table 33: WGS Kinetics and Characteristics of the Iron Catalysts

Reference	Catalyst	Operating Conditions			Equation	k_{WGS}		b	K_{eq}		ρ (g/L)	d (mm)
		T (C)	P (MPa)	H$_2$/CO		k_0	Ea		k_0	Ea		
Chang et al. [57]	Fe/Cu/K/SiO$_2$	250-290	0.95-2.55	0.65-1.51	$r_{WGS} = k_{WGS} \dfrac{P_{CO}P_{H_2O} - \dfrac{P_{CO_2}P_{H_2}}{K_{eq}}}{P_{H_2}^{0.5} + bP_{CO}P_{H_2O}}$	3.16E-6	35.6	0.0183	0.689	-8.14	5000 [1]	< 44 (34)[1]
Yang et al. [64]	Fe/Mn	283-328	1.5-3.05	1.02-3.13	$r_{WGS} = k_{WGS} \dfrac{P_{CO}P_{H_2O} - \dfrac{P_{CO_2}P_{H_2}}{K_{eq}}}{P_{H_2}^{0.5} + bP_{CO}P_{H_2O}}$	1.08E-4	58.4	8.73E-5	0.689	-8.14	-	305
Zimmerman and Bukur [37]	Prec. Fe/Cu/K	235-265	1.5-3.0	0.6-1.0	$r_{WGS} = k_{WGS} \dfrac{P_{CO}P_{H_2O} - \dfrac{P_{CO_2}P_{H_2}}{K_{eq}}}{P_{CO} + bP_{H_2O}}$	9.25E+6	132	21	0.0132	-38.1	5474	< 44 (34)[1]
	Reduced Fe/Cu/K/SiO$_2$	235-265	1.5-3.0	0.6-1.0	$r_{WGS} = k_{WGS} \dfrac{P_{CO}P_{H_2O} - \dfrac{P_{CO_2}P_{H_2}}{K_{eq}}}{P_{CO}P_{H_2}}$	5.84E+11	137	-	0.0132	-38.1	4469	< 44 (34)[1]

Table 34: F-T Kinetics and Characteristics of the Cobalt Based Catalysts

Reference	Catalyst	Operating Conditions			Equation	k_{FT}		b		ρ (g/L)	d (mm)
		T (C)	P (MPa)	H₂/CO		k_0	Ea	b_0	Ea		
van Steen and Schulz [86]	Co/MgO/ThO₂/SiO₂	190-210	$P_{H2} = 0.01\text{-}1.93$ $P_{CO} = 0.05\text{-}2.54$		$r_{FT} = k_{FT} \dfrac{P_{H_2}^{3/2} P_{CO}}{P_{H_2O}\left(1 + \dfrac{bP_{H_2}P_{CO}}{P_{H_2O}}\right)^2}$	54003	142	1.24E-11	-40.7	4089	Unknown (70)[1]
Withers et al. [99]	Co/Zr/SiO₂	220-280	2.1	0.5-2.0	$r_{FT} = k_{FT} \dfrac{P_{H_2}^2 P_{CO}}{P_{CO}P_{H_2} + bP_{H_2O}}$	5962	102	9.38E+5	-18.9	2852	70
Yates and Satterfield [100]	Co/MgO/SiO₂	220-240	1.5-3.5	1.5-3.5	$r_{FT} = k_{FT} \dfrac{P_{H_2}P_{CO}}{(1 + bP_{CO})^2}$	2.592E-9	37.4	1.24E-12	-68.5	3154	72

[1] values assumed

The skeletal density of each catalyst listed in Tables 32 through 34 was estimated, when it was not given, based on its composition. The composition of the catalyst used by Huff and Satterfield [76] was estimated assuming the balance of the partial composition provided by the authors and the catalyst is equally composed of FeO and Fe_2O_3. The skeletal density of the catalyst used by Withers et al. [99] was estimated according to its composition given by the authors, assuming the balance is made only of SiO_2. Finally, the density of the catalyst by Chang et al. [57] was assumed to be 5,000 kg/m³.

Neither the mean catalyst particle size nor size distribution was given in most of the available literature. The majority of the authors, however, mentioned the maximum particles size as they sieved the catalyst prior to their experiments. In these cases, a mean particles size equal to 10 microns lower than the maximum size was arbitrarily assumed. Yates and Satterfield [100] provided the upper and lower limits of the particles size distribution, and the particles diameter in this case was estimated as the average of these two limits. van Steen and Schulz [86] did not provide any information about the particle and in this situation, an arbitrarily value of 70 μm was assumed. Also, for Withers et al. [99] the particles size was assumed to be identical to the particles diameter of the support used to prepare the catalyst (SiO_2).

The values of the kinetic rate constant (k_{FT}) shown in Table 32 are valid for a FT rate expression based on the rate of CO disappearance as:

$$r_{FT} = -\frac{dn_{CO}}{dt} \tag{6-59}$$

In some literature, however, the value of the rate constant k_{FT} was given based on the rate of syngas ($H_2 + CO$) disappearance as:

$$r_{H_2+CO} = -\frac{dn_{CO}}{dt} - \frac{dn_{H_2}}{dt} \tag{6-60}$$

It was therefore converted for the rate of CO disappearance using the following relationships based on the stoichiometry of the FT (Equation (2-4)) and WGS (Equation (2-5)) reactions:

$$r_{CO} = -\frac{dn_{CO}}{dt} = r_{FT} + r_{WGS} \tag{6-61}$$

$$r_{H_2} = -\frac{dn_{H_2}}{dt} = \left(1 + \frac{m}{2n}\right) r_{FT} - r_{WGS} \tag{6-62}$$

$$r_{H_2+CO} = r_{H_2} + r_{CO} = \left(2 + \frac{m}{2n}\right) r_{FT} \tag{6-63}$$

$$r_{FT} = \frac{1}{\left(2 + \frac{m}{2n}\right)} r_{(H_2+CO)} \qquad\qquad\qquad (6\text{-}64)$$

The kinetic rate constants by Deckwer et al.,[80] Ledakowicz et al. [78] and Withers et al. [99] were based on the slurry concentrations. Those values were converted to pressures using Henry's Law constants taken from Soriano [254] for H_2 and CO, and from Marano and Holder [337] for H_2O. The kinetic rate constant by Atwood and Bennett [73] was based on the catalyst bed concentration. Using the bed density mentioned by the authors and the skeletal density of the catalyst, the void fraction was calculated and used to convert the bed concentrations into pressures. Zimmerman and Bukur [37] provided kinetic rate constants based only on one temperature, although the authors reported activation energies for both F-T and WGS first order kinetic rate constants. These reported activation energies were used to calculate the kinetic rate constants as given in Table 32.

6.3.3.4 Heat Transfer Coefficient

The heat transfer coefficient from the dispersed phase (slurry + gas) was estimated using the correlation by Cho et al. [338] and including the effect of solids particles by replacing the liquid viscosity with the slurry viscosity:

$$h_o = 11710 U_G^{0.445} (\mu_{SL} \times 10^3)^{-0.060} (P \times 10^{-6})^{0.176} \qquad\qquad (6\text{-}65)$$

6.3.3.5 Slurry Viscosity

The viscosity of the slurry-phase was estimated using Deckwer et al. [108, 316] correlation:

$$\mu_{SL} = \mu_L (1 + 4.5 c_V) \qquad\qquad\qquad (6\text{-}66)$$

6.3.3.6 Gas Solubilities and Products Distribution

The knowledge of the solubilities of the gases involved in the F-T synthesis is essential to correctly estimate the rate of absorption of the gases into the liquid-phase. Since the F-T process can produce wide range of products, the nature and properties of the liquid-phase will vary depending on the operating conditions of the reactor. The solubilities of the different gases in wax were estimated from the work by Soriano [254] who measured the solubilities of H_2, CO, N_2

and He in Sasol wax in a small agitated autoclave under Fischer-Tropsch conditions. The Henry's law constant was expressed as a function of temperature as:

$$\ln(H_i) = \ln(H_{i,0}) + \frac{A}{T^2} + \frac{B}{T}$$ (6-67)

The coefficients of Equation (6-67) are listed in Table 35.

Table 35: Coefficients for Henry's Law Constant from Soriano [254]

Gas	A	B	$H_{i,0}$
N_2	$-2.214 \cdot 10^5$	1,267	51.62
He	$-5.442 \cdot 10^5$	3,336	53.17
H_2	$-1.929 \cdot 10^5$	1,345	42.18
CO	$-3.651 \cdot 10^5$	1,873	22.87

The solubilities of other gases (H_2O, CO_2, CH_4, etc…) were estimated from Marano and Holder [337] using their multi-component vapor liquid equilibria (VLE) model. This model coupled with the superposition of 2-α distributions for predicting the product distributions was used to perform equilibrium calculations in order to estimate the final composition of the gaseous and liquid hydrocarbon products. As explained in Section 2.1.3, two different growth probability factors (α_1 and α_2) are introduced in the 2-α model for the small and long chain products, respectively [52]. This model also relies on the term ζ corresponding to the break point of the distribution. The mole fraction of the n-carbons chain length products can be expressed as [52]:

$$x_n = \frac{\alpha_1^{n-1} + \left(\frac{\alpha_1}{\alpha_2}\right)^{\xi-1} \alpha_2^{n-1}}{\frac{1}{1-\alpha_1} + \left(\frac{\alpha_1}{\alpha_2}\right)^{\xi-1} \frac{1}{1-\alpha_2}}$$ (6-68)

The values of the chain growth probability factors α_1 and α_2 as well as the term ζ were estimated in the case of iron catalyst from the reported values by Donnelly et al. [52] and are shown in Table 36 along with the values for cobalt based catalysts that were estimated from the product selectivity obtained by Withers et al. [99].

Table 36: Hydrocarbon Products Distribution Parameters

Catalyst	α_1	α_2	ζ
Iron	0.62	0.89	7
Cobalt	0.78	0.89	13

It should be noted that in this expression, x_n represents both alkanes and α-olefins products. Few studies provide a method to estimate the ratio of α-olefins to alkanes. The data of Fontenelle and Fernandes [339] obtained with cobalt based catalyst were used to develop the following relationship between carbon number and α-olefins to alkanes ratio:

$$if\ n < 5 \qquad Rop_n = -2.68n^2 + 16.95n - 22.8$$
$$if\ n \geq 5 \qquad Rop_n = 14.69e^{-0.342n}$$

$$(6\text{-}69)$$

When using Iron catalyst, the data from Chang et al. [57] was used to develop the following correlation for the α-olefins to alkanes ratio:

$$if\ n < 5 \qquad Rop_n = -1.06n^2 + 7.18n - 6.25$$
$$if\ n \geq 5 \qquad Rop_n = -0.000115n^4 + 0.00804n^3 - 0.188n^2 + 1.40n + 1.47$$

$$(6\text{-}70)$$

6.3.4 Heat Exchanger Model

An important aspect of the F-T synthesis is its high exothermicity. The successful design of its heat exchanger is therefore a critical part in the design of an F-T reactor. The main role of the heat exchanger is to remove the heat produced by the reaction, but also to convert this "extra heat" into valuable products or commodities such as steam. The different calculations required for the design of cooling pipes needed for heat removal from a commercial large-scale SBCR are presented in the following sections.

6.3.4.1 Model Assumptions and Heat Balance

The cooling medium is pressurized water. The heat exchanger consists of a bundle of vertical parallel tubes where water is fed either from the bottom or the top. Depending of the inlet water pressure, vaporization may occur and therefore the following assumptions were made: (1) the temperatures of the liquid water and vapor phases are equal; (2) the temperature of the two-phase fluid inside the cooling tubes is uniform in the radial direction; and (3) no conduction occur in the z direction across the tubes. The properties of water and steam were estimated from Wagner et al. [340] and Yaws [252], and the size, conductivity and roughness of the cooling tubes were taken from Nayyar and Mohinder [341]. The heat balance over a finite volume of cooling tube can be written as in equation (6-71).

$$\frac{dT}{dz} + \frac{2r_o U_{heat}}{\rho C_p v r_i^2}(T - T_r) = 0 \tag{6-71}$$

U_{heat} is the overall heat transfer coefficient:

$$U_{heat} = \frac{1}{\dfrac{r_o ln\left(\frac{r_o}{r_i}\right)}{k_t} + \dfrac{1}{h_o} + \dfrac{r_o}{r_i h_i} + R_o + \dfrac{r_o}{r_i}R_i} \tag{6-72}$$

The temperature profile inside the cooling tubes can be calculated by integrating Equation (6-71) with the following boundary conditions:

$$inlet: T = T_{inlet} \tag{6-73}$$

$$outlet: \frac{dT}{dz} = 0 \tag{6-74}$$

The knowledge of the temperature profile across the cooling pipes is also required:

$$\frac{d}{dr}\left(r\frac{dT_t}{dr}\right) = 0 \tag{6-75}$$

With the boundary conditions:

$$r = r_i: \frac{1}{\dfrac{1}{h_i} + R_i}(T_t - T) = k\frac{dT_t}{dr}\Big|_{r=r_i} \tag{6-76}$$

$$r = r_o: \frac{1}{\dfrac{1}{h_o} + R_o}(T_r - T_t) = k\frac{dT_t}{dr}\Big|_{r=r_o} \tag{6-77}$$
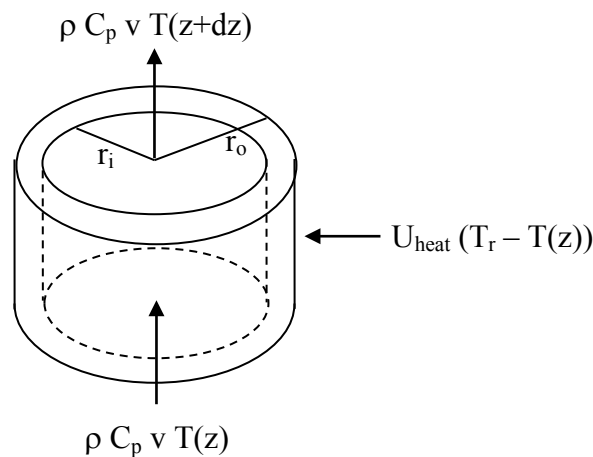
Figure 66: Finite Volume of One Cooling Tube
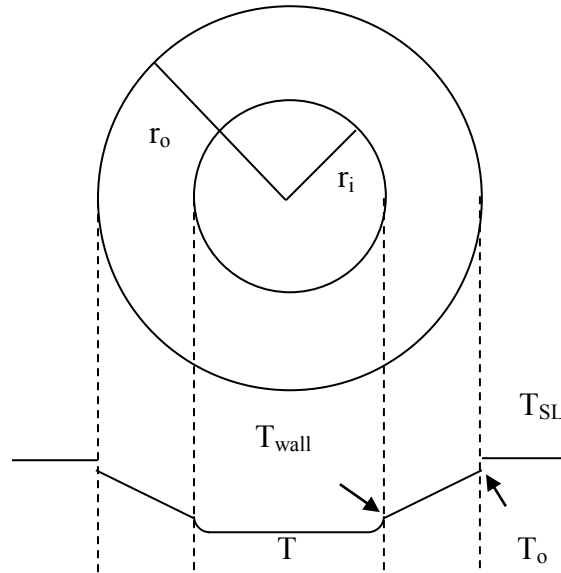
Figure 67: Temperature Profile across the Cooling Tube

6.3.4.2 Heat Transfer

To find the solutions of this set of equations and correctly design the heat exchanger, precise knowledge of all resistances to heat transfer across the cooling tubes as well as pressure drop along the tubes is required. The heat transfer coefficient for the outside of the cooling tubes was obtained from profiles computed using the developed F-T SBCR model. When a fluid such as water is flowing along a heated tube, the heat transfer and flow behavior varies with the heat flux and condition of the fluid. Three main regimes can be distinguished [342, 343]: (1) the heat flux is low and temperature of the fluid is below its boiling point, convective heat transfer takes place across the boundary layer without change of phase; (2) the heat flux is high enough for the wall temperature to rise a few degrees above boiling point, nucleate boiling takes place; and (3) at even higher heat fluxes the bubbles near the surface become closely packed until a continuous vapor film is formed on the surface. The heat transfer coefficient for the inside of the cooling tubes will therefore depend on which regime is occurring. In case of convective turbulent flow regime in closed pipes containing a fluid being heated, the Dittus and Boelter correlation [344] has been widely used. This equation is valid for the following dimensionless number ranges: $Re > 10^4$; $0.7 < Pr < 100$; $\frac{L}{d} > 60$ and only for convective heat transfer with no change of phase. Pethukov [345] developed other correlations for heat transfer in turbulent flow after conducting extensive experiments; and later Gnielinski [346] improved those equations to include

157

transitional flow regime in the range $2300 < Re < 5.10^6$ [347]. Once the temperature of boiling point is reached, water starts to vaporize and evaporative forced-flow conditions occur, the heat transfer in this case includes both a convective contribution and a nucleate boiling contribution [342]. A popular correlation for estimating the heat transfer as the sum of a convection term and a nucleation term was developed by Chen [348, 349]. More recently, Steiner and Taborek [350] used more than 13,000 data points mostly obtained with water to develop a new correlation for heat transfer in evaporative flows. Finally, the dirtiness of the cooling pipes was also accounted for by estimating fouling factors for the water-side and the slurry-side using the values from Table 37.

Table 37: Fouling Factors [351]

Fluid	R_i or R_o $(10^{-4} m^2.K/W)$
Water in Closed System	88
River Water	3.5 - 7
Heavy Fuel Oils	8.8

6.3.4.3 Pressure Drop

As mentioned above, the pressure drop is also an important parameter for designing the cooling tubes. Under forced convective boiling conditions the total pressure drop is the sum of a frictional term corresponding to the variation of the fluid kinetic energy due to the friction against the walls of the tubes and fittings such as bends and valves, a gravitational term corresponding to the change in potential energy and finally an acceleration term due to the increase in momentum when water vaporizes. The head loss due to friction in closed pipes can be expressed as:

$$\left(\frac{dP}{dz}\right)_f = \frac{2fG^2}{\rho d} \tag{6-78}$$

The frictional factor could be estimated using Haaland [352] correlation:

$$\frac{1}{\sqrt{f}} = -3.6 \, log \left(\frac{6.9}{Re} + \left(\frac{e}{3.7d}\right)^{\frac{10}{9}}\right) \tag{6-79}$$

This correlation is valid over the range: $4.10^4 < Re < 10^8$, and $0 < e/d < 0.05$. The roughness of the stainless steel cooling pipes (e) can be estimated as: $e = 0.00015$ ft [353].

In the case of evaporative flow, the frictional pressure drop in the cooling tubes must be corrected for the presence of two phases. One popular model found in the literature is the

Lockhart–Martinelli [354] method which introduce a two-phase multiplier to estimate the two-phase pressure drop based on the liquid phase pressure drop:

$$\Phi_{LO}^2 = \frac{\left(\frac{dP}{dz}\right)_{f,2\varphi}}{\left(\frac{dP}{dz}\right)_{f,L}}$$

(6-80)

$\Delta P_{f,L}$ is the frictional pressure drop when only water is flowing in the tube. The method, however, predicts pressure drop with large errors under high pressure [355]. An improvement of this model was latter developed by Armand and Treshchev [348, 356] where they considered the total mass flux (water & steam) to calculate $\left(\frac{dP}{dz}\right)_{f,L}$ term in Equation (6-80). A simpler correlation was later developed by Müller-Steinhagen and Heck [357] and was tested against existing literature correlations over a database of 9300 measurements obtained in water and several other refrigerants. It was found to be as good or better at predicting 2-phase pressure drop and was not limited to certain conditions as most of the correlations tested were.

There can also be a small increase in the frictional pressure loss due to the effective roughness of the tube surface being altered by the bubble formation under evaporative conditions. This effect, however, was found to be negligible [343] and therefore was not taken into account in the present study.

The pressure drop due to fittings can generally be expressed as:

$$\Delta P_{fit} = K_{fit} \frac{G^2}{2\rho}$$

(6-81)

The values of the coefficient K which depends on the type of fitting were taken from Welty et al. [358] and in case of two-phase flow, only the mass flux of liquid was used to estimate the pressure loss.

The pressure drop due to gravity can be estimated as a function of the void fraction [359]:

$$\left(\frac{dP}{dz}\right)_g = [\rho_L(1-\alpha) + \rho_G\alpha]g$$

(6-82)

$$\text{with } \alpha = \left[1 + 0.28\left(\frac{1-x}{x}\right)^{0.64}\left(\frac{\rho_G}{\rho_L}\right)^{0.36}\left(\frac{\mu_L}{\mu_G}\right)^{0.07}\right]^{-1}$$

(6-83)

In the case of two-phase convective boiling flows, the pressure drop resulting from the increase in momentum of the mixture as water flows through the cooling tubes and vaporizes into steam

should also be included in the total pressure drop calculations [343]. The head loss due to acceleration can be estimated by the following expression:

$$\Delta P_{acc} = \frac{G^2}{\rho} K_{acc} \tag{6-84}$$

Where K_{acc} is a function of the steam quality and void fraction and can be estimated from [359]:

$$K_{acc} = \frac{x^2}{\alpha}\left(\frac{\rho_L}{\rho_G}\right) + \frac{(1-x)^2}{(1-\alpha)} - 1 \tag{6-85}$$

Thom [343] provided direct values of the acceleration coefficient obtained from experimental data with water and steam in vertical heated tubes. From his listed values, K_{acc} was correlated as a function of steam quality and operating pressure instead of void fraction:

$$K_{acc} = \left(-28.9248 + \frac{31.7224P}{350.8551 + P}\right) \times \left(1 - (1+x)^{\left(\frac{119}{P^{0.8839}} + 1.9546\right)}\right) \tag{6-86}$$

$with\ P\ in\ Psi$

6.3.5   Numerical Solution

All differential material balance equations for all components along with the equation parameters and boundary conditions were incorporated in a simulator with a graphical user interface developed for both Windows and Mac operating systems (see Figure 68). The set of equations are numerically solved using the finite elements method (Galerkin Weighted Residual Approach [360]) with the free FORTRAN compiler g95. The equations of the heat exchanger model are solved numerically by the iterative method included in the MS Excel software.

Table 38: Heat Transfer Correlations for Fluid Flows in Vertical Tubes

Authors	Heat Transfer Correlation
Dittus and Boelter [344]	$Nu = 0.023Re^{0.8}Pr^{0.4}$
Gnielinski [346]	$Nu = \dfrac{\frac{f}{8}(Re-1000)Pr}{1 + 12.7\sqrt{\frac{f}{8}}(Pr^{2/3}-1)}$ $\qquad f = \dfrac{1}{(1.82logRe-1.64)^2}$
Chen [349]	$h_i = h_L + h_{NB}$ $\qquad h_L = 0.023Re^{0.8}Pr^{0.4}\dfrac{k_{water}}{d_i}F$ $X_{tt} = \left(\dfrac{(1-x)}{x}\right)^{0.9}\left(\dfrac{\rho_{steam}}{\rho_{water}}\right)^{0.5}\left(\dfrac{\mu_{water}}{\mu_{steam}}\right)^{0.1}$ $\qquad \begin{cases} if\ \dfrac{1}{X_{tt}} \le 0.1\ then\ F = 1 \\ if\ \dfrac{1}{X_{tt}} > 0.1\ then\ F = 2.35\left(0.213 + \dfrac{1}{X_{tt}}\right)^{0.736} \end{cases}$ $h_{NB} = 0.00122\dfrac{k_{water}^{0.79}C_{P,water}^{0.45}\rho_{water}^{0.49}}{\sigma_{water}^{0.5}\mu_{water}^{0.29}\Delta H_{vap}^{0.24}\rho_{steam}^{0.24}}\Delta T_{sat}^{0.24}\Delta P_{sat}^{0.75}S$ $Re_{TP} = F^{1.25}Re_{water}$ $\qquad S = \dfrac{1}{1 + 2.53.10^{-6}Re_{TP}^{1.17}}$ $\Delta T_{sat} = T_{wall} - T_{water}$ $\qquad \Delta P_{sat} = P_{wall} - P_{water}$
Steiner and Taborek [350]	$h_i = \left((h_L F)^3 + (h_{NB,0}F_{NB})^3\right)^{1/3}$ $\qquad q_{NB} = \dfrac{2\sigma T_{sat}h_L}{r_{nuc}\rho_G\Delta H_{vap}}$ $\begin{cases} if\ q > q_{NB}: F = \left[(1-x)^5 + 1.9x^{0.6}\left(\dfrac{\rho_{water}}{\rho_{steam}}\right)^{0.35}\right]^{1.1} \\ if\ q < q_{NB}: F = \left[(1-x)^5 + 1.9x^{0.6}(1-x)^{0.01}\left(\dfrac{\rho_{water}}{\rho_{steam}}\right)^{0.35}\right]^{-2.2} + \left[\dfrac{h_G}{h_L}x^{0.01}[1 + 8(1-x)^{0.7}]\left(\dfrac{\rho_{water}}{\rho_{steam}}\right)^{0.67}\right]^{-0.5} \end{cases}$ $F_{NB} = \left[2.816P_R^{0.45} + \left(3.4 + \dfrac{1.7}{1-P_R^7}\right)P_R^{3.7}\right] \times \left(\dfrac{q}{q_0}\right)^{0.8-0.1exp(1.75P_R)}\left(\dfrac{d_i}{d_{i,0}}\right)^{-0.4}\left(\dfrac{e}{e_0}\right)^{0.133}$ $\times\ [0.377 + 0.199ln(M_W) + 0.000028427M_W^2]$

Table 39: 2-Phase Pressure Drop Correlations

Authors	Frictional Pressure Drop Correlation
Lockhart and Martinelli [354]	$\left(\dfrac{dP}{dz}\right)_{f,2\varphi} = \Phi_{LO}^2 \left(\dfrac{dP}{dz}\right)_{f,L}$ $\left(\dfrac{dP}{dz}\right)_{f,L} = \dfrac{2fG^2(1-x)}{\rho d}$ $Re_L = \dfrac{G(1-x)d}{\mu_L}$ $\begin{cases} Re_L < 2300 & f = \dfrac{64}{Re_L} \\[2mm] Re_L > 2300 & f = \dfrac{0.079}{Re_L^{0.25}} \end{cases}$ $\Phi_{LO}^2 = 1 + \dfrac{20}{X_{tt}} + \dfrac{1}{X_{tt}^2}$ X_{tt} is the Martinelli parameter as defined in Table 38
Armand and Treshchev [356]	$\left(\dfrac{dP}{dz}\right)_{f,2\varphi} = \Phi_{LO}^2 \left(\dfrac{dP}{dz}\right)_{f,L}$ $\left(\dfrac{dP}{dz}\right)_{f,L} = \dfrac{2fG^2}{\rho d}$ $\beta = \dfrac{x}{x + (1-x)\dfrac{\rho_G}{\rho_L}}$ $R_G = \beta(0.833 + 0.05 lnP)$ with P in bar $\begin{cases} \text{If } \beta < 0.9 \begin{cases} \text{if } R_G < 0.5 & \Phi_{LO}^2 = \dfrac{(1-x)^{1.75}}{(1-R_G)^{1.2}} \\[3mm] \text{if } R_G > 0.5 & \Phi_{LO}^2 = \dfrac{0.48(1-x)^{1.75}}{(1-R_G)^{1.9+0.00148P}} \quad \text{with P in bar} \end{cases} \\[6mm] \text{If } \beta > 0.9 \quad \Phi_{LO}^2 = \dfrac{0.0025P + 0.055}{(1-\beta)^{1.75}}(1-x)^{1.75} \end{cases}$
Müller-Steinhagen and Heck [357]	$\left(\dfrac{dP}{dz}\right)_{f,2\varphi} = \left[\left(\dfrac{dP}{dz}\right)_{f,L} + 2\left(\left(\dfrac{dP}{dz}\right)_{f,G} - \left(\dfrac{dP}{dz}\right)_{f,L}\right)x\right](1-x)^{1/3} + \left(\dfrac{dP}{dz}\right)_{f,G}x^3$ $\left(\dfrac{dP}{dz}\right)_{f,L} = \dfrac{2f_L G^2}{\rho_L d}$ $\left(\dfrac{dP}{dz}\right)_{f,G} = \dfrac{2f_G G^2}{\rho_G d}$ $\begin{cases} Re_L \; ; \; Re_G < 1184 & f_L = \dfrac{64}{Re_L} \quad ; \quad f_G = \dfrac{64}{Re_G} \\[3mm] Re_L \; ; \; Re_G > 1184 & f_L = \dfrac{0.3164}{Re_L^{1/4}} \quad ; \quad f_G = \dfrac{0.3164}{Re_G^{1/4}} \end{cases}$
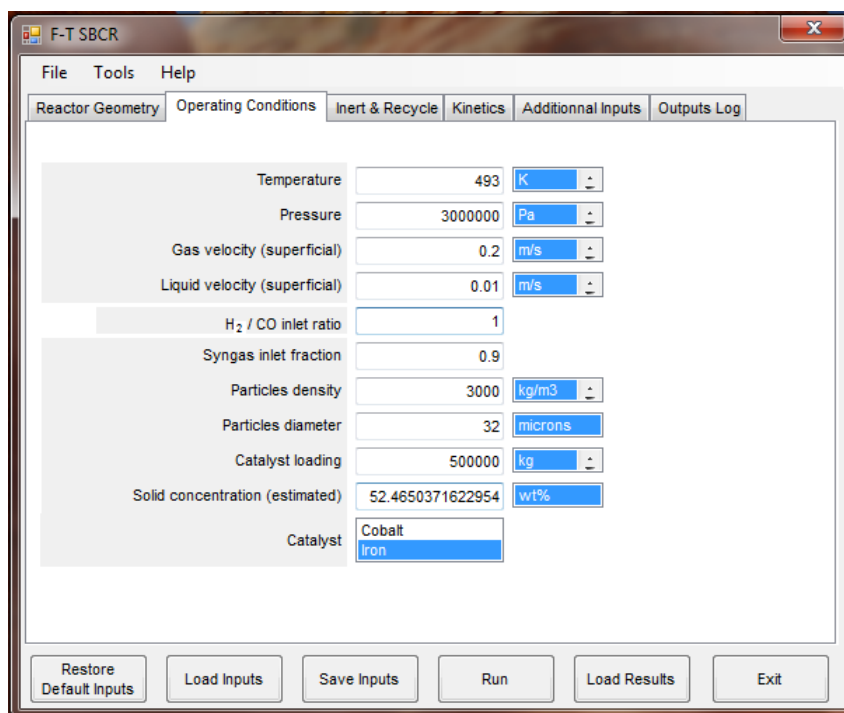
Figure 68: Graphical User Interface of the Simulator

6.4   SIMULATION OF A CONCEPTUAL COMMERCIAL-SCALE REACTOR

The purpose of this section is to use the model developed for the design of a commercial-size F-T SBCR to produce 10,000 barrel per day (bbl/day) of synthetic liquid hydrocarbons. The model will be also used to optimize the performances of such a commercial reactor.

The reaction rate expression from Yates and Satterfield [100] was chosen to describe the Fischer-Tropsch kinetics in the presence of a cobalt-based catalyst. As mentioned before, this reaction rate was developed with the reactants concentrations expressed as partial pressures. Therefore in the present model, Henry's coefficients were introduced to express the rate in terms of liquid concentrations in a similar manner to Inga and Morsi [322]. Also, the resistance to mass transfer between the liquid bulk and the catalyst active sites can be neglected due to the small size of the catalyst particles and consequently the huge surface area available for adsorption. Finally the Water-Gas-Shift reaction is neglected as water does not adsorb on the catalyst

surface. The rate of reaction for the Fischer-Tropsch synthesis over cobalt-based catalyst finally becomes:

$$r_{FT,Co} = k_{FTCo} \frac{P_{H_2} P_{CO}}{(1 + aP_{CO})^2} = k_{FT,Co} \frac{He_{H_2} C_{L,H_2} He_{CO} C_{L,CO}}{(1 + aHe_{CO} C_{L,CO})^2} \qquad (6\text{-}87)$$

$$k_{FT,Co} = k_0 e^{-\frac{E_1}{RT}} \qquad (6\text{-}88)$$

$$a = a_0 e^{-\frac{E_2}{RT}} \qquad (6\text{-}89)$$

The constants values can be found in Table 40.

Table 40: Kinetic Constants Used in the Simulations

Constant	Value	Unit
k_0	$8.037 \ 10^{-9}$	$mol/kg_{catakyst} \ Pa^2 \ s$
E_1	37,369.5	J/mol
a_0	$1.243 \ 10^{-12}$	Pa^{-1}
E_2	-68,474.1	J/mol

The reaction term in the liquid phase mass balance (see Equation (6-12)) becomes:

$$r_i = \upsilon_{FT,i} C_s r_{FT,Co} \qquad (6\text{-}90)$$

The term for the rate of heat released by the reaction (see Equation (6-25)) becomes:

$$r_{Heat} = -\Delta H_{R,FT} r_{FT,Co} \qquad (6\text{-}91)$$

It should be noted that in the following simulations, the value of the cross-flow mass exchange term in Equations (6-15) and (6-16) was set to 0. Moreover, the axial dispersion coefficient for the large gas bubbles was estimated from the correlation of Field and Davidson [332] while the dispersion coefficient of the small gas bubbles was assumed to be equal to that of the liquid phase.

The simulator was used to study the effects of different operating variables, including reactor inside diameter, reactor height, superficial gas velocity, and catalyst concentration on the performance of an SBCR operating in the churn-turbulent flow regime. The ranges of all operating variables in addition to sparger type/geometry, catalyst particle size/density, slurry superficial velocity, and cooling pipes number/size used in the simulator are given in Table 41.

The performance of the reactor was evaluated using the CO conversion, the liquid hydrocarbon yield, space time yield (STY) and catalyst productivity. The STY is defined similar to de Swart [228] as the mass of liquid hydrocarbons produced (kg) per reactor volume (m^3) per

unit time (hour). The catalyst productivity was also defined as the mass of liquid hydrocarbons produced (kg) per mass of catalyst in the reactor (kg) per unit time (hour).

The effects of reactor inside diameter (ID) and height (L) on the performances of an F-T SBCR operating at constant superficial gas velocity (U_G = 0.3 m/s) and catalyst concentration (C_S = 37.5 wt %) are shown in Figure 69. As can be seen in Figure 69-(a), CO conversion appears to increase by more than 50% with increasing reactor height from 30 to 50 m. This behavior agrees with that by de Swart [228] who reported an increase of CO conversion with increasing the height of a 7.5 m ID SBCR from 10 to 30 m. Figure 69-(a) also shows that CO conversion slightly decreases with increasing reactor ID. The effect of reactor ID and height on the hydrocarbon yield, depicted in Figure 69-(b), can be directly related to their effects on CO conversion. The increase of hydrocarbon yield with increasing reactor ID and height was expected since larger diameter and height leads to larger gas throughput and consequently greater hydrocarbon production.

Table 41: Operating Variables Used in the Simulator for F-T SBCR

System	H_2/CO (2/1) - Al_2O_3-supported cobalt-based catalyst	
	L, m	30 - 50
	d_R , m	6 - 8
Reactor and Sparger Geometry	N_O, -	1033 - 1367
	$d_{orf.}$, m	0.065 - 0.075
	Sparger type	M-ON
	T , K	500
	P , MPa	3
	U_G , m/s	0.15 - 0.45
Operating Variables	U_{SL} , m/s	0.01
	d_P , μm	42
	ρ_P , kg/m^3	3218
	C_S , wt.%	25 - 50

Figure 69 also shows the effects of reactor height and ID on the space time yield (STY) (c) and the catalyst productivity (d). As can be seen, at constant reactor length, both STY and catalyst productivity appear to slightly decrease with increasing reactor ID; whereas at constant reactor diameter, both STY and catalyst productivity appear to increase with reactor length by about 5% and then level off after a reactor height of 40 m. This can be related to the fact that the overall F-T reaction rate and accordingly the volumetric hydrocarbons production rate is expected to decrease due to the decrease of the syngas velocity, CO and H_2 partial pressures, and catalyst concentrations with the reactor height. Thus, Figure 69 leads one to conclude that in order to

produce about 10,000 bbl/day of liquid hydrocarbons, an SBCR with an internal diameter of 7 m and a height of 30 m, could be used.
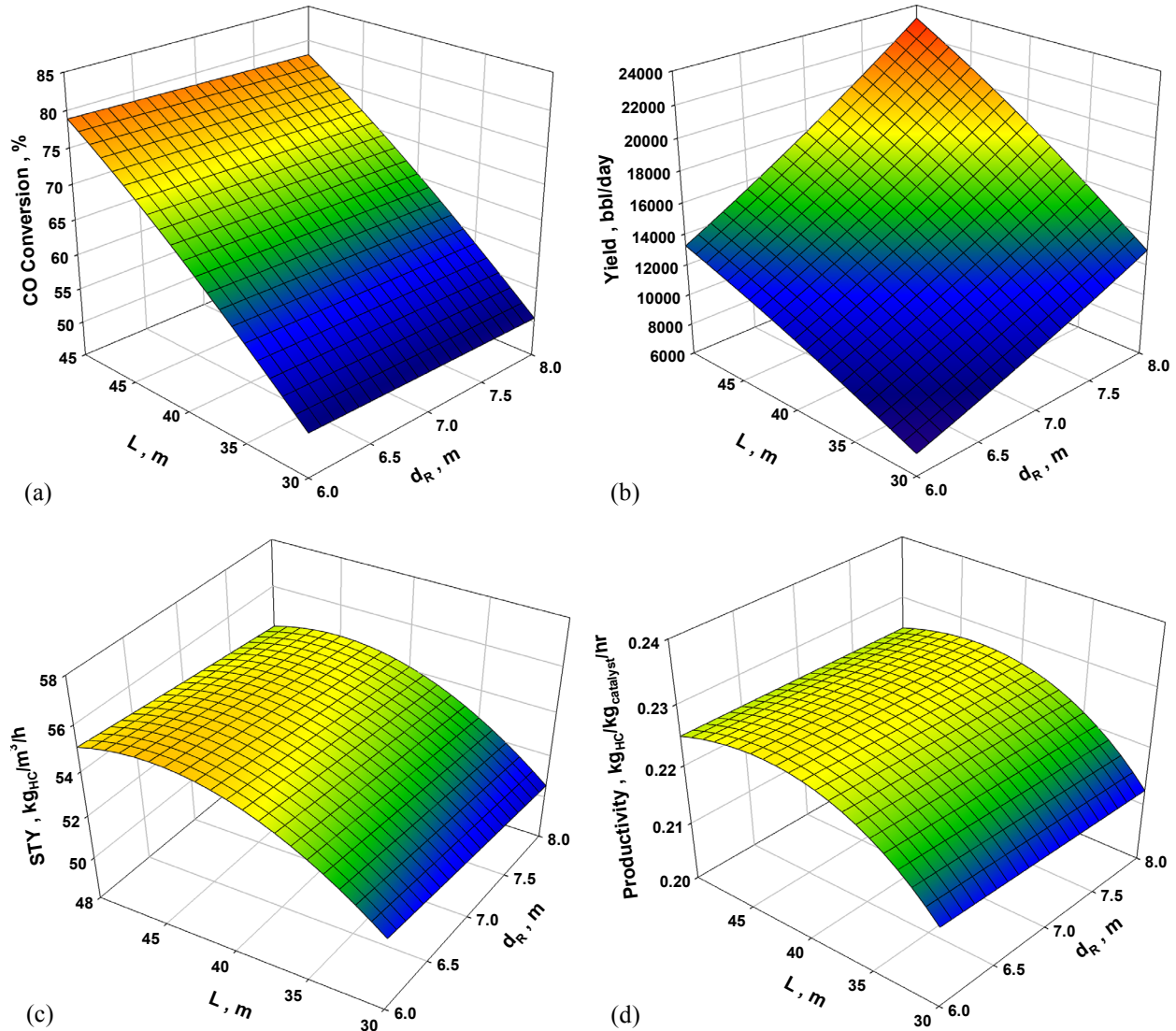
Figure 69: Effect of Reactor Geometry on the Performances of the F-T SBCR (U_G = 0.3 m/s, C_S = 37.5 wt.%)

The effects of the superficial gas velocity and catalyst concentration on the performance of an SBCR with the geometry given above (ID = 7 m and 30 m height) are illustrated in Figure 70. As can be seen in Figure 70-(a), the CO conversion decreases with increasing superficial gas velocity suggesting a small increase of the mass transfer rate compared to the decrease of the residence time of the gaseous reactants (CO and H_2) which becomes too short for converting more CO. Figure 70-(a) also shows that increasing catalyst concentration, on the other hand,

166

increases the CO conversion. For low gas velocity (~ 0.15m/s) CO conversion appears to level off at high catalyst loading. This can be attributed to the fact that increasing catalyst concentration above 40 wt.% (or 13 vol.%) decreases the mass transfer coefficients (k_La) and consequently the mass transfer rate, which drives the SBCR to operate in a mass transfer-controlled regime, leading to a maximum of CO conversion (~ 86 %). This effect of catalyst concentration on the CO conversion agrees with the findings by Inga and Morsi [322] who simulated a 4.8 m ID and 12 m height F-T SBCR using iron catalyst and reported that the syngas conversion reached a maximum and then decreased with increasing catalyst loading. It should be pointed out that few studies [34, 247] found a plateau of conversion at lower superficial gas velocities when increasing solid concentration; and other authors [228, 324, 326], who did not find a maximum of conversion when increasing catalyst concentration up to 35 vol%. This could be related to the difference in the catalyst size, density and activity as well as the absence of catalyst concentration in the mass transfer coefficients correlations used by these authors. Figure 70-(a) also shows that increasing gas velocity will shift the region of mass transfer controlled regime towards higher catalyst concentrations. Figure 70-(b) illustrates the effects on superficial gas velocity and catalyst concentration on the liquid hydrocarbon yield, and as can be observed at constant superficial gas velocity, the liquid hydrocarbon yield increases with increasing catalyst concentration, which is similar to the behavior of the CO conversion. At low catalyst concentration (< 35 wt. %), the hydrocarbon yield decreases with increasing the superficial gas velocity, whereas, for catalyst concentrations greater than 35 wt. %, the liquid hydrocarbons yield appears to increase with superficial gas velocity, reach a maximum and then decrease.

Figure 70-(c) shows the effects of catalyst concentration and superficial gas velocity on the space time yield (STY); and as expected the STY follows the same trend of the yield because the reactor volume under these conditions is constant. Figure 70-(d) illustrates the effects of catalyst concentration and superficial gas velocity on the catalyst productivity; and as can be observed the catalyst productivity reaches a maximum at catalyst concentration of 25 wt. % and superficial gas velocities between 0.2 and 0.25 m/s; and generally decreases with increasing catalyst concentration up to 40 wt. %. At catalyst concentrations > 40 wt. %, however, the catalyst productivity appears to increase with increasing the superficial gas velocity. At superficial gas velocities > 0.25 m/s, the catalyst productivity increases with catalyst concentrations, levels off, and then decreases. From these four plots, Figure 70 clearly shows that

maximum STY can be achieved using operating conditions (high catalyst loading and high superficial gas velocities) which are fundamentally different from those needed to obtain maximum catalyst productivity (low catalyst loading and average superficial gas velocities).
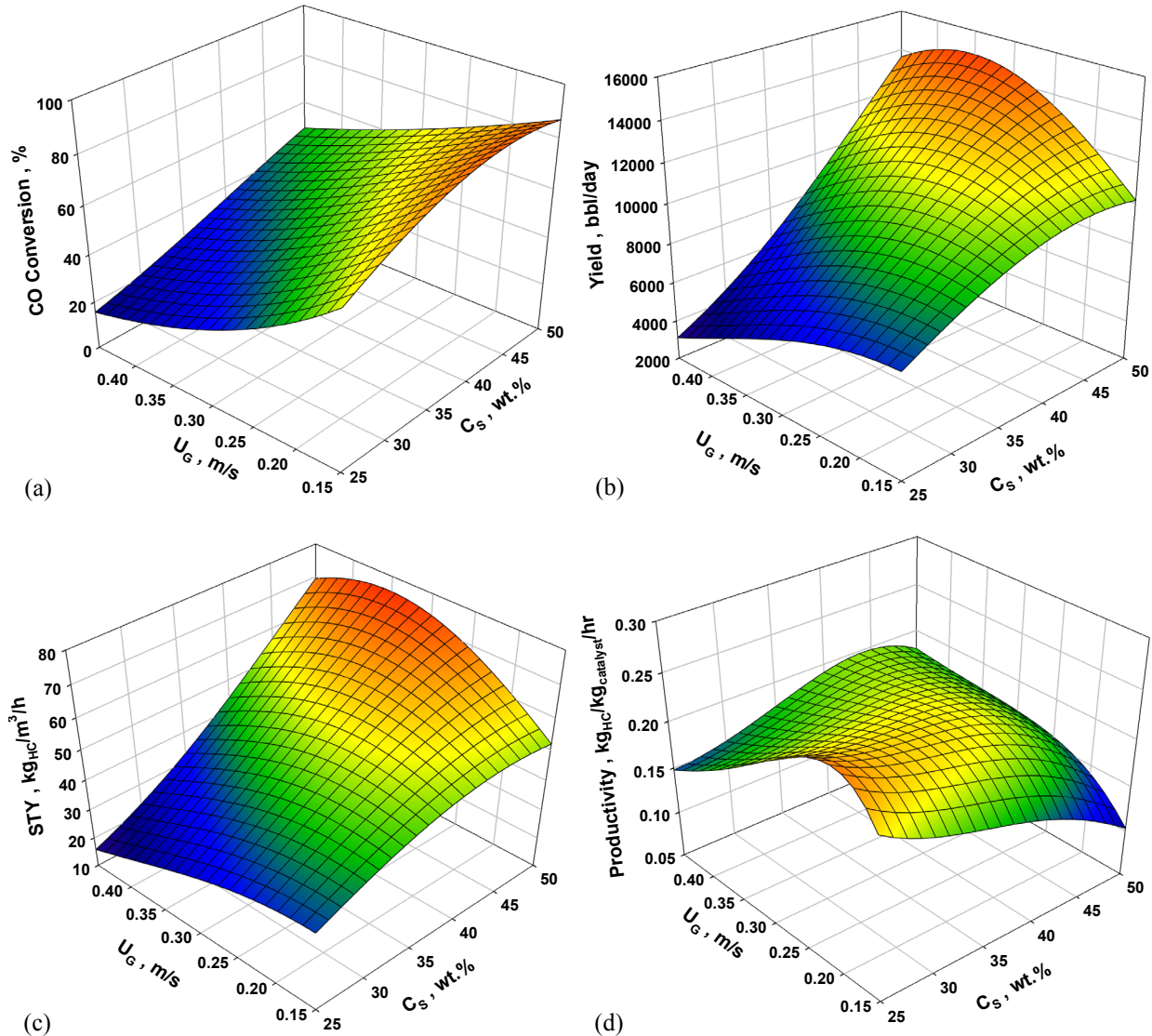
Figure 70: Effect of Superficial Gas Velocity and Catalyst Concentration on the Performances of the F-T SBCR ($d_R = 7$ m, $L = 30$ m)

Thus, Figure 70 leads to conclude that it is possible to produce a 10,000 bbl/day of liquid hydrocarbons using different operating conditions; however, since the conditions for maximum STY would require greater capital and operating costs than those for maximum catalyst productivity, the conditions corresponding to the maximum productivity should be used.

Table 42 summarizes the geometry and operating conditions of the optimized F-T SBCR with the ancillaries given in Table 41 in order to produce a 10,000 bbl/day of liquid hydrocarbons. Table 42 also shows the performance characteristic of this SBCR.

Table 42: Geometry and Operating Conditions of the Optimized F-T SBCR to Produce 10,000 bbl/day of Liquid Hydrocarbons

Variable	Units	Value
Reactor Inside Diameter (d_R)	m	7
Reactor length (L)	m	30
Superficial gas velocity (U_G)	m/s	0.255
Catalyst loading (C_S)	wt.%	37.5
CO conversion	%	60.6%
Yield	bbl/day	10,808
Space-Time-Yield (STY)	$kg_{HC}/m^3_{reactor}/hr$	55.04
Catalyst productivity	$kg_{HC}/kg_{catalyst}/hr$	0.225
Heat Produced	MW	206.5

The total heat produced by the optimized reactor amounts to 206.5 MW. This energy is potentially worth between 24.7 to 42.0 million $/y depending on the steam (pressure) it would be converted into. The reactor also produces 83 ton/h of water directly through the F-T reactions. This water ends up leaving the reactor mostly in the form of steam mixed with the unreacted syngas as well as the gaseous hydrocarbon products. This stream is generally cooled to condense and separate the hydrocarbons products and water from the volatile products such as methane gas and the unreacted syngas which can then be recycled or burned for power generation. Once the water has been separated from the condensed products and cleaned using conventional processes, it can then be used as a cooling utility. Assuming a price of 0.4 $/ton, this water represents a potential value of 0.29 million $/year minus the cost of its treatment.

Table 43: Heating & Cooling Utilities Costs and Potential Savings

	Low-Pressure Steam	13.6 $/MW [361]
Utility	High-Pressure Steam	23.2 $/MW [361]
	Water	0.4 $/ton [361]
Total Heat Produced		211.4 MW
Potential Value/Cost Savings		24.7 – 42.3 million $/year

The heat exchanger model described in section 6.3.4 was used to predict the steam quality and the heat of reaction removal efficiency with a given safety factor. It should be emphasized that the volume fraction of the pipes in the reactor should not exceed 20 vol.% since the correlations

used in the SBCR model (detailed in section 6.1.8) would not be applicable when the volume of internals exceeds 20 vol.%, and the SBCR should be operating at almost isothermal conditions. Actually, operating the SBCR under isothermal conditions in needed to avoid the wide spectrum of the products distribution which will be obtained if the reactor is not operating isothermally.

Considering the above facts, the cooling pipes (heat exchanger) should meet the following requirements: (1) the temperature change of the water (cooling fluid) should be minimum so the water can be directly recycled; (2) the temperature difference between the cooling medium and the slurry inside the reactor should be small so that assumption of uniform temperature in the reactor is valid, (3) the cross-section area occupied by cooling tubes must remain below 20 % of the reactor cross section area, and (4) the heat exchanger should be able to remove enough heat for the reactor to operate isothermally.

The heat exchanger considered is composed of a bundle of cooling pipes made of carbon steel schedule 40. Table 44 lists the maximum number of different pipes that can be used depending on their size and safety factor with the condition that its volume remain below 20 % of the reactor volume.

Table 44: Maximum Number of Cooling Pipes

Pipe Nominal Diameter	Maximum Number of Cooling Pipes	Relative Amount of Material
1"	8,785	1
1 ¼"	5,513	0.85
1 ½"	4,208	0.78
2"	2,693	0.67
2 ½"	1,838	0.72
3"	1,241	0.64
3 ½"	950	0.59
4"	751	0.55

Using the different configurations listed in Table 44, simulations were performed by varying the water inlet temperature and pressure for a fixed mass flow rate of 70 kg/m²/s. Figure 71 shows that all the configurations listed in the table are able to remove the heat from the reactor and easily reach safety factor values $\geq$ 30 %. It should be noted that in all cases, the difference in temperature between the inlet water stream and the outlet steam/water stream is less than 3 K. However, the larger the pipes size used is the smaller would be the surface area available for heat transfer and accordingly higher temperature difference between the slurry inside the reactor and the cooling water is required to efficiently remove the heat of the F-T reactions. By using 1"

pipes, maximum temperature differences between the reactor slurry and the cooling pipes (ΔT_{max}) as low as 10 K can be achieved allowing proper isothermal operation of the F-T reactor. For 4" pipes, however, the temperature difference (ΔT_{max}) above 30 K is required, which is undesirable conditions for the SBCR operation.
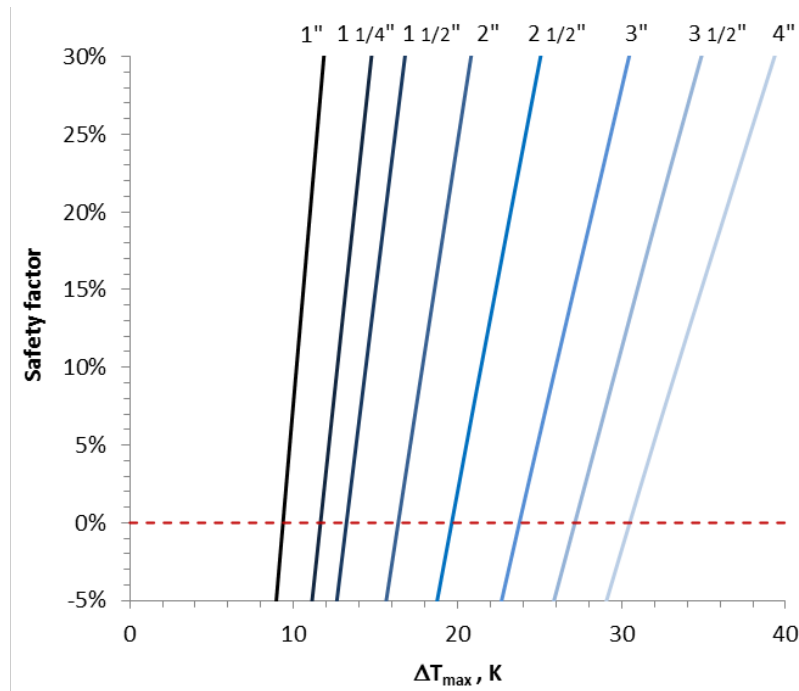
Figure 71: Effect of Pipes Size and Water-Reactor Temperature Gradient on the Performance of the Heat Exchanger

Based on the profiles shown in Figure 71 and the relative amount of materials listed in Table 44, 2" pipes appear to be a good compromise in order to minimize the temperature gradient between the slurry inside the reactor and the cooling pipes below 20 K at a relatively low cost. Indeed only 67% of the amount of material required to build the heat exchanger with 1" pipes is needed when using 2" pipes. Several simulations using 2" pipes were performed at different water flow rates and the effect water flow rate on the pressure drop, steam quality and safety factor can be seen in Figure 72. The steam quality decreases with increasing the water flow rates while both the amount of heat removed (safety factor) and the pressure drop increase. In order to minimize the steam required and stay within the domain of application of the different correlations used in the heat exchanger model, water flow rates above 150 $kg/m^2/s$ should be selected. This is because under different water inlet flow rates, the steam quality remain under 15 %; the pressure

drop values in the heat exchanger remain low (< 16 Psi) and all the heat produced by the F-T reactions is removed with a safety factor above 10 %.
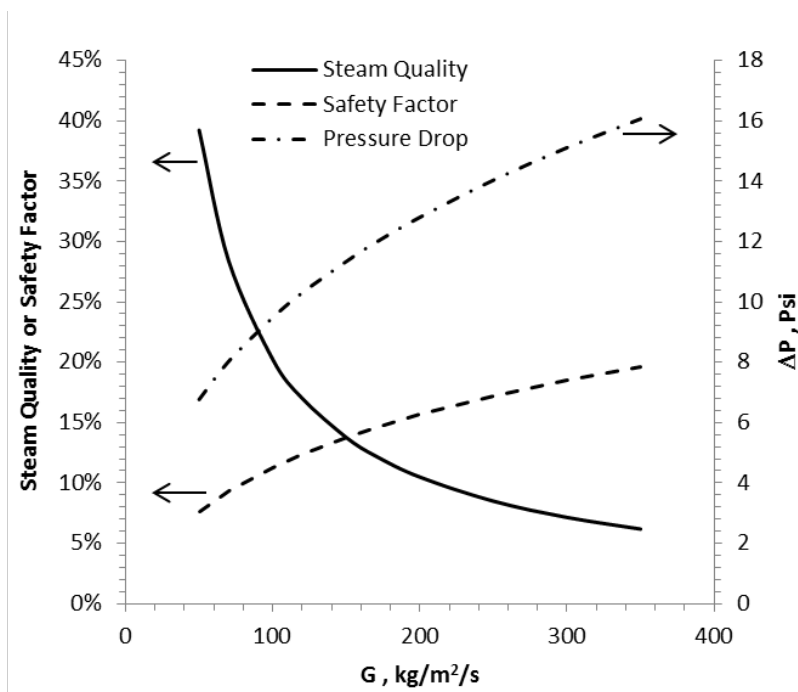
Figure 72: Safety Factor, Steam Quality and Pressure Drop across the Heat Exchanger Made of 2" pipes

6.5   COMPARATIVE SIMULATIONS OF AN F-T SBCR OVER VARIOUS CATALYSTS

The F-T SBCR performance is affected by the hydrodynamics, heat and mass transfer as well as the reaction kinetics, where the latter is strongly dependent on the type of catalyst used. There are several studies on the F-T reaction kinetics available in the literature; however, most of modeling attempts of F-T SBCRs were carried out taking into account only one kinetic rate expression. Literature data, however, showed that for the same catalyst, iron for instance, different kinetic rate expressions are available which is rather confusing for F-T SBCRs simulation.

172

The aim of this section is to investigate the effect of the different kinetic rate expressions for iron and cobalt-based catalysts available in the literature on the performance of a conceptual commercial-scale SBCR for F-T synthesis whose dimensions are similar to that of the latest large commercial F-T reactors of the Oryx GTL plant in Qatar (9-m ID and 50-m height). Also, the effects of various operating variables, such as pressure, temperature, superficial gas velocity, syngas inlet composition (H_2/CO ratio) and catalyst concentration on the performance of this conceptual commercial-scale SBCR are discussed. This large-scale SBCR was simulated using the reactor model described in sections 6.3.2 and 6.3.3.

6.5.1 Effect of Catalyst Concentration

The influence of catalyst concentration on the syngas conversions for cobalt and iron catalysts is shown in Figures 74 and 73, respectively. The three different cobalt catalysts and corresponding kinetics used led to different behaviors. When using the catalyst with high activity (van Steen and Schulz [86]), the conversion is surprisingly high (above 90%) and remains at first unaffected by the increase of catalyst concentration. Upon reaching higher catalyst concentrations the conversion starts to quickly decline. On the other hand, the catalyst by Withers et al. [99] displays low activity and over the range of catalyst concentration simulated, the conversion only increases up to 30 %, levels off and then decreases slowly with further increase of catalyst concentration. The third catalyst by Yates and Satterfield [100] exhibits a behavior in between these other two catalysts, where the conversion starts low at low solid loadings, increases with increasing catalyst concentration, reaches a maximum of 65 % and then quickly drops.

Table 45: Operating Variables Used in the Simulator for F-T SBCR

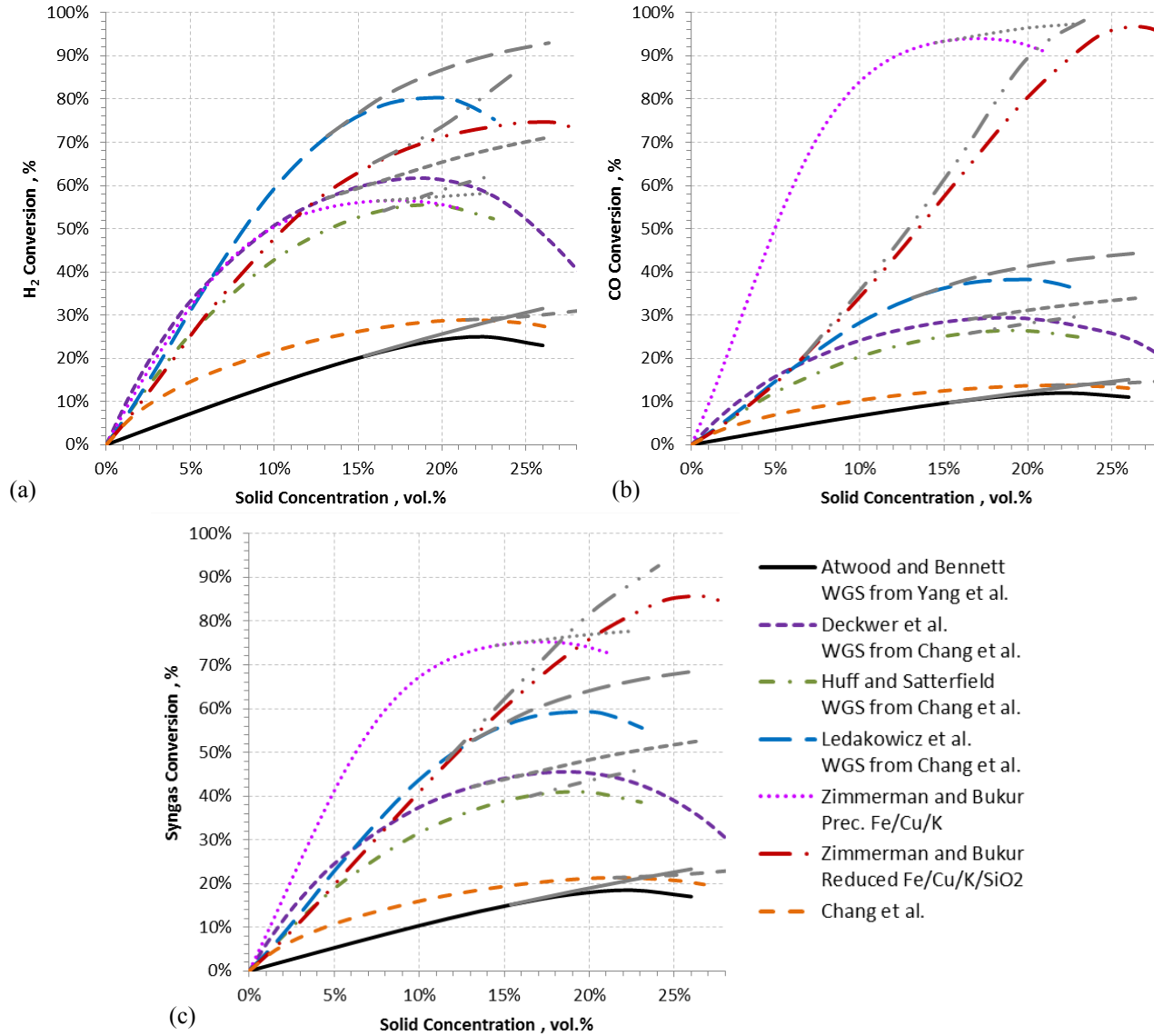| System	Catalyst	Iron or Cobalt
	H_2/CO	0 - 4
Reactor and Sparger Geometry	L, m	50
	d_R , m	9
	N_O, -	1000
	$d_{orf.}$, m	0.05
	Sparger Type	M-ON
Operating Variables	T , K	480 - 540
	P , MPa	1 - 5
	U_G , m/s	0.1-0.5
	U_{SL} , m/s	0.01
	C_S , vol.%	Up to 50

173

(a)

(b)

(c)

Figure 73: Effect of Catalyst Concentration on Conversions using Fe Catalysts

(Lighter Lines: mass transfer resistance not included in model) (H_2/CO ratio = 1, and U_G = 0.3 m/s)

174

Similar behaviors were obtained when using iron catalysts. As shown in Figure 73 for all iron catalysts/kinetics used, both CO and H_2 conversions increase more or less rapidly with increasing catalyst concentration, reach a maximum and then drop at high catalyst concentrations. Increasing catalyst concentration is supposed to raise the kinetic rate and CO and H_2 conversions, however, at high catalyst concentrations, the gas-liquid mass transfer coefficients decrease leading to the sharp drop of the syngas, H_2 and CO conversions. Thus, increasing catalyst concentration changes the SBCR operation from kinetic-controlled to mass transfer-controlled regime. This was confirmed by performing simulations in which the mass transfer resistance was made negligible by assigning an arbitrarily high value for k_La_L. The resulting syngas conversions are represented in Figures 74 and 73 by the gray lines and as can be seen, in the absence of mass transfer resistance the conversion continues to increase for all kinetics expressions considered.
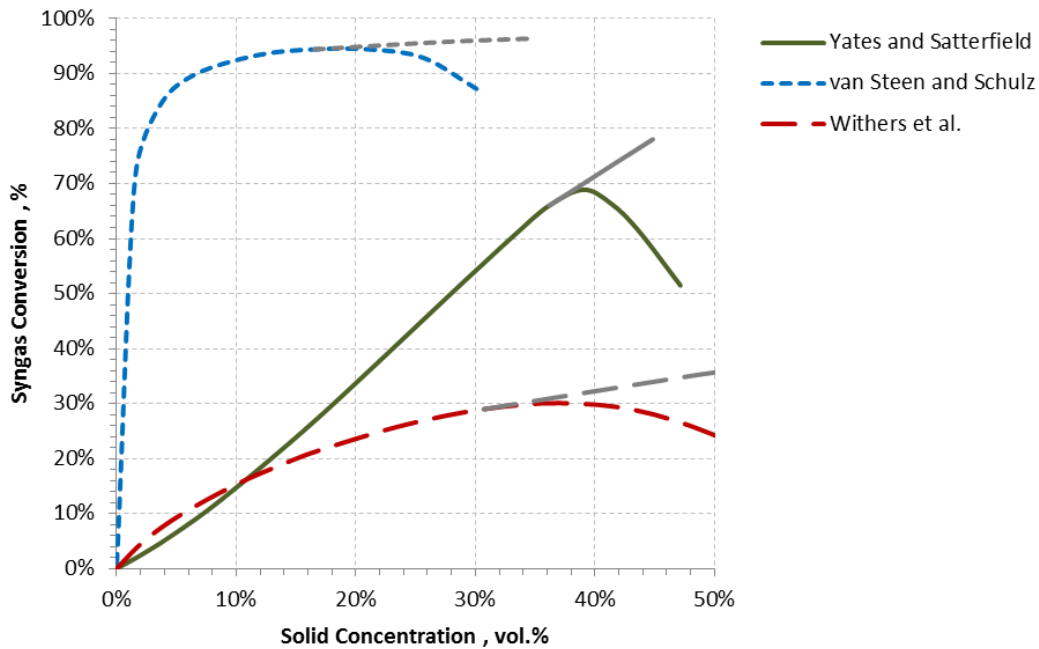

Figure 74: Influence of Solid Loading on the Conversion using Cobalt-Based Catalysts
(Lighter Lines: mass transfer resistance not included in model)

Several authors [315-317, 322] have attempted to characterize the relative importance of the gas-liquid mass transfer resistance in the overall process using Equation (6-92).

175

$$\beta_i = \frac{R_{mass\ transfer}}{R_{total}} = \frac{\dfrac{1}{k_L a_i}}{\dfrac{1}{k_L a_i} + \dfrac{1}{k_H \varepsilon_L}} \tag{6-92}$$

It should be noted that the above equation is valid assuming that the F-T reaction follows first order kinetic for H_2 with k_H representing the rate constant for hydrogen consumption. In order to include the full kinetic expressions of both the F-T and WGS reactions, Inga and Morsi [322] introduced a pseudo first-order rate constant k_i defined as:

$$k_i = \frac{C_S r_i}{C_{i,L}} \tag{6-93}$$

Using this pseudo first-order rate constant in Equation (6-92), the relative importance of the mass transfer resistance for H_2 and CO were calculated for the conditions simulated in Figures 74 and 73.

Figure 75: Influence of Solid Loading on the Relative Extent of the Mass Transfer Resistance using Cobalt-Based Catalysts (Darker Lines: CO, Lighter Lines: H_2)

The influence of catalyst concentration on the relative relevance of the mass transfer resistance (β) is illustrated in Figures 75 and 76; and as can be noticed in all cases, β values for both H_2 and CO increases with increasing catalyst concentration. It should be noted that when using cobalt-

based catalyst and H_2/CO ratio similar to the stoichiometry of the F-T synthesis, the β values for CO and H_2 are almost identical at first then deviate from each other as the catalyst concentration increases. In the case of the catalyst by Yates and Satterfield, [100] β values for CO increase above 50% for catalyst concentration above 38 vol.% indicating that the resistance due to mass transfer becomes significant and accordingly the SBCR moves from kinetics-controlled to mass transfer-controlled regime. This leads to the maximum and the subsequent decrease of the conversion shown in Figure 74. The highly active cobalt-based catalyst is also affected in a similar way. In this case, the SBCR reaches the mass transfer-controlled region leading to a drop in conversion according to Figure 74 for catalyst concentration above 20 vol.% corresponding to β values for CO and H_2 about 35%. The SBCR operated with the catalyst by Withers et al. [99] reaches the mass transfer-controlled regime at solid concentrations above 35 vol.% as can be seen in Figure 74. This corresponds to low β value for CO about 10 % as depicted in Figure 75.
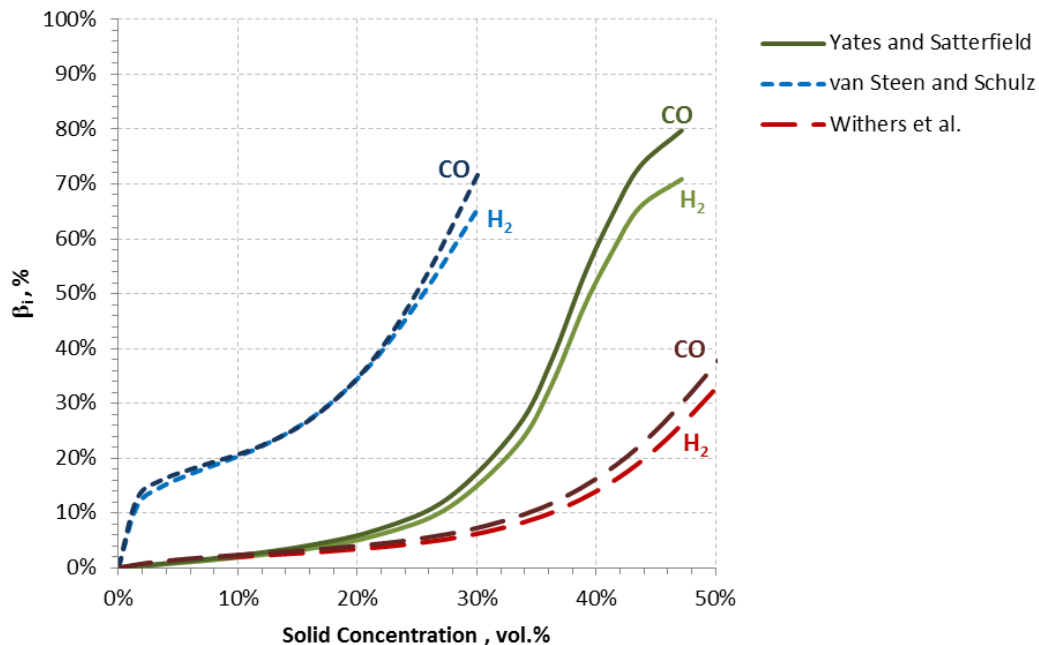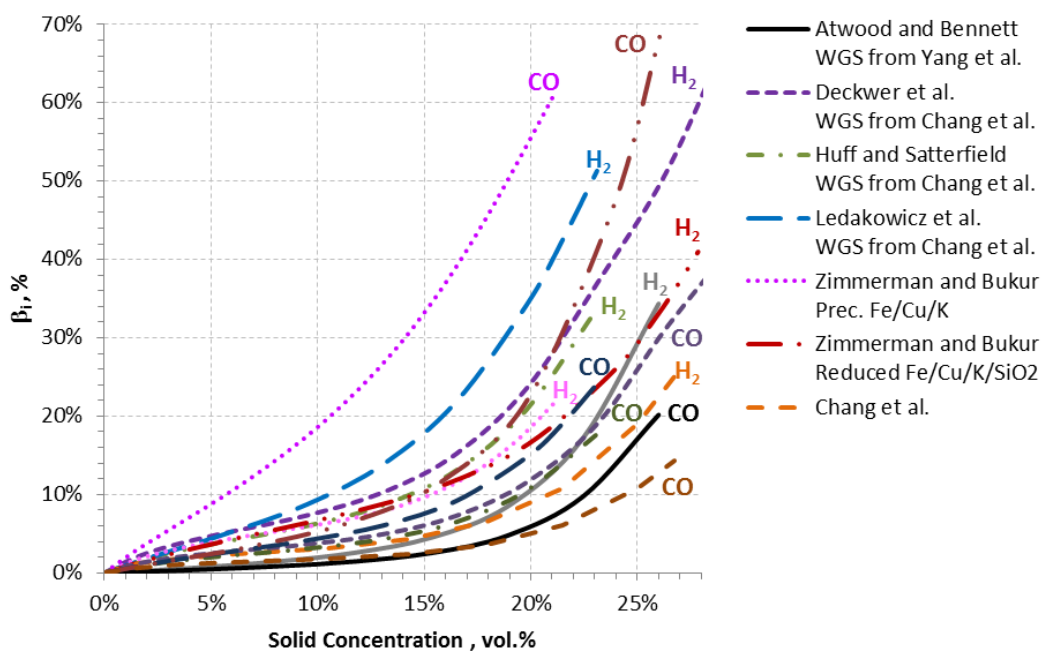

Figure 76: Influence of Solid Loading on the Relative Extent of the Mass Transfer Resistance using Iron Catalysts (darker lines: CO; lighter lines: H_2)

Similar behavior was obtained for the iron catalysts as can be observed in Figure 76. In these cases, β values for H_2 or CO range from 10% to 45% at the transition from kinetics-controlled to mass transfer-controlled regions. Therefore, there is no particular value of β which will

characterize the transition from kinetic-controlled to mass transfer-controlled region because the β value at this transition varies depending on the catalyst and kinetic rate expression used (see Table 46).). This means that Equation (6-92) cannot be used alone to predict where the transition from kinetics-controlled to mass transfer-controlled regime will take place.

Table 46: Values of the Relative Extent of the Gas-Liquid Mass Transfer Resistance at the Regimes Transition

Catalyst	F-T Rate Reference	WGS Rate Reference	Limiting Reactant	β
Reduced Nitrided Fused $Fe/K_2O/Al_2O_3/SiO_2$	Atwood and Bennett [73]	Yang et al. [64]	H_2	10%
$Fe/Cu/K/SiO_2$	Chang et al. [57]	Chang et al. [57]	H_2	18%
Reduced Prec. Fe/K	Deckwer et al.[80]	Chang et al. [57]	H_2	17%
Reduced Fused $Fe/K_2O/CaO/SiO_2$	Huff and Satterfield [76]	Chang et al. [57]	H_2	16%
Reduced Prec. Fe/K	Ledakowicz et al. [78]	Chang et al. [57]	H_2	20%
Prec. Fe/Cu/K	Zimmerman and Bukur [37]	Zimmerman and Bukur [37]	CO	45%
Reduced $Fe/Cu/K/SiO_2$	Zimmerman and Bukur [37]	Zimmerman and Bukur [37]	CO	10%
$Co/MgO/ThO_2/SiO_2$	van Steen and Schulz [86]	-	H_2 & CO	35%
$Co/Zr/SiO_2$	Withers et al. [99]	-	CO	10%
$Co/MgO/SiO_2$	Yates and Satterfield [100]	-	CO	50%

Under the same operating conditions, depending on the kinetic rate expression used, the limiting reactant varies between CO and H_2. Among the iron catalysts considered, β values are greater for CO in the case of Zimmerman and Bukur [37] kinetics expressions, while for the others iron catalysts/kinetics H_2 exhibits greater values of β. This behavior corresponds to the differences in the values of CO and H_2 conversions shown in Figure 73 due to the presence of the WGS reaction and the relative differences in the respective rates of the F-T and WGS reactions. According to reaction kinetics by Zimmerman and Bukur,[37] most of the CO is consumed rapidly by the WGS reaction to produce H_2 leading to high CO conversions above 90 % under high catalyst concentration while the rates of the WGS predicted by Chang et al. [57] and Yang et al. [64] are much lower, leading to higher H_2 conversions under the conditions used. Table 46 shows also that when using the rate of Chang et al. [57] for the WGS coupled with 4 different F-T reaction rates, the transition from kinetic-controlled to mass transfer-controlled region occurs at similar values of β for H_2 within the range 16-20. This underscores the impact of the WGS reaction on the performance of the F-T SBCR.
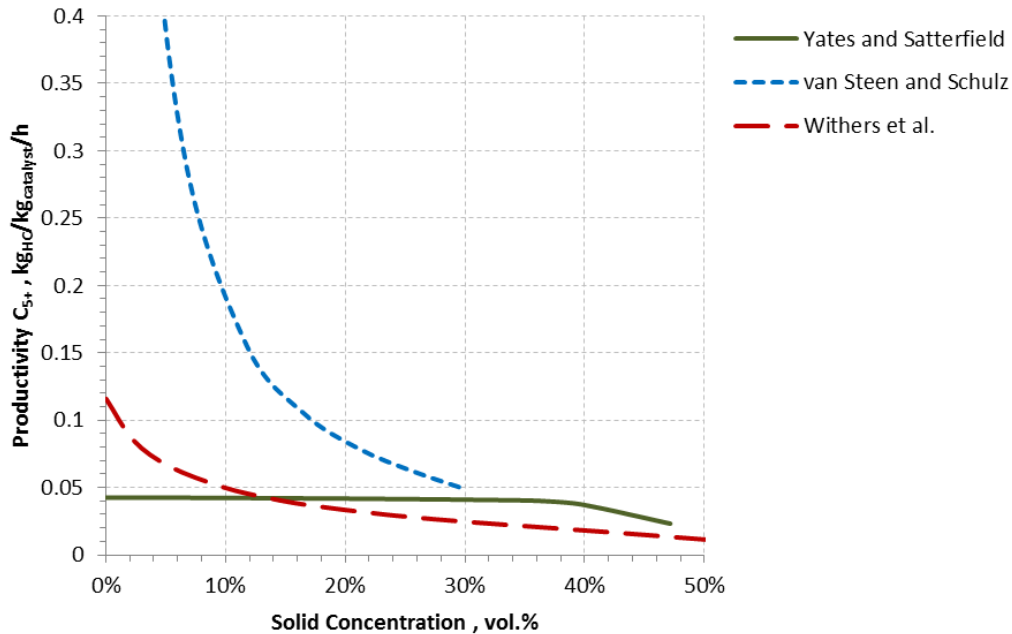
Figure 77: Influence of Solid Loading on Catalyst Productivity using Cobalt Catalyst

While increasing catalyst concentration in the F-T SBCR leads to high H_2 and CO conversions provided that the reactor is in kinetic-controlled regime, the productivity of the reactor, defined as the amount of hydrocarbons produced per mass of catalyst per unit of time, decreases as shown in Figures 77 and 78 for cobalt and iron catalyst, respectively. The productivity appears to greatly decrease with increasing catalyst concentration. However, when using the kinetic rate expressions by Yates and Satterfield [100] and Atwood and Bennett, [73] the productivity remains unaffected until the mass transfer-controlled regime is reached.

6.5.2   Effect of Inlet H_2/CO Ratio

The composition of the syngas to the F-T SBCR will vary depending on the feedstock used for its production. The gasification of biomass and/or coal for example produces syngas with low H_2/CO ratio values less or about 1, while natural gas reforming or partial oxidation provides syngas with significantly higher H_2/CO ratio values (≈ 2). The syngas from biomass and/or coal may be shifted in a dedicated WGS unit prior to the F-T SBCR in order to increase the H_2/CO ratio.
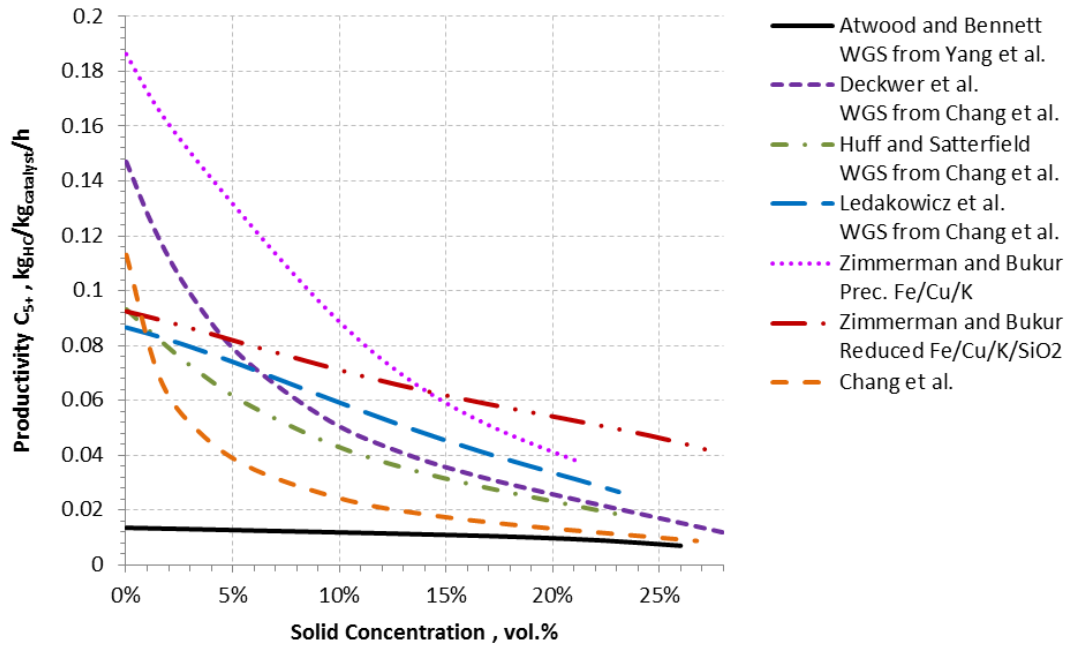
Figure 78: Influence of Solid Loading on Catalyst Productivity using Iron Catalyst

Figure 79 shows the effect of the inlet H_2/CO ratio on the syngas conversions. As can be seen higher H_2/CO ratios increase the CO conversion for all the kinetic rate expressions used. The H_2 conversion, however, follows different trends as it decreases when using the kinetic rate expressions by van Steen and Schulz, [86] increases in the case of Yates and Satterfield, [100] while for Withers et al. [99] it increases sharply at low H_2/CO ratios before decreasing. These behaviors result in a maximum syngas (H_2 + CO) conversion at an inlet H_2/CO ratio of 2, except when using the kinetics by Yates and Satterfield [100] where the syngas conversion appears to always increase with H_2/CO ratios. Iliuta et al. [303] reported an identical behavior to this latter one when simulating an F-T SBCR with cobalt catalyst over a range of H_2/CO inlet ratio values from 1.4 to 2.2. When using iron catalysts, the F-T SBCR was found to behave similarly for all the kinetic rate expressions used. Figure 80 shows that CO conversion always increases with increasing H_2/CO ratios in the feed gas, whereas H_2 conversion increases sharply at low inlet H_2/CO ratios and then decreases or levels off. Again, this behavior is in agreement with the findings of Iliuta et al. [303] for an iron catalyst. The maximum syngas conversion occurs at different H_2/CO ratios varying from 0.8 to 3 depending on the kinetic rate expression used. The maximum syngas conversion occurring at an inlet ratio of 0.8 in the case of precipitated iron catalyst by Zimmerman and Bukur[37] agrees well with experimental data obtained by Deckwer et al. [362]

180

and Kuo [318] as well as with simulations carried out by Stern et al. [308] and Bukur and Zimmerman.[302] No maximum is reached using the kinetics rate expressions by Zimmerman and Bukur [37] for their reduced catalyst as well as the F-T kinetics by Ledakowicz et al. [78] coupled with WGS kinetics by Chang et al.[57] It is important to note that all the kinetic rate expressions considered in this study except that by Zimmerman and Bukur [37] for precipitated catalyst, predict better SBCR performances for both catalysts at inlet H_2/CO ratios of 2 or above.
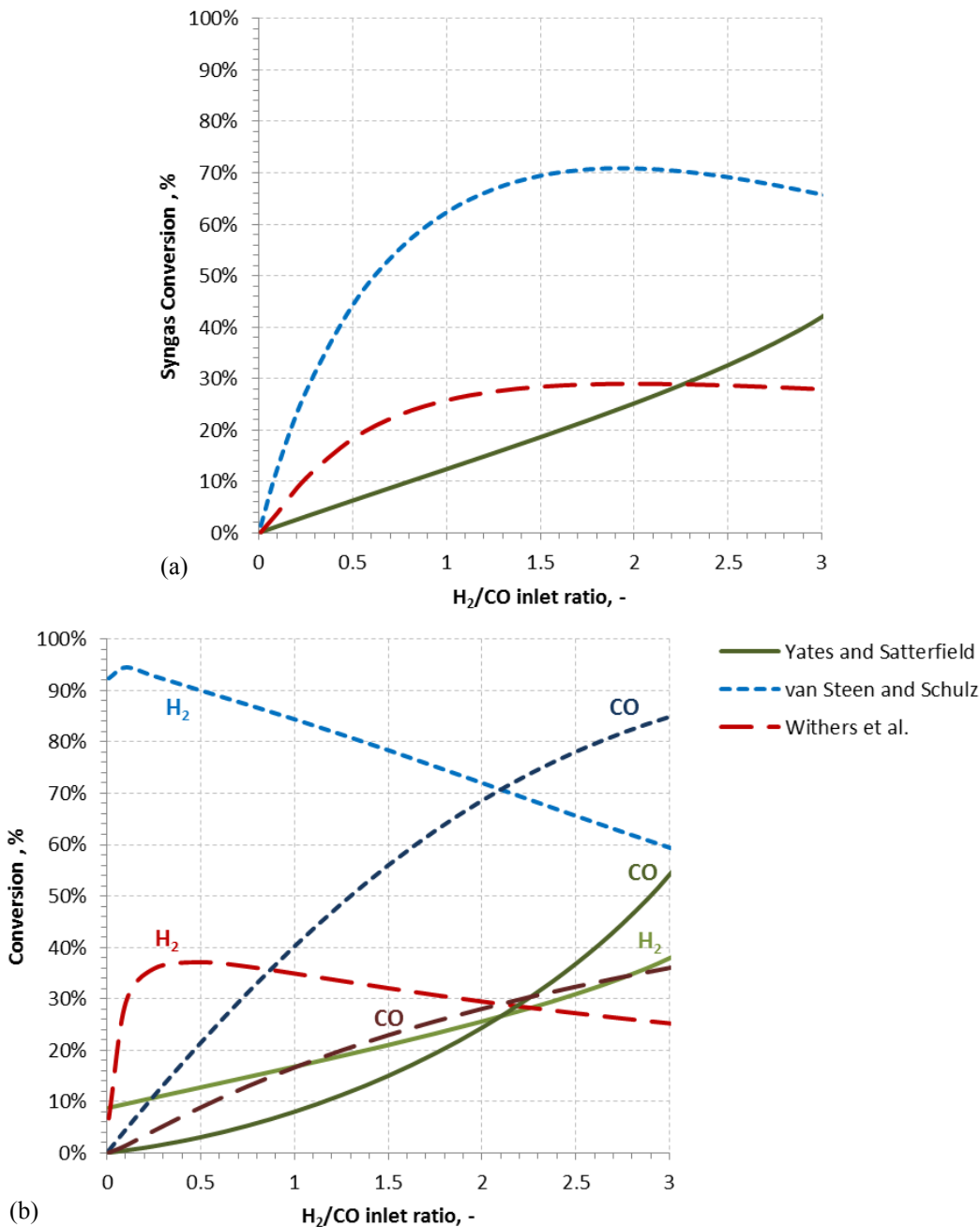
Figure 79: Effect of Inlet H_2/CO Ratio on Syngas Conversion in the Presence of Co Catalyst

181
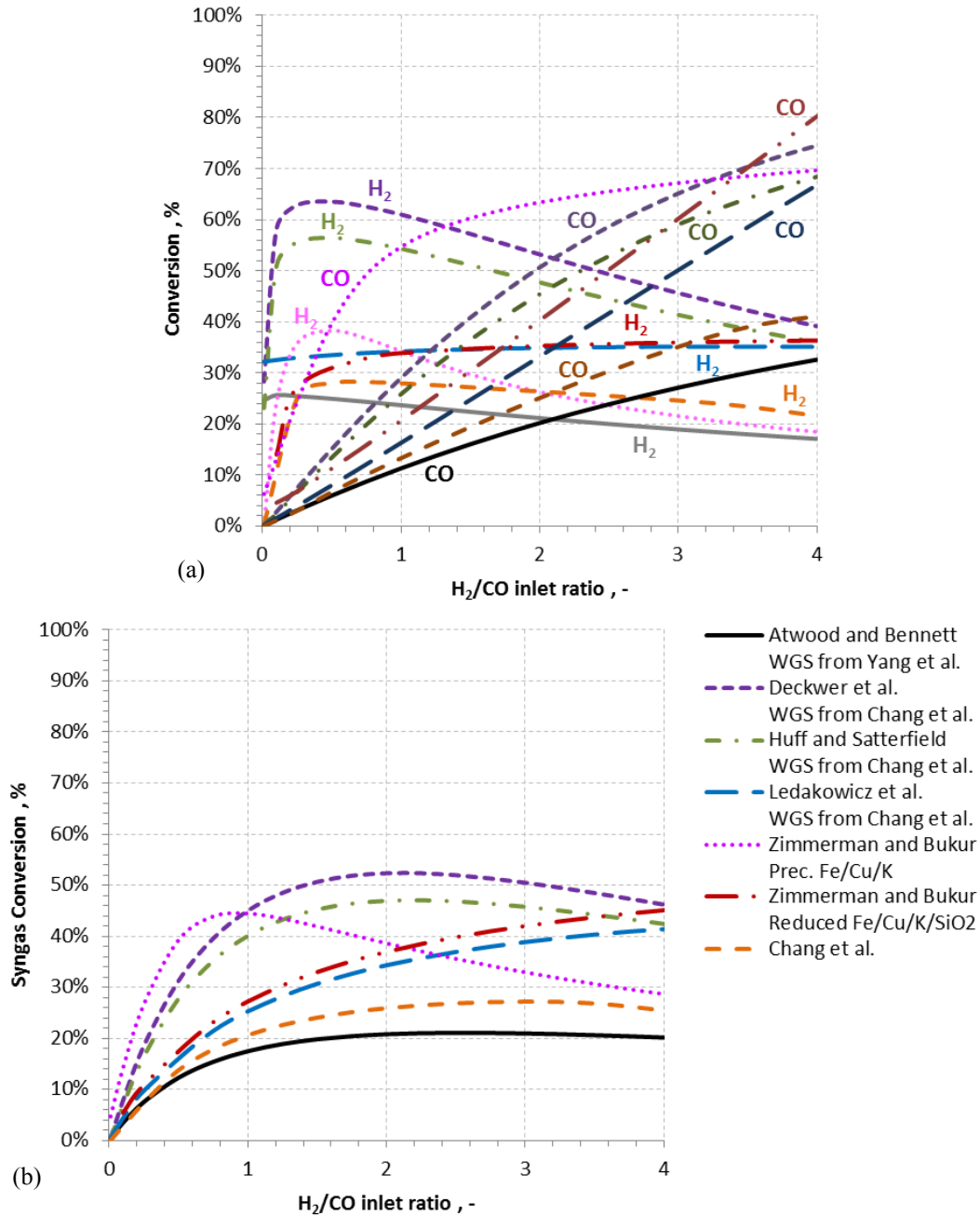
Figure 80: Effect of Inlet H_2/CO Ratio on Syngas Conversion in the Presence of Fe Catalyst ($U_G = 0.3$ m/s)

Figure 81, however, shows that when using the kinetic expression by Chang et al. [57] a maximum conversion occurs at a H_2/CO ratio of 3. It should be mentioned that increasing the H_2/CO ratio above 1 appears to increase the production of lighter distillates, such as CH_4 and other gases and the selectivity of heavier and more valuable products, such as wax greatly decreases at H_2/CO ratios greater than 2. The selectivity of diesel and wax products appears to

peak at a H_2/CO ratio of 1.5. This behavior can be attributed to the higher hydrogen concentration present in the liquid bulk at high H_2/CO ratios, which increases the termination of the adsorbed olefins and subsequently decreases the chain growth probability. These results are similar to those by Wang et al. [309] whose simulations predicted an increase of lighter distillates and a decrease of heavier distillates products with increasing H_2/CO ratio in the inlet feed with an optimum gasoline and diesel products selectivity for H_2/CO ratios between 1 to 1.5. van der Laan et al. [34] also reported that increasing the H_2/CO ratio in the feed increased the selectivity of CH_4 and light gases and decreased the selectivity of the diesel-wax fraction when simulating an F-T SBCR over an iron catalyst.
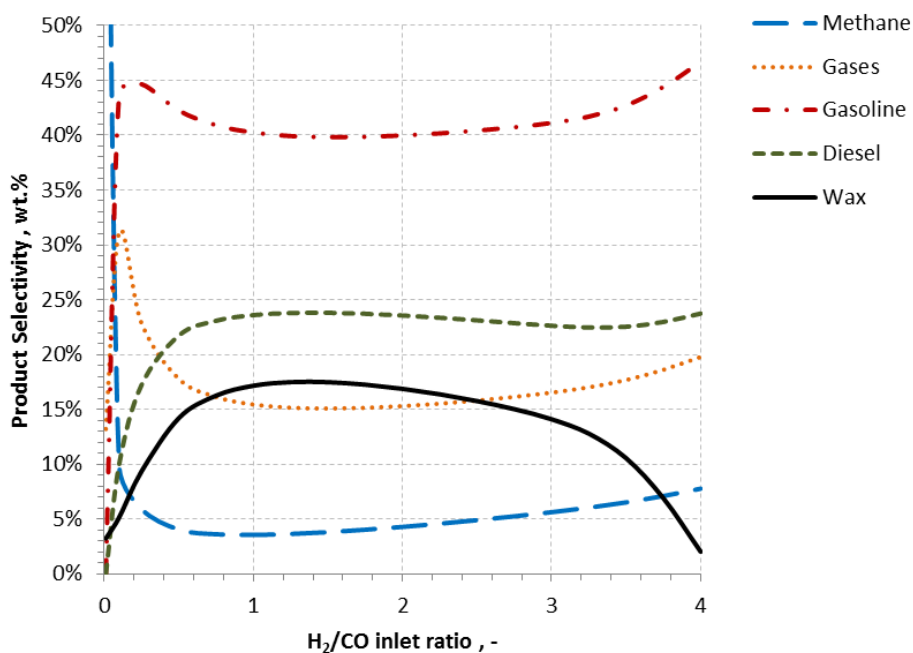
Figure 81: Effect of Inlet H_2/CO Ratio on Product Selectivity in the case of Chang et al [57] kinetics (Fe Catalyst)

6.5.3   Effect of Superficial Gas Velocity

The effect of the superficial gas velocity on the syngas conversion and the hydrocarbons space time yield (STY), expressed in kg of hydrocarbons produced per unit reactor volume per unit time, is presented in Figures 82 through 85. As can be observed in these figures, increasing the

superficial gas velocity decreases the syngas conversion and increases the STY for all the catalysts and kinetic rate expressions used. Under the operating conditions employed in the simulation, the smallest superficial gas velocities lead to the highest syngas conversion due primarily to the long residence time of the gaseous reactants in the reactor; whereas the highest superficial gas velocities give the greatest STY. The STY, however, is improved by about 50 % up to 200 % when increasing the superficial gas velocity from 0.15 m/s to 0.45 m/s. It can also be observed that the kinetic rate expressions by Yates and Satterfield, [100] Atwood and Bennett [73] as well as by Zimmerman and Bukur [37] for their reduced catalyst, lead to a decrease of the syngas conversion and no improvements in STY with increasing the superficial gas velocity. Figure 86 shows that when using the kinetic rate expression by Chang et al.,[57] increasing the superficial gas velocity decreases the selectivity of lighter hydrocarbon distillates, such as CH_4, gases and gasoline while the selectivity of heavier hydrocarbons, such as diesel and wax is increased. Thus, the choice of an optimal superficial gas velocity for a commercial-scale F-T SBCR should be made considering higher throughputs of the valuable products versus lower syngas conversion and high operating costs associated with running the SBCR at high superficial gas velocities.
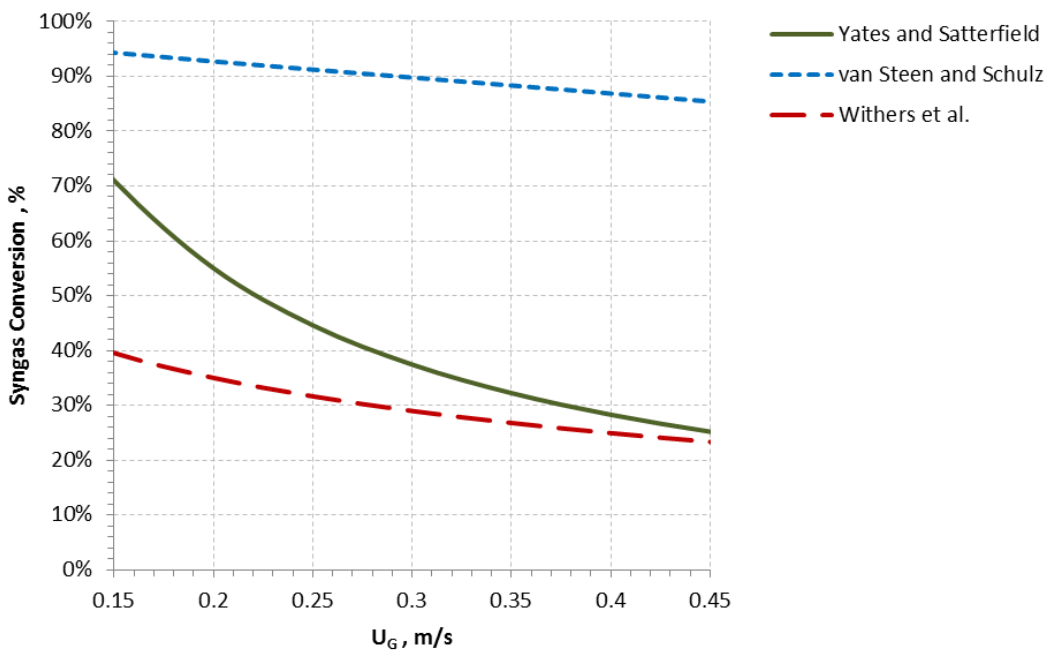
Figure 82: Effect of Superficial Gas Velocity on Syngas Conversion using Cobalt Catalyst
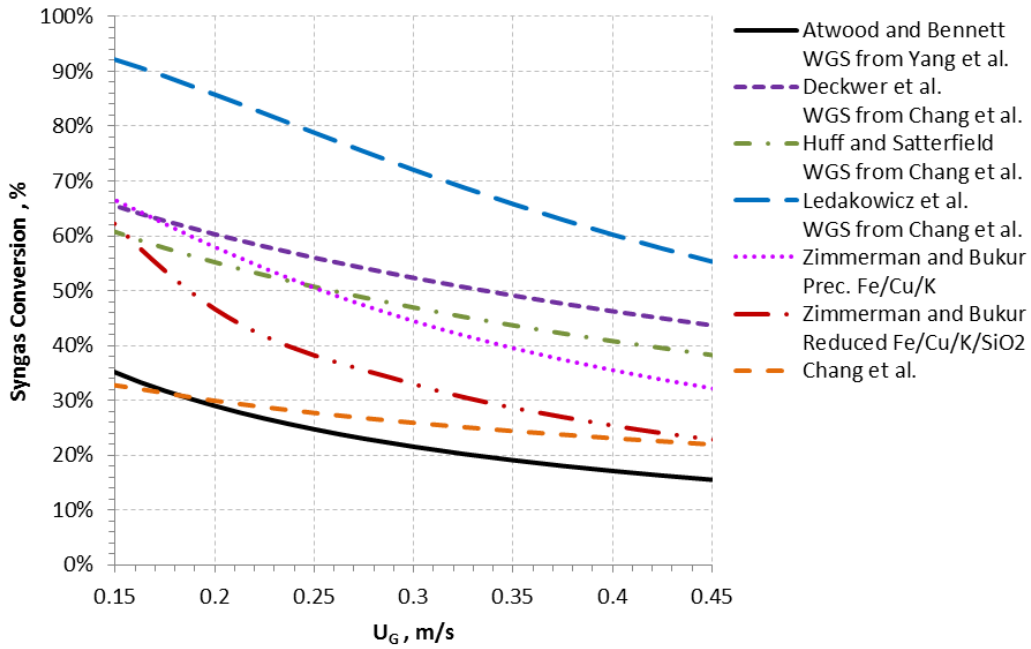
Figure 83: Effect of Superficial Gas Velocity on Syngas Conversion using Iron Catalyst
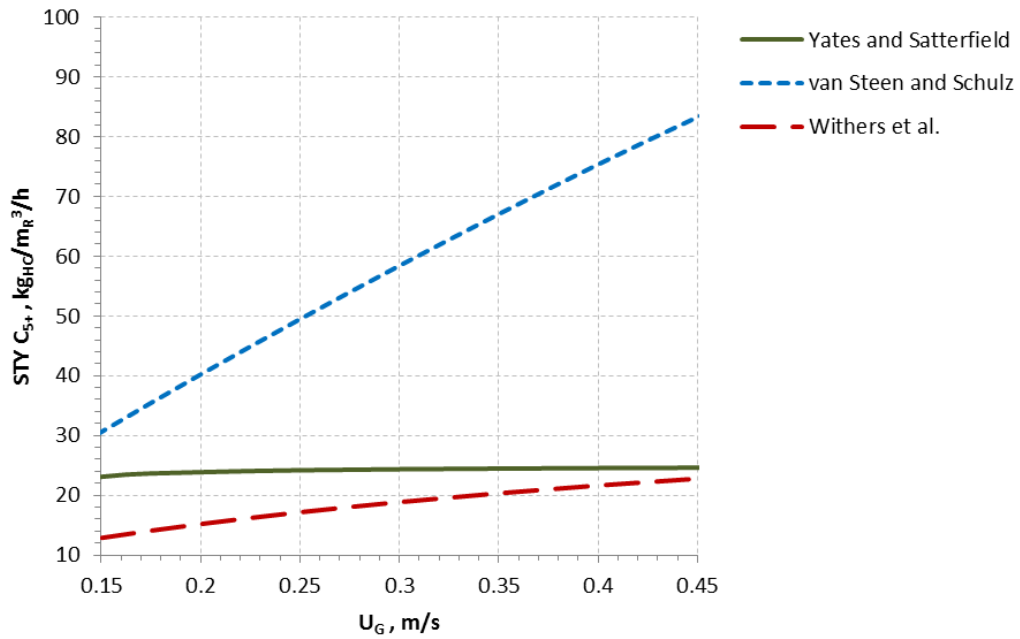
Figure 84: Effect of Superficial Gas Velocity on STY using Cobalt Catalyst

185
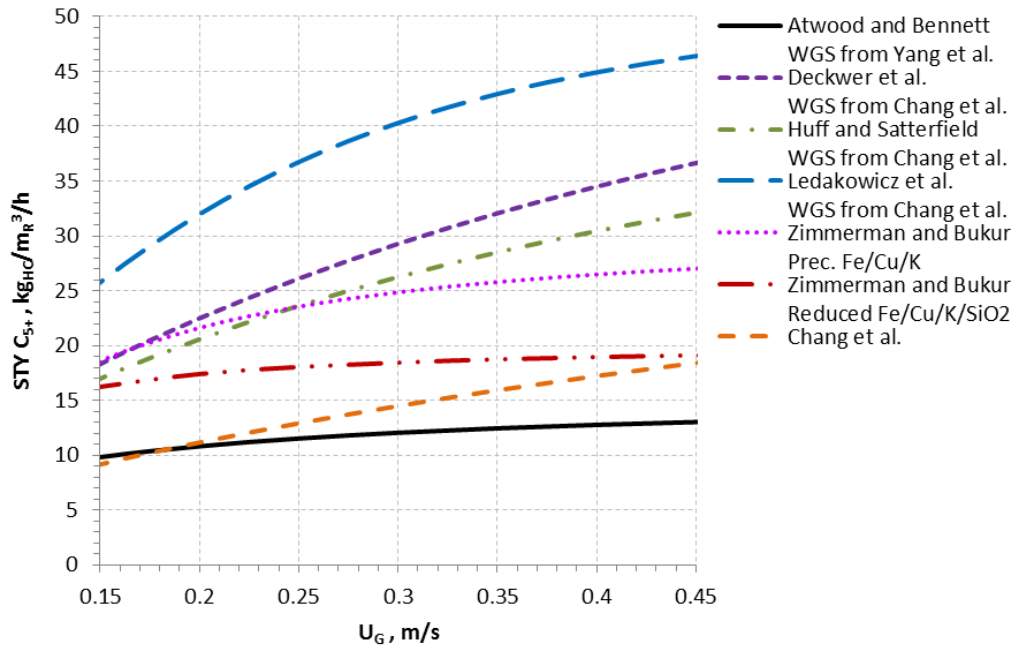
Figure 85: Effect of Superficial Gas Velocity on STY using Iron Catalyst
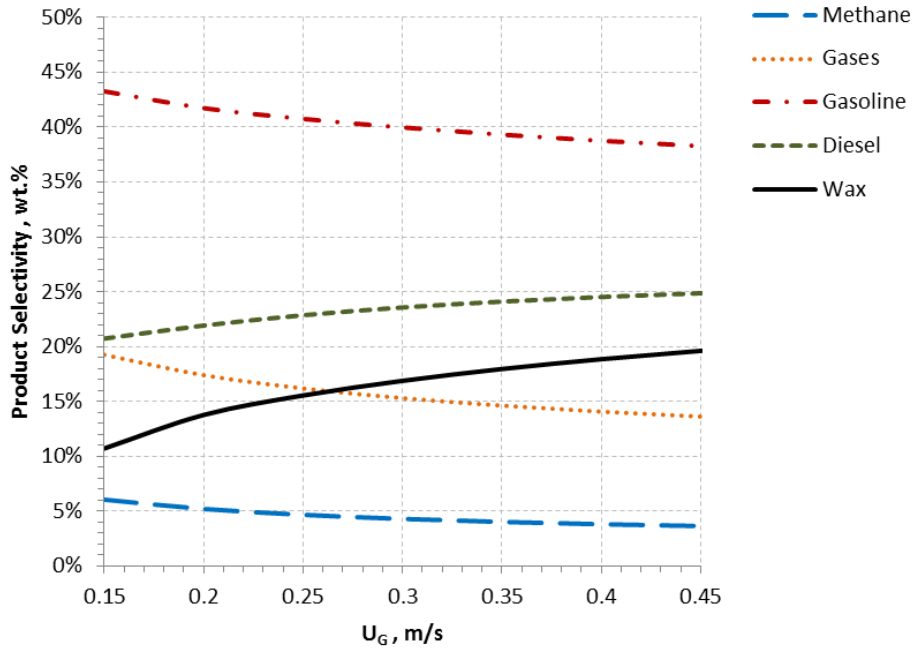
Figure 86: Effect of Superficial Gas Velocity on Product Selectivity in the case of Chang et al [57] kinetics (Fe Catalyst)

186

6.5.4 Effect of Temperature

The effect of operating temperature on the F-T SBCR performance can be seen in Figures 18 through 89, which show that increasing the reactor temperature increases the rate of CO and H_2 consumption and leads in all cases investigated to higher syngas conversions. Running the SBCR at high temperatures, however, produces large quantities of gaseous products and significantly decreases the throughput of valuables heavy product which is illustrated in Figure 89. For instance, when using the kinetic rate expression by Chang et al. [57] in the temperature range from 480 to 540 K, the selectivities for gases and gasoline cuts increases from 40 to 400 % while the selectivities for diesel and wax cuts drops by 30 and 63 %, respectively.
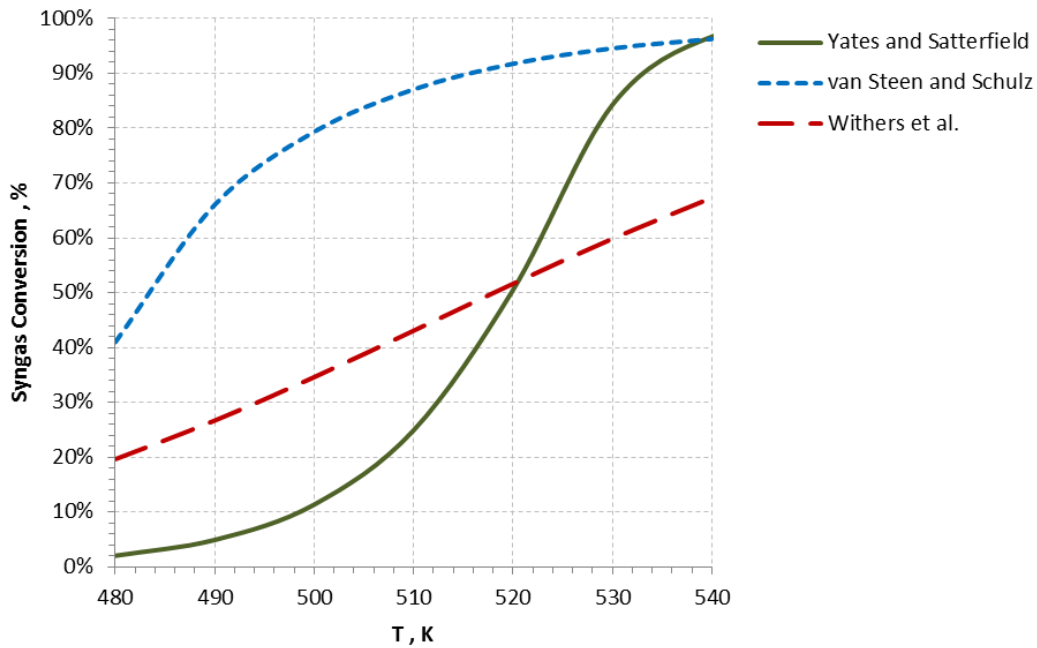
Figure 87: Effect of Temperature on Syngas Conversion

Figure 88: Effect of Temperature on Syngas Conversion
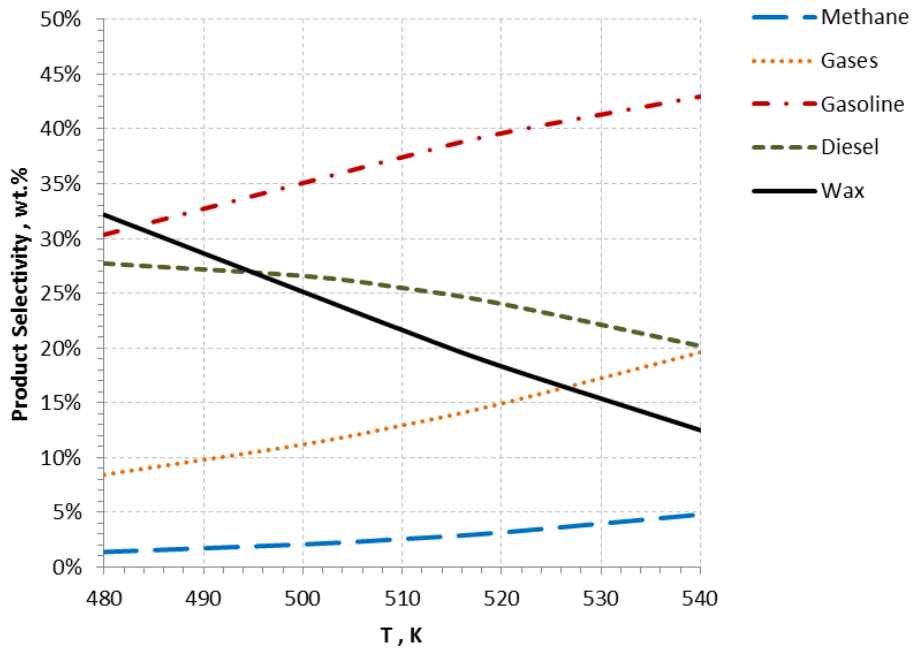
Figure 89: Effect of Temperature on Product Selectivity in the case of Chang et al [57] kinetics (Fe Catalyst)

6.5.5 Effect of Pressure

The effect of pressure on the performance of the SBCR is illustrated in Figures 90 and 91; and as can be observed depending on the catalyst and kinetic rate expression used, the behavior of the SBCR reacts differently to the increase of the operating pressure. The syngas conversion appears to decrease as with the kinetic rate expressions by Yates and Satterfield [100] and Zimmerman and Bukur [37] for cobalt and iron catalysts, respectively. The syngas conversion, on the other hand, appears to increase as with the other kinetics expression for cobalt catalysts and the kinetic rate expressions by Deckwer et al. [80] and Huff and Satterfield [76] for iron catalysts. In the case of the other kinetics expressions for iron catalysts, the syngas conversion remains unaffected by the operating pressure. When using the kinetic rate expression by Chang et al.,[57] a maximum syngas conversion is reached for an operating pressure of 25 bar. Also, the selectivities of diesel and wax cuts increases by increasing the operating pressure as can be seen in Figure 92. The selectivities of CH_4 and light cuts, however, decrease and the gasoline selectivity displays a maximum about 22 bar. Similar behavior of the product selectivities was reported by Wang et al [309] for their simulated F-T SBCR over iron catalyst.

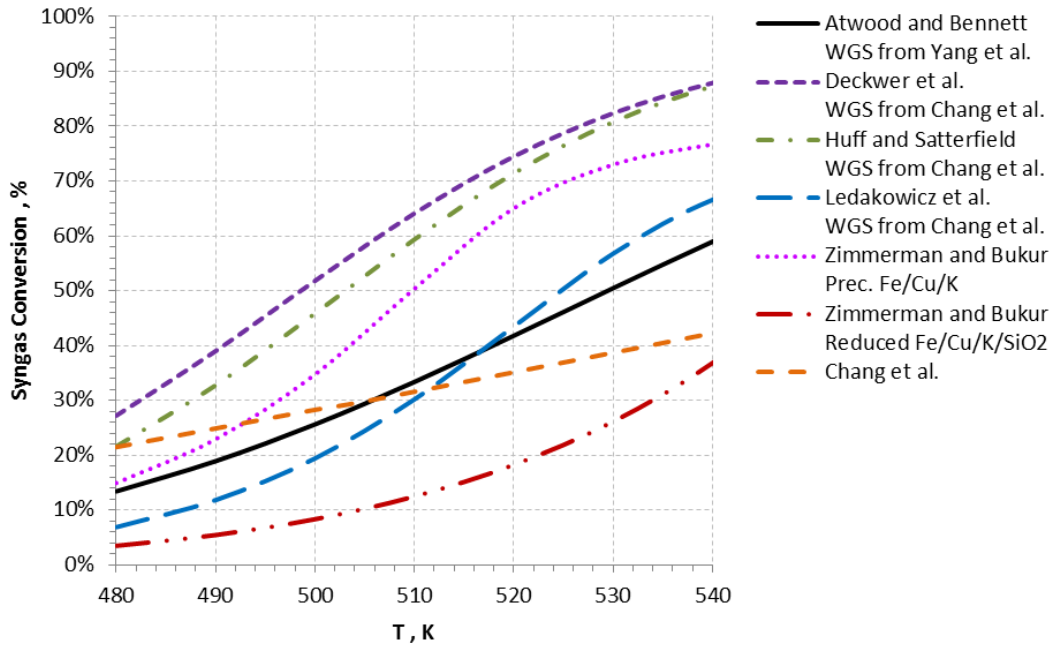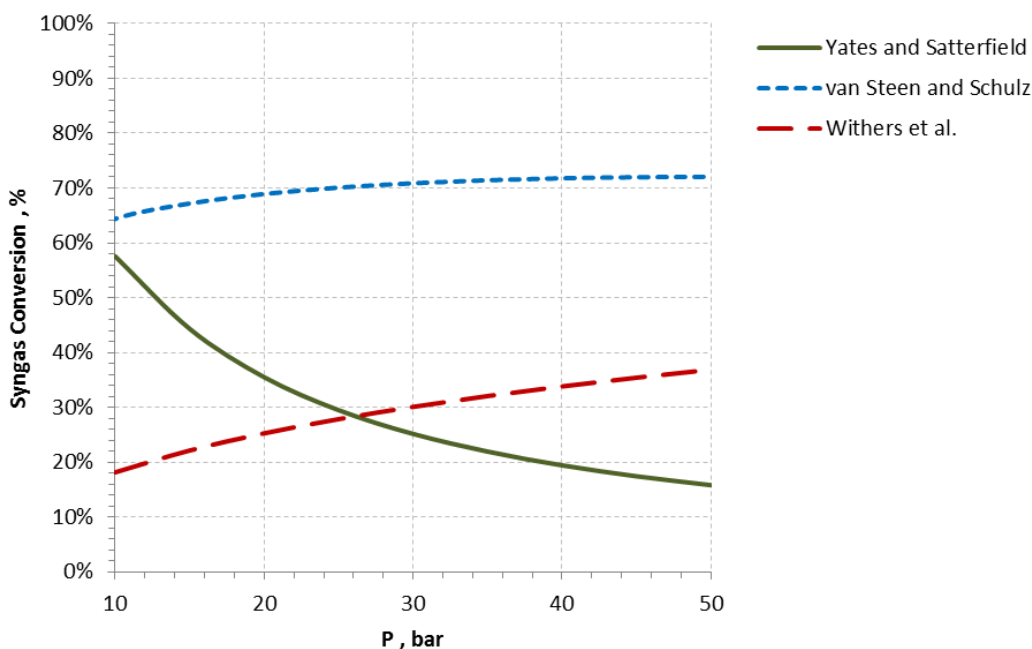
Figure 90: Effect of Pressure on Syngas Conversion
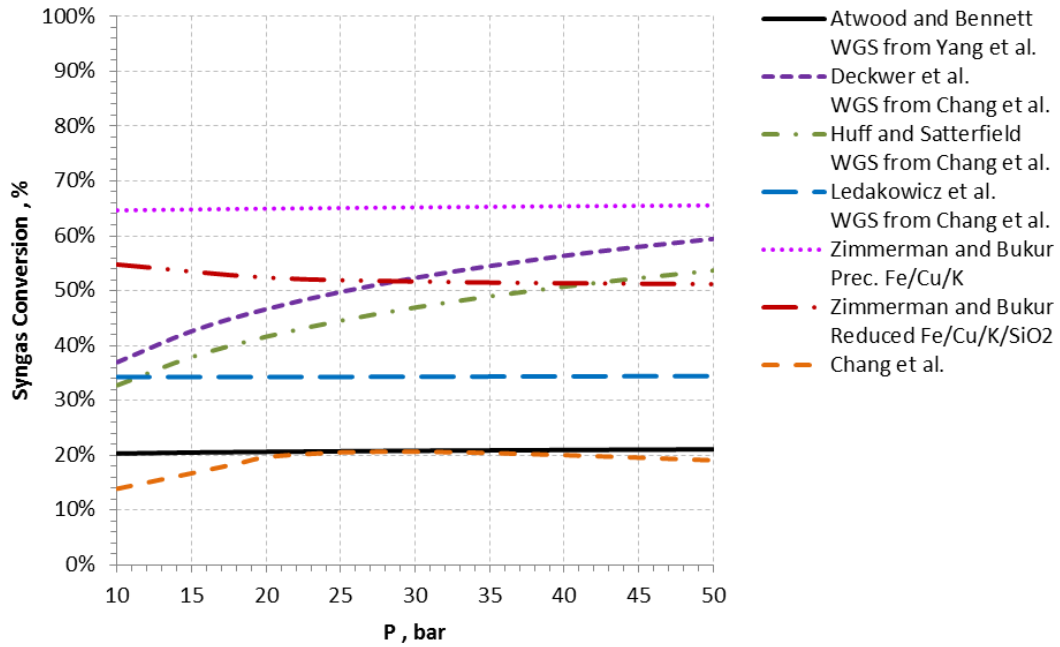
Figure 91: Effect of Pressure on Syngas Conversion
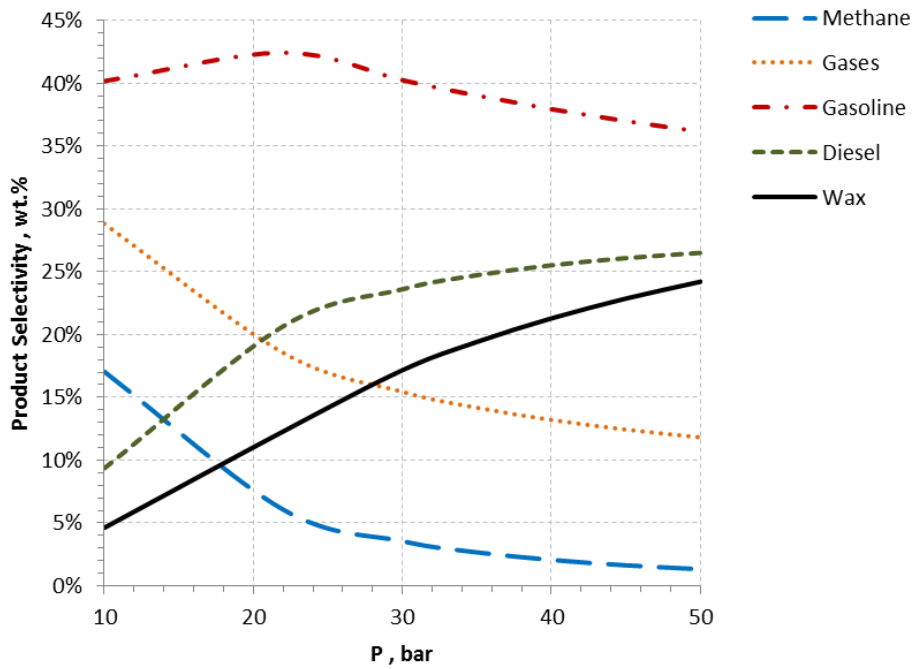
Figure 92: Effect of Pressure on Product Selectivity in the case of Chang et al [57] kinetics (Fe Catalyst)

7.0   CONCLUSIONS

The volumetric mass transfer coefficients, the gas holdup, the Sauter mean bubble diameter and bubble size distribution profiles were obtained for N_2 and He as single gases and for N_2/He gaseous mixtures in three different F-T liquids: a paraffins mixture, a molten F-T reactor wax and a molten Sasol wax in the absence and presence of three different solids using a pilot-scale SBCR. The reactor was operated in the churn-turbulent flow regime within a wide range of operating conditions typifying those of the Fischer-Tropsch synthesis with solid concentrations up to 20 vol. %.

Increasing the total pressure was found to increase the overall k_La values and gas holdup in the three liquids used under most of the operating conditions investigated. High pressures or high gas density decreased the Sauter mean bubble diameter by increasing the population of the small gas bubbles. Increasing temperature increased the gas holdup in the liquids used, except for N_2-molten reactor wax, where the gas holdup remained constant from 400 to 500 K. Increasing temperature, however, decreased the Sauter mean bubble diameter, whereas, the addition of solid particles was found to reverse this trend in some cases, especially for light gaseous mixtures with high He mole fractions. The addition of solid particles decreased the gas holdup and the overall mass transfer coefficients and increased the Sauter mean bubble diameter under all conditions used. At high temperature, the presence of solid particles had less effect on the Sauter mean bubble diameter than at lower temperatures. The k_La values for the gaseous mixture in the three liquids used strongly increased with increasing temperature due to the decrease of the liquid viscosity and surface tension.

Operating the SBCR at high superficial gas velocities led to high gas holdups and overall volumetric mass transfer coefficients while the Sauter mean bubble diameter either increased or decreased due to high rates of gas bubbles breakup and coalescence. Increasing the mole fraction of He in the He/N_2 gaseous mixture at constant pressure led to lower gas holdup while it

191

increased the Sauter mean bubble diameter. Under similar conditions, k_La values of He as a single gas were always lower than those of N_2 as a single gas. The increase of N_2 mole fraction in the N_2/He gaseous mixture increased the interfacial area and consequently k_La values of both gases, whereas increasing the He mole fraction in the gaseous mixture had the opposite effect. At constant gas density, however, the gas mixture composition was found to have little effect on the gas holdup and k_La. The gas bubbles size distribution and Sauter mean diameter, however, were directly affected by the gas mixture composition. The gas holdup and gas bubbles size were slightly larger for N_2 in the paraffins mixture than in the molten reactor wax. However, the gas bubble population was narrower in the paraffins mixture and a greater number of large gas bubbles were present when using the molten reactor wax. Due to the low viscosity, the resulting high k_La values for N_2 were greater in the paraffins mixture, especially at low solid concentrations. With the addition of solid particles, the gas-liquid interfacial area decreased faster in the paraffins mixture than in the molten reactor wax. Operating the SBCR with the molten F-T wax led to the lowest gas holdup and the largest gas bubble sizes resulting in the lowest gas-liquid interfacial area and consequently k_La values.

The solid particles distribution profile at the wall of the reactor was obtained in the pilot SBCR using the paraffins mixture containing Puralox alumina particles as slurry-phase. The "dispersion-sedimentation model" was found to fit well the experimental solid concentration data. The solid concentrations measured at the wall indicated that the dispersion of the solid particles was not uniform throughout the cross-sectional area of the reactor; and the gas nature and composition were found to affect the solid distribution profile at the reactor wall by affecting the bubbles size distribution. Larger population of small gas bubbles led to greater solid concentrations at the reactor wall.

A model was developed to simulate a commercial F-T SBCR. Novel empirical correlations for the hydrodynamic and mass transfer parameters were developed using the data obtained in this study along with available literature values. The new correlations as well as a new relationship between the axial dispersion of the large gas bubbles and their average diameter were included in the model. The simulator predictions for F-T SBCR indicated the following:

- At constant superficial gas velocity (0.3 m/s) and catalyst concentration (37.5 wt %), the CO conversion and liquid hydrocarbon yield increased with increasing reactor height. Also, the CO conversion slightly decreased with increasing reactor ID, whereas the

hydrocarbon yield increased with increasing reactor ID. Both the space-time-yield and reactor productivity increased with reactor length by about 5% and then leveled off after a reactor height of 40 m. Also, both space-time-yield and reactor productivity appeared to slightly decrease with increasing reactor ID.

- At constant reactor inside diameter (7 m) and height (30 m), the CO conversion decreased with increasing the superficial gas velocity and increased with catalyst concentration. Increasing the catalyst concentration above 40 wt% drove the SBCR to operate in a mass transfer-controlled regime. Also, the liquid hydrocarbon yield and space-time-yield increased with increasing catalyst concentration at constant superficial gas velocity. At low catalyst concentration (< 35 wt %), both the hydrocarbon yield and space-time-yield decreased with increasing the superficial gas velocity, whereas, for catalyst concentrations > 35 wt %, the liquid hydrocarbons yield increased with superficial gas velocity, reached a maximum and then decreased. The catalyst productivity reached a maximum at the lowest catalyst concentration of 25 wt% and superficial gas velocities between 0.2 and 0.25 m/s, and generally decreased with increasing catalyst concentration up to 40 wt%. At catalyst concentrations greater than 40 wt%, however, the catalyst productivity increased with superficial gas velocity. At superficial gas velocities > 0.25 m/s, the catalyst productivity increased with catalyst concentrations, levels off, and then decreased. Thus, the maximum space-time-yield occurred at the highest superficial gas velocity and catalyst concentration, whereas the maximum catalyst productivity occurred at a medium superficial gas velocity and the lowest catalyst concentration.

- An SBCR (7 m ID and 30 m height), operating with 37.5 wt% of cobalt-supported catalyst at 0.255 m/s superficial gas velocity, 3 MPa, and 500 K, was found to be able to produce 10,000 bbl/day of F-T liquid hydrocarbons. The SBCR should be provided with a multi-nozzle distributor with (1200) nozzles, and (2693) 2" cooling pipes representing 20% of the total reactor volume in order to remove all the heat of the F-T reaction with a safety factor above 10%. Cooling water flow rates above 150 kg/m^2/s were found sufficient to keep the steam quality below 15 % with pressure drops not exceeding 16 Psi. The reactor would produce 10,808 bbl/day of liquid hydrocarbons at CO conversion of

60.6% with space-time-yield of 55.04 $kg_{HC}/m^3_{reactor}/hr$ and catalyst productivity of 0.225 $kg_{HC}/kg_{catalyst}/hr$.

Different kinetic rate expressions from the available literature were tested in the simulator to predict the performances of a conceptual commercial-scale F-T SBCR (9-m ID, 50-m height) operating with iron or cobalt-based catalyst. The performance of the F-T SBCR was found to be strongly dependent on the catalyst/kinetic rate expressions used for both catalysts. At low catalyst concentrations, the SBCR operated in kinetic-controlled regime with increased syngas conversion and catalyst productivity, however, increasing catalyst concentration led the reactor to operate in a mass transfer-controlled regime with decreased syngas conversion and catalyst productivity. The transition from kinetic- to mass transfer-controlled regimes occurred at different solid concentrations depending on the kinetic rate expressions and operating conditions used. High H_2/CO ratios in the inlet syngas feed to the SBCR resulted in high syngas conversion, whereas the selectivity of the valuable products, such as wax cuts and diesel appeared to decrease. Increasing the superficial velocity of the syngas to the SBCR decreased the gas residence time which decreased the syngas conversions, however, it led to high selectivity of diesel and wax cuts for both catalysts and kinetic rate expressions used. High temperature always resulted in high syngas conversion; yet, increasing temperature resulted in significant decrease in the selectivity of the valuable products, such as wax cuts. The effect of operating pressure on the SBCR performance was dependent on the catalyst and kinetic rate expressions used; since increasing pressure led to low or high or no effect on the syngas conversion.

APPENDIX A

DISPERSION COEFFICIENT MEASURING TECHNIQUES

The possibility of modifying the existing pilot scale SBCR in order to carry out gas and liquid phases dispersion coefficients measurements was considered. Shah et al. [363], and more recently Wild and Poncin [110] and Boyer et al. [264] reviewed different techniques used for measuring the liquid-phase dispersion coefficient in multiphase reactors. A short summary of these techniques as well as comments regarding the present study and existing setup follows.

A.1   LIQUID PHASE DISPERSION

Salt tracers with conductimetry measurements or titration [192, 364-366]

This technique is essentially used with aqueous liquids and therefore cannot be employed with the hydrocarbons liquids used in this study.

Colored tracers with optical measurements [367]

Since the SBCR is opaque (stainless steel walls), colored tracers cannot be used for RTD experiments.

Radioactive isotope tracers [368]

This technique could be applied to the existing system; however, numerous modifications would have to be implemented on the experimental setup to handle safely radioactive materials and to create a space for the radiation measuring apparatus.

Tracers interacting with neutrons [369]

195

Instead of using hazardous radioactive materials, a tracer that interacts with neutrons could be used. This technique has already been used in high temperature and pressure conditions [370] (coal liquefaction process). However it involves the purchase of an expensive neutron source.

Refractory technique [264]

For the investigations of RTD in petrochemical reactors, Boyer et al. [264] recommended the use of a liquid tracer with a refractive index different from the liquid phase used. Optical probes placed at different positions along the reactor can then be used to measure tracer concentrations and dispersion. However in this technique, the slurry phase is simulated using a liquid with a viscosity similar to that of the slurry.

Electromagnetic buoyant particles [110]

Due to the presence of the solid suspension, this technique cannot be applied to measure liquid dispersion; instead it can be used to measure solid dispersion.

Heat [371, 372]

Thermocouples can be used to measure the temperature profile along the reactor and estimate liquid dispersion. However the presence of heating elements in the existing setup around the reactor walls will introduce errors in the recorded temperature profiles.

A.2   GAS-PHASE DISPERSION

Investigation of the gas dispersion is more difficult [264] than that of liquid since absorption and desorption phenomena of the gas tracer in the liquid phase also take place and have to be taken into account [373]. Furthermore, measuring the concentrations of the gas tracer in the existing system would be a complicated task, since the techniques to measure concentrations in the gas-phase which are mainly optical ones cannot be employed in this case due to the presence of the solid phase and the opaque stainless steel walls.

APPENDIX B

HYDROCYCLONE DESIGN FOR SOLID SEPARATION

Hydrocyclones are used to separate solid-liquid suspensions by means of centrifugal sedimentation. The advantages of hydrocyclones reside in their high capacity when compared with equipment size, wide capacity range, small floor space requirements, low investment cost, and wide cut sizes [374]. Their disadvantages, however, include inflexibility (a given cut size can be achieved only with a give hydrocyclone sizes), performance limitations, and sometimes high operating cost. The hydrocyclone performance depends on the slurry flow rate and solids concentrations. In some cases, multi-hydrocyclones arranged in parallel have to be used in order to improve the separation efficiency.

A hydrocyclone consists of a principal cylindrical pipe bounded at the top by a plate having an opening in the form of small cylindrical tube (vortex finder), which allows the liquid to exit at the top. The bottom of the main cylinder is a conical shape with an aperture to allow the liquid exit as can be seen in Figure 93. The slurry phase is injected tangentially into the upper part of the cylindrical section, causing rotation in the hydrocyclone. When the solid phase has a density greater than the liquid phase, the upper tube discharges the clarified liquid (overflow), while the bottom outlet discharges the concentrated solids (underflow).

The hydrocyclone diameter can be selected from the slurry flow-rate needed to be separated using Figure 94 [374]. Once the hydrocyclone diameter is selected from, the other dimensions of the hydrocyclone can be obtained from the following equations [374]:

Height of the cylindrical body of hydrocyclone:

$$h_{cyl} = [0.7D - 2D] \tag{B-1}$$

Length of cyclone from top plate to apex:

$$L = [3D - 8D] \tag{B-2}$$

Vortex finder diameter:

$$D_o = [2.3D - 8D] \tag{B-3}$$

Inlet diameter:

$$D_i = [0.14D - 0.33L] \tag{B-4}$$

Vortex finder lengths:

$$h = [0.33D - 1D] \tag{B-5}$$

Apex diameter:

$$D_u = 0.2D \tag{B-6}$$
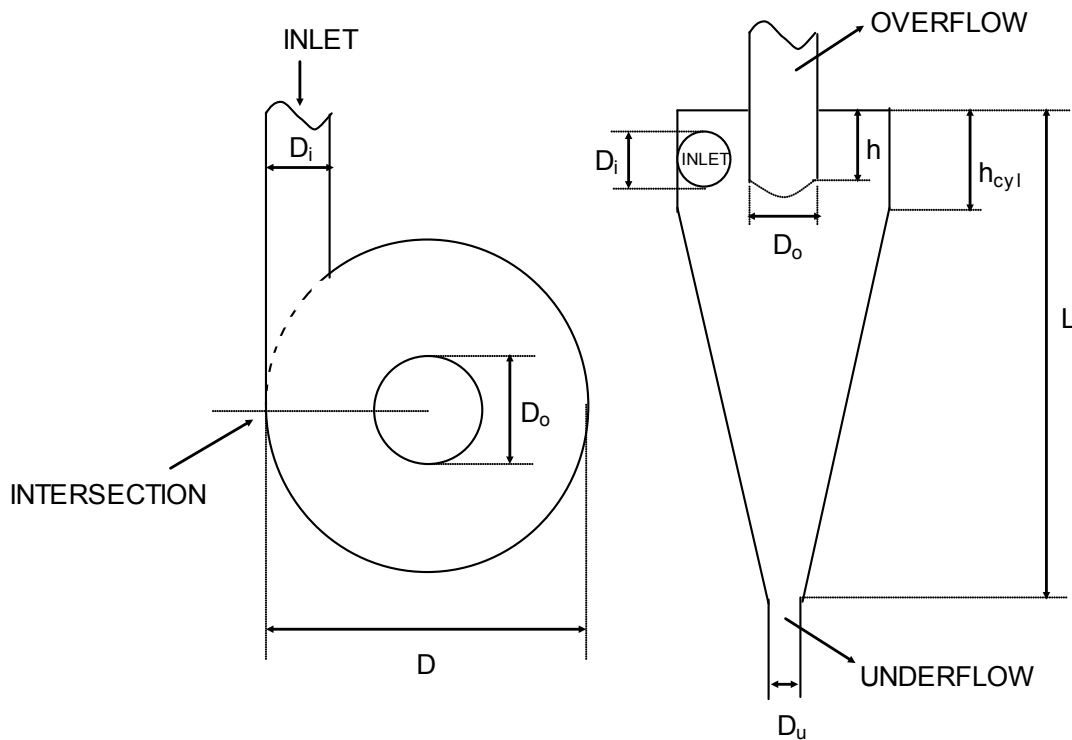
Figure 93: Schematic of a Hydrocyclone

The cut size (d_{50}) can be calculated using one of the following equations [374-378]:

$$d_{50} = 3 \times 10^3 \frac{(D_o D_i)^{0.68}}{F^{0.53}\sqrt{(\rho_S - \rho_{SL})}} \tag{B-7}$$

$$d_{50} = 0.2 \times 10^6 \frac{D^{0.1}D_o^{0.8}D_i^{0.6}\sqrt{\mu_{SL}}}{\sqrt{F\sqrt{(\rho_S - \rho_{SL})}}} \tag{B-8}$$

$$d_{50} = 85.1 \frac{D^{0.46}D_o^{1.21}D_i^{0.6}\exp(6.3c_V)}{D_u^{0.71}h^{0.58}F^{0.45}\sqrt{(\rho_S - \rho_{SL})}} \tag{B-9}$$

$$d_{50} = 64.4 \frac{D^{0.46}D_o^{1.21}D_i^{0.6}\sqrt{\mu_{SL}\exp(6.3c_V)}}{D_u^{0.71}h^{0.58}F^{0.45}\dfrac{(\rho_S - \rho_{SL})}{(\rho_{Skv} - \rho_{SL})}} \tag{B-10}$$
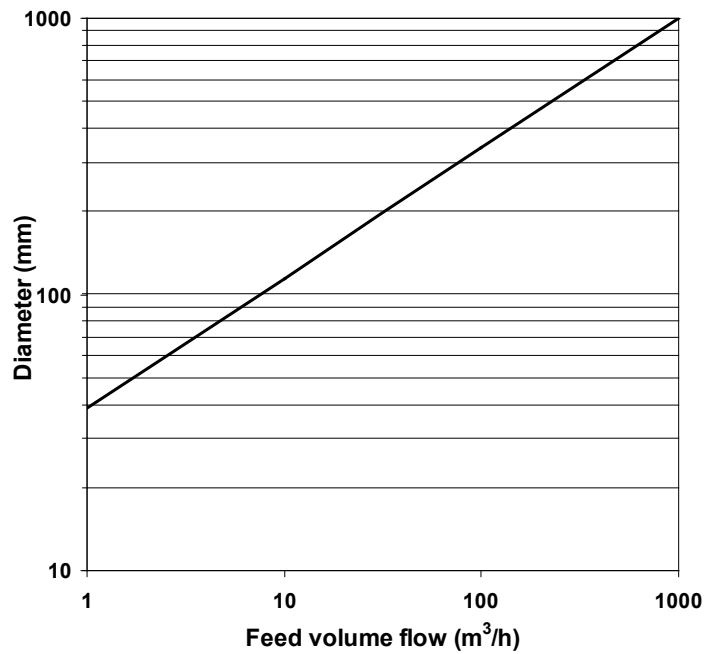
Figure 94: Hydrocyclone Capacity versus Hydrocyclone Diameter

The separation parameter (*M*), the ratio of the underflow rate to the feed rate (*Rv*), and the separation efficiency (η) can be estimated using the following equations [374-378]:

$$M = 2.96 \left(\frac{D^2h}{F}\right)^{0.15} \exp(-1.58Rv) \tag{B-11}$$

$$Rv = \frac{S}{S+1} \tag{B-12}$$

$$S = 2.3F^y \left(\frac{D_u}{D_o}\right)^x \tag{B-13}$$

With - 0.75 < y < - 0.44 and 1.75 < x < 4.4

The separation efficiency can be calculated from [374]:

$$\eta = 1 - \exp\left(-0.693\left(\frac{d}{d_{50}}\right)^M\right) \tag{B-14}$$

Once the geometry of the hydrocyclone has been chosen, the pressure drop across the hydrocyclone can be calculated [374] using the following equation :

$$\Delta P = 2.86 \frac{F^2 \rho_{SL}\left(1 - \frac{D_i}{D}\right)^{1.6}\left[\left(\frac{D}{D_o}\right)^{1.6} - 1\right]}{D^{2.26}D_o^{1.6}} \tag{B-15}$$

In this study, the geometric characteristics of the hydrocyclone chosen are listed in Table 47 and its efficiency as a function of the particles size is shown in Figure 95. The efficiency of the hydrocyclone was estimated using different correlations found in the literature [375-378].

Table 47: Characteristics of the Hydrocyclone

Parameter	Value	Units
D	0.061	
h_{cyl}	0.082	
L	0.335	
D_o	0.012	m
D_i	0.012	
h	0.030	
D_u	0.012	

The overall efficiency of the hydrocyclone was calculated using the solid distribution of the catalyst that was measured in our laboratory. The resulting efficiencies are listed in Table 48. As can be seen in Figure 95 and Table 48 the efficiency predicted varies between 49.7% and 99.9% depending upon the correlation is used. Thus, it was decided it would be risky to rely on any of such correlations to design a hydrocyclone for our solid separation and other options were sought.

Table 48: Hydrocyclone Overall Efficiency

Equation	Overall Efficiency
Yoshioka and Hotta [378]	49.7%
Dahlstrom [375]	92.3%
Flintoff et al. [376]	98.5%
Plitt et al. [377]	99.9%
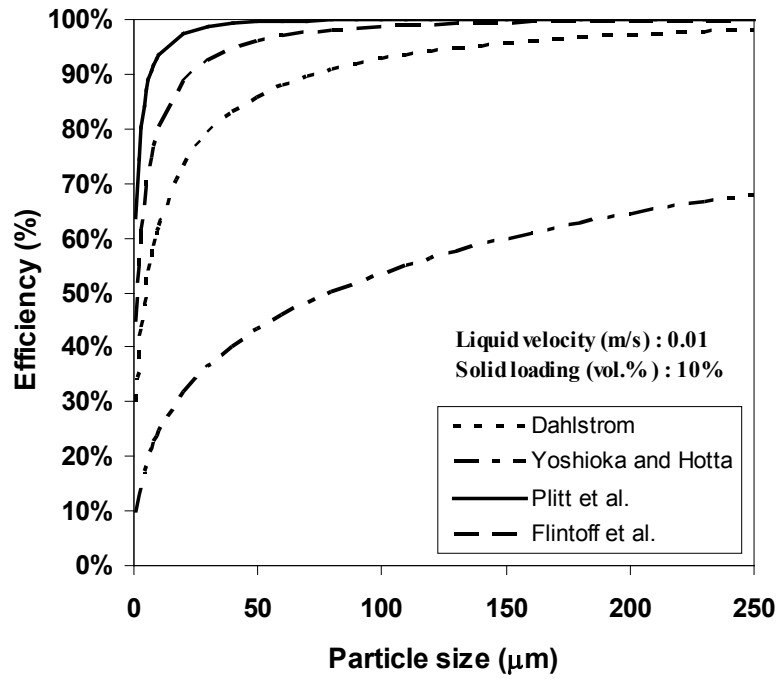
Figure 95: Hydrocyclone Efficiency

APPENDIX C

DIMENSIONLESS MASS & ENERGY BALANCES

C.1   LIQUID-PHASE

$$\frac{\partial\left(\varepsilon_L C'_{i,L}\right)}{\partial\tau_L} = \frac{\partial}{\partial\xi}\left(\frac{\varepsilon_L}{Pe_L}\frac{\partial C'_{i,L}}{\partial\xi}\right) - \frac{\partial C'_{i,L}}{\partial\xi} + St_{L,i,large}\left(C'_{i,G,large} - C'_{i,L}\right)$$
$$+ St_{L,i,small}\left(C'_{i,G,small} - C'_{i,L}\right) + \varepsilon_L r_i \tag{C-1}$$

Steady state developed form:

$$\frac{1}{Pe_L}\left[\left(-\frac{\varepsilon_L}{Pe_L}\frac{\partial Pe_L}{\partial\xi} + \frac{\partial\varepsilon_L}{\partial\xi}\right)\frac{\partial C'_{i,L}}{\partial\xi} + \varepsilon_L\frac{\partial^2 C'_{i,L}}{\partial\xi^2}\right] - \frac{\partial C'_{i,L}}{\partial\xi} + St_{L,i,large}\left(C'_{i,G,large} - C'_{i,L}\right)$$
$$+ St_{L,i,small}\left(C'_{i,G,small} - C'_{i,L}\right) + \varepsilon_L r_i = 0 \tag{C-2}$$

Boundary conditions:

$$\xi = 0 \qquad\qquad \frac{\varepsilon_L}{Pe_L}\frac{\partial C'_{i,L}}{\partial\xi} - C'_{i,L} = 0 \tag{C-3}$$

$$\xi = 1 \qquad\qquad \frac{\partial C'_{i,L}}{\partial\xi} = 0 \tag{C-4}$$

The reaction term in the liquid phase mass balance can be written in dimensionless form for the cobalt-based catalyst as:

$$r_i = \upsilon_{FT,i} K_{FT,i} r_{FT,Co} \tag{C-5}$$

With the following dimensionless terms:

$$r_{FT,Co} = \frac{C'_S C'_{H_2,L} C'_{CO,L}}{1 + aRT_{inlet} C'_{CO,L} C_{CO,G,inlet}} \tag{C-6}$$

$$K_{FT,i,Co} = \frac{LC_0 k_{FT,Co} R\theta T_{inlet} C_{H_2,G,inlet} C_{CO,G,inlet} He_i}{U_L C_{i,G,inlet}} \tag{C-7}$$

In the case of iron catalyst, the reaction term in the liquid phase mass balance becomes:

$$r_i = \upsilon_{FT,i} K_{FT,i} r_{FT} + \upsilon_{WGS,i} K_{WGS,i} r_{WGS} \tag{C-8}$$

With the dimensionless terms:

$$r_{FT,Fe} = \frac{C_S' C_{H_2,L}' C_{CO,L}'}{C_{CO,L}' C_{CO,G,inlet} + a C_{H_2O,L}' C_{H_2O,G,inlet}} \tag{C-9}$$

(in m^3/mol)

$$r_{WGS,Fe} = \frac{C_S' \left(C_{CO,L}' C_{CO,G,inlet} C_{H_2O,L}' C_{H_2O,G,inlet} - \dfrac{C_{H_2,L}' C_{H_2,G,inlet} C_{CO_2,L}' C_{CO_2,G,inlet}}{K_{eq}} \right)}{C_{CO,L}' C_{CO,G,inlet} + a C_{H_2O,L}' C_{H_2O,G,inlet}} \tag{C-10}$$

(in mol/m^3)

$$K_{FT,i,Fe} = \frac{LC_0 k_{FT,Fe} C_{H_2,G,inlet} C_{CO,G,inlet} He_i}{U_L C_{i,G,inlet}} \tag{C-11}$$

(in mol/m^3)

$$K_{WGS,i,Fe} = \frac{LC_0 k_{WGS,Fe} He_i}{U_L C_{i,G,inlet}} \tag{C-12}$$

(in m^3/mol)

C.2   GAS-PHASE

$$\frac{\partial \left(\varepsilon_{G,small} C_{i,G,small}' \right)}{\partial \tau_G}$$

$$= \frac{\partial}{\partial \xi} \left(\frac{\varepsilon_{G,small}}{Pe_{G,small}} \frac{\partial C_{i,G,small}'}{\partial \xi} \right) - \frac{\partial \left(U_{G,small}' C_{i,G,small}' \right)}{\partial \xi} \tag{C-13}$$

$$- St_{G,i,small} \left(C_{i,G,small}' - C_{i,L}' \right)$$

$$- \left(U_{G,large}' - U_{G,small}' \right) K \left(C_{G,small}' - C_{G,large}' \right)$$

$$\frac{\partial\left(\varepsilon_{G,large}C'_{i,G,large}\right)}{\partial\tau_G}$$

$$= \frac{\partial}{\partial\xi}\left(\frac{\varepsilon_{G,large}}{Pe_{G,large}}\frac{\partial C'_{i,G,large}}{\partial\xi}\right) - \frac{\partial\left(U'_{G,large}C'_{i,G,large}\right)}{\partial\xi} \tag{C-14}$$

$$- St_{G,i,large}\left(C'_{i,G,large} - C'_{i,L}\right)$$

$$- \left(U'_{G,large} - U'_{G,small}\right)K\left(C'_{G,large} - C'_{G,small}\right)$$

Steady state developed form:

$$\frac{1}{Pe_{G,small}}\left[\left(-\frac{\varepsilon_{G,small}}{Pe_{G,small}}\frac{\partial Pe_{G,small}}{\partial\xi} + \frac{\partial\varepsilon_{G,small}}{\partial\xi}\right)\frac{\partial C'_{i,G,small}}{\partial\xi} + \varepsilon_{G,small}\frac{\partial^2 C'_{i,G,small}}{\partial\xi^2}\right]$$

$$- U'_{G,small}\frac{\partial C'_{i,G,small}}{\partial\xi} - C'_{i,G,small}\frac{\partial U'_{G,small}}{\partial\xi} - St_{L,i,small}\left(C'_{i,G,small} - C'_{i,L}\right) \tag{C-15}$$

$$- \left(U'_{G,large} - U'_{G,small}\right)K\left(C'_{G,small} - C'_{G,large}\right) = 0$$

$$\frac{1}{Pe_{G,large}}\left[\left(-\frac{\varepsilon_{G,large}}{Pe_{G,large}}\frac{\partial Pe_{G,large}}{\partial\xi} + \frac{\partial\varepsilon_{G,large}}{\partial\xi}\right)\frac{\partial C'_{i,G,large}}{\partial\xi} + \varepsilon_{G,large}\frac{\partial^2 C'_{i,G,large}}{\partial\xi^2}\right]$$

$$- U'_{G,large}\frac{\partial C'_{i,G,large}}{\partial\xi} - C'_{i,G,large}\frac{\partial U'_{G,large}}{\partial\xi} - St_{L,i,large}\left(C'_{i,G,large} - C'_{i,L}\right) \tag{C-16}$$

$$- \left(U'_{G,large} - U'_{G,small}\right)K\left(C'_{G,large} - C'_{G,small}\right) = 0$$

Boundary conditions:

$$\xi = 0$$

$$\frac{\varepsilon_{G,small}}{Pe_{G,small}}\frac{\partial C'_{i,G,small}}{\partial\xi} - U'_{G,small}\left(C'_{i,G,small} - 1\right) = 0 \tag{C-17}$$

$$\frac{\varepsilon_{G,large}}{Pe_{G,large}}\frac{\partial C'_{i,G,large}}{\partial\xi} - U'_{G,large}\left(C'_{i,G,large} - 1\right) = 0$$

$$\xi = 1$$

$$\frac{\partial C'_{i,G,small}}{\partial\xi} = 0 \tag{C-18}$$

$$\frac{\partial C'_{i,G,large}}{\partial\xi} = 0$$

C.3   GAS VELOCITY

$$\frac{\partial U'_G}{\partial \xi} + \sum_i \left[\frac{St_{G,i,small}}{C'_{i,G,small}} \left(C'_{i,G,small} - C'_{i,L} \right) + \frac{St_{G,i,large}}{C'_{i,G,large}} \left(C'_{i,G,large} - C'_{i,L} \right) \right] = 0 \qquad \text{(C-19)}$$

Boundary conditions:

$$\xi = 0 \qquad\qquad\qquad U'_G = 1 \qquad\qquad\qquad\qquad \text{(C-20)}$$

$$\xi = 1 \qquad\qquad\qquad \frac{\partial U'_G}{\partial \xi} = 0 \qquad\qquad\qquad\qquad \text{(C-21)}$$

C.4   SOLIDS SUSPENSION

$$\frac{\partial \left((1 - \varepsilon_G) C'_S \right)}{\partial \tau_L} = \frac{\partial}{\partial \xi} \left(\frac{(1 - \varepsilon_G)}{Pe_S} \frac{\partial C'_S}{\partial \xi} \right) + \frac{\partial \left(\left((1 - \varepsilon_G) U'_P - 1 \right) C'_S \right)}{\partial \xi} \qquad \text{(C-22)}$$

Steady state developed form:

$$\frac{1}{Pe_S} \left[(1 - \varepsilon_G) \frac{\partial^2 C'_S}{\partial \xi^2} - \frac{\partial C'_S}{\partial \xi} \left(\frac{\partial \varepsilon_G}{\partial \xi} + \frac{(1 - \varepsilon_G)}{Pe_S} \frac{\partial Pe_S}{\partial \xi} \right) \right]$$

$$+ \frac{\partial C'_S}{\partial \xi} [(1 - \varepsilon_G) U'_P - 1] + C'_S \left[(1 - \varepsilon_G) \frac{\partial U'_P}{\partial \xi} - U'_P \frac{\partial \varepsilon_G}{\partial \xi} \right] = 0 \qquad \text{(C-23)}$$

Boundary conditions:

$$\xi = 0 \qquad\qquad \frac{(1 - \varepsilon_G)}{Pe_S} \frac{\partial C'_S}{\partial \xi} + [(1 - \varepsilon_G) U'_P - 1] C'_S + x = 0 \qquad \text{(C-24)}$$

$$\xi = 1$$

$$C'_S = \left[\frac{1}{(1 - \varepsilon_G) U'_P - 1} \right] \left[\frac{BoL}{1 - e^{-BoL}} \left(x + \frac{(1 - \varepsilon_G) U'_P - 1}{1} \right) e^{-BoL} - x \right] \qquad \text{(C-25)}$$

C.5　ENERGY BALANCE

$$\frac{\partial\big((1-\varepsilon_{\mathrm{G}})\rho'_{\mathrm{SL}}\theta\big)}{\partial\tau_{\mathrm{L}}}$$

$$=\frac{\partial}{\partial\xi}\left(\rho'_{\mathrm{SL}}\frac{(1-\varepsilon_{\mathrm{G}})}{\mathrm{Pe_H}}\frac{\partial\theta}{\partial\xi}\right)-\frac{\partial(\rho'_{\mathrm{SL}}\theta)}{\partial\xi}-\mathrm{St_H}(\theta-\theta_{\mathrm{cool}})$$

$$+\,(1-\varepsilon_{\mathrm{G}})r_{\mathrm{Heat}}$$

(C-26)

Steady state developed form:

$$\frac{\rho'_{\mathrm{SL}}}{\mathrm{Pe_H}}\left[\left(-\frac{(1-\varepsilon_{\mathrm{G}})}{\mathrm{Pe_H}}\frac{\partial \mathrm{Pe_H}}{\partial\xi}-\frac{\partial\varepsilon_{\mathrm{G}}}{\partial\xi}\right)\frac{\partial\theta}{\partial\xi}+(1-\varepsilon_{\mathrm{G}})\frac{\partial^2\theta}{\partial\xi^2}\right]+\frac{(1-\varepsilon_{\mathrm{G}})}{\mathrm{Pe_H}}\frac{\partial\rho'_{\mathrm{SL}}}{\partial\xi}\frac{\partial\theta}{\partial\xi}$$

$$-\,\rho'_{\mathrm{SL}}\frac{\partial\theta}{\partial\xi}-\theta\frac{\partial\rho'_{\mathrm{SL}}}{\partial\xi}-\mathrm{St_H}(\theta-\theta_{\mathrm{cool}})+(1-\varepsilon_{\mathrm{G}})r_{\mathrm{Heat}}=0$$

(C-27)

Boundary conditions:

$$\xi\;=\;0 \qquad\qquad \rho'_{\mathrm{SL}}\frac{(1-\varepsilon_{\mathrm{G}})}{\mathrm{Pe_H}}\frac{\partial\theta}{\partial\xi}-[\rho'_{\mathrm{SL}}\theta-(\rho'_{\mathrm{SL}}\theta)_0]=0$$

(C-28)

$$\xi\;=\;1 \qquad\qquad \frac{\partial\theta}{\partial\xi}=0$$

(C-29)

BIBLIOGRAPHY

1.   *Energy Information Administration*. 2008; Available from: http://www.eia.gov/.

2.   Hubbert, M.K., *Energy from Fossil Fuels.* Science, 1949. **109**(2823): p. 103-109.

3.   Hubbert, M.K., *The Energy Resources of the Earth.* Energy and Power, 1971. **3**: p. 31-40.

4.   Cavallo, A.J., *Predicting the Peak in World Oil Production.* Natural Resources Research, 2002. **11**(3): p. 187-195.

5.   Hakes, J. *Long Term World Oil Supply*. Proceedings of the Meeting of the American Association of Petroleum Geologists. 2000. New Orleans, LA.

6.   Laherrère, J.H. *Estimates of Oil Reserves*. Proceedings of the IIASA International Energy Workshop. 2001. Luxembourg.

7.   Hirsch, R.L., et al., *Peaking of World Oil Production: Impacts, Mitigation, & Risk Management*. 2005, U.S. Department of Energy, National Energy Technology Laboratory.

8.   Bakhtiari, A.M.S., *World Oil Production Capacity Model Suggests Output Peak by 2006-07.* Oil & Gas Journal, 2004.

9.   Simmons, M.R. Proceedings of the ASPO Workshop. 2003.

10.   Skrebowski, C., *Oil Field Mega Projects - 2004.* Petroleum Review, 2004.

11.   Deffeyes, K.S., *Hubbert's Peak -The Impending World Oil Shortage*. 2003: Princeton University Press.

12.   Goodstein, D., *Out of Gas – The End of the Age of Oil*. 2004: W.W. Norton.

13.   Campbell, C.J., *Industry Urged to Watch for Regular Oil Production Peaks, Depletion Signals.* Oil & Gas Journal, 2003.

14.   *Drivers of the Energy Scene*. 2003, London, United Kingdom: World Energy Council.

15.   Laherrere, J. Proceedings of the Seminar Center of Energy Conversion. 2003. Zurich.

16. *Long Term World Oil Supply*. 2000, U.S. Department of Energy, Energy Information Administration.

17. Jackson, P., et al., *Triple Witching Hour for Oil Arrives Early in 2004 – But, As Yet, No Real Witches*. CERA Alert., 2004.

18. Davis, G., *Meeting Future Energy Needs*. The Bridge. 2003: National Academies Press.

19. Lynch, M.C., *Petroleum Resources Pessimism Debunked in Hubbert Model and Hubbert Modelers' Assessment*. Oil & Gas Journal, 2003.

20. Dry, M.E., *Commercial conversion of carbon monoxide to fuels and chemicals*. Journal of Organometallic Chemistry, 1989. **372**(1): p. 117-127.

21. Stranges, A.N. *Germany's Synthetic Fuel Industry 1927-45*. Proceedings of the AIChE 2003 Spring National Meeting. 2003. New Orleans, LA.

22. *Survey of Energy Resources*. 2004, London, United Kingdom: World Energy Council.

23. *International Energy Annual 2004*. 2004, U.S. Department of Energy, Energy Information Administration.

24. Schulz, H., *Short history and present trends of Fischer-Tropsch synthesis*. Applied Catalysis A: General, 1999. **186**: p. 3-12.

25. WEC, *2004 Survey of Energy Resources*. 2004, Amsterdam, The Netherlands: Elsevier.

26. WEC, *2007 Survey of Energy Resources*. 2007, London, United Kingdom: World Energy Council.

27. Dry, M.E., *The Fischer-Tropsch process: 1950-2000.* Catalysis Today, 2002. **71**(3-4): p. 227-241.

28. Dry, M.E., *Present and future applications of the Fischer-Tropsch process*. Applied Catalysis A: General, 2004. **276**(1-2): p. 1-3.

29. Vosloo, A.C., *Fischer-Tropsch: a futuristic view*. Fuel Processing Technology, 2001. **71**(1-3): p. 149-155.

30. Wilhelm, D.J., et al., *Syngas production for gas-to-liquids applications: technologies, issues and outlook.* Fuel Processing Technology, 2001. **71**(1-3): p. 139-148.

31. Schill, S.R., *The Fischer-Tropsch/Fat Connection*, in *Biomass Magazine*. 2007.

32. *Financial Forecast Center*. 2006; Available from: http://www.neatideas.com/data/data/OILPRICE.htm.

33. Espinoza, R.L., et al., *Low temperature Fischer-Tropsch synthesis from a Sasol perspective.* Applied Catalysis A: General, 1999. **186**(1-2): p. 13-26.

34. van der Laan, G.P., et al., *Multicomponent reaction engineering model for Fe-catalyzed Fischer-Tropsch synthesis in commercial scale slurry bubble column reactors.* Chemical Engineering Science, 1999. **54**(21): p. 5013-5019.

35. Nigam, K.D.P. and A. Schumpe, *Three-Phase Sparged Reactors.* Topics in Chemical Engineering, ed. R. Hughes. Vol. 8. 1996, Amsterdam, The Netherlands: Gordon and Breach Science Publishers.

36. Satterfield, C.N. and G.A. Huff, *Product Distribution from Iron Catalyst in Fischer-Tropsch Slurry Reactors.* Industrial & Engineering Chemistry Process Design and Development, 1982. **21**(3): p. 465-470.

37. Zimmerman, W.H. and D.B. Bukur, *Reaction kinetics over iron catalysts used for the Fischer-Tropsch synthesis.* Canadian Journal of Chemical Engineering, 1990. **68**(2): p. 292-301.

38. Fox, J.M., *Fischer-Tropsch Reactor Selection.* Catalysis Letter, 1990. **7**: p. 281.

39. Sabatier, P. and J.D. Senderens, *Nouvelles Syntheses du Methane.* Comptes Rendus, 1902. **134**: p. 514.

40. Steynberg, A. and M. Dry, *Fischer-Tropsch Technology.* Studies in Surface Science and Catalysis, ed. G. Centi. Vol. 152. 2004: Elsevier Science.

41. Callaghan, C.A., *Kinetics and Catalysis of the Water-Gas-Shift Reaction: A Microkinetic and Graph Theoretic Approach.* Ph.D. Dissertation, Worcester Polytechnic Institute, Worcester, USA, 2006

42. Osaki, T. and T. Mori, *Kinetics of the reverse-boudouard reaction over supported nickel catalysts.* Reaction Kinetics and Catalysis Letters, 2006. **89**(2): p. 333-339.

43. Steynberg, A.P. and H.G. Nel, *Clean coal conversion options using Fischer–Tropsch technology.* Clean coal technology, 2004. **83**(6): p. 765-770.

44. Zhang, J., et al., *Recent Technological Developments in Cobalt Catalysts for Fischer-Tropsch Synthesis.* Journal of Natural Gas Chemistry, 2002. **11**(3): p. 99-108.

45. Brady, R.C. and R. Pettit, *On the Mechanism of the Fischer-Tropsch Reaction. The Chain Propagation Step.* Journal of the American Chemical Society, 1981. **103**(5): p. 1287-1289.

46. van Dijk, H.A.J., *The Fischer-Tropsch synthesis: A mechanistic study using transient isotopic tracing.* Ph.D. Dissertation, Technische Universiteit Eindhoven, Eindhoven, Netherlands, 2001

47. Inderwildi, O.R., et al., *Fischer-Tropsch Mechanism Revisited: Alternative Pathways for the Production of Higher Hydrocarbons from Synthesis Gas.* The Journal of Physical Chemistry C, 2008. **112**: p. 1305-1307.

48.   Jager, B. and R. Espinoza, *Advances in low temperature Fischer-Tropsch synthesis.* Catalysis Today, 1995. **23**(1): p. 17-28.

49.   Komaya, T. and A.T. Bell, *Estimates of rate coefficients for elementary processes occurring during Fischer-Tropsch synthesis over Ru/TiO2.* Journal of Catalysis, 1994. **146**(1): p. 237-248.

50.   Kuipers, E.W., et al., *Non-ASF Product Distributions Due to Secondary Reactions during Fischer–Tropsch Synthesis.* Journal of Catalysis, 1996. **158**(1): p. 288-300.

51.   Wojciechowski, B.W., *The Kinetics of the Fischer-Tropsch Synthesis.* Catalysis Reviews Science and Engineering, 1988. **30**(4): p. 629-702.

52.   Donnelly, T.J., et al., *Analysis and Prediction of Product Distributions of the Fischer-Tropsch Synthesis.* Energy & Fuels, 1988. **2**(6): p. 734-739.

53.   Dictor, R.A. and A.T. Bell, *Fischer-Tropsch synthesis over reduced and unreduced iron catalysts.* Journal of Catalysis, 1986. **97**(1): p. 121-136.

54.   Donnelly, T.J. and C.N. Satterfield, *Product Distributions of the Fischer-Tropsch Synthesis on Precipitated Iron Catalysts.* Applied Catalysis, 1989. **52**(1): p. 93-114.

55.   Sarup, B. and B.W. Wojciechowski, *Studies of the Fischer-Tropsch Synthesis on a Cobalt Catalyst. I. Evaluation of Product Distribution Parameters from Experimental Data.* Canadian Journal of Chemical Engineering, 1988. **66**(5): p. 831-842.

56.   Patzlaff, J., et al., *Studies on product distributions of iron and cobalt catalyzed Fischer-Tropsch synthesis.* Applied Catalysis A: General, 1999. **186**(1-2): p. 109-119.

57.   Chang, J., et al., *Kinetic modeling of Fischer–Tropsch synthesis over Fe-Cu-K-SiO2 catalyst in slurry phase reactor.* Chemical Engineering Science, 2007. **62**(18-20): p. 4983-4991.

58.   van der Laan, G.P., *Kinetics, Selectivity and Scale Up of the Fischer-Tropsch Synthesis.* Ph.D. Dissertation, University of Groningen, Groningen, Netherlands, 1999

59.   Satterfield, C.N., et al., *Effect of water on the iron-catalyzed Fischer-Tropsch synthesis.* Industrial & Engineering Chemistry Product Research and Development, 1986. **25**(3): p. 407-414.

60.   Lox, E.S. and G.F. Froment, *Kinetics of the Fischer-Tropsch reaction on a precipitated promoted iron catalyst. 2. Kinetic modeling.* Industrial & Engineering Chemistry Research, 1993. **32**(1): p. 71-82.

61.   Lox, E.S. and G.F. Froment, *Kinetics of the Fischer-Tropsch reaction on a precipitated promoted iron catalyst. 1. Experimental procedure and results.* Industrial & Engineering Chemistry Research, 1993. **32**(1): p. 61-70.

62.   Wang, Y.-N., *Modelization and Simulation of Fixed-Bed Fischer-Tropsch Synthesis: Kinetics, Pellet and Reactor*. Ph.D. Dissertation, Institute of Coal Chemistry, Chinese Academy of Sciences, Taiyuan, China, 2001

63.   Wang, Y.-N., et al., *Kinetics modelling of Fischer–Tropsch synthesis over an industrial Fe–Cu–K catalyst.* Fuel, 2003. **82**(2): p. 195-213.

64.   Yang, J., et al., *Detailed Kinetics of Fischer-Tropsch Synthesis on an Industrial Fe-Mn Catalyst.* Industrial & Engineering Chemistry Research, 2003. **42**(21): p. 5066-5090.

65.   Brotz, W.Z., *Zur Systematik der Fischer-Tropsch-Katalyse.* Zeitschrift für Elektrochemie, 1949. **5**: p. 301-306.

66.   Hall, C.C., et al., *A comparison of the fixed-bed, liquid phase ('slurry'), and fluidized-bed techniques in the Fischer-Tropsch synthesis.* Journal of the Institute of Petroleum, 1952. **38**: p. 845-876.

67.   Anderson, R.B., *Catalysis*, ed. Reinhold. Vol. 4. 1956, New York: P. H. Emmet

68.   Anderson, R.B. and F.S. Karn, *A Rate Equation for the Fischer-Tropsch Synthesis on Iron Catalysts.* The Journal of Physical Chemistry, 1960. **64**(6): p. 805-808.

69.   Kölbel, H., et al., *Kinetics and reaction mechanism of the hydrocarbon synthesis from carbon monoxide and water vapor on iron, cobalt, and nickel catalysts.* Actes du 2ème Congrès International de Catalyse. Paris, 1960. **1**: p. 953-972.

70.   Anderson, R.B., et al., *Kinetics of the Fischer-Tropsch Synthesis on Iron Catalysts.* US Bureau of Mines, Bulletin 614, 1964.

71.   Dry, M.E., et al., *Rate of the Fischer-Tropsch reaction over iron catalysts.* Journal of Catalysis, 1972. **25**(1): p. 99-104.

72.   Dry, M.E., *Advances in Fishcher-Tropsch Chemistry.* Industrial & Engineering Chemistry Product Research and Development, 1976. **15**(4): p. 282-286.

73.   Atwood, H.E. and C.O. Bennett, *Kinetics of the Fischer-Tropsch Reaction over Iron.* Industrial & Engineering Chemistry Process Design and Development, 1979. **18**(1): p. 163-170.

74.   Thomson, W.J., et al., *Applied Fischer-Tropsch kinetics for a flame sprayed iron catalyst.* Preprint Papers - American Chemical Society, Division of Fuel Chemistry 1979. **25**(2): p. 101-118.

75.   Feimer, J.L., et al., *Steady-state study of the Fischer-Tropsch reaction.* Industrial & Engineering Chemistry Product Research and Development, 1981. **20**(4): p. 609-615.

76. Huff, G.A. and C.N. Satterfield, *Intrinsic kinetics of the Fischer-Tropsch synthesis on a reduced fused-magnetite catalyst.* Industrial & Engineering Chemistry Process Design and Development, 1984. **23**(4): p. 696-705.

77. Leib, T.B. and J.C.W. Kuo. *Modeling the Fischer-Tropsch Synthesis in Slurry Bubble-Column Reactors.* Proceedings of the AIChE Annual Meeting. 1984. San Fransisco, CA.

78. Ledakowicz, S., et al., *Kinetics of the Fischer-Tropsch Synthesis in the Slurry Phase on a Potassium-Promoted Iron Catalyst.* Industrial & Engineering Chemistry Process Design and Development, 1985. **24**(4): p. 1043-1049.

79. Nettelhoff, H., et al., *Studies on the kinetics of Fischer-Tropsch synthesis in slurry phase.* German Chemical Engineering, 1985. **8**: p. 177-185.

80. Deckwer, W.D., et al., *Kinetic studies of Fischer-Tropsch synthesis on suspended iron/potassium catalyst - rate inhibition by carbon dioxide and water.* Industrial & Engineering Chemistry Process Design and Development, 1986. **25**(3): p. 643-649.

81. Shen, W.J., et al., *Kinetics of Fischer-Tropsch synthesis over precipitated iron catalyst.* Journal of Natural Gas Chemistry, 1994. **4**: p. 385-400.

82. Liu, Z.-T., et al., *Intrinsic kinetics of Fischer–Tropsch synthesis over an Fe–Cu–K catalyst.* Journal of the Chemical Society, Faraday Transactions, 1995. **91**(18): p. 3255-3261.

83. van der Laan, G.P. and A.A.C.M. Beenackers, *Hydrocarbon Selectivity Model for the Gas-Solid Fischer-Tropsch Synthesis on Precipitated Iron Catalysts* Industrial & Engineering Chemistry Research, 1999. **38**(4): p. 1277-1290.

84. van der Laan, G.P. and A.A.C.M. Beenackers, *Intrinsic kinetics of the gas–solid Fischer–Tropsch and water gas shift reactions over a precipitated iron catalyst* Applied Catalysis A: General, 2000. **193**(1-2): p. 39-53.

85. Jess, A., et al., *Fischer-Tropsch-synthesis with nitrogen-rich syngas: Fundamentals and reactor design aspects.* Applied Catalysis A: General, 1999. **186**(1-2): p. 321-342.

86. van Steen, E. and H. Schulz, *Polymerisation kinetics of the Fischer-Tropsch CO hydrogenation using iron and cobalt based catalysts.* Applied Catalysis A: General, 1999. **186**(1-2): p. 309-320.

87. Eliason, S.A. and C.H. Bartholomew, *Reaction and deactivation kinetics for Fischer-Tropsch synthesis on unpromoted and potassium-promoted iron catalysts.* Applied Catalysis A: General, 1999. **186**(1-2): p. 229-243.

88. Wang, Y.-N., et al., *Modeling of Catalyst Pellets for Fischer-Tropsch Synthesis* Industrial & Engineering Chemistry Research, 2001. **40**(20): p. 4324-4335.

89.   Teng, B.-T., et al., *A comprehensive kinetics model of Fischer-Tropsch synthesis over an industrial Fe-Mn catalyst.* Applied Catalysis A: General, 2006. **301**(1): p. 39-50.

90.   Keyser, M.J., et al., *Fischer-Tropsch Kinetic Studies with Cobalt-Manganese Oxide Catalysts.* Industrial & Engineering Chemistry Research, 2000. **39**(1): p. 48-54.

91.   Blekkan, E.A., et al., *Fischer-Tropsch synthesis on cobalt catalysts: the effect of water.* Catalysis, 2007. **20**: p. 13-32.

92.   Storsoeter, S., et al., *Effect of Water on the Fischer-Tropsch Synthesis on Supported Cobalt Catalysts.* Fuel Chemistry Division Preprints, 2002. **47**(1): p. 158-159.

93.   Karandikar, B.M., et al., *Effect of water on the solubility and mass transfer coefficients of CO and H2 in a Fischer-Tropsch liquid.* The Chemical Engineering Journal, 1986. **33**(3): p. 157-168.

94.   Karandikar, B.M., et al., *Effect of water on the solubilities and mass transfer coefficients of gases in a heavy fraction of Fischer-Tropsch products.* Canadian Journal of Chemical Engineering, 1987. **65**(6): p. 973-981.

95.   Yang, C.H., et al. Advances in Chemistry Series. Vol. 178. 1979. 35.

96.   Pannell, R.B., et al. Proceedings of the 7th International Congress on Catalysis. 1980. Tokyo.

97.   Rautavuoma, A.O.I. and H.S. van der Baan, *Kinetics and mechanism of the fischer tropsch hydrocarbon synthesis on a cobalt on alumina catalyst.* Applied Catalysis, 1981. **1**(5): p. 247-272.

98.   Sarup, B. and B.W. Wojciechowski, *Studies of the Fischer-Tropsch Synthesis on a Cobalt Catalyst. II. Kinetics of Carbon Monoxide Conversion to Methane and to Higher Hydrocarbons.* Canadian Journal of Chemical Engineering, 1989. **67**(1): p. 62-74.

99.   Withers, H.P., Jr., et al., *Slurry-Phase Fischer-Tropsch Synthesis and Kinetic Studies over Supported Cobalt Carbonyl Derived Catalysts.* Industrial & Engineering Chemistry Research, 1990. **29**(9): p. 1807-1814.

100.   Yates, I.C. and C.N. Satterfield, *Intrinsic kinetics of the Fischer-Tropsch synthesis on a cobalt catalyst.* Energy & Fuels, 1991. **5**(1): p. 168-173.

101.   Chang, J., et al., *Detailed kinetic study of Fischer-Tropsch synthesis on Co/ZrO2/SiO2 catalyst II. Construction and regression of kinetic models.* Chinese Journal of Catalysis, 2005. **26**(10): p. 859-868.

102.   Visconti, C.G., et al., *Development of a complete kinetic model for the Fischer-Tropsch synthesis over Co/Al2O3 catalysts.* Chemical Engineering Science, 2007. **62**(18-20): p. 5338-5343.

103. Anfray, J., et al., *Kinetic study and modeling of Fischer-Tropsch reaction over a Co/Al2O3 catalyst in a slurry reactor.* Chemical Engineering Science, 2007. **62**(18-20): p. 5353-5356.

104. Dry, M.E., *The fischer-tropsch process - commercial aspects.* Catalysis Today, 1990. **6**(3): p. 183-206.

105. Spath, P.L. and D.C. Dayton, *Preliminary Screening — Technical and Economic Assessment of Synthesis Gas to Fuels and Chemicals with Emphasis on the Potential for Biomass-Derived Syngas.* 2003, U.S. Department of Energy, National Renewable Energy Laboratory.

106. Guettel, R., et al., *Reactors for Fischer-Tropsch Synthesis.* Chemical Engineering & Technology, 2008. **31**(5): p. 746-754.

107. Oshinowo, T. and M. Charles, *Vertical Two-Phase Flow. Part I. Flow Pattern Correlations.* Canadian Journal of Chemical Engineering, 1974. **52**(1): p. 25-35.

108. Deckwer, W.-D., et al., *Hydrodynamic Properties of the Fischer-Tropsch Slurry Process.* Industrial & Engineering Chemistry Process Design and Development, 1980. **19**(4): p. 699-708.

109. Vial, C., et al., *Study of hydrodynamic behaviour in bubble columns and external loop airlift reactors through analysis of pressure fluctuations.* Chemical Engineering Science, 2000. **55**(15): p. 2957-2973.

110. Wild, G. and S. Poncin, *Hydrodynamics of Three-Phase Sparged Reactors.* Three-Phase Sparged Reactors, ed. K.D.P. Nigam and A. Schumpe. 1996, New York: Gordon and Breach Science Publishers.

111. Zahradník, J., et al., *Duality of the gas-liquid flow regimes in bubble column reactors.* Chemical Engineering Science, 1997. **52**(21-22): p. 3811-3826.

112. Magaud, F., et al., *Experimental study of bubble column hydrodynamics.* Chemical Engineering Science, 2001. **56**(15): p. 4597-4607.

113. Sarrafi, A., et al., *Gas Holdup in Homogeneous and Heterogeneous Gas-Liquid Bubble Column Reactors.* Canadian Journal of Chemical Engineering, 1999. **77**(1): p. 11-21.

114. Lee, S.-Y. and Y.P. Tsui, *Succeed at gas/liquid contacting.* Chemical Engineering Progress, 1999. **95**(7): p. 23-48.

115. Saxena, S.C. and Z.D. Chen, *Hydrodynamics and Heat Transfer of Baffled and Unbaffled Slurry Bubble Columns.* Reviews in Chemical Engineering, 1994. **10**(3-4): p. 195-400.

116. Anderson, J.L. and J.A. Quinn, *The transition to slug flow in bubble columns.* Chemical Engineering Science, 1970. **25**(2): p. 338-340.

117. de Swart, J.W.A., et al., *Size, Structure and Dynamics of "Large" Bubbles in a Two-Dimensional Slurry Bubble Column.* Chemical Engineering Science, 1996. **51**(20): p. 4619-4629.

118. Shah, Y.T., et al., *Design Parameters Estimations for Bubble Column Reactors.* AIChE Journal, 1982. **28**(3): p. 353-379.

119. Vermeer, D. and R. Krishna, *Hydrodynamics and mass transfer in bubble columns in operating in the churn-turbulent regime.* Industrial & Engineering Chemistry Process Design and Development, 1981. **20**(3): p. 475-482.

120. Behkish, A., et al., *Gas holdup and bubble size behavior in a large-scale slurry bubble column reactor operating with an organic liquid under elevated pressures and temperatures.* Chemical Engineering Journal, 2007. **128**(2-3): p. 69-84.

121. Grund, G., et al., *Gas-Liquid mass transfer in a bubble column with organic liquids.* Chemical Engineering Science, 1992. **47**(13-14): p. 3509-3516.

122. Krishna, R., et al., *Gas holdup in bubble columns: influence of alcohol addition versus operation at elevated pressures.* Chemical Engineering and Processing, 2000. **39**(4): p. 371-378.

123. Lemoine, R., et al., *Hydrodynamic and Mass Transfer Characteristics in Organic Liquid Mixtures in a Large-Scale Bubble Column Reactor for the Toluene Oxidation Process.* Industrial & Engineering Chemistry Process Design and Development, 2004. **43**(19): p. 6195-6212.

124. Fan, L.S., et al., *Some aspects of high-pressure phenomena of bubbles in liquids and liquid–solid suspensions* Chemical Engineering Science, 1999. **54**(21): p. 4681-4709.

125. Raje, A., et al., *Fischer-Tropsch synthesis: Process considerations based on performance of iron-based catalysts.* Fuel, 1997. **76**(3): p. 273-280.

126. Lewis, W.K. and W.G. Whitman, *Principles of Gas Absorption.* Industrial & Engineering Chemistry, 1924. **16**(12): p. 1215-1220.

127. Behkish, A., *Hydrodynamic and Mass Transfer Parameters in Large-Scale Slurry Bubble Column Reactors.* Ph.D. Dissertation, University of Pittsburgh, Pittsburgh, USA, 2004

128. Hikita, H., et al., *Gas hold-up in bubble columns.* The Chemical Engineering Journal, 1980. **20**(1): p. 59-67.

129. Jordan, U. and A. Schumpe, *The gas density Effect on Mass Transfer in Bubble Columns with Organic Liquids.* Chemical Engineering Science, 2001. **56**(21-22): p. 6267-6272.

130. Jordan, U., et al., *Mass transfer in High-Pressure Bubble Columns with Organic Liquids.* Chemical Engineering & Technology, 2002. **25**(3): p. 262-265.

131. Reilly, I.G., et al., *The Role of Gas Phase Momentum in Determining Gas Holdup and Hydrodynamic Flow Regimes in Bubble Column Operations.* Canadian Journal of Chemical Engineering, 1994. **72**(1): p. 3-13.

132. Wilkinson, P.M. and L.L. v. Dierendonck, *Pressure and gas density effects on bubble break-up and gas hold-up in bubble columns.* Chemical Engineering Science, 1990. **45**(8): p. 2309-2315.

133. Inga, J.R., *Scaleup and Scaledown of Slurry Reactors: A New Methodology.* Ph.D. Dissertation, University of Pittsburgh, Pittsburgh, USA, 1997

134. Letzel, H.M., et al., *Effect of Gas Density on Large-Bubble Column Reactors.* AIChE Journal, 1998. **44**: p. 2333-2336.

135. Lin, T.J., et al., *Bubble Flow Characteristics in Bubble Columns at Elevated Pressure and Temperature.* AIChE Journal, 1998. **44**(3): p. 545-560.

136. Clark, K.N., *The effect of high pressure and temperature on phase distributions in a bubble column.* Chemical Engineering Science, 1990. **45**(8): p. 2301-2307.

137. Sauer, T. and D.-C. Hempel, *Fluid dynamics and mass transfer in a bubble column with suspended particles.* Chemical Engineering & Technology, 1987. **10**(1): p. 180-189.

138. Zou, R., et al., *Studies on gas holdup in a bubble column operated at elevated temperatures.* Industrial & Engineering Chemistry Research, 1988. **27**(10): p. 1910-1916.

139. Hughmark, G.A., *Holdup and Mass Transfer in Bubble Columns.* Industrial & Engineering Chemistry Process Design and Development, 1967. **6**(2): p. 218-220.

140. Akita, K. and F. Yoshida, *Gas Holdup and Volumetric Mass Transfer Coefficient in Bubble Columns. Effects of Liquid Properties.* Industrial & Engineering Chemistry Process Design and Development, 1973. **12**(1): p. 76-80.

141. Fair, J.R., et al., *Heat Transfer and Gas Holdup in a Sparged Contactor.* Industrial & Engineering Chemistry Process Design and Development, 1962. **1**(1): p. 33-36.

142. Godbole, S.P., et al., *Hydrodynamics and mass transfer in non-Newtonian solutions in a bubble column.* AIChE Journal, 1984. **30**(2): p. 213-220.

143. Koide, K., et al., *Gas holdup and volumetric liquid-phase mass transfer coefficient in solid-suspended bubble columns.* Journal of Chemical Engineering of Japan, 1984. **17**(5): p. 459-466.

144. Godbole, S.P., *Study of hydrodynamic and mass transfer characteristics of multiphase bubble column reactor.* Ph.D. Dissertation, University of Pittsburgh, Pittsburgh, USA, 1983

145. Neme, F., et al., *Gas holdup and mass transfer in solid suspended bubble columns in presence of structured packings.* Chemical Engineering & Technology, 1997. **20**(5): p. 297-303.

146. Akita, K. and F. Yoshida, *Bubble size, Interfacial Area, and Liquid-Phase Mass Transfer Coefficient in Bubble Columns.* Industrial & Engineering Chemistry Process Design and Development, 1974. **13**(1): p. 84-91.

147. Kluytmans, J.H.J., et al., *Gas Holdup in a Slurry Bubble Column: Influence of Electrolyte and Carbon Particles.* Industrial & Engineering Chemistry Research, 2001. **40**(23): p. 5326-5333.

148. Pohorecki, R., et al., *Hydrodynamics of a bubble column under elevated pressure.* Chemical Engineering Science, 1999. **54**(21): p. 5187-5193.

149. Wilkinson, P.M., et al., *Design Parameters Estimation for Scale-up of High-Pressure Bubble Columns.* AIChE Journal, 1992. **38**(4): p. 544-554.

150. Hikita, H., et al., *The Volumetric Mass Transfer Coefficient in Bubble Columns.* The Chemical Engineering Journal, 1981. **22**(1): p. 61-69.

151. Jamialahmadi, M. and H. Müller-Steinhagen, *Effect of Solid Particles on Gas Hold-Up in Bubble Columns.* Canadian Journal of Chemical Engineering, 1991. **69**(1): p. 390-393.

152. Kara, S., et al., *Hydrodynamics and axial mixing in a three-phase bubble column.* Industrial & Engineering Chemistry Process Design and Development, 1982. **21**(4): p. 584-594.

153. Kelkar, B.G., et al., *Hydrodynamics and axial mixing in a three-phase bubble column. Effects of slurry properties.* Industrial & Engineering Chemistry Process Design and Development, 1984. **23**(2): p. 308-313.

154. Chabot, J. and H.I. Lasa, *Gas Holdups and Bubble Characteristics in a Bubble Column Operated at High Temperature.* Industrial & Engineering Chemistry Research, 1993. **32**(11): p. 2595-2601.

155. Pohorecki, R., et al., *Hydrodynamics of a Pilot Plant Bubble Column Under Elevated temperature and Pressure.* Chemical Engineering Science, 2001. **56**(3): p. 1167-1174.

156. Kang, Y., et al., *Diagnosis of Bubble Distribution and Mass Transfer in Pressurized Bubble Columns with Viscous Liquid Medium.* Chemical Engineering Science, 1999. **54**(21): p. 4887-4893.

157. Kemoun, A., et al., *Gas holdup in bubble columns at elevated pressure via computed tomography.* International Journal of Multiphase Flow, 2001. **27**(5): p. 929-946.

158. Kojima, H., et al., *Effect of pressure on volumetric mass transfer coefficient and gas holdup in bubble column.* Chemical Engineering Science, 1997. **52**(21-22): p. 4111-4116.

159. Letzel, H.M., et al., *Characterization of regimes and regime transitions in bubble columns by chaos analysis of pressure signals.* Chemical Engineering Science, 1997. **52**(24): p. 4447-4459.

160. Letzel, H.M., et al., *Gas holdup and mass transfer in bubble column reactors operated at elevated pressure.* Chemical Engineering Science, 1999. **54**(13-14): p. 2237-2246.

161. Letzel, H.M., et al., *Influence of elevated pressure on the stability of bubbly flows.* Chemical Engineering Science, 1997. **52**(21-22): p. 3733-3739.

162. Luo, X., et al., *Maximum Stable bubble size and gas holdup in high-pressure slurry bubble columns.* AIChE Journal, 1999. **45**(4): p. 665-680.

163. Oyevaar, M.H., et al., *Interfacial areas and gas hold-ups in gas--liquid contactors at elevated pressures from 0.1 to 8.0 MPa.* Chemical Engineering Science, 1991. **46**(5-6): p. 1217-1231.

164. Stegeman, D., et al., *Interfacial Area and Gas Holdup in a Bubble Column Reactor at Elevated Pressures.* Industrial & Engineering Chemistry Research, 1996. **35**(11): p. 3842-3847.

165. Wilkinson, P.M., et al., *Mass Transfer and Bubble Size in a Bubble Column under Pressure.* Chemical Engineering Science, 1994. **49**(9): p. 1417-1427.

166. Behkish, A., et al., *Mass transfer characteristics in a large-scale slurry bubble column reactor with organic liquid mixtures.* Chemical Engineering Science, 2002. **57**(16): p. 3307-3324.

167. Dewes, I., et al., *Gas Density effect on Mass Transfer in Three-Phase Sparged Reactors.* Transactions of the Institution of Chemical Engineers, 1995. **73**(A): p. 697-700.

168. Dewes, I. and A. Schumpe, *Gas density effect on mass transfer in the slurry bubble column.* Chemical Engineering Science, 1997. **52**(21-22): p. 4105-4109.

169. Bukur, D.B., et al., *Gas holdup and solids dispersion in a three-phase slurry bubble column.* AIChE Journal, 1990. **36**(11): p. 1731-1735.

170. Jianping, W. and X. Shonglin, *Local hydrodynamics in a gas-liquid-solid three-phase bubble column reactor.* Chemical Engineering Journal, 1998. **70**(1): p. 81-84.

171. Jin, H., et al., *Measurement of gas holdup profiles in a gas liquid cocurrent bubble column using electrical resistance tomography.* Flow Measurement and Instrumentation, 2007. **18**(5-6): p. 191-196.

172. Gandhi, B., et al., *Hydrodynamic behavior of slurry bubble column at high solids concentrations.* Powder Technology, 1999. **103**(2): p. 80-94.

173. Kojima, H., et al., *Axial mixing in bubble column with suspended solid particles.* Journal of Chemical Engineering of Japan, 1986. **19**(3): p. 232-234.

174. Krishna, R., et al., *Design and scale up of a bubble column slurry reactor for Fischer-Tropsch synthesis.* Chemical Engineering Science, 2001. **56**(2): p. 537-545.

175. Lee, D.J., et al., *Gas disengagement technique in a slurry bubble column operated in the coalesced bubble regime.* Chemical Engineering Science, 1999. **54**(13-14): p. 2227-2236.

176. Salvacion, J.L., et al., *Effects of Alcohols on Gas Holdup and Volumetric Liquid-Phase Mass Transfer Coefficient in Gel-Particle-Suspended Bubble Column.* Journal of Chemical Engineering of Japan, 1995. **28**(4): p. 434-442.

177. Quicker, G., et al., *Gas-liquid interfacial areas in a bubble column with suspended solids.* Chemical Engineering Science, 1984. **39**(1): p. 179-183.

178. Schumpe, A., et al., *Gas/liquid mass transfer in a slurry bubble column.* Chemical Engineering Science, 1987. **42**(7): p. 1787-1796.

179. Yoshida, F. and K. Akita, *Performance of Gas Bubble Columns: Volumetric Liquid-Phase Mass Transfer Coefficient and Gas Holdup.* AIChE Journal, 1965. **11**(1): p. 9-13.

180. Eickenbusch, H., et al., *Mass transfer into viscous pseudoplastic liquid in large-diameter bubble columns.* Chemical Engineering and Processing, 1995. **34**(5): p. 479-485.

181. Moustiri, S., et al., *A unified correlation for predicting liquid axial dispersion coefficient in bubble columns.* Chemical Engineering Science, 2001. **56**(3): p. 1041-1047.

182. Guy, C., et al., *Mixing Characteristics and Gas Holdup of a Bubble Column.* Canadian Journal of Chemical Engineering, 1986. **64**(1): p. 23-35.

183. Pino, L.Z., et al., *Effect of Operating Conditions on Gas Holdup in Slurry Bubble Columns with a Foaming Liquid.* Chemical Engineering Communications, 1992. **117**(1): p. 367-382.

184. Behkish, A., et al., *Novel Correlations for Gas Holdup in Large-Scale Slurry Bubble Column Reactors Operating under Elevated Pressures and Temperatures.* Chemical Engineering Journal, 2006. **115**(3): p. 157-171.

185. Saxena, S.C., et al., *Gas Phase Holdup in Slurry Bubble Column for Two- and Three-Phase Systems.* The Chemical Engineering Journal, 1992. **49**(3): p. 151-159.

186. O'Dowd, W., et al., *Gas and solids behavior in a baffled and unbaffled slurry bubble column.* AIChE Journal, 1987. **33**(12): p. 1959-1970.

187. Chen, J., et al., *Fluid dynamic parameters in bubble columns with internals.* Chemical Engineering Science, 1999. **54**(13-14): p. 2187-2197.

188.   Yamashita, F., *Effects of Vertical Pipe and Rod Internals on Gas Holdup in Bubble Columns.* Journal of Chemical Engineering of Japan, 1987. **20**(2): p. 204-206.

189.   Krishna, R., et al., *Gas Holdup in Slurry Bubble Columns: Effect of Column Diameter and Slurry Concentrations.* AIChE Journal, 1997. **43**: p. 311-316.

190.   Vandu, C.O., et al., *Volumetric mass transfer coefficient in a slurry bubble column operating in the heterogeneous flow regime.* Chemical Engineering Science, 2004. **59**(22-23): p. 5417-5423.

191.   Woo, K.-J., et al., *Performance of a slurry bubble column reactor for Fischer-Tropsch synthesis: Determination of optimum condition.* Fuel Processing Technology, 2010. **91**(4): p. 434-439.

192.   Argo, W.B. and D.R. Cova, *Longitudinal Mixing in Gas-Sparged Tubular Vessels.* Industrial & Engineering Chemistry Process Design and Development, 1965. **4**(4): p. 352-359.

193.   Bach, H.F. and T. Pilhofer, *Variation of Gas Hold-Up in Bubble Columns with Physical Properties of Liquids and Operating Parameters of Columns.* German Chemical Engineering, 1978. **1**(5): p. 270-275.

194.   Gestrich, W., et al., *Liquid-side mass transfer coefficient in bubble layers.* International Chemical Engineering, 1978. **18**(1): p. 38-47.

195.   Mersmann, A., *Design and Scale-up of Bubble and Spray Columns.* German Chemical Engineering, 1978. **1**: p. 1-11.

196.   Tarmy, B.L., et al. *Three Phase Hydrodynamic Characteristics of The EDS Coal Liquefaction Reactors: Their Development and Use in Reactor Scaleup.* Proceedings of the Institution of Chemical Engineers Symposium Series. 1984.

197.   Molerus, O. and M. Kurtin, *Hydrodynamics of Bubble Columns in the Uniform Bubbling Regime.* Chemical Engineering Science, 1985. **40**: p. 647-652.

198.   Grover, G.S., et al., *Effect of temperature on flow regime and gas holdup in a bubble column.* Canadian Journal of Chemical Engineering, 1986. **64**: p. 501-504.

199.   Idogawa, K., et al., *Effect of gas and liquid properties on the behavior of bubbles in a column under high pressure.* International Chemical Engineering, 1987. **27**(1): p. 93-99.

200.   Kawase, Y., et al., *Theoretical Prediction of Volumetric Mass Transfer Coefficients in Bubble Columns for Newtonian and Non-Newtonian Fluids.* Chemical Engineering Science, 1987. **42**: p. 1609-1617.

201.   Moo Young, M.K., Y., *Gas Holdup And Mass Transfer In A Bubble Column With Viscoelastic Fluids.* Canadian Journal of Chemical Engineering, 1987. **65**(1): p. 113-118.

202. öztürk, S.S., et al., *Organic liquids in a bubble column: Holdups and mass transfer coefficients.* AIChE Journal, 1987. **33**(9): p. 1473-1480.

203. Popovic, M. and C.W. Robinson, *The specific interfacial area in external-circulation-loop airlifts and a bubble column-I. Aqueous sodium sulphite solution.* Chemical Engineering Science, 1987. **42**(12): p. 2811-2824.

204. Popovic, M. and C.W. Robinson, *The specific interfacial area in external-circulation-loop airlifts and a bubble column-II. Carboxymethyl cellulose/sulphite solution.* Chemical Engineering Science, 1987. **42**(12): p. 2825-2832.

205. Cho, J.S. and N. Wakao, *Determination of liquid-side and gas-side volumetric mass transfer coefficients in a bubble column.* Journal of Chemical Engineering of Japan, 1988. **21**(6): p. 576-581.

206. de Bruijn, T.J.W., et al., *Gas Holdup in a Two Phase Vertical Tubular Reactor at High Pressure.* Canadian Journal of Chemical Engineering, 1988. **66**(2): p. 330-333.

207. Akita, A., *Effect Of The Electrolyte On The Mass Transfer Characteristics Of A Bubble Column.* International Chemical Engineering, 1989. **29**(1): p. 127-135.

208. Allen, D.G. and C.W. Robinson, *Hydrodynamics and mass transfer in Aspergillus niger fermentations in bubble column and loop bioreactors.* Biotechnology and Bioengineering, 1989. **34**(6): p. 731-740.

209. Halard, B., et al., *Mass Transfer in a Pilot Plant Scale Airlift Column with non-Newtonian Fluids.* Industrial & Engineering Chemistry Research, 1989. **28**(2): p. 243-245.

210. Medic, L., et al., *Volumetric gas-liquid mass transfer coefficients in a rectangular bubble column with a rubber aeration pad.* The Chemical Engineering Journal, 1989. **41**(3): p. B51-B54.

211. Popovic, M.K. and C.W. Robinson, *Mass transfer studies of external-loop airlifts and a bubble column.* AIChE Journal, 1989. **35**(3): p. 393-405.

212. Uchida, S., et al., *Flow Regimes And Mass Transfer In Counter-Current Bubble Columns.* Canadian Journal of Chemical Engineering, 1989. **67**(5): p. 866-869.

213. Vatai, G.Y. and M.N. Tekic, *Gas hold-up and mass transfer in bubble columns with pseudoplastic liquids.* Chemical Engineering Science, 1989. **44**(10): p. 2402-2407.

214. Seno, T., et al., *Mass transfer in countercurrent and cocurrent bubble columns.* Chemical Engineering & Technology, 1990. **13**(1): p. 113-118.

215. Huynh, L.X., et al., *Hydrodynamics and mass transfer in an upward venturi/bubble column combination.* Canadian Journal of Chemical Engineering, 1991. **69**(3): p. 711-722.

216. Kawase, Y. and M. Moo-Young, *Oxygen transfer in slurry bioreactors.* Biotechnology and Bioengineering, 1991. **37**(10): p. 960-966.

217. Rodemerck, U. and A. Seidel, *Analysis of transient mass transfer measurements in bubble columns.* Chemical Engineering Science, 1991. **46**(3): p. 908-912.

218. Suh, I.S., et al., *Gas Liquid Mass Transfer in the Bubble Column with Viscoelastic Liquid.* Canadian Journal of Chemical Engineering, 1991. **69**(2): p. 506-512.

219. Terasaka, K. and H. Tsuge, *Mass transfer in highly viscous liquids in a bubble column with constant-flow nozzles.* Journal of Chemical Engineering of Japan, 1991. **24**(4): p. 424-429.

220. Daly, J.G., et al., *Measurement of gas holdups and sauter mean bubble diameters in bubble column reactors by dynamics gas disengagement method.* Chemical Engineering Science, 1992. **47**(13–14): p. 3647-3654.

221. Goto, S. and P.D. Gaspillo, *The effect of static mixer on mass transfer in draft tube bubble column and in external loop column.* Chemical Engineering Science, 1992. **47**(13-14): p. 3533-3539.

222. Merchuk, J.C. and S. Ben-Zvi, *A novel approach to the correlation of mass transfer rates in bubble columns with non- Newtonian liquids.* Chemical Engineering Science, 1992. **47**(13-14): p. 3517-3523.

223. Muller, F.L. and J.F. Davidson, *On the Contribution of Small Bubbles to Mass Transfer in Bubble Columns Containing Highly Viscous Liquids.* Chemical Engineering Science, 1992. **47**(13-14): p. 3525-3532.

224. Kawasaki, H., et al., *Relationship between Gas Holdup and Volumetric Mass Transfer Coefficient in a Bubble Column with Single Hole Orifice.* Journal of Chemical Engineering of Japan, 1994. **27**(5): p. 667-668.

225. Kawasaki, H., et al., *Effect of Multiple Draft Tubes with Perforated Plates on Gas Holdup and Volumetric Mass Transfer Coefficient in a Bubble Column.* Journal of Chemical Engineering of Japan, 1994. **27**(5): p. 669-670.

226. Sotelo, J.L., et al., *Gas holdup and mass transfer coefficients in bubble columns. 1. Porous glass-plate diffusers.* International Chemical Engineering, 1994. **34**(1): p. 82-90.

227. Zhao, M., et al., *Mass transfer to viscous liquids in bubble columns and air-lift reactors: influence of baffles.* Chemical Engineering Science, 1994. **49**(14): p. 2359-2369.

228. de Swart, J.W.A., *Scale-Up of a Fischer-Tropsch Slurry Reactor.* Ph.D. Dissertation, University of Amsterdam, Amsterdam, Netherlands, 1996

229. Krishna, R. and J. Ellenberger, *Gas holdup in bubble column reactors operating in the churn-turbulent flow regime.* AIChE Journal, 1996. **42**(9): p. 2627-2634.

230. Laari, A., et al., *Gas-liquid mass transfer in bubble columns with a T-junction nozzle for gas dispersion.* Chemical Engineering & Technology, 1997. **20**(8): p. 550-556.

231. Miyahara, T.H., H., et al., *Gas Holdup Gas-Liquid Interfacial Area and Mass Transfer Coefficient in External-Loop Airlift Bubble Column Containing Low Density Particles.* Journal of Chemical Engineering of Japan, 1997. **30**: p. 958-961.

232. Soong, Y., et al., *Hydrodynamic study in a slurry-bubble-column reactor.* Catalysis Today, 1997. **35**(4): p. 427-434.

233. Terasaka, K., et al., *Mass Transfer in Bubble Columns studied with an oxygen optode.* Chemical Engineering Science, 1998. **53**(17): p. 3181-3184.

234. Lin, T.J., et al., *On the measurements of regime transition in high-pressure bubble columns.* The Canadian Journal of Chemical Engineering, 1999. **77**(2): p. 370-374.

235. Álvarez, E., et al., *Mass Transfer and Influence of Physical Properties of Solutions in a Bubble Column.* Chemical Engineering Research and Design, 2000. **78**(6): p. 889-893.

236. Vázquez, G., et al., *Application of the Danckwerts method in a bubble column: Effects of surfactants on mass transfer coefficient and interfacial area.* Chemical Engineering Journal, 2000. **78**(1): p. 13-19.

237. Vázquez, G., et al., *Determination of Interfacial Areas in a Bubble Column by Different Chemical Methods.* Industrial & Engineering Chemistry Research, 2000. **39**(7): p. 2541-2547.

238. Bouaifi, M., et al., *A comparative study of gas hold-up, bubble size, interfacial area and mass transfer coefficients in stirred gas-liquid reactors and bubble columns.* Chemical Engineering and Processing, 2001. **40**(2): p. 97-111.

239. Ishibashi, H., et al., *Gas holdup in slurry bubble column reactors of a 150 t/d coal liquefaction pilot plant process.* Fuel, 2001. **80**(5): p. 655-664.

240. Jordan, U., et al., *Stoffubergang in Druckblasensaulen mit Organischen Flussigkeiten.* Chemie Ingenieur Technik, 2001. **73-8**.

241. Pohorecki, R., et al., *Modelling of the coalescence/redispersion processes in bubble columns.* Chemical Engineering Science, 2001. **56**(21-22): p. 6157-6164.

242. Yang, W., et al., *Mass Transfer Characteristics of Syngas Components in Slurry System at Industrial Conditions.* Chemical Engineering & Technology, 2001. **24**(6): p. 651-657.

243. Urseanu, M.I., et al., *Influence of operating pressure on the gas hold-up in bubble columns for high viscous media.* Chemical Engineering Science, 2003. **58**(3-6): p. 697-704.

244. Lau, R., et al., *Gas−Liquid Mass Transfer in High-Pressure Bubble Columns.* Industrial & Engineering Chemistry Research, 2004. **43**(5): p. 1302-1311.

245. Reilly, I.G., et al., *A Correlation for Gas Holdup in Turbulent Coalescing Bubble Columns.* Canadian Journal of Chemical Engineering, 1986. **64**: p. 705-717.

246. Fukuma, M., et al., *Specific Gas-Liquid Interfacial Area and Liquid-Phase Mass Transfer Coefficient in a Slurry Bubble Column.* Journal of Chemical engineering of Japan, 1987. **20**: p. 321-324.

247. Krishna, R. and S.T. Sie, *Design and Scale-up of the Fischer-Tropsch bubble Column Slurry Reactor.* Fuel Processing Technology, 2000. **64**(1): p. 73-105.

248. Yang, G.Q., et al., *Heat-Transfer Characteristics in Slurry Bubble Columns at Elevated Pressures and Temperatures.* Industrial & Engineering Chemistry Research, 2000. **39**(7): p. 2568-2577.

249. Chen, C.-M. and L.-P. Leu, *Hydrodynamics and mass transfer in three-phase magnetic fluidized beds.* Powder Technology, 2001. **117**(3): p. 198-206.

250. GKN Sinter metals. *Filter-Elements/Metal Membranes*. Available from: http://www.gkn-filters.com/.

251. KRAL-USA. *Operating Principle*. Available from: http://www.kral.at/.

252. Yaws, C.L., *Chemical Properties Handbook.* 1999: McGraw-Hill.

253. Gao, W., et al., *Improved Correlations for heavy n-paraffin physical properties.* Fluid Phase Equilibria, 2001. **179**(1-2): p. 207-216.

254. Soriano, J.P., *Mass Transfer Characteristics in an Agitated Slurry Reactor Operating Under Fischer-Tropsch Conditions*. M.S. Thesis, University of Pittsburgh, Pittsburgh, USA, 2005

255. Marano, J.J. and G.D. Holder, *A General Equation for Correlating the Thermophysical Properties of n-Paraffins, n-Olefins, and Other Homologous Series. 3. Asymptotic Behavior Correlations for Thermal and Transport Properties.* Industrial & Engineering Chemistry Research, 1997. **36**(6): p. 2399-2408.

256. Marano, J.J. and G.D. Holder, *General Equation for Correlating the Thermophysical Properties of n-Paraffins, n-Olefins, and Other Homologous Series. 2. Asymptotic Behavior Correlations for PVT Properties.* Industrial & Engineering Chemistry Research, 1997. **36**(5): p. 1895-1907.

257. Kudchadker, A.P. and B.J. Zwolinski, *Vapor pressures and boiling points of normal alkanes, C21 to C100.* Journal of Chemical & Engineering Data, 1966. **11**(2): p. 253-255.

258. Wilke, C.R. and P. Chang, *Correlation of diffusion coefficients in dilute solutions.* AIChE Journal, 1955. **1**: p. 264-270.

259. Erkey, C., et al., *A Correlation for Predicting Diffusion Coefficients in Alkanes.* The Canadian Journal of Chemical Engineering, 1990. **68**: p. 661-665.

260. Chang, M.Y., *Mass Transfer Characteristics of Gases in Aqueous and Organic Liquids at Elevated Pressures and Temperatures in Agitated Reactors.* Ph.D. Dissertation, University of Pittsburgh, Pittsburgh, USA, 1991

261. Poling, B.E., et al., *The Properties of Gases and Liquids (5th Ed.).* 2001, New York, NY: McGraw-Hill.

262. Lemoine, R., *Hydrodynamics, Mass Transfer and Modeling of the Liquid-Phase Toluene Oxidation Process.* Ph.D. Dissertation, University of Pittsburgh, Pittsburgh, USA, 2005

263. Mason, R.L., et al., *Statistical design and analysis of experiments : with applications to engineering and science*, New York: Wiley.

264. Boyer, C., et al., *Measuring techniques in gas-liquid and gas-liquid-solid reactors.* Chemical Engineering Science, 2002. **57**: p. 3185-3215.

265. Gharat, S.D. and J.B. Joshi, *Transport phenomena in bubble column reactors, II: pressure drop.* The Chemical Engineering Journal, 1992. **48**(3): p. 153-166.

266. Inga, J.R. and B.I. Morsi, *Effect of Operating Variables on the Gas Holdup in a Large-Scale Slurry Bubble Column Reactor Operating with an Organic Liquid Mixture.* Industrial & Engineering Chemistry Research, 1999. **38**(3): p. 928-937.

267. Sriram, K. and R. Mann, *Dynamic Gas Disengagement: A New Technique for Assessing the Behavior of Bubble Columns.* Chemical Engineering Science, 1977. **32**(6): p. 571-580.

268. Fukuma, M., et al., *Properties of bubble swarn in a slurry bubble column.* Journal of Chemical Engineering of Japan, 1987. **20**(1): p. 28-33.

269. Tarmy, B., et al., *Hydrodynamic characteristics of three phase reactors.* The Chemical Engineer, 1984. **407**: p. 18-23.

270. Kato, Y., et al., *The behavior of suspended solid particles and liquid in bubble columns.* Journal of Chemical Engineering of Japan, 1972. **5**(2): p. 112-118.

271. Smith, D.N. and J.A. Ruether, *Dispersed solid dynamics in a slurry bubble column.* Chemical Engineering Science, 1985. **40**(5): p. 741-754.

272. de Swart, J.W.A. and R. Krishna, *Simulation of the transient and steady state behavior of a bubble column slurry reactor for Fisher-Tropsch synthesis.* Chemical Engineering and Processing, 2002. **41**(1): p. 35-47.

273. Gupta, P., et al., *Comparison of single- and two-bubble class gas-liquid recirculation models-application to pilot-plant radioactive tracer studies during methanol synthesis.* Chemical Engineering Science, 2001. **56**(3): p. 1117-1125.

274. Shah, Y.T., et al., *Two-bubble class model for churn turbulent bubble-column reactor.* Industrial & Engineering Chemistry Process Design and Development, 1985. **24**(4): p. 1096-1104.

275. Lemoine, R., et al., *An Algorithm for Predicting the Hydrodynamic and Mass Transfer Parameters in Slurry Bubble Column Reactors for Fischer-Tropsch Synthesis.* Proceedings of the Twenty Second Annual International Pittsburgh Coal Conference, Pittsburgh, PA, September 12-16, 2005.

276. Behkish, A., et al., *Prediction of the Gas Holdup in Industrial-Scale Bubble Columns and Slurry Bubble Column Reactors using Back-Propagation Neural Networks.* International Journal of Chemical Reactor Engineering, 2005. **3**(A53).

277. Lemoine, R., et al., *An Algorithm for Predicting the Hydrodynamic and Mass Transfer Parameters in Bubble Column and Slurry Bubble Column Reactors.* Fuel Processing Technology, 2008. **89**(4): p. 322-343.

278. De, S.K., et al., *Gas hold-up in two-phase system with internals.* Indian Chemical Engineer, 1999. **41**(2): p. 112-116.

279. Forret, A., et al., *Liquid dispersion in large diameter bubble columns, with and without internals.* Canadian Journal of Chemical Engineering, 2003. **81**(3-4): p. 360-366.

280. Joseph, S., *Hydrodynamic and Mass Transfer Characteristics of a Bubble Column.* Ph.D. Dissertation, University of Pittsburgh, Pittsburgh, USA, 1985

281. Shah, Y.T., et al., *Back-Mixing Characteristics of a Bubble Column with vertically Suspended Tubes.* Transactions of the Institution of Chemical Engineers, 1978. **56**(2): p. 107-112.

282. Inga, J.R. and B.I. Morsi, *Effect of Catalyst loading on Gas/Liquid Mass Transfer in a Slurry Reactor: a Statistical Experimental Approach.* Canadian Journal of Chemical Engineering, 1997. **75**(5): p. 872-881.

283. Botton, R., et al., *Influence of Column Diameter and High Gas Throughputs on the Operation of a Bubble Column.* The Chemical Engineering Journal, 1978. **16**: p. 107-115.

284. Bukur, D.B. and J.G. Daly, *Gas hold-up in bubble columns for Fischer-Tropsch synthesis.* Chemical Engineering Science, 1987. **42**: p. 2967-2969.

285. Camarasa, E., et al., *Influence of Coalescence Behavior of the Liquid and Gas Sparging on Hydrodynamics and Bubble Characteristics in Bubble Column.* Chemical Engineering and Processing, 1999. **38**: p. 329-344.

286. Chen, W., et al., *Scale-up effects on the time-averaged and dynamic behavior in bubble column reactors.* Chemical Engineering Science, 2001. **56**(21-22): p. 6149-6155.

287. Choi, K.H., et al., *Comparative evaluation of hydrodynamic and gas-liquid mass transfer characteristics in bubble column and airlift slurry reactors.* The Chemical Engineering Journal and the Biochemical Engineering Journal, 1996. **62**(3): p. 223-229.

288. Ellenberger, J. and R. Krishna, *A unified approach to the scale-up of gas-solid fluidized bed and gas-liquid bubble column reactors.* Chemical Engineering Science, 1994. **49**: p. 5391-5411.

289. Han, L. and M.H. Al-Dahhan, *Gas-liquid mass transfer in a high pressure bubble column reactor with different sparger designs.* Chemical Engineering Science, 2007. **62**(1-2): p. 131-139.

290. Hyndman, C.L., et al., *Understanding gas-phase hydrodynamics in bubble columns: a convective model based on kinetic theory.* Chemical Engineering Science, 1997. **52**(1): p. 63-77.

291. Idogawa, K., et al., *Behavior of bubbles of the air-water system in a column under high pressure.* International Chemical Engineering, 1986. **26**(3): p. 468-474.

292. Jiang, P., et al., *Flow Visualization of High Pressure (21mpa) Bubble Column: Bubble Characteristics.* Transactions of the Institution of Chemical Engineers, 1995. **73**(A): p. 269-274.

293. Jordan, U., et al., *Dynamic Gas Disengagement in a High-Pressure Bubble Column.* Canadian Journal of Chemical Engineering, 2003. **81**: p. 491-498.

294. Kataoka, H., et al., *Mass Transfer in a Large Bubble Column.* Journal of Chemical Engineering of Japan, 1979. **12**(12): p. 105-110.

295. Li, H., et al., *Effect of micron-sized particles on hydrodynamics and local heat transfer in a slurry bubble column.* Powder Technology, 2003. **133**: p. 177-184.

296. Pino, L.R.Z., et al., *Hydrodynamics of a semibatch slurry bubble column with a foaming liquid.* AIChE Journal, 1990. **36**: p. 1758-1762.

297. Shimizu, K., et al., *Phenomenological model for bubble column reactors: prediction of gas hold-ups and volumetric mass transfer coefficients.* Chemical Engineering Journal, 2000. **78**(1): p. 21-28.

298. Vandu, C.O. and R. Krishna, *Volumetric mass transfer coefficients in slurry bubble columns operating in the churn-turbulent flow regime.* Chemical Engineering and Processing, 2004. **43**(8): p. 987-995.

299. Veera, U.P., et al., *Gas hold-up in foaming liquids in bubble columns.* Chemical Engineering Journal, 2001. **84**: p. 247-256.

300.   Wezorke, H., *Einflüss von Grössblasen in Blasensäulenreaktoren*. Ph.D. Dissertation, University of Dortmund, Dortmund, Germany, 1986

301.   Kastanek, F., et al., *Scaling-up of bubble reactors on basis of laboratory data.* Chemical Engineering Science, 1980. **35**: p. 456-462.

302.   Bukur, D.B. and W.H. Zimmerman, *Modeling of bubble column slurry reactors for multiple reactions.* AIChE Journal, 1987. **33**(7): p. 1197-1206.

303.   Iliuta, I., et al., *Comparative Simulations of Cobalt- and Iron-Based Fischer-Tropsch Synthesis Slurry Bubble Column Reactors.* Industrial & Engineering Chemistry Research, 2008. **47**(11): p. 3861-3869.

304.   Prakash, A., *On the effects of syngas composition and water-gas-shift reaction rate on FT synthesis over iron based catalyst in a slurry reactor.* Chemical Engineering Communications, 1994. **128**(1): p. 143-158.

305.   Rados, N., et al., *Dynamic Modeling of Slurry Bubble Column Reactors.* Industrial & Engineering Chemistry Research, 2005. **44**(16): p. 6086-6094.

306.   Sehabiague, L., et al., *Modeling and optimization of a large-scale slurry bubble column reactor for producing 10,000 bbl/day of Fischer-Tropsch liquid hydrocarbons.* Journal of the Chinese Institute of Chemical Engineers, 2008. **39**(2): p. 169-179.

307.   Song, H.-S., et al., *Multiplicity and sensitivity analysis of Fischer-Tropsch bubble column slurry reactors: plug-flow gas and well-mixed slurry model.* Chemical Engineering Science, 2003. **58**(12): p. 2759-2766.

308.   Stern, D., et al., *A theoretical model for the performance of bubble-column reactors used for Fischer-Tropsch synthesis.* Chemical Engineering Science, 1985. **40**(9): p. 1665-1677.

309.   Wang, Y., et al., *Modeling of the Fischer-Tropsch synthesis in slurry bubble column reactors.* Chemical Engineering and Processing: Process Intensification, 2008. **47**(2): p. 222-228.

310.   Baird, M.H.I. and R.G. Rice, *Axial dispersion in large unbaffled columns.* The Chemical Engineering Journal, 1975. **9**(2): p. 171-174.

311.   Rados, N., et al., *Modeling of the Fischer–Tropsch synthesis in slurry bubble column reactors.* Catalysis Today, 2003. **79-80**: p. 211-218.

312.   Iliuta, I., et al., *Multicomponent multicompartment model for Fischer-Tropsch SCBR.* AIChE Journal, 2007. **53**(8): p. 2062-2083.

313.   Calderbank, P.H., et al., *Catalysis in Practice.* Proceedings of the Symposium of The Institution of Chemical Engineers, 1963: p. 66.

314. Satterfield, C.N. and G.A. Huff, *Effects of mass transfer on Fischer-Tropsch synthesis in slurry reactors.* Chemical Engineering Science, 1980. **35**(1-2): p. 195-202.

315. Deckwer, W.-D., et al., *On the relevance of mass transfer limitations in the Fischer-Tropsch slurry process.* Chemical Engineering Science, 1981. **36**(4): p. 765-771.

316. Deckwer, W.D., et al., *Modeling the Fischer-Tropsch synthesis in the slurry phase.* Industrial & Engineering Chemistry Process Design and Development, 1982. **21**(2): p. 231-241.

317. Bukur, D.B., *Some comments on models for Fischer-Tropsch reaction in slurry bubble column reactors.* Chemical Engineering Science, 1983. **38**(3): p. 440-446.

318. Kuo, J.C.W., *Slurry Fischer-Tropsch/Mobil Two Stage Process of Converting Syngas to High Octane Gasoline.* 1983, U.S. Department of Energy: Washington, DC.

319. Stern, D., et al., *Effects of mass transfer on the performance of slurry reactors used for fischer-tropsch synthesis.* Chemical Engineering Science, 1983. **38**(4): p. 597-605.

320. Turner, J.R. and P.L. Mills, *Comparison of axial dispersion and mixing cell models for design and simulation of fischer-tropsch slurry bubble column reactors.* Chemical Engineering Science, 1990. **45**(8): p. 2317-2324.

321. Leib, T.M., et al., *Evaluation of Neural Networks for Simulation of Three-Phase Bubble Column Reactors.* Chemical Engineering Research and Design, 1995. **73**(A6): p. 690.

322. Inga, J.R. and B.I. Morsi, *A Novel Approach for the Assessment of the Rate-Limiting Step in Fischer-Tropsch Slurry Process.* Energy & Fuels, 1996. **10**(3): p. 566-572.

323. Mills, P.L., et al., *Three-Phase Sparged Reactors; The Fischer-Tropsch Synthesis in Slurry Bubble Column Reactors: Analysis of reactor Performance Using the Axial Dispersion Model.* Topics in Chemical Engineering, ed. R. Hughes. Vol. 8. 1996, Amsterdam, The Netherlands: Gordon and Breach Science Publishers.

324. Maretto, C. and R. Krishna, *Modelling of a bubble column slurry reactor for Fischer-Tropsch synthesis.* Catalysis Today, 1999. **52**(2-3): p. 279-289.

325. Song, H.-S., et al., *Operating Strategies for Fischer-Tropsch Reactors: A Model-Directed Study.* Korean Journal of Chemical Engineering, 2004. **21**(2): p. 308-317.

326. Fernandes, F.A.N., *Modeling and Product Grade Optimization of Fischer-Tropsch Synthesis in a Slurry Reactor.* Industrial & Engineering Chemistry Research, 2006. **45**(3): p. 1047-1057.

327. Guettel, R. and T. Turek, *Comparison of different reactor types for low temperature Fischer-Tropsch synthesis: A simulation study.* Chemical Engineering Science, 2009. **64**(5): p. 955-964.

328. Troshko, A.A. and F. Zdravistch, *CFD modeling of slurry bubble column reactors for Fisher-Tropsch synthesis.* Chemical Engineering Science, 2009. **64**(5): p. 892-903.

329. Yang, G.Q. and L.S. Fan, *Axial Liquid Mixing in High Pressure Bubble Columns.* AIChE Journal, 2003. **49**(8): p. 1995-2008.

330. Mangartz, K.-H. and T. Pilhofer, *Untersuchungen zur Gasphasendispersion in Blasensaulenreaktoren.* Verfahrenstechnik (Mainz) 1980. **14**: p. 40-44.

331. Towell, G.D. and G.H. Ackerman, *Axial mixing of liquid and gas in large bubble reactors.* Proceedings of Fifth European/Second International Symposium on Reaction Engineering, Amsterdam, 1972. **B-1**.

332. Field, R.W. and J.F. Davidson, *Axial dispersion in bubble columns.* Transactions of the Institution of Chemical Engineers, 1980. **58**(4): p. 228-236.

333. Ramachandran, P.A. and R.V. Chaudhari, *Three phase catalytic reactors.* 1983, New York, NY: Gordon and Breach.

334. Rakymkul, Y., *Solubilities and Mass Transfer Coefficients of Gases in Heavy Synthetic Hydrocarbon Liquids*. M.S. Thesis, University of Pittsburgh, Pittsburgh, USA, 2011

335. Cussler, E.L., *Diffusion: Mass Transfer in Fluid Systems*. 1997, New York: Cambridge University.

336. Calderbank, P.H. and M.B. Moo-Young, *The continuous phase heat and mass-transfer properties of dispersions.* Chemical Engineering Science, 1961. **16**: p. 39-54.

337. Marano, J.J. and G.D. Holder, *Characterization of Fischer-Tropsch liquids for vapor-liquid equilibria calculations.* Fluid Phase Equilibria, 1997. **138**(1-2): p. 1-21.

338. Cho, Y.J., et al., *Dynamic characteristics of heat transfer coefficient in pressurized bubble columns with viscous liquid medium.* Chemical Engineering and Processing, 2002. **41**(8): p. 699-706.

339. Fontenelle, A.B. and F.A.N. Fernandes, *Comprehensive Polymerization Model for Fischer-Tropsch Synthesis.* Chemical Engineering & Technology, 2011. **34**(6): p. 963-971.

340. Wagner, W., et al., *The IAPWS Industrial Formulation 1997 for the Thermodynamic Properties of Water and Steam.* Journal of Engineering for Gas Turbines and Power, 2000. **122**(1): p. 150-182.

341. Nayyar and L. Mohinder, *Piping Handbook (7th Edition)*. 2000: McGraw-Hill.

342. Bejan, A. and A.D. Kraus, *Heat Transfer Handbook.* 2003: John Wiley & Sons.

343.   Thom, J.R.S., *Prediction of Pressure Drop During Forced Circulation Boiling of Water.* International Journal of Heat and Mass Transfer, 1964. **7**(7): p. 709-724.

344.   Dittus, F.W. and L.M.K. Boelter, *Heat transfer in automobile radiators of the tubular type.* University of California Publications in Engineering, 1930. **2**: p. 443.

345.   Pethukov, B.S., *Heat Transfer and friction in turbulent pipe flow with variable physical properties.* Advances in Heat Transfer, ed. T.F. Irvine and J.P. Hartnett. Vol. 6. 1970, New York: Academic Press, Inc. 504-564.

346.   Gnielinski, V., *New equations for heat and mass transfer in turbulent pipe and channel flow.* International Chemical Engineering, 1976. **16**: p. 359-368.

347.   Lienhard, J.H., IV and J.H. Lienhard, V, *A Heat Transfer Textbook.* 3rd edition ed. 2000, Cambridge, MA: J. H. Lienhard V.

348.   Bergles, A.E., et al., *Two-Phase Flow and Heat Transfer in the Power and Process Industries.* 1981: Mc Graw-Hill.

349.   Chen, J.C., *Correlation for Boiling Heat Transfer to Saturated Fluids in Convective Flow.* Industrial & Engineering Chemistry Process Design and Development, 1966. **5**(3): p. 322-329.

350.   Steiner, D. and J. Taborek, *Flow Boiling Heat Transfer in Vertical Tubes Correlated by an Asymptotic Model.* Heat Transfer Engineering, 1992. **13**(2): p. 43 - 69.

351.   Frankel, M., *Facility Piping Systems Handbook (2nd Edition).* 2002: McGraw-Hill.

352.   Haaland, S.E., *Simple and explicit formulas for the friction-factor in turbulent pipe flow.* Transactions of the American Society of Mechanical Engineers, Journal of Fluids Engineering, 1983. **105**: p. 89.

353.   Moody, L.F., *Friction factors for pipe flow.* Transactions of the American Society of Mechanical Engineers, 1944. **66**(8): p. 671-684.

354.   Lockhart, R.W. and R.C. Martinelli, *Proposed correlation of data for isothermal two phase, two-component flow in pipes.* Chemical Engineering Progress, 1949. **45**: p. 39–48.

355.   Das, S.K. and A.R. Balakrishan, *Process Heat Transfer.* 2005: Alpha Science Int'l Ltd.

356.   Armand, A.A. and G.G. Treshchev, *Investigation of the resistance during the movement of steam-water mixtures in a heated boiler at high pressures.* AERE Lib./Trans., 1959: p. 816.

357.   Müller-Steinhagen, H. and K. Heck, *A simple friction pressure drop correlation for two-phase flow in pipes.* Chemical Engineering and Processing, 1986. **20**(6): p. 297-308.

358.   Welty, J.R., et al., *Fundamentals of Momentum, Heat, and Mass Transfer (4th Ed.)*. 2000: Wiley & Sons.

359.   Yildiz, S., *Effect of porous coating on two-phase pressure drop of water during up-flow boiling in tubes.* International Communications in Heat and Mass Transfer, 2008. **35**(3): p. 326-337.

360.   Hoffman, J.D., *Numerical Methods for Engineers and Scientists*. 2nd ed. 2001, New York: Marcel Dekker, Inc.

361.   Bao, B., et al., *Simulation, integration, and economic analysis of gas-to-liquid processes.* Fuel Processing Technology, 2010. **91**(7): p. 703-713.

362.   Deckwer, W.D., et al., *Fischer-Tropsch synthesis in the slurry phase on manganese/iron catalysts.* Industrial & Engineering Chemistry Process Design and Development, 1982. **21**(2): p. 222-231.

363.   Shah, Y.T., et al., *Backmixing in Gas-Liquid Reactors.* AIChE Journal, 1978. **24**(3): p. 369-400.

364.   Eissa, S.H. and K. Schugerl, *Holdup and Backmixing Investigations in Cocurrent and Countercurrent Bubble Columns.* Chemical Engineering Science, 1975. **30**: p. 1251.

365.   Gondo, S., et al., *Liquid Mixing by Large Gas Bubbles in Bubble Columns.* Chemical Engineering Science, 1973. **28**: p. 1437.

366.   Hikita, H. and H. Kikukawa, *Liquid-Phase Mixing in Bubble Columns: Effect of Liquid Properties.* The Chemical Engineering Journal, 1974. **8**: p. 191.

367.   Reith, T., et al., *Gas hold-up and axial mixing in the fluid phase of bubble columns.* Chemical Engineering Science, 1968. **23**: p. 619-629.

368.   Blet, V., et al., *Characterization of a Packed Column Using Radioactive Tracers.* Chemical Engineering Science, 1999. **54**: p. 91-101.

369.   Clark, K.N. and N.R. Foster, *Application of Neutron Techniques to Studies of Reactor Fluid Dynamics.* The Chemical Engineering Journal, 1987. **34**: p. 35-46.

370.   Sakai, N., et al., *Fluid dynamics in coal liquefaction reactors using neutron absorption tracer technique.* AIChE Journal, 2000. **46**: p. 1688-1693.

371.   Cova, D.R., *Axial Mixing in the Liquid Phase in Gas-Sparged Columns.* Industrial & Engineering Chemistry Process Design and Development, 1974. **13**(3): p. 292-296.

372.   Deckwer, W.-D., et al., *Mixing and Mass Transfer in Tall Bubble Column.* Chemical Engineering Science, 1974. **29**(11): p. 2177-2188.

373. Joseph, S. and Y.T. Shah, *Errors Caused by Tracer Solubility in the Measurement of Gas Phase Axial Dispersion.* Canadian Journal of Chemical Engineering, 1986. **64**: p. 380-386.

374. Heiskanen, K., *Particle Classification*. 1993: Chapman & Hall.

375. Dahlstrom, D.A., *Cyclone operating factors and capacities on coal refuse slurries.* Transactions of the American Institute of Mechanical Engineers, 1949. **184**: p. 331-344.

376. Flintoff, B.C., et al., *Cyclone modeling: a review of present technology*, in *CIM Bulletin*. 1987. p. 39-50.

377. Plitt, L.R., et al. *Modeling the hydrocyclone classifier*. Proceedings of the European Symposium of Particle Technology, 224th event EFCE. 1980. Amsterdam.

378. Yoshioka, N. and Y. Hotta, *Liquid cyclone as a hydraulic classifier.* Journal of Chemical Engineering of Japan, 1955. **19**: p. 632-640.